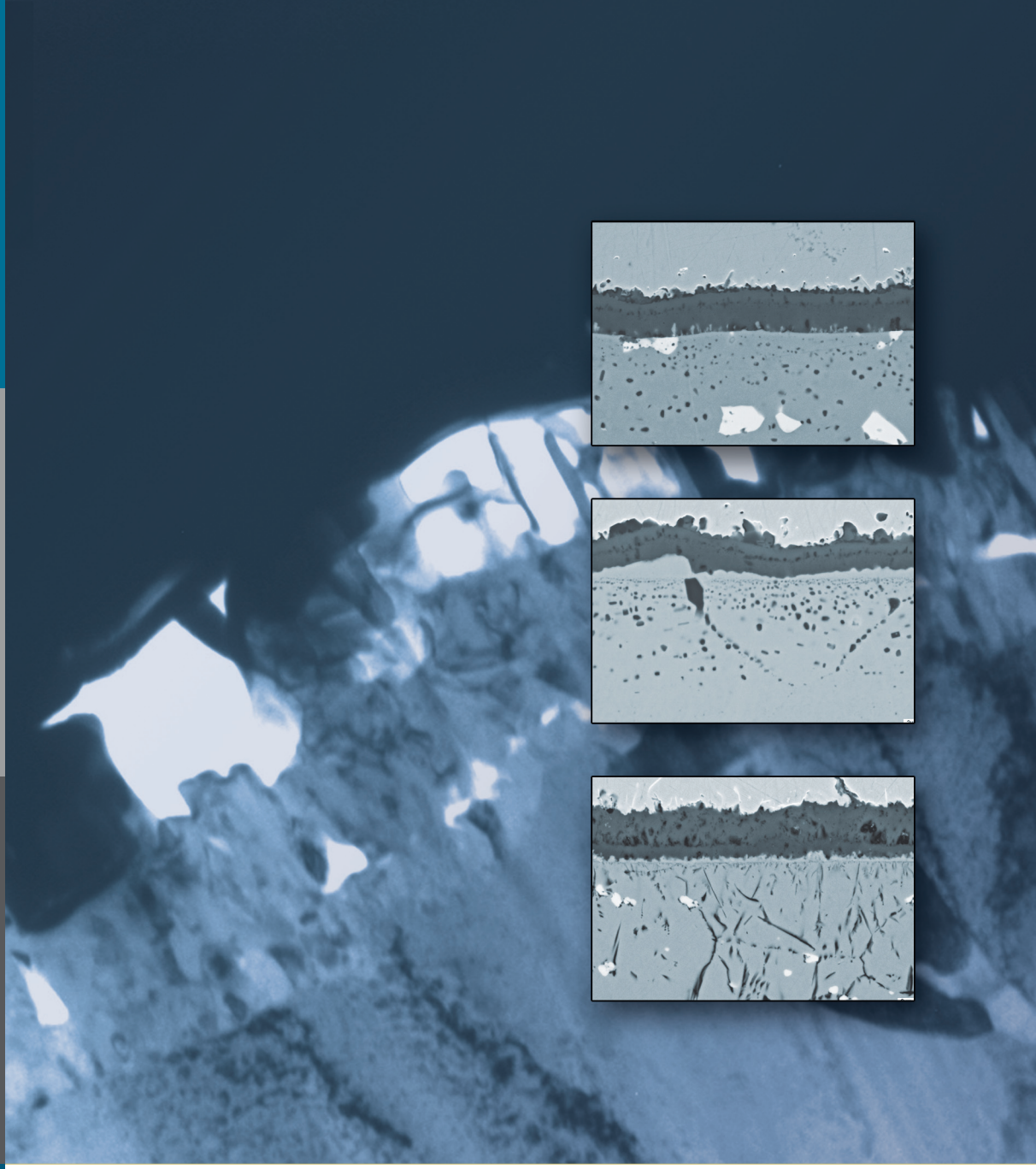

Ferritic Steel Interconnectors and their Interactions with Ni Base Anodes in Solid Oxide Fuel Cells (SOFC)

Jan Froitzheim

Mitglied der Helmholtz-Gemeinschaft

JÜLICH
FORSCHUNGSZENTRUM

Schriften des Forschungszentrums Jülich
Reihe Energie & Umwelt / Energy & Environment Band / Volume 16

Forschungszentrum Jülich GmbH
Institut für Energieforschung (IEF)
Werkstoffstruktur und Eigenschaften (IEF-2)

Ferritic Steel Interconnectors and their Interactions with Ni Base Anodes in Solid Oxide Fuel Cells (SOFC)

Jan Froitzheim

Schriften des Forschungszentrums Jülich
Reihe Energie & Umwelt / Energy & Environment Band / Volume 16

ISSN 1866-1793 ISBN 978-3-89336-540-1

Bibliographic information published by the Deutsche Nationalbibliothek.
The Deutsche Nationalbibliothek lists this publication in the Deutsche Nationalbibliografie; detailed bibliographic data are available in the Internet at http://dnb.d-nb.de.

Publisher and Distributor:	Forschungszentrum Jülich GmbH Zentralbibliothek, Verlag D-52425 Jülich phone:+49 2461 61-5368 · fax:+49 2461 61-6103 e-mail: zb-publikation@fz-juelich.de Internet: http://www.fz-juelich.de/zb
Cover Design:	Grafische Medien, Forschungszentrum Jülich GmbH
Printer:	Grafische Medien, Forschungszentrum Jülich GmbH
Copyright:	Forschungszentrum Jülich 2008

Schriften des Forschungszentrums Jülich
Reihe Energie & Umwelt / Energy & Environment Band / Volume 16

D 82 (Diss., RWTH Aachen, 2008)

ISSN 1866-1793
ISBN 978-3-89336-540-1

The complete volume is freely available on the Internet on the Jülicher Open Access Server (JUWEL) at http://www.fz-juelich.de/zb/juwel

Zusammenfassung

In den letzten Jahren haben sich ferritische Stähle, wie z.B. Crofer 22 APU, als Konstruktionsmaterialien für Interkonnektoren in Hochtemperaturbrennstoffzellen (SOFC) weitgehend durchgesetzt, da diese preisgünstig sind und die Verarbeitung vergleichsweise einfach ist. Es konnte gezeigt werden, dass eine sehr niedrige Konzentration von Al und Si erforderlich ist, um eine optimale Oxidationsbeständigkeit und eine gute Schichthaftung zu erzielen. Neben höheren Herstellungskosten führt dies jedoch zu einer niedrigen Kriechbeständigkeit. Als Folge dessen ergeben sich höhere Oxidwachstumsraten für dünne Komponenten. Das Ziel der vorliegenden Arbeit war die Entwicklung eines ferritischen Stahls mit einer erhöhten Kriechbeständigkeit und einer größeren Toleranz für herstellungsbedingte Verunreinigungen (insbesondere Al und Si) im Vergleich zu Crofer 22 APU.

Zu diesem Zweck wurden Varianten von Crofer 22 APU mit unterschiedlichen Gehalten von W, Nb, Al und Si hergestellt und in Bezug auf SOFC-relevante Eigenschaften untersucht. Die Legierungselemente W und Nb wurden ausgewählt, da sie potentiell geeignet sind, die Kriechbeständigkeit der Legierung aufgrund von Mischkristallverfestigung (W) bzw. Ausscheidungshärten (Nb) zu erhöhen. Die Untersuchungen der Legierungen umfassten Oxidationstests in Luft sowie in simuliertem Anodengas bei 800 und 900°C für bis zu 10000h, Kriechversuche, Messungen der elektrischen Leitfähigkeit der gewachsenen Oxidschichten sowie Messungen des thermischen Ausdehnungskoeffizienten.

Während die Zugabe von W keinen signifikanten Einfluss auf das Oxidationsverhalten hatte, führte die Zugabe von Nb zu erheblich höheren Oxidationsraten. Darüber hinaus konnte gezeigt werden, dass Ausscheidungen von Laves-Phasen, die durch die Zugabe von Nb gebildet werden, eine hohe Affinität für Si besitzen. Dies führt zu einer niedrigeren Si Konzentration in der Legierung. Folglich können Si Verunreinigungen in Nb-haltigen Legierungen toleriert und niedrigere Produktionskosten erzielt werden. Gleichzeitig minimiert Si, indem es die Laves-Phase stabilisiert, den negativen Effekt von Nb auf das Oxidationsverhalten. Dies führt bei Komponenten mit einer Dicke von 1-2mm zu Oxidationsraten, die nahezu identisch mit denen von Crofer 22 APU sind. Durch die höhere Kriechfestigkeit zeigen die neuen Legierungen nur eine schwache Dickenabhängigkeit der Oxidationsrate. Daher ist die Oxidationsrate für dünne Komponenten mit einer Dicke von wenigen Zehntel mm erheblich geringer als die von Crofer 22 APU. Zusammenfassend zeigt sich, dass sorgfältig aufeinander abgestimmte Zugaben von W, Nb und Si zu einer Legierung mit einem vergleichbaren thermischen Ausdehnungskoeffizienten, ähnlicher Duktilität und geringen Oxidationsraten für dünne Komponenten führen.

Neben dem Interkonnektormaterial selbst stellen Kompatibilitätsprobleme mit anderen SOFC Komponenten ein erhebliches Hindernis in der SOFC Entwicklung dar. Für die Kathodenseite ist dies weitgehend bekannt und bereits Gegenstand intensiver Untersuchungen. Auf der Anodenseite hingegen wurde derartigen Problemen bisher kaum Beachtung geschenkt. Daher wurden verschiedene metallische Beschichtungen auf ihre Eignung als Barriereschicht zwischen ferritischem Stahl und Anode bzw. Ni-Netz untersucht. Allerdings konnte keine der untersuchten Schichten alle Anforderungen erfüllen. Gute Barriereeigenschaften zeigten hingegen keramische Schichten aus CeO_2. Des Weiteren konnte gezeigt werden, dass die elektrische Leitfähigkeit von CeO_2 für SOFC Zwecke ausreichend ist. Ein erheblicher Teil des Kontaktwiderstandes von CeO_2 beschichteten Crofer 22 APU Proben ist auf die gewachsene Oxidschicht auf der Stahloberfläche, sowie auf Übergangswiderstände, zurückzuführen. Letztere konnten durch eine Cu-Zwischenschicht erheblich reduziert werden.

Abstract

In recent years high Cr ferritic steels such as Crofer 22 APU became the most widespread construction materials for solid oxide fuel cell (SOFC) interconnects mainly due to low cost and the ease of fabrication compared to ceramic materials. It was shown that optimum properties with respect to oxide scale growth and adherence could only be obtained by very low, carefully controlled concentrations of minor alloying additions such as Al and Si. This required sophisticated alloy manufacturing methods, including vacuum induction melting, resulting in higher manufacturing costs. The high alloy purity also has as result a low creep strength of the material which indirectly resulted in increased oxidation rates of thin components. The aim of the present project was the development of a ferritic steel with improved creep strength and less restrictions with respect to alloy purity (especially Al or Si levels) than in the case of Crofer 22 APU

For this purpose modifications of Crofer 22 APU with various amounts of W, Nb, Al and Si were investigated with respect to SOFC relevant properties. The alloying additions W and Nb were chosen because they are potentially suitable to increase creep strength by solid solution strengthening (W) and precipitation strengthening (Nb). The investigations included oxidation tests in air and anode atmosphere at 800 and 900°C for up to 10000h, creep tests, investigation of the electrical resistance of the surface oxide scale as well as measurements of the coefficient of thermal expansion (CTE).

While the addition of W did not have a major effect on the oxidation behaviour, the addition of Nb resulted in significantly increased oxidation rates. Further it could be shown that the Nb containing precipitates of the Laves phase type had a high affinity for Si which results in a reduced amount of Si in the alloy matrix. Thus, in Nb containing alloys Si impurities can be tolerated which causes lower alloy manufacturing costs. At the same time Si additions suppress the adverse effect of Nb on the oxidation behaviour by stabilising the Laves phase which results in an oxidation rate which, for 1-2mm thick specimens, is almost identical to that of Crofer 22 APU.

Due to the higher creep strength the new alloys exhibited only a slight thickness dependence of the oxidation rates with the consequence, that for thin components of a few tenths of a mm the oxidation rates for the new alloy were smaller than for Crofer 22 APU. Thus, if the amounts of W, Nb and Si were carefully adjusted the new material had, compared to Crofer 22 APU, similar CTE, similar ductility and lower oxidation rates for thin components.

Apart from the interconnect material itself, issues related to compatibility of the interconnect with other cell components are a major problem in the SOFC. While compatibility related issues on the cathode side are widely known and have been extensively studied, diffusion related problems on the anode side have been hardly addressed until now. In the second part of the project a number of metallic coatings were investigated to check their potential suitability for inhibiting interdiffusion processes between ferritic steel and Ni base anode or wire mesh. However, none of the tested coatings could fulfil the requirements. In contrast, CeO_2 turned out to be an efficient diffusion barrier, and its electronic conductivity appeared to be sufficient for SOFC purposes. Measurements of ceria coatings on Crofer 22 APU substrates showed that a considerable part of the area specific resistance is related to the thermally grown oxide scale on the steel surface and to interfacial resistances. The latter can be reduced substantially if an intermediate Cu coating is applied between the steel substrate and CeO_2 barrier layer.

Table of Contents

1. Introduction

In recent years it has become clear that clean electricity production is one of the major engineering tasks of our time. Especially if one considers the steep economic growth of emerging nations like China or India, it becomes apparent that fossil fuels in combination with current technologies cannot cover the worldwide demand for electricity without having a major impact on the world's climate [1]. Nuclear energy could provide some relief, but its use has some severe drawbacks e.g. the risk of accidents, proliferation related hazards and the waste management problem.

Fuel cells are discussed as one of technologies that might offer a contribution to solve this dilemma. They provide high efficiency and, if pure hydrogen is used as fuel, the only reaction product is water. From the different types of fuel cells available, solid oxide fuel cells (SOFC) are maybe one of the most promising technologies. A main advantage of SOFCs is the fact that due to their high operating temperature they can be fuelled not only with hydrogen but also with hydrocarbons. This is an advantage that cannot be underestimated, since all hydrogen has to be produced first, which will take at least the amount of energy that it can later provide in the fuel cell. Hydrocarbon fuels can be produced from renewable as well as fossil sources, although the latter is undesirable due to global warming. However, hydrogen also has significant drawbacks compared to hydrocarbons with respect to storage and transport and thus a hydrogen economy does not seem to be feasible [2].

In recent years much effort has been given to the improvement of SOFC technology and major advances could be established. Nonetheless, further development is needed to make the SOFC a competitive technology. One of the possibilities for improvement is materials selection for all components which include anode, electrolyte, cathode and interconnect. For the latter stainless steels proved to be the group of materials with the most advantageous combination of properties.

The specific requirements for the interconnect application are quite demanding and sometimes even contradictory. These include high temperature oxidation resistance in cathode and anode atmosphere, high electrical conductivity of oxide scales and a thermal expansion coefficient which matches to the other SOFC components. Based on these criteria high chromium ferritic

steels are the most promising interconnect construction materials. There is a wide range of commercial ferritic alloys on the market. However, none of them could fulfil all requirements to the desired level [3]. Thus specific alloys for the SOFC interconnect application were designed recently, one of the most successful ones, is Crofer 22 APU by ThyssenKrupp VDM.

This work investigates a number of alloy modification based on Crofer 22 APU. Different alloying elements were added to increase the creep strength of the material. The effect of these additions as well as the effect of manufacturing related impurities was investigated with respect to oxidation behaviour and other SOFC relevant properties.

2. Aims

Metallic materials are now widely used as interconnect materials in SOFCs operating at approximately 800°C. At these temperatures metallic materials, ferritic steels in particular, offer a number of advantages over La-based ceramics e.g. higher electric conductivity, lower cost and ease of fabrication [4]. However, the use of ferric steels also causes some materials compatibility problems. The cathode poisoning by volatile Cr species is well known but interaction processes on the anode side have not been a major issue in SOFC research so far. This work will elucidate interdiffusion mechanism at the anode side and investigate possible solutions by applying different types of diffusion barrier coatings.

With the progress in SOFC technology cell designs become more ambitious in order to optimise fuel cell costs as well as size and or weight. The latter is especially important if one considers mobile applications in cars. One of the strategies is to reduce the thickness of the interconnect. However, with thinner cross-sections the mechanical properties, especially with respect to creep strength of the material, become more significant.

This problem gained importance as earlier works showed that the level of residual impurities must be kept very low to achieve sufficient corrosion protection [5]. This not only resulted in higher manufacturing costs but also led to reduced creep strength of the material. Indications were found, that this low creep strength had as result that the oxidation rates of thin components of a few tenth's of a mm were substantially higher than that of thick components [6, 7].

In this work the development of a new generation of interconnect material will be discussed which allows higher amounts of manufacturing related impurities to be present and also significantly higher creep strength to be achieved. At the same time other SOFC relevant properties e.g. oxidation resistance, scale conductivity, thermal expansion coefficient should not be adversely affected. An important aim of the development was to reduce the thickness dependence of the oxidation rate previously found for ferritic steels with lower creep strength.

3. Literature Review

3.1 Fuel Cells

Fuel cells are devices that convert chemical energy into electrical energy. In this respect they are similar to usual batteries. However, batteries have a limited amount of electrical energy stored internally and have to be replaced or recharged by reverse current when this storage is consumed. Fuel cells on the other hand are pure conversion devices, fuel has to be supplied externally and as long as this is provided, the fuel cell will operate [8]. In this way they are similar to conventional engines. Engines however, convert heat into power and are thus limited by the Carnot efficiency while fuel cells are not and thus can reach much higher efficiencies.

The concept of fuel cells is by no means new; the invention dates back to the middle of the 19th century when Groves and Schönbein independently built simple fuel cells. Both used platinum as electrodes and sulphuric acid as electrolyte. Within the next century further improvement in understanding of electrochemical theory helped to establish the principle behind the fuel cell, and a number of researchers improved the technology. However, due to the invention of the internal combustion engine it was not until the 1960s that fuel cells found their application. In the space programs Gemini and Apollo as well as in the Space Shuttle, fuel cells were used to produce electricity, with the advantage that the reaction product was water, a needed resource [8-10].

3.2 Principle of a Fuel Cell

Fuel cells vary widely in design, but all types need three components which are required for the electrochemical reaction; these are electrolyte, an anode and a cathode. Generally to prevent direct combustion the electrolyte is separating the anode compartment filled with fuel (e.g. hydrogen) from the cathode compartment where the oxidant (air) is present. On the other hand the electrolyte must have a selective permeability for one of the reactants in order to allow the reaction to proceed. Thus, the electrolyte is separating the reaction into two half reactions. Therefore it is required that the electrolyte is an ion conductor. Ions will pass

through the electrolyte and react to water (in the case of hydrogen fuel) at the anode side. The charge separation due to the ion movement is balanced by a counter flow of electrons and this current can be used for the specific application [8, 10].

3.3 Types of Fuel Cells

Fuel cells can be generally divided into six classes usually named after the electrolyte which is utilised. These types vary significantly in performance, fuel, operating temperature and design; Table 1 gives a brief overview indicating the most important features.

Type	Mobile Ion	Operating Temperature	Fuel	Applications
Alkaline (AFC)	OH^-	50-200°C	H_2	Used for the Apollo mission
Proton exchange membrane (PEMFC)	H^+	30-100°C	H_2	Vehicles and mobile applications
Direct methanol (DMFC)	H^+	20-90°C	Liquid methanol	Portable electronics, low power, running for long times
Molten carbonate (MCFC)	H^+	~220°C	Hydrocarbons, H_2, CO	Suitable for medium to large scale systems
Phosphoric acid (PAFC)	CO_3^{2-}	~650°C	H_2	Large numbers of 200kW units in use
Solid oxide (SOFC)	O^{2-}	600-1000°C	Hydrocarbons, H_2, CO	Potentially Suitable for all sizes from a few kW to multi MW

Table 1: Typical characteristics of different types of fuel cells [11]

All those systems have specific disadvantages e.g. the PEMFC and the AFC need high purity hydrogen fuel, the latter is even sensitive to CO_2 in ambient air. The PAFC and especially the MCFC have the drawback of highly corrosive electrolytes while the DMFC has a low power output [11]. A more detailed discussion of different fuel cell types is beyond the scope of this work which will only focus on the SOFC, but can be found elsewhere e.g. in [11].

3.4 Solid Oxide Fuel Cells (SOFCs)

The main features that distinguish SOFCs from other types of fuel cells are their all solid design and their high operating temperature [12]. This results in some specific advantages, most importantly the fact that SOFCs do not need pure hydrogen as fuel but can also run on hydrocarbons. Other advantages are that no electrolyte management is necessary and due to the high temperature no precious metal catalysts are required. On the other hand the ceramic design in combination with the high temperatures results in other SOFC specific disadvantages. For example the thermal stresses generated when changing temperature between ambient air and the high operating temperature (e.g. 600-900°C) require careful matching of thermal expansion coefficients, otherwise the cell will be damaged during heating or cooling [8]. Fig. 3.1 shows the concept of the SOFC. In order to produce an electric current which can be used a charge separation is required; this is caused by the oxygen ions which migrate through the electrolyte to the fuel side where they react with hydrogen to water vapour. The driving force for the reaction to happen is a steep oxygen gradient through the electrolyte. At the air side the oxygen partial pressure is approximately 0.2bar if air of 1bar is used as oxidant gas. On the fuel side oxygen partial pressures of approximately 10^{-18}bar are common. The specific components of a SOFC will be discussed briefly in the following sections [13, 14].

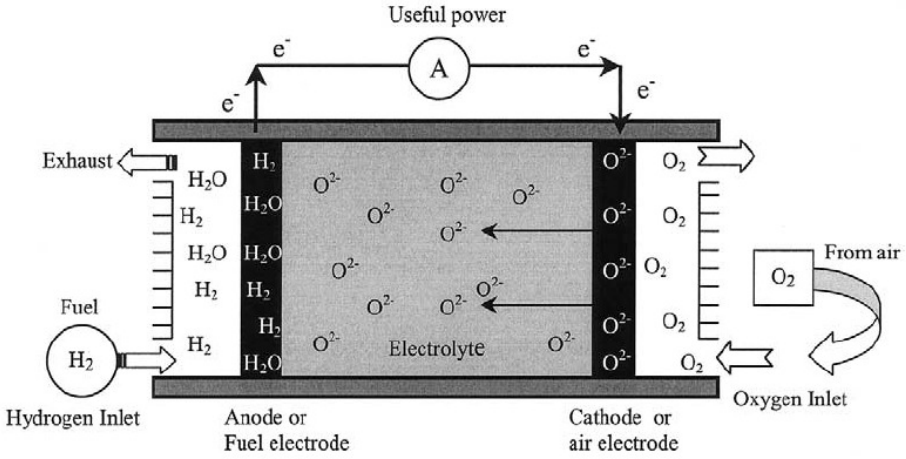

Fig. 3.1: Principle of a SOFC [8]

3.4.1 Electrolyte

The electrolyte is the heart of every fuel cell. Since it is exposed to anode and cathode atmospheres it must be stable both in reducing and in oxidising environments. Further, it has to be gas-tight and provide sufficient mechanical stability. In order to achieve good cell performance a high ionic conductivity in combination with a very low electronic conductivity is necessary. The most widespread electrolyte material used in SOFCs is yttrium (8-10 wt.%) doped ZrO_2 (YSZ). The yttrium doping stabilises the tetragonal phase and leads to an increase in oxygen vacancy concentration since Y^{3+} ions replace Zr^{4+} which is balanced by formation of oxygen vacancies. This results in higher conductivity of O^{2-} ions. However, as this is a solid state diffusion process, it requires high temperatures around 800°C to allow significant numbers of ions to pass. Other materials like doped ceria (CeO_2) or materials with perovskite structure are discussed as electrolyte materials as well, but yttria-stabilised zirconia is by far the most widespread [15, 16].

3.4.2 Cathode

One of the most important properties for cathode materials is a high catalytic activity for the reduction of oxygen. Further important are: high electrical conductivity, chemical compatibility with the electrolyte and matching coefficients of thermal expansion (CTE). The very first SOFCs designs used platinum cathodes, but due to high costs ceramics with perovskite structure soon gained attention. Since then a wide number of materials, mainly

doped La based perovskites, have been suggested and used as cathode materials. The most common material today is strontium-doped lanthanum manganite (LSM). However, at lower temperatures LSM suffers from a low oxygen ion conductivity and other materials like $(La,Sr)(Co,Fe)O_3$ (LSCF) gained importance. Generally, the cathode is made of a porous material to allow rapid gas transport and an increased surface area [16, 17].

3.4.3 Anode

The anode requires a similar set of properties as the cathode. Here the fuel becomes oxidised by the oxygen ions that migrated through the electrolyte. Thus a porous structure with high electronic conductivity and catalytic properties is required. Further, chemical compatibility and a match of CTE with other components are needed. Early anodes were made of platinum or nickel. In the 1960s the first Ni/YSZ ceramic metal composites (cermets) where used; these materials are now the most commonly applied anodes. However, other anode materials e.g. ceria-based materials are discussed as well [16, 18].

3.4.4 Interconnect

The interconnect or bipolar plate is the connecting unit between the single cells in a stack. It has two main functions: first it has to provide electrical contact between the single cells, and second it has to separate the fuel and air sides and distribute the gases to the cells. Earlier SOFC stacks used lanthanum chromite ceramics as interconnect materials. However, in recent years there was a trend towards lower operating temperatures and metallic interconnects then become more attractive [19, 20]. Compared to ceramic interconnects metallic materials have the advantage of lower cost and easier fabrication. Nonetheless, metallic interconnects have certain disadvantages, a major problem is caused by chromium diffusing out of the interconnect poisoning the cathode by blocking electrochemically active sites. Therefore, additional protective coatings seem to be required [4, 11, 21].

A critical requirement for metallic interconnects is the formation of a protective oxide scale which at the same time possesses a high electronic conductivity. Further requirements are a thermal expansion coefficient that matches to the other cell components and suitable mechanical properties. In the subsequent chapters fundamental aspects concerning these properties will be discussed and in section 3.9 metallic interconnect development will be discussed in more detail [4].

3.4.5 SOFC Design

Based on their design SOFCs can be divided into two groups. First there is a tubular design developed by Siemens Westinghouse in the 1970s which was revised and improved several times. The advantage of the tubular design is that it does not require any high temperature sealing; disadvantageous are high costs and low power density. The other major design variation is the planar design. This design allows significantly higher power densities than the tubular design. On the other hand the planar design is very sensitive to thermal stresses, thus thermal cycling becomes problematic. The planar design can be subdivided into different concepts depending on which part is providing the mechanical support as shown schematically in Fig. 3.2. For self-supported cells it is either the anode, the cathode or the electrolyte that provides the mechanical support. The supporting layer is generally thicker, in the case of electrolyte supported cells usually >100µm. This requires higher operating temperatures due to high ohmic losses in the electrolyte. The Forschungszentrum Jülich works with an anode-supported cell design which allows lower operating temperatures because of the higher conductivity of the anode material [22]. Externally supported cells have a metallic substrate which has superior conductivity while the ceramic layers can be manufactured thinner. However, material compatibility issues may cause additional problems [16, 23].

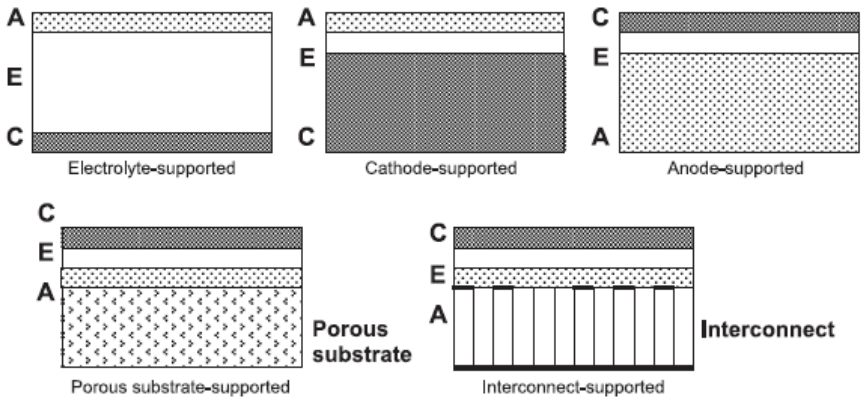

Fig. 3.2: Different planar SOFC designs [12] A- anode E- electrolyte C – cathode

3.5 Fundamentals of Oxidation

3.5.1 Thermodynamics

Whether a chemical reaction is going to occur or not can be derived from the second law of thermodynamics. It states:

$$\Delta G = \Delta H - T\Delta S$$

where ΔG represents the change in Gibbs free energy, ΔH is the difference in enthalpy and T and ΔS correspond to temperature and change in entropy, respectively. For all values where ΔG is negative the reaction can proceed, at $\Delta G = 0$ thermodynamic equilibrium is reached while positive ΔG values energy has to be added to make the processes go.

According to thermodynamics an oxidation process

$$xM + \frac{y}{2}O_2 = M_xO_y$$

can be described as

$$\Delta G = \Delta G° + RT \ln\left(\frac{a(M_xO_y)}{a(M)^x a(O_2)^{\frac{y}{2}}}\right)$$

where $\Delta G°$ is the free energy change when all species are in their standard states. R corresponds to the ideal gas constant and a denotes the activity for the specific specie. The equation can be simplified by setting the activities of pure solids to unity. In equilibrium ΔG equals zero thus the equation can be rewritten as

$$\Delta G° = -RT \ln\left(\frac{1}{a(O_2)^{\frac{y}{2}}}\right)$$

if one approximates the oxygen activity with the partial pressure of oxygen this reduces to

$$p_{O_2} = exp\left(\frac{\Delta G°}{RT}\frac{2}{y}\right)$$

Knowing the free energy of formation this equation can be used to calculate the partial pressure of oxygen where metal and oxide are in equilibrium at a given temperature; this is called the dissociation pressure of the oxide. A graphical representation of this is the so called

Ellingham/Richardson diagram, which can be seen in Fig. 3.3. Each line corresponds to the dissociation pressure of a specific oxide at different temperatures (x-axis). This allows the comparison of the thermodynamic stability of different oxides directly with each other: the lower the dissociation pressure of the oxide, the more stable it is thermodynamically [24].

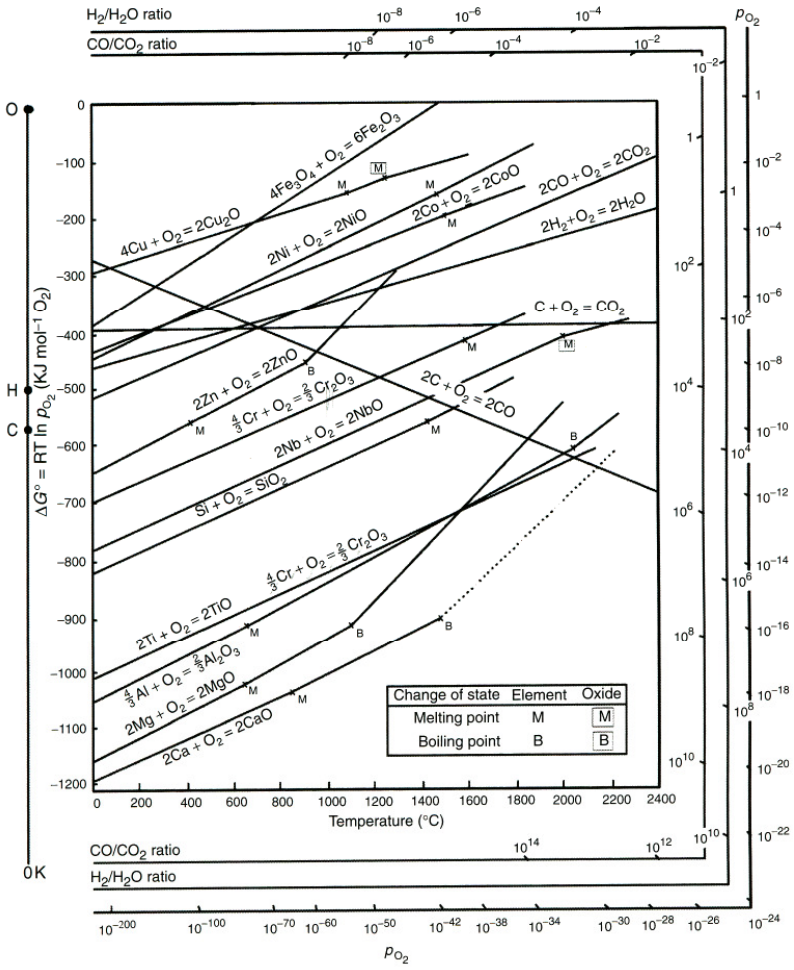

Fig. 3.3: Free energy of formation for selected oxides (Ellingham/Richardson diagram) [24]

3.5.2 Kinetics of Oxidation

Considering the Ellingham/Richardson diagram one can see that at higher temperatures all oxides become less stable, thus the driving force for the reaction is reduced. This is against common sense as it is known that higher temperatures will result in faster oxidation. However, this correct observation is due to the fact that the kinetics of oxidation is usually governed by diffusion processes in the oxide scale. In fact if a fresh metal surface is exposed to an atmosphere which allows oxidation it is almost instantaneously covered with an extremely thin oxide layer. The reactants are now separated and any further reaction is governed by solid state diffusion through the oxide scale.

Oxides are ionic crystals; this means they are formed by an ordered array of oxygen anions and metal cations. However, no crystal is perfect but features some defects which govern its diffusion properties. In fact all oxides are slightly non-stochiometric, this means their exact composition is not as it appears in their chemical formula but instead metal or oxygen can be in excess or deficient. Oxides are classified like semiconductors as n- or p-type depending whether the transport of electric charge is governed by electrons (n-type) or electron holes (p-type).

The defects in an n type oxide can be either metal interstitials (excess metal) or oxygen vacancies (oxygen deficient) or a combination of both. This can be explained as followed: an interstitial metal cation has a positive charge compared to the perfect lattice. This has to be balanced by extra electrons in the conduction band. The same applies for the oxygen vacancies; the lack of an oxygen anion corresponds to a positive charge with respect to the normal lattice and has to be balanced by electrons as well. In contrast, p-type oxides have metal vacancies or oxygen interstitials corresponding to a negative charge with respect to the lattice in this case the charge is compensated by electron holes.

Frequently the transport through the oxide scale is the rate determining step for the oxide growth. To what extent material transport through the scale is possible depends on the oxide defect structure. Oxygen ions can diffuse through materials which have oxygen vacancies since the transport of an oxygen ion can also be considered as the movement of a vacancy in the opposite direction. Metal ions can diffuse either as interstitials or on their usual lattice sites by vacancy diffusion in the opposite direction. Whether oxygen anions or metal cations

are the mobile species affects the scale growth mechanism. If oxygen ions are the mobile species they will penetrate through the oxide scale and the new oxide will be formed at the metal-scale interface. On the other hand, if metal ions can diffuse outwards they will react with oxygen at the scale-gas interface and the fresh oxide will be formed there.

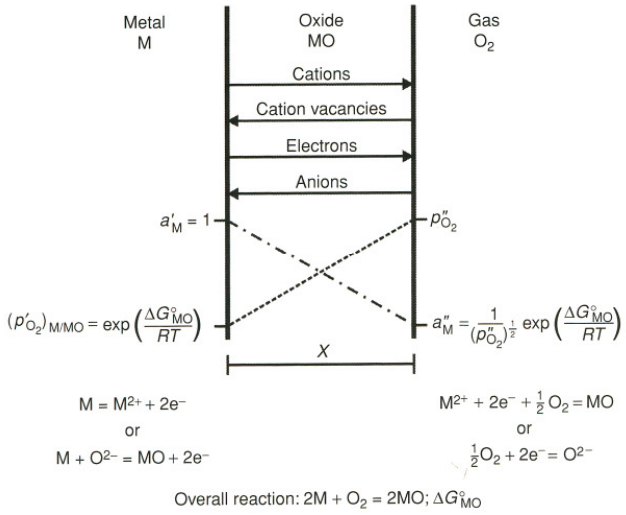

Fig. 3.4: Schematic representation of Wagner's model of oxidation [24]

Generally, non-stochiometric oxides which have a large number of defects grow fast while oxides like Cr_2O_3 or Al_2O_3 have very few point defects and thus grow slowly. The first description of high temperature oxidation was given by Wagner [25]. For his theory several assumptions are required. The most important is that the diffusion through the scale is the rate-controlling step and thus thermodynamic equilibrium is established at both interfaces. Hence an oxygen activity gradient is present: at the scale surface the oxygen partial pressure corresponds to that of the ambient atmosphere while it equals the dissociation pressure of the oxide at the metal-scale interface. According to Fick's first law the flux of ions (j) is proportional to the gradient of the chemical potential ($\Delta\mu$) through the scale of thickness (x):

$$j = -D\frac{\Delta\mu}{x}$$

Scale growth can be considered as a flux of ions times the molar volume of the formed oxide.

$$\frac{dx}{dt} = j * V_{ox}$$

Integration yields to

$$x^2 = 2K_p * t$$

where *Kp* substitutes the product of diffusion coefficient, molar volume of the oxide and chemical potential gradient.

$$K_p = DV_{ox}\Delta\mu$$

This approach yields to a parabolic growth rate which is often observed in high temperature corrosion environments. Other growth mechanisms are also possible e.g. linear growth kinetics may occur if the gas phase transport to the surface is the rate-determining step. This is usually the case in the initial stages of oxidation when the scale is extremely thin. Another important simplification in Wagner's theory is that it does not take into account short circuit diffusion. This term describes diffusion along dislocations or grain boundaries which is several orders of magnitude faster than lattice diffusion and is more important than lattice diffusion at lower and intermediate temperatures [24, 26].

3.5.3 Oxidation of Fe-Cr Alloys

Oxidation of alloys is more complex than the oxidation of pure metals, but the same principles apply. In the case of Fe-Cr alloys a number of different oxides may form. Chromium forms Cr_2O_3 while iron may form up to three different oxides: FeO, Fe_3O_4 and Fe_2O_3. Additionally a mixed $(Fe,Cr)_3O_4$ spinel may form as well as various solid solutions between the various oxides. According to the Ellingham Richardson diagram (Fig. 3.3) Cr_2O_3 is the more stable than the iron oxides. For the mixed oxides one can assume as first approximation that the stability of the respective mixed oxide is situated between the corresponding pure oxides, thus $(Fe,Cr)_3O_4$ is more stable than FeO but less stable than Cr_2O_3. Generally, any multilayered oxide scale on a pure metal will have the least stable oxide on top where the oxygen partial pressure is highest. In equilibrium at the bottom of that top layer the oxygen partial pressure equals the dissociation pressure of the respective oxide - thus it is unstable below that value. However, any oxides with lower dissociation pressure may still form. Thus, below the top oxide layer the second least stable oxide can form a layer, below this second layer more stable oxides may be present. A schematic drawing of this behaviour is presented in Fig. 3.5 for Fe-Cr alloys at 1000°C. It can be seen that the formation and composition of the multilayered oxide strongly depends on the composition of the alloy. If the

Cr content is sufficiently high, Fe-oxide formation is suppressed and a pure Cr_2O_3 layer is formed. However, after longer times, depletion of Cr might cause a change in behaviour [6].

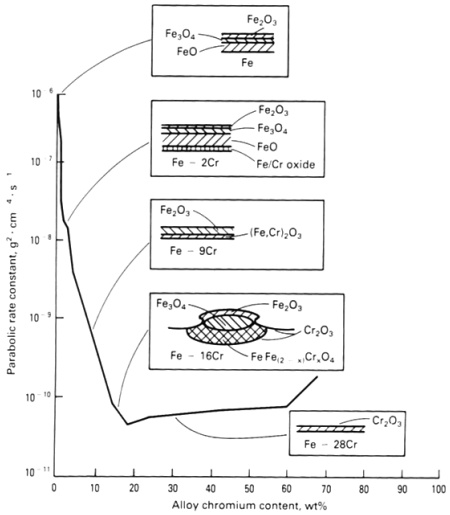

Fig. 3.5: Schematic representation of the formed oxide scales on Fe-Cr alloys with different Cr contents at 1000°C [27]

Since Cr_2O_3 is a slowly growing oxide the growth mechanism and defect structure of Cr_2O_3 are difficult to determine and literature data are sometimes contradictory. It is widely accepted that Cr_2O_3 behaves as n-type semiconductor at low oxygen partial pressures while it shows p-type behaviour at higher pO_2. Kofstad suggests that Cr vacancies predominate at higher pO_2 while Cr interstitials are the dominant defects at low pO_2 [28]. The slow growth rate of Cr_2O_3 makes it one of the most important surface oxides for corrosion protection.

Minor element additions in Fe-Cr alloys can have a significant effect on the oxide scale composition and properties. The most important elements for interconnect applications are Mn, Si, Al, Ti and so called reactive elements (RE). The first three elements are usually present in ferritic steels at levels of around 1 wt.%; Ti and other oxygen active elements, are, if added, commonly present in contents of approximately 0.1%.

Additions of Mn cause the formation of a two-layer oxide scale with a top layer of $(Cr,Mn)_3O_4$ spinel and an inner layer of chromia. Minor additions of Si and Al can be found in most alloys as the elements are needed to reduce the oxygen levels in the alloy melt. Their

oxides (SiO_2 and Al_2O_3 respectively) are more stable than Cr_2O_3 and thus are commonly found below the Cr rich surface oxide scale. SiO_2 can be usually found at the scale metal interface, and if a sufficient amount of Si is available, it may form a continuous layer causing a steep drop in scale conductivity. Another negative effect of silica subscale formation is that its low thermal expansion coefficient may cause increased spallation of the oxide scale during thermal cycling. Al_2O_3 can be mainly found at the steel grain boundaries. If Ti is present it can be often found internally oxidised below the oxide scale. Internal oxidation takes place when oxygen becomes dissolved in the alloy below the oxide scale. Here it reacts with metals that have the highest affinity to oxygen. The term reactive element refers to a number of elements such as La, Y, Ce and Hf. It is widely known that small additions of these elements may have a significant effect on the oxidation resistance of the alloy because they tend to improve the scale adherence. However, the mechanisms which are responsible for this effect are not completely understood [24]. A number of them have been proposed in numerous studies. Quadakkers compared a conventional Ni-Cr alloy with an ODS alloy containing Y_2O_3 by tracer studies [29]. He showed that, while in the case of conventional alloy the scale grows by inward diffusion of oxygen and outward diffusion of metal ions, the presence of yttria blocks outward diffusion of metal and thus reduces the growth rate. The decreased outward cation diffusion is accompanied by a reduced inward flux of cation vacancies resulting in a improved scale adherence. Other mechanisms proposed for the improved scale adherence include for example: oxide particles serve as vacancy sinks and thereby reduce void formation or reduced growth stresses due to a different growth mechanism [24, 26].

3.6 Electrical conductivity basics

In order to achieve a high power output the ohmic losses within the SOFC should be as low as possible. The resistance R which governs the useful current of an SOFC depends on the component's dimensions, while the conductivity σ depends only on the material.

$$R = \frac{1}{\sigma} * \frac{L}{A}$$

Usually the length L and the area A are given in cm and cm² respectively, consequently the conductivity is given in $\Omega^{-1}cm^{-1}$ or S/cm. In the case of oxides grown on metals or alloys data in the literature are often given as contact or area specific resistance (ASR) in $\Omega * cm^2$.

$$ASR = R * A = \frac{L}{\sigma}$$

The metallic interconnect has a conductivity which is several orders of magnitudes higher than any ceramic material used in the SOFC. Thus the resistance of the interconnect will be governed by the oxide scale formed on the metal surface. Unfortunately, oxides with good protective properties have to be oxides with few point defects; this, however, generally results in low electrical conductivity. Al_2O_3 and SiO_2 are known to be insulators thus their formation must be avoided by keeping Si and Al levels in the alloy very low. The electrical conductivity of Cr_2O_3 is poor compared to the La based ceramics proposed as interconnect materials. However, it is much higher than that of other protective oxides on high temperature alloys i.e. SiO_2 and Al_2O_3. Furthermore it has to be considered, that the thickness of the Cr_2O_3 scale will be only in the range of a few µm compared to an all ceramic interconnect, so that the resistance of the chromia surface scale will be smaller than that of a $LaCrO_3$ interconnect of a few mm thickness.

The electronic conductivity of Cr_2O_3 like that of any other semiconductor strongly depends on the temperature where higher temperatures lead to higher conductivity. Apart from that the conductivity is governed by the defect structure of the material which is in equilibrium with the ambient atmosphere. For example low pO_2 atmospheres may result in an increase of the oxygen vacancy concentration in the material, which affects the conductivity. Cr_2O_3 is a p-type oxide at atmospheric pressure while at pressures close to its decomposition pressure Cr_2O_3 has excess metal with Cr interstitials as the dominating point defects [30]. At temperatures below 1000°C measurements become increasingly difficult and results indicate that impurities govern the conductivity mechanism at these temperatures. A study by Holt and Kofstad showed the influence of Mg and Ti doping on the conductivity. Ti has a higher valency than Cr ions. At low pO_2 the excess charge of the Ti is compensated by electrons, which leads to an increase in conductivity of approximately one order of magnitude [31, 32]. Literature data about the conductivity of Cr-Mn spinels as a function of pO_2 are rare, except for a study by Sakai et al. [33]. According to their data the electrical conductivity of the $MnCr_2O_4$ spinel is similar to that of chromia at ambient pO_2 but is approximately one order of magnitude lower in typical SOFC anode atmospheres.

3.7 Fundamentals of alloy creep

Creep is time dependent plastic deformation of materials at high temperatures due to an applied load. Even if this load is significantly lower than the yield strength of the material at high temperatures (>0.5 T_m) it is sufficient to cause plastic deformation by a number of thermally assisted mechanisms after longer times. These mechanisms include diffusional creep, grain boundary sliding and dislocation creep. The first mechanism describes the flux of vacancies or atoms to sites of lower energy, however, this mechanism usually does not play a substantial role except at very high temperatures or at intermediate temperatures in combination with low stresses. The amount of grain boundary sliding naturally depends on the grain size and describes a mechanism where grains slide along each other whereas dislocation creep refers to movement of dislocations within the grains. It is well known that as plastic deformation proceeds the number of dislocations increases. However at higher dislocation densities they can obstruct each other resulting in hardening of the material. Such immobile dislocations may become mobile again by dislocation climb which is a thermally activated process [34, 35].

Fig. 3.6 shows a typical creep curve of a metallic material. The curve can be divided into three parts which are termed primary, secondary and tertiary creep. At the end of the first phase the creep rate is slowing down as is becomes more difficult for dislocations to move. In the second part the creep rate is constant, hardening mechanisms are balanced mainly by dislocation climb which allows further deformation. In the last part of the curve void formation occurs and the creep rate accelerates until finally fracture occurs [36].

There are two major mechanisms for improving the creep resistance of alloys: solid solution- and precipitation strengthening. Solid solution strengthening refers to foreign atoms in the alloy which occupy either normal lattice or interstitial sites. Such added atoms cause a stress field in their vicinity which interacts with the stress field of a dislocation. Precipitation hardening describes hardening by secondary phases forming precipitates. Such precipitates also act as obstacles for dislocation movement. However, during long term service at high temperatures the number of precipitates decreases due to Ostwald ripening which results in fewer obstacles to dislocation movement.

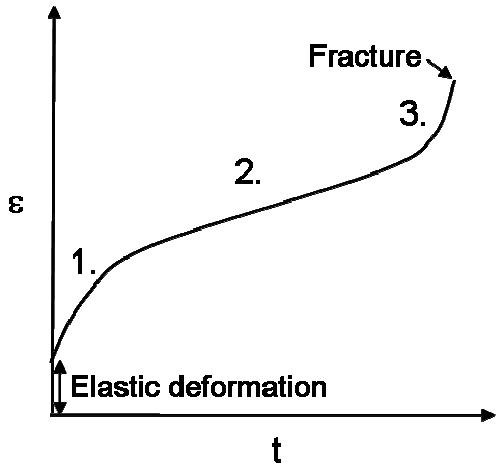

Fig. 3.6: Typical creep curve of a metallic material at constant stress

3.8 Ferritic Steels

The term ferritic steel refers to a material with the same body-centred cubic (bcc) crystal structure as ferrite or α-iron. Nearly all commercially available steels for high temperature application contain chromium as main alloy element. The iron chromium phase diagram is depicted in Fig. 3.7. The two most important features are the closed γ-phase field, with the result that γ cannot be stable beneath 851°C, and the formation of the σ-phase below 820°C in alloys with high Cr content. The γ-phase is termed austenite and possesses a face-centred cubic (fcc) structure. It is not stable at Cr contents above 14% unless additional elements are added; strong austenite stabilizers are e.g. Ni. or C [37]. The σ-phase is an intermetallic phase and its formation is known to cause embrittlement of the material [38]. The maximum rate of formation is at 750°C. Higher temperatures decrease the amount of nuclei while below 600°C the growth rate becomes very slow. Steels with Cr contents exceeding approximately 20%, as they are used for SOFC applications can be subject of σ phase embrittlement, depending on the exact composition of the material. E.g. ferrite stabilizing elements like Si and Mo promote the formation of σ phase. Small amounts of Mn also stabilize the σ phase while higher concentrations retard its formation [38, 39].

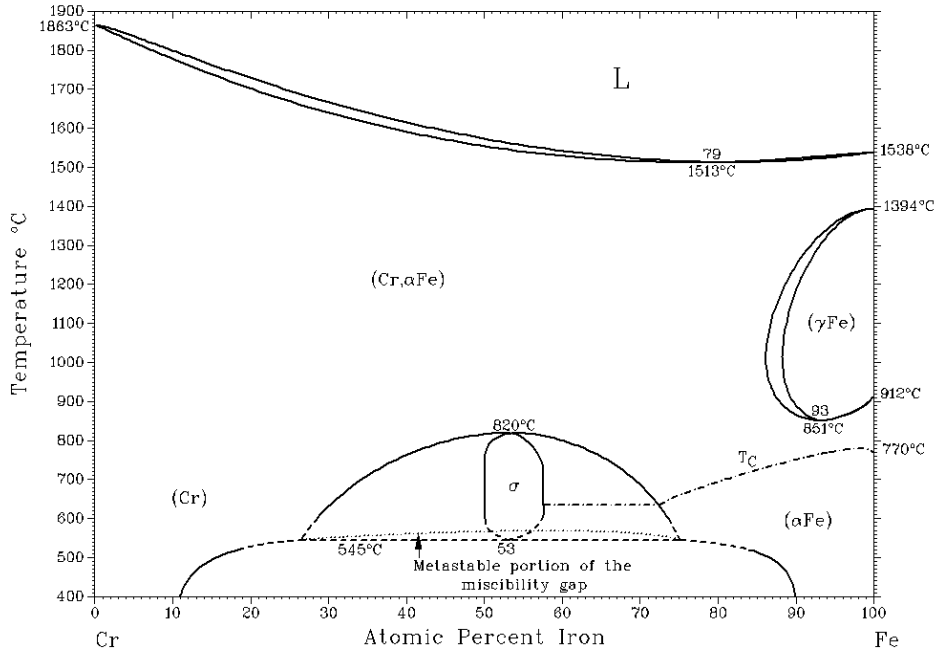

Fig. 3.7: Cr-Fe Phase diagram [40]

3.9 Metallic Interconnect Development

The main properties required for a material used as SOFC interconnect are [4]:

- High electronic conductivity, including formed surface oxide scales
- Thermal stability in air and anode environment at operating temperature
- Coefficient of thermal expansion (CTE) which matches closely to other cell components
- Gas tightness
- Suitable mechanical properties

All these requirements are met by La-chromite ceramics which were used as a common interconnect material. However, the La-chromites are relatively expensive, brittle and cannot be machined. Therefore, there is a general trend in SOFC research towards lower operating temperatures. While operating temperatures of 1000°C were discussed a few years ago more recent studies focus on operating temperatures of 800°C or even 500°C [41, 42]. This allows

to consider metallic materials which can be manufactured at lower costs than ceramics as construction material for interconnects [4, 43].

The use of noble metals as construction material for interconnects is not feasible due to their high costs. Therefore, a number of high temperature alloys have been considered for the interconnect applications. These alloys rely on three possible elements that are known to form protective scales. These are Cr, Si and Al which form protective Cr_2O_3, SiO_2 or Al_2O_3 scales respectively. The latter two oxides have insulating properties, and are therefore not suitable for SOFC applications since the interconnect has to provide the electrical contact of the single cells in the stack. Cr_2O_3 possesses a much higher electronic conductivity, although it is poor compared to some La-based perovskites. This is, however, not a major drawback because there will be just a few µm thick Cr_2O_3 scale compared to an all ceramic interconnect with a thickness in the range of approximately 0.1mm [44].

For this reason, the oxidation protection of metallic materials for interconnects can only be achieved by Cr_2O_3 scales while the amounts of Si and Al have to be kept low to avoid formation of a continuous scale of these oxides. Another important property for the interconnect application is a coefficient of thermal expansion (CTE) matching to the other cell components. The electrolyte material YSZ has a CTE of 9.4-11 * 10^{-6} K^{-1} [16] the Ni/YSZ cermet commonly used for anodes has a CTE of approximately 12.5 * 10^{-6} K^{-1} [4, 45]. Two widespread types of high temperature alloys, Ni-based alloys and austenitic steels possess significantly higher CTE values (15-20 * 10^{-6} K^{-1} [43]) and thus their application is not feasible unless a special cell design is used that can tolerate strains generated during temperature changes. The restrictions due to CTE matching limits the choice of interconnect materials to Cr-based alloys and ferritic stainless steels [4]. Metallwerke Plansee AG developed a Cr-based alloy with 5wt% iron and 1wt% yttria, which possesses a CTE close to that of the electrolyte. The alloy has to be produced by powder metallurgical methods: the metals and fine Y_2O_3 particles are mixed by high energy ball milling, pressed and sintered. This type of alloy is termed oxide dispersion strengthened (ODS) alloy. ODS alloys usually have superior mechanical properties compared to conventionally manufactured alloys, however, the manufacturing process is far more expensive so that the cost advantage compared to ceramic interconnects is partly lost. High Cr ferritic stainless steels on the other hand are common construction materials and are cheap compared to ODS alloys. Their CTE

and oxidation resistance make them potentially suitable for SOFC applications if the operating temperatures are not too high [4, 16].

3.10 Ferritic steels designed for SOFC applications

Pirón et al. [3] extensively tested a variety of commercial ferritic steels and it turned out that hardly any of the commercial available alloys can fulfil the specific requirements for SOFC interconnect application. Especially the contact resistances of the oxide scales proved to be critical due to the presence of Si and Al which resulted in the formations of electrically insulating scales. Also the adherence of the surface oxide scales appeared in most cases to be quite poor [46].

Pirón et al. [3] also tested model alloys to find an optimum composition for the SOFC interconnect application. In this work the effects of different amounts of Cr, Mn, Ti and La were investigated. The element that requires probably most careful control is La. From the common reactive elements it turned out to be the one with the most beneficial effect, probably due to the fact that it does not form any intermetallic phases with iron and thus distributes more evenly in the alloy than other reactive elements [4]. As all reactive elements it has a major impact on oxidation resistance in that it significantly reduces scale growth and improves scale adherence. Pirón [3] et al. tested alloys with La contents between 0.1 and 0.8 wt. %. It turned out that high La concentrations lead to higher oxidation rates and a content of approximately 0.1 wt. % was found to be most beneficial. Consequently, careful control of La content and distribution is required, and one also has to take into account that La becomes easily oxidised during the manufacturing process. Ti has a number of effects; first it results in the formation of an internal oxidation zone below the oxide scale. These oxide precipitates result in a locally increased mechanical strength of the material and can prevent buckling due to scale growth induced stresses. Second, it has a beneficial effect by reducing the ASR due to doping of the chromia scale [32]. On the other hand a too high titanium content, the highest amount investigated by Pirón and Quadakkers [3] was 0.15 wt. %, causes extensive internal oxidation at the alloy grain boundaries. This leads to plastic deformation of the alloy, buckling and probably spallation of the scale. High Ti contents also substantially increase the chromia growth rate. The addition of Mn results in two-layered oxide scale structure, the outer layer being a $MnCr_2O_4$ scale while the inner layer consists of Cr_2O_3. This is advantageous because the outer spinel layer reduces the chromium evaporation as will be

explained in chapter 3.11. The amount of Cr in the alloy is not only critical to obtain oxidation protection but also it affects the thermal expansion coefficient. A value of 22 wt.% Cr yields to a CTE of $12*10^{-6}$ K^{-1} (between room temperature and 800°C) which matches well to the CTE of the anode [3].

The outcome of the research by Pirón and Quadakkers was a semi-commercial alloy termed JS-3. This material was commercialised by ThyssenKrupp VDM as Crofer 22 APU [47, 48]. However, due to the large scale manufacturing process in an electric arc furnace the levels of Si and Al were not as low as in JS-3 as can be seen in Table 2. The higher levels of Si and Al led to substantial internal oxidation, and resulted in significantly higher oxidation rates as shown in Fig. 3.8. [6]. Huczkowski et al. [6] also investigated model alloys similar to JS-3 with additions of 0.1 wt.% Al or Si. The corresponding weight gain curves are also shown in Fig. 3.8. It can be seen that especially the addition of Al causes higher oxidation rates due to internal oxidation of Al. Fig. 3.9 shows SEM images of the corresponding cross-sections. Comparison between JS-3 and Crofer 22 APU (1^{st}) (also known as Crofer 22 A) shows that the oxide scale is almost twice as thick on the industrial material than on JS-3. Below the oxide scale both alloys show an internal oxidation zone (IOZ). In the case of JS-3 only spherical Ti-oxide particles can be found due to the low levels of Al and Si. The internal oxidation zone of Crofer 22 APU (1^{st}) mainly consists of needle shaped Al_2O_3 precipitates and a silica layer can be found at the metal/oxide interface. Also at the metal/oxide interface metal protrusions in the oxide can also be found. According to Huczkowski [6] these protrusions develop because of compressive stresses in the alloy due to internal oxidation. The effect of Si and Al can be seen if one looks at the JS-3 based model alloys with the respective additions. Both alloys show a metal oxide interface with metal protrusions in the oxide and oxide nodules within the alloy due to the amount of internal oxidation. The major difference between the Si and Al addition is the morphology of the IOZ: Al_2O_3 forms the typical needle shaped oxides in the alloy while silica can be mainly found at the metal oxide interface and the IOZ comprises mainly of Ti-oxides.

	Batch	Fe	Cr	Mn	Ti	La	Si	Al
JS-3	JEX	Bal.	23.3	0.4	0.047	0.089	0.009	0.005
Crofer 22 APU 1st	JDA	Bal.	22.5	0.42	0.05	0.075	0.1	0.12
Crofer 22 APU 2nd	KCB	Bal.	22.2	0.45	0.065	0.096	0.011	0.022

Table 2: Compositions of the ferritic steels JS-3, Crofer 1st and 2nd in wt.% [6]

It also turned out that a strong reaction of the first commercial heat of Crofer 22 APU with the Pb containing glass-ceramic sealant of joined SOFC stacks occurred [49, 50]. This caused deterioration resulting in stack lifetimes one order of magnitude shorter than with JS-3 [51]. It could be shown, that the enhanced attack was related to Pb-vapour formed in the anode side gas. Molecular transport of this vapour through the oxide scale resulted in a weakening of the steel grain boundaries and consequently to enhanced internal oxidation of Cr. The vapour phase transport through the scale was promoted by the poorer protective properties of the scale as a result of the internal oxidation of Al and Si as explained above.

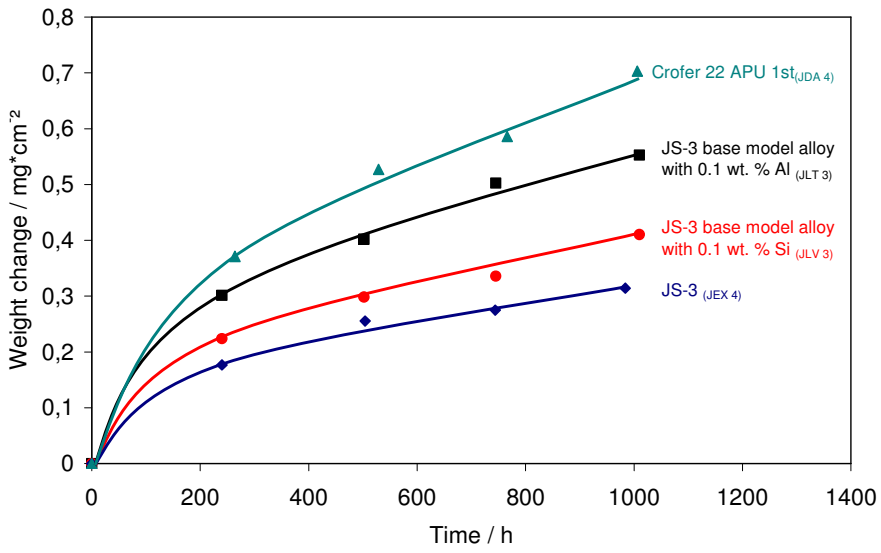

Fig. 3.8: Weight gain of JS-3 and Crofer 22 APU 1st as well as JS-3 type model alloys with Si or Al addition during 1000h oxidation at 800°C in air [6]

In November 2003 ThyssenKrupp VDM changed the production process for Crofer 22 APU from electric arc furnace to vacuum induction melting. Though this resulted in higher production costs it allowed the level of residual elements to be reduced to a level very close to that of JS-3 (see Table 2) which consequently resulted in a very similar oxidation behaviour. The latter material (Crofer 22 APU 2nd) was used as a starting point for the alloy development.

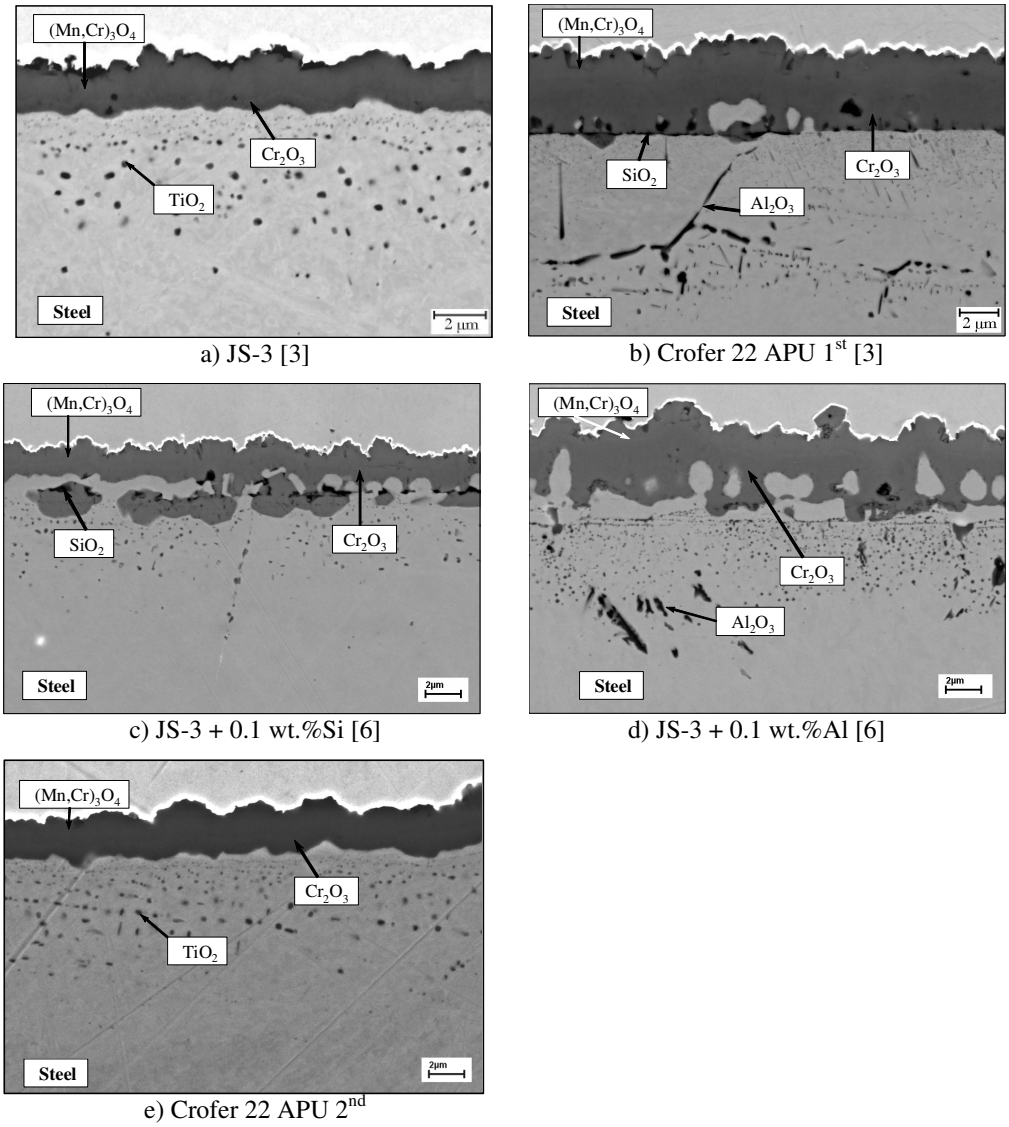

Fig. 3.9: SEM images of cross-sections of JS-3 and Crofer 22 APU 1st and 2nd as well as JS-3 type model alloys with Si or Al addition after 1000h oxidation at 800°C in air.

3.11 Materials Compatibility Issues

It is widely known that Cr may form volatile oxide species under SOFC cathode conditions, the most important is $CrO_2(OH)_2$ [52, 53]. These volatile species migrate to the cathode and the cathode/electrolyte interface thereby blocking electrochemically active sites which results in a decreased performance. This is one of the most important degradation processes in SOFCs and is referred to as cathode poisoning. All metallic materials forming chromia scales are subject to this problem. Mn-containing materials like Crofer 22 APU form a Cr/Mn spinel layer on top of the chromia scale which reduces the evaporation of Cr significantly [53]. Whether this reduction is sufficient to achieve tolerable degradation is still subject to debate. The most widespread solution to this problem is the introduction of protective coatings. This strategy is applied by many research groups and a wide variety of metallic and ceramic coatings has been proposed to overcome the Cr evaporation problem [19, 53].

Compatibility problems of the interconnect on the anode side do not play such a dominant role in SOFC research. In the case of the porous substrate design the anode is coated onto a porous substrate which is often made of ferritic interconnect material. Except corrosion problems due to the large surface area, the direct contact of Ni cermet with ferritic steel may cause interdiffusion of Ni in the steel and steel components in the anode thus degrading the performance of the cell. Anode side compatibility issues are mainly reported in this context where interdiffusion causes severe problems [54, 55]. However, in the case of self-supported cells the anode is usually joined to the interconnect by a Ni mesh. In such a design interdiffusion might cause similar problems; Ni can diffuse into the interconnect and e.g. Fe and Cr into the Ni mesh, where oxides are formed which decrease the conductivity of the cell [16]. However, it is believed that the diffusion of Ni into the interconnect might be the more harmful mechanism. At 800°C a Ni content of approximately 3wt.% will cause the formation of austenite [56]. This could have a substantial effect on stack lifetimes as the CTE of ferrite matches well to the other cell components while austenite has a CTE that is significantly higher [4, 43]. This effect might be especially harmful if thin interconnect sheets are used as a considerable part of the cross-section will have transformed to austenite. This degradation mechanism and a possible solution by a diffusion barrier will be discussed in chapter 7. The formation of austenite may also adversely affect the oxidation properties of the interconnect. Cr diffusion in austenite is known to be substantially smaller than that in ferrite and therefore

the critical Cr content required for protective chromia scale formation an a ferritic steel is substantially smaller than in the case of a austenitic steel [3].

4. Layout of the work

The current work can be divided into two parts. The first part deals with the development of ferritic interconnect materials with increased creep strength compared to presently available ferritic steels. The focus of the material testing is put on oxidation experiments but other SOFC relevant properties like thermal expansion coefficient or electrical conductivity of the scale are investigated as well. In the second part interdiffusion barriers between interconnect and Ni-rich component at the SOFC anode side are studied.

The development of steels with increased creep strength commonly relies on two strengthening mechanisms. The first mechanism is solid solution strengthening which requires an alloying element that has a substantial solubility in the alloy matrix. In the current study W was chosen as solid solution strengthening element, based on literature data and existing binary and ternary alloy phase diagrams. The other important strengthening mechanism is precipitation strengthening. This mechanism requires an alloying element with a low temperature dependence of the solubility in the alloy matrix and instead forms precipitates of a secondary phase at the operating temperature. Nb was chosen to act as precipitation strengthening element due to its ability to form Laves phase precipitates [57]. Due to the above described problems with manufacturing related impurities a special focus was put on the interaction of Al and Si with the Laves phase forming elements.

Model alloys with different amounts of W, Nb Si and Al were produced and subsequently tested with respect to the main SOFC relevant properties. A special focus is put on the investigation of the oxidation behaviour of the different alloy modifications because, as shown above, minor differences in alloy composition can have a major impact on the oxidation resistance. For this purpose samples were tested at different temperatures in air and simulated anode gas in the temperature range 700-1000°C. Special emphasis was put on the estimation of the thickness dependence of the oxidation rate especially during cyclic oxidation, since this aspect is of special importance if thin components are going to be used e.g. in SOFCs for mobile applications. Further, the alloy modifications were investigated with respect to creep strength, electrical conductivity of the scales and thermal expansion coefficient.

In the second part of the work the interdiffusion between ferritic steel and Ni-rich anode side material is investigated. In contrast to the interconnect/cathode this interface has hardly been investigated although interdiffusion across this interface may cause degradation of the cell performance. Based on data concerning mutual solubilities and electronic properties a number of metallic and ceramic materials were investigated with respect to their suitability as diffusion barrier coating.

5. Experimental

5.1 Materials

The composition of JS-3 / Crofer 22 APU 2nd was used as a starting point for the alloy development. The amounts of Cr, Mn, Ti and La where kept constant while the effect of additions of Nb and W, which where added for increased creep strength, was investigated. The focus of the work was to develop an alloy with higher creep strength without substantially deteriorating other SOFC relevant properties. In order to investigate the effect of the different alloying elements a number of model alloys were produced.

The alloy development philosophy is illustrated by the data in Table 3-6 in which the main alloying element variations are listed. Details and concentrations of minor alloying elements are given in Table 10 in the appendix.

	Batch	Fe	Cr	Mn	Ti	La	Si	Al
JS-3	JEX	Bal.	23.3	0.4	0.047	0.089	0.009	0.005
Crofer 22 APU 1st	JDA	Bal.	22.5	0.42	0.05	0.075	0.1	0.12
Crofer 22 APU 2nd	KCB	Bal.	22.2	0.45	0.065	0.096	0.011	0.022

Table 3: The composition variation of Crofer 22 APU 1st and 2nd in wt.% [6].

2 mm	16mm	Cr	Mn	La	Ti	Nb	W	Al	Si	Designation
KCR	KCP	23.2	0.53	0.16	0.06	-	-	0.006	0.03	Reference
KCW	KCU	22.3	0.51	0.12	0.1	-	0.9	0.01	-	1%W
KDN	KDM	20.7	0.53	0.13	0.11	-	2.7	0.01	0.06	2.7%W
KCL	KCM	22.23	0.52	0.16	0.15	1.11	-	0.001	0.02	1%Nb

Table 4: The composition of the reference alloy, which is very similar to Crofer 22 APU 2nd and several alloys which aimed at studying the effect of the single alloy additions Nb and W on materials properties. Inserted in the table as well are designations that will be used throughout the text in addition to the batch designations. All data are given in wt% measured by ICP-OES in the central division of analytical chemistry (ZCH) at FZJ.

2 mm	16mm	Cr	Mn	La	Ti	Nb	W	Al	Si	Designation
KCS	KCK	22.2	0.5	0.12	0.1	1.05	-	0.012	0.25	Nb+0.25%Si
KTA	KSZ	22.5	0.44	0.09	0.07	1	-	0.006	0.42	Nb+0.4%Si
KCO	KCN	22.7	0.52	0.15	0.12	1.07	-	0.15	0.07	Nb+0.15%Al
KUA	KUB	22.3	0.43	0.06	0.06	0.48	2.02	0.009	0.24	2%W+0.5%Nb+ 0.25%Si
LJF	LJG	22.6	0.46	0.09	0.07	-	4.91	0.01	0.28	4.9%W+0.3%Si
LJH	LJK	22.7	0.47	0.15	0.06	-	7.2	0.01	0.25	7%W+0.25%Si
LJN	LJO	18.5	0.44	0.12	0.06	0.51	1.88	0.01	0.27	18%Cr

Table 5: Alloys with single or combined Nb/W additions in combination with the alloy impurities Si/Al. All data in wt%.

2 mm	Cr	Mn	La	Ti	Nb	W	Al	Si	other	Designation
KYU	22.4	0.40	0.01	0.05	-	-	<0.01	0.03	2.0Mo	2%Mo
KYW	23.1	0.41	0.13	0.05	-	-	<0.01	0.02	0.5 V	0.5%V
LWU	22.4	<0.01	<0.01	<0.01	1.0	1.5	<0.01	0.63		-

Table 6: A number of 50g melts which were studied to investigate effects of further alloying additions as will be illustrated later in the respective sections. All data in wt%.

In our laboratory all materials have a three letter designation commonly referred to as batch identification. This designation allows identification of the material, the initial thickness, the manufacturer etc. These designations will also be used in the current work. Sheets of different thickness made from the same melt also receive different designations. Thus the batch referred to during oxidation experiments differs from the batch used for creep tests, because sheets of different thickness were used to manufacture the samples. For the experiments discussed in chapter 6.3 2mm sheets were used and ground to the respective thickness.

JDA and KCB/KMT are industrially produced heats of Crofer 22 APU (1^{st} and 2^{nd} respectively) the other alloys were manufactured by ThyssenKrupp VDM by vacuum melting and ingots of approximately 10 kg were cast and subsequently hot rolled to plates of 2 and 16 mm thickness. The alloys KYW, KYU and LWU were produced in a different way. For KYW and KYU approximately 50g of KCP (16mm designation for the reference material) were alloyed with V and Mo respectively. The mixtures were subsequently molten by levitation melting at IFF in Forschungszentrum Jülich. During the process the materials are inductively

molten in Ar atmosphere, and then cast into a Cu mould of 1cm diameter and subsequently quenched in water. LWU was made out of high purity materials in the same facility.

In the as received state the materials show only few very small precipitates. As an example Fig. 5.1a shows an image of the microstructure of KUA (2%W+0.5%Nb+0.25%Si) in the as received state. The white spots with a diameter of 200-300nm correspond to the beginning of Laves phase precipitation. Fig. 5.1b shows a TEM brightfield image of a very similar alloy (KSX). Only one precipitate can be seen but a considerable number of dislocations are present due to the hot rolling process.

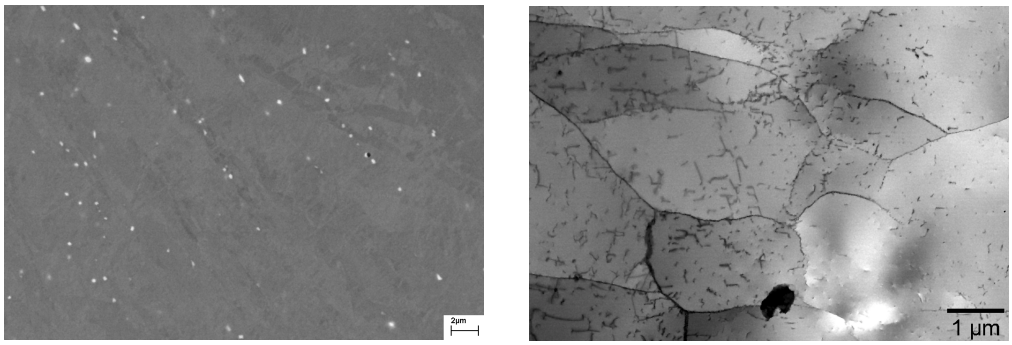

a) b)

Fig. 5.1: Material in the as received state. Fig. 5.1a shows a cross-section of KUA (2%W+0.5%Nb +0.25%Si). Fig. 5.1b shows KSX (1.75%W+0.6%Nb+0.25%Si no La) in the as received state. The dark grain at the bottom of the figure is one of the few Laves phase precipitates that can be found.

5.2 Oxidation Tests

Specimens of dimensions 20 x 10 x 2 mm^3 or 10 x 10 x 2 mm^3 were machined for oxidation testing from the 2 mm thick plates. A 2mm hole was drilled into the specimens to mount the samples in the test facility. During the test the samples were suspended on a Pt wire through the hole. Before the testing the samples were ground to P1200 grit surface finish and subsequently cleaned ultrasonically in ethanol.

In the SOFC stack the interconnect material is exposed to two different atmospheres. First the cathode environment which is usually air with a pO_2 of approx. 0.2bar and second the anode

(fuel) atmosphere. The detailed composition depends not only on the fuel that is used but also on the fuel utilisation. There is a gradient through the stack along which the concentration of fuel, e.g. H_2, decreases while the amount of water vapour increases due to the reaction of oxygen ions with the fuel [58]. In the current work Ar-4%H_2-H_2O atmospheres are used to simulate the anode gas. For the exposures at 800°C a water vapour content of 2% was chosen which corresponds to an equilibrium oxygen partial pressure of 10^{-19}bar. At 900°C Ar-4H_2-20% H_2O was used which corresponds to an oxygen partial pressure of 10^{-15}bar. The higher water vapour content was chosen because at 900°C Ar-4%H_2-2%H_2O corresponds to a pO_2 of 10^{-17} bar which is very close to the dissociation pressure of FeO at the respective temperature. This could make the interpretations of results difficult as minor deviations in the furnace atmosphere could have a significant impact on the oxidation behaviour.

The second important parameter is temperature; there is a wide range of temperatures proposed for SOFCs though for metallic interconnects a temperature below 800°C seems applicable [4]. Thus in the current work the focus of experiments is on 800°C and 900°C. Although 900°C is probably too high as service temperature, it is a common way of materials testing to simulate lower temperature behaviour after longer times of exposure which cannot be carried out due to limited lab capacity. The experiments were carried out discontinuously whereby the specimens where cooled to room temperature every 250h for weight measurements.

Except for the 10000h experiments all discontinuous oxidation tests were carried out materials with duplicate specimens. The weight gain curves do not show average values but a single sample because the averaging might obstruct discontinuities in the curves e.g. by spallation. Fig. 6.18 shows the respective errors after 1000h oxidation at 900°C in air and simulated anode gas.

5.2.1 Thermogravimetry (TG)

The isothermal oxidation experiments discussed in chapter 6.1.4 were carried out in synthetic air (mixture of nitrogen with 20 vol.% oxygen) using a thermo balance (Setaram TG 92). The specimens were heated to the test temperature with a rate of 90°C per minute, kept at temperature for 72 h, and subsequently furnace cooled with 10°C/min.

5.2.2 Cyclic oxidation studies

The cyclic oxidation tests were carried out at 900°C in lab air. Each cycle consists of 2h heating and 15min cooling. The samples are moved in a vertical furnace which is always heated at the test temperature. During the cooling step the specimens are removed out of the furnace and lab air is blown on the samples. A more detailed description of the process can be found elsewhere [6].

5.3 Characterisation of oxidised specimens

5.3.1 Optical Metallography/Electron Microscopy

After exposure a thin Au coating was applied by sputtering to obtain a electrically conductive sample surface. Subsequently a galvanic Ni coating was applied to provide better contrast between oxide layer and mounting material. The Ni coating can be seen on the top part of most images where it appears as bright layer. After coating the samples where embedded in resin and a polished cross-section was prepared. For SEM (Scanning Electron Microscope) investigations, the cross-sections were coated with Pt. The samples were investigated with a LEO 440 SEM equipped with an Inca EDX (Energy Dispersive X-Ray Analysis) System. For the WDX (Wavelength Dispersive X-ray Analyses) analyses a Zeiss Supra 50 instrument equipped with Inca WDX was used. The TEM (Transmission Electron Microscope) samples were obtained using a LEO Focused Ion Beam (FIB) instrument by in-situ lift out method and investigated with a Philips CM 200 TEM.

5.3.2 SNMS analysis

Sputtered Neutrals Mass Spectroscopy (SNMS, INA-3) was used to characterise oxide scales. For the studies discs of 1cm diameter and 2mm thickness were polished to 1µm prior to the oxidation treatment. More detailed information and a description of the quantification procedure can be found in [59].

5.3.3 Raman spectroscopy

For the measurements the samples were irradiated with an He-Ne laser with a wavelength of 632.8 nm. The corresponding Raman spectrum was recorded with a Dilor HR800 spectrometer.

5.4 Electrical resistance measurements

The contact resistances of the oxide scales were measured using a conventional four-point method at a constant current of 100mA. Specimens of 10x10x2 mm were ground to a P1200 grit surface finish and then pre-oxidised for 100h at 800°C in air. Subsequently, a layer of Pt-paste was applied to both oxidised surfaces and afterwards the edges of the samples were ground to make sure that the Pt-paste does not short circuit the scales. When the samples were inserted in the sample holder they were placed between two Pt-meshes which were used for the electrical connection. Thus the electrical resistance of the scale on both sides was measured and consequently the ASR values were divided by two. Subsequently the samples were covered with an alumina cover and a 35g weight to improve the contact between Pt covered samples and the Pt-mesh. The contact resistance was monitored in-situ for 300 h of exposure at 800°C in air and subsequently during step-wise cooling to 750°C, 700°C, 650°C, and 600°C, where by at each stage the temperature was kept constant for 10 h. The exposure times were limited to 300 h because it was previously shown that during longer exposure times the oxidation kinetics and the oxide scale morphology became substantially affected by the presence of a deposited Pt-contact layer [6]. At least two specimens were tested for each material to check the reproducibility of the results.

5.5 Creep tests

For the creep tests, cylindrical specimens were machined from the 16 mm-thick plates. The specimens were 6.4 mm in gauge diameter and the gauge length was 50 mm. Creep tests were performed at 600-800°C in air under various stresses, whereby the specimens were cooled to

room temperature after the first 500 h and later every 1000 h for strain measurements. The experiments were carried out according to DIN 50118 in a multispecimen testing machine.

5.6 Coefficient of thermal expansion

The measurements were carried out by F. Tietz and co-workers in IEF-1 at Forschungszentrum Jülich. The data were measured with a Netzsch dilatometer under Ar atmosphere. The heating and cooling rates were 3K/min.

5.7 Manufacturing of coatings

As substrates for the experiments with anode side protective coatings 1 or 2mm thick samples of Crofer 22 APU (2^{nd}) were used (batch KCB). The samples were ground to P1200 grit surface finish and cleaned in ethanol. Immediately before the coating process the samples were plasma cleaned for 15min by a pre-sputtering step; a voltage is applied onto the substrate holder and the sample is cleaned in a Ar plasma. The coatings were manufactured by magnetron sputtering in a Pfeiffer Classic 500 SP magnetron sputtering apparatus. The coatings were produced by DC (for metal coatings) and RF (for oxide coatings) sputtering at an Ar pressure of $3*10^{-2}$mbar. The sputter targets were 99.99% purity materials supplied by MaTeck (Jülich, Germany).

The conductivity measurements were carried out in a set-up identical to the one described in section 5.4. The measurement of the conductivity of the CeO_2 coating on an alumina substrate was carried out with a two-point measurement with a Keithley 2611 Sourcemeter. In this case a two-point measurement was sufficient as the resistance of the sample is in the order of several kΩ and contact resistances can be neglected.

6. Development of improved ferritic interconnect materials

6.1 Oxidation in Air

6.1.1 Oxidation in Air, 800°C, 1000h

Fig. 6.1 shows the weight gains for different alloys during 1000h discontinuous oxidation in air at 800°C. The curve of KCR corresponds to the reference alloy which has a similar composition as JS-3 or Crofer 22 APU 2nd. Comparison with the curve of JS-3 in Fig. 3.8 shows that the weight gains are also very similar. KCW corresponds to an alloy with almost the same composition as the reference alloy except for the addition of 1 wt.% W, which seems to have no negative effect on the growth rate. The curve of KDN corresponds to an alloy with higher W content. The addition of 1wt.% Nb (KCL) results in a significant increase in weight gain from 0.3mg/cm² to 0.5mg/cm² after 1000h.

Fig. 6.2 shows a second set of alloys which all contain Nb and vary in their Al and Si levels. Also included are, an alloy with combined additions of W, Nb and Si and, for comparison, the reference alloy (KCR). It can be seen that the combined additions of Nb and Al cause an even higher oxidation rate than Nb alone or Al alone. Huczkowski [6] exposed a JS-3 type alloy with 0.1 wt% Al under the same conditions and recorded a weight gain of 0.7mg/cm² after 1000h. Contrary to this, the oxidation rates for the alloys with combined Nb and Si additions are similar to those of the reference alloy.

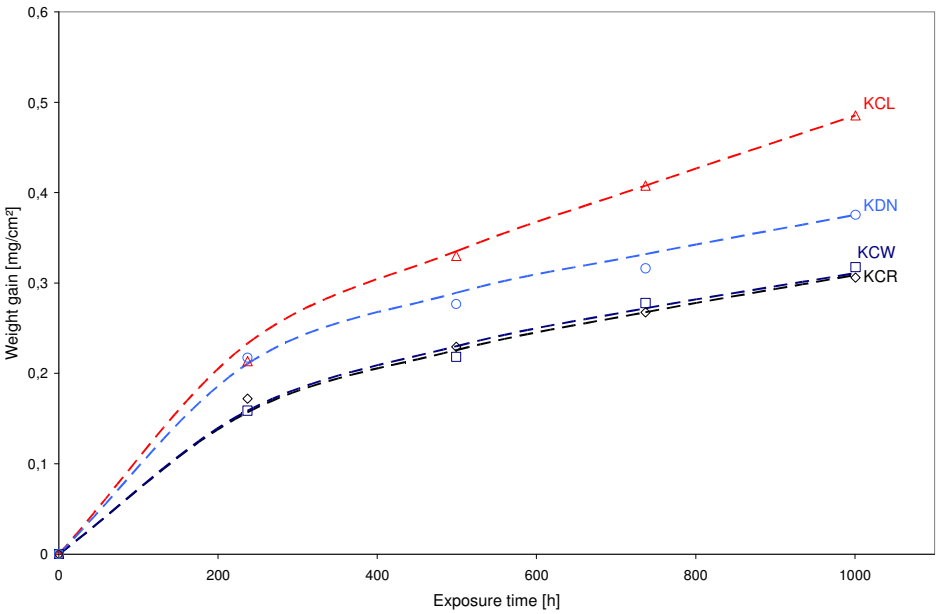

Fig. 6.1: Weight gain during discontinuous oxidation of KCR (Reference), KCL (Nb Addition), KCW, KDN (1 and 2.7% W respectively) at 800° in air. Duplicate specimens showed very similar weight gains which did not differ more than 0.02mg/cm².

An important result is that the negative effect of Nb additions on the oxidation behaviour can be compensated by the addition of Si, even though Si alone seems to have a slightly negative effect as well (see Fig. 3.8 in section 3.10). In order to investigate the interplay between W, Nb and Si, the alloy KUA (2%W+0.5%Nb+0.25%Si) was tested. It can be seen that it has a similar oxidation behaviour as the reference alloy.

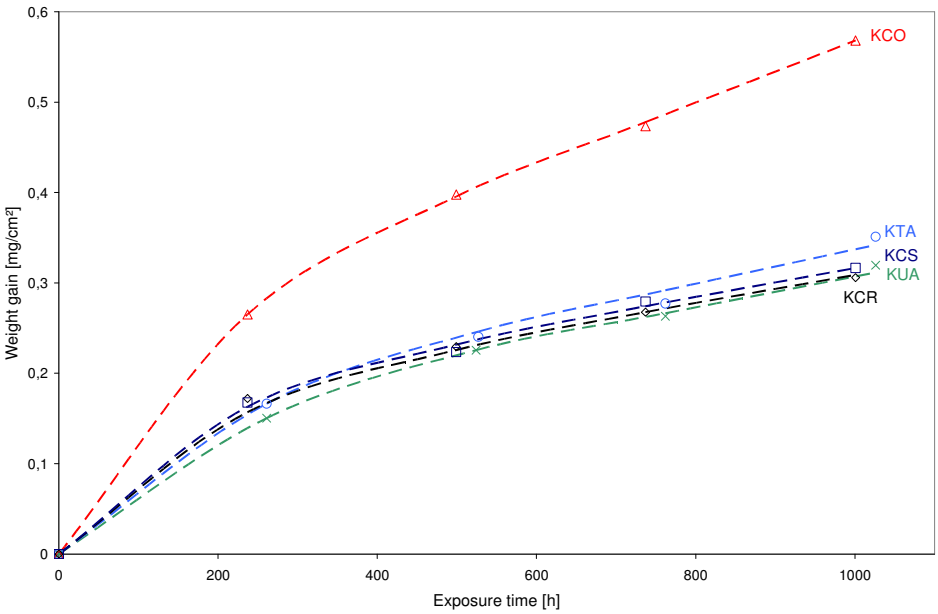

Fig. 6.2: Weight gain during discontinuous oxidation of KCR (Reference), KCS (Nb+0.25%Si), KTA (Nb+0.4%Si), KCO (1%Nb+0.15%Al) and KUA (2%W+0.5%Nb+0.25%Si) at 800° in air. Duplicate specimens showed similar weight gains which did not differ more than 0.05mg/cm².

Fig. 6.3 shows backscattered electron images of the respective samples. The reference alloy and the alloys with W addition (KCW and KDN) do not show any major differences. All three alloys have an approximately 2µm thick oxide scale and the interface between the chromia and spinel layer is not clearly defined. Below the oxide scale an approximately 5µm deep internal oxidation zone (IOZ) of titanium oxide can be seen. In the reference alloy fewer precipitates can be seen, probably due to the fact that the Ti content is slightly lower than in the other two alloys. In the case of the reference alloy (KCR) it seems that more precipitation of titanium oxide occurs at the alloy grain boundaries. In the high W alloy (KDN) the precipitates seem to be slightly larger than in the alloys KCR (Reference) and KCW (1%W addition).

The addition of Nb leads to a two phase microstructure with Laves phase precipitates which will be discussed in more detail in section 6.4. For the oxidation behaviour it is important to note that close to the sample surface an approximately 10µm deep precipitate depleted zone (NbDZ) exists. In Fig. 6.3d it can be seen that all but the largest Laves phase precipitates in this area are dissolved. In contrast, fine precipitates of approximately 1µm diameter exist as

well as larger ones with a diameter of 5-10 µm deeper in the alloy. The alloys with combined Nb and Si additions do not show a depletion zone close to the sample surface. Directly below the sample surface Laves phase precipitates can be found. On the alloy KCS (1%Nb+0.25%Si) an approximately 1µm thick scale that exhibits substantial buckling can be observed. The alloy KTA (1%Nb+0.4%Si) shows very little internal oxidation of titanium which can be attributed to the fact that the Ti level in that alloy is comparably low. The combined addition of Al and Nb not only results in the highest weight gain but also results in a different oxide morphology. Below the scale massive internal oxidation can be observed. In contrast to the other alloys where mainly Ti oxidises internally forming spherical particles, here the addition of Al results in a typical lath shaped morphology of internal oxides. The dissolution of Laves phase precipitates near the sample surface seems to be slowed down by Al additions.

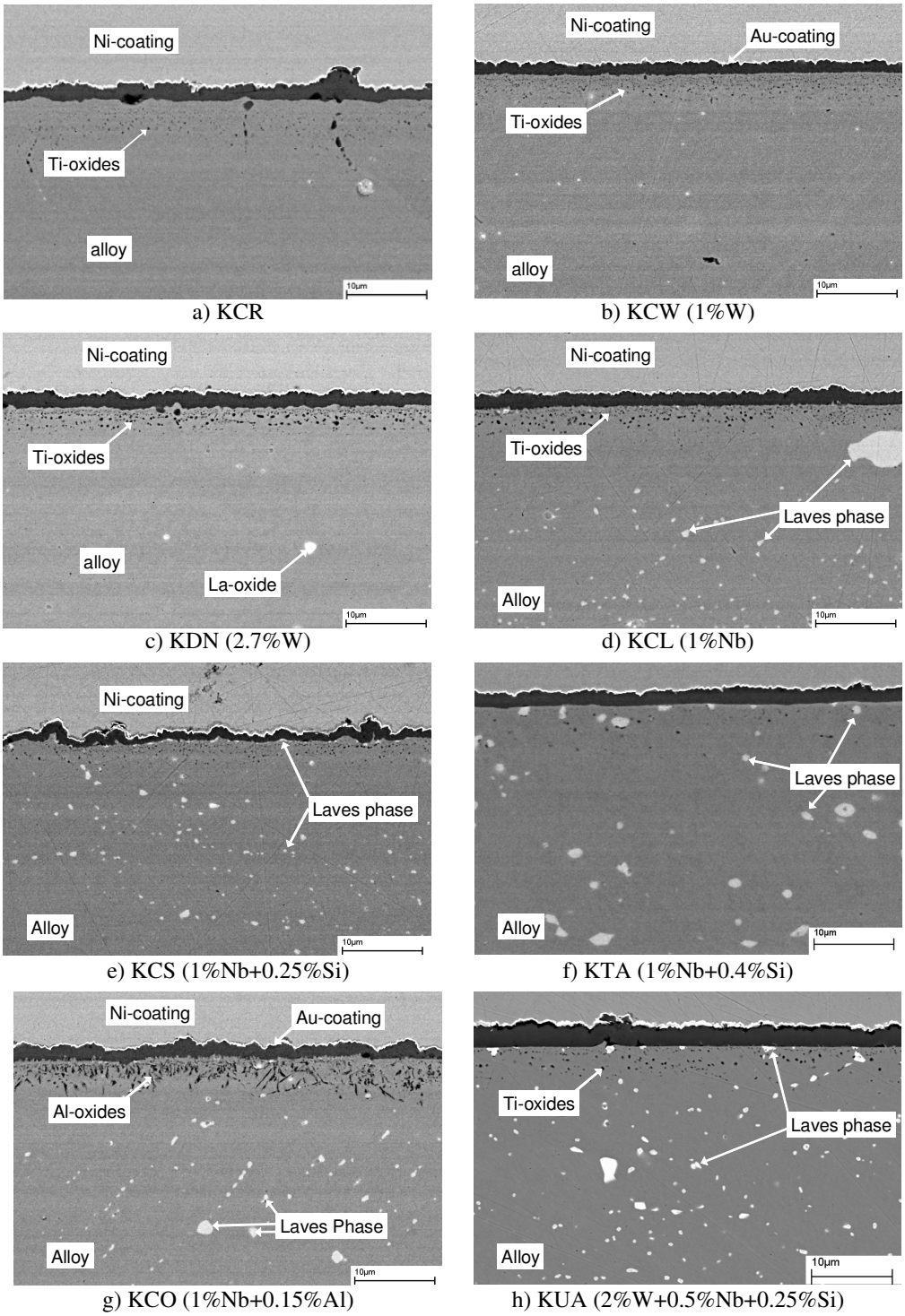

Fig. 6.3: SEM images of cross-sections of different alloys after 1000h at 800°C in air.

The alloy with combined additions of W, Nb and Si (KUA) exhibits a similar scale morphology as the alloys containing only Nb and Si (KCS, KTA). The Laves phase precipitates can be seen directly below the oxide scale. Comparison between the alloys KCS and KUA shows that the former exhibits a thin scale which is buckling while the latter shows a comparatively thick scale (2.2µm) where the scale/metal interface is perfectly flat. Such a difference cannot be observed in the weight gain curves (see Fig. 6.2), so the depicted area seems to be not representative. However, all weight gains are fairly low and the investigation of longer exposure times and higher temperatures in the following chapters will allow better understanding of the differences.

6.1.2 Oxidation in Air, 900°C, 1000h

Although 900°C is probably higher than the actual service temperature of the SOFC, it is useful to investigate higher temperatures because the results can be used to simulate the long term behaviour at lower temperatures and is thus commonly used method for a first screening of materials or e.g. to estimate the adherence of thick oxide scales. Fig. 6.4 shows the weight gain of samples exposed to air for 1000h at 900°C. KCR corresponds to the reference alloy while KCL designates an alloy with 1% Nb addition. It can be seen that the Nb addition leads to an increase of weight gain from 1.4mg/cm² for KCR to 2.5mg/cm². In contrast, the addition of 1 or 2.7wt.% W does not have a significant effect on the oxidation rate. Fig. 6.5 shows the weight gain of various alloys during 1000h exposure in air at 900°C. These alloys all contain Nb but the content of Al and Si is varied. The reference alloy (KCR) and the alloy with combined additions of W, Nb and Si (KUA) are inserted to this graph. The alloy with Nb and Al additions (KCO) shows the highest weight gain, which is even higher than the weight gain observed for the sample with only Nb addition (KCL). However, the combined addition of Nb and Si seems to have a beneficial effect. The alloy with Nb and 0.4% Si (KTA) exhibits a lower weight gain than KCL. The alloy with 1%Nb and 0.25%Si addition (KCS) shows an even lower weight gain which is comparable to that of the reference alloy. Thus, it seems that the additions of Nb and Si, which are deleterious if one of them is added to the alloy, somehow reduce each others negative effects. The same can be derived form the results of the alloy with W, Nb and Si (KUA) which shows a similar weight gain as KCS (1%Nb+0.25%Si). It seems that W has no significant effect on the oxide growth rate; the

combined addition of Nb and Si apparently has the same effect as in the W-free alloy. Compared to the 800°C exposures in air, all alloys show significantly higher weight gains. The differences between the single alloys could be confirmed at 900°C, though the latter exposures might be more significant because the higher weight gains reduce the effect of any measuring inaccuracies. E.g. the high weight gain of KDN (2.7%W) compared to the reference alloy at 800°C cannot be confirmed at 900°C, on the other hand KTA (1%Nb+0.4%Si) which performed at 800°C as good as KCR shows a higher weight gain at 900°C.

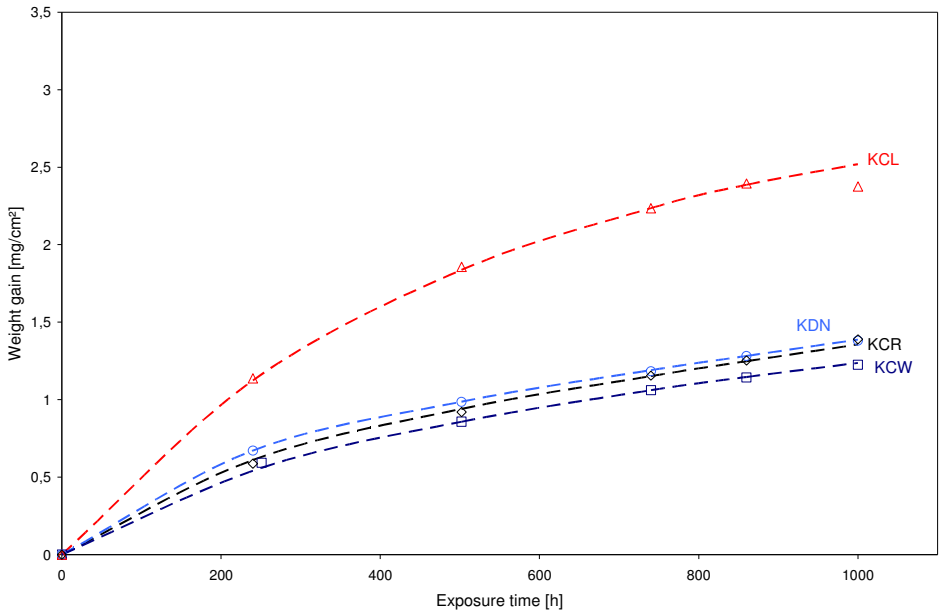

Fig. 6.4: Weight gain during discontinuous oxidation of KCR (Reference), KCL (Nb Addition), KCW, KDN (1% and 2.7% respectively) at 900° in air.

Fig. 6.6 shows the SEM images of cross-sections of the respective samples shown in Fig. 6.4 and Fig. 6.5. As indicated by the similar weight gains, the oxide scale thicknesses of the alloys with W additions and the reference alloy are similar with approximately 8µm. The outer part of the scale consists of $(Cr,Mn)_3O_4$ which appears slightly brighter in the backscattered electron image than the Cr_2O_3 that is formed beneath the spinel layer. Below the oxide scale a 20-30µm deep internal oxidation zone (IOZ) of small spherical titanium oxide particles can be seen. In agreement with oxidation theory [26] the particle size increases and the particle concentration decreases with increasing distance form the metal/scale interface.

Between the reference alloy and the 1wt.% W alloy hardly any difference can be observed. There seem to be slightly more Ti-oxides which can be attributed to the fact that the Ti content is slightly higher in the latter alloy. The alloy with the higher W content (KDN) looks somewhat different; the spinel layer seems to be more porous and the internal oxidation zone shows far more Ti-oxide precipitates especially at the alloy grain boundaries. On the other hand the IOZ seems to be not as deep as in the case of the other two alloys.

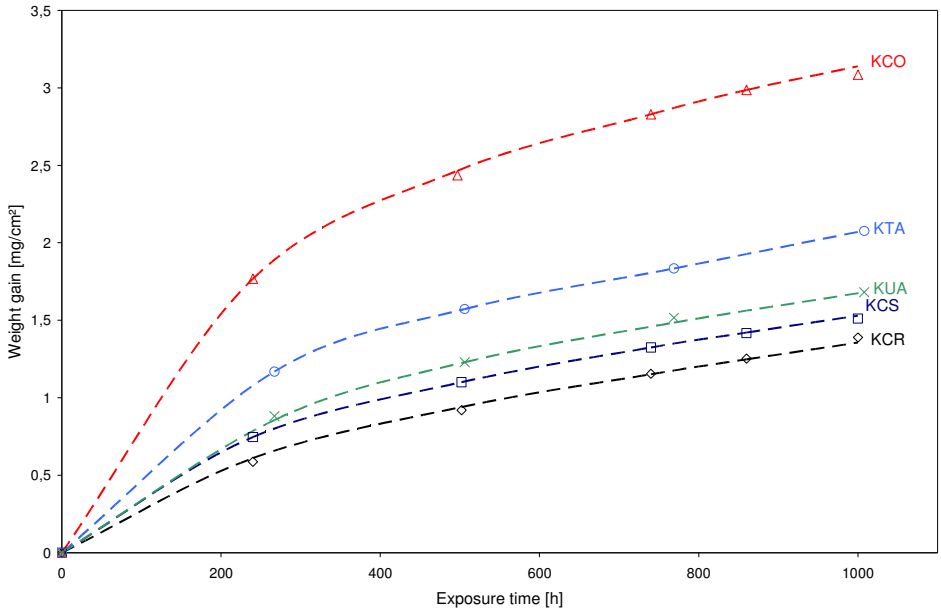

Fig. 6.5: Weight gain during discontinuous oxidation of KCR (Reference), KCS (1%Nb+0.25%Si), KTA (1%Nb+0.4%Si), KCO (1%Nb+0.15%Al) at 900° in air.

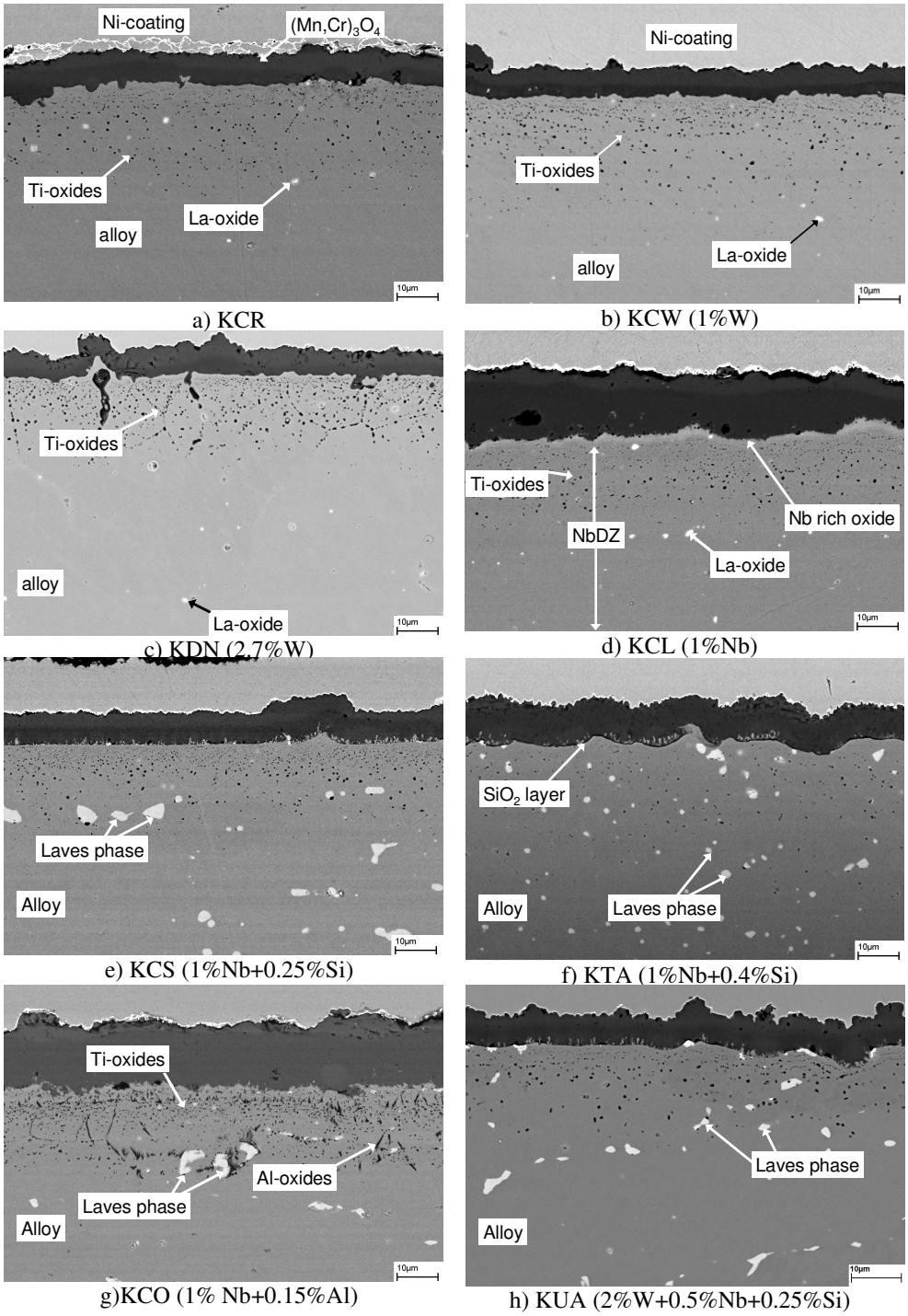

Fig. 6.6: SEM images of cross-sections after 1000h of exposure at 900°C in air. Note the slightly different magnification of KUA.

The alloy with Nb addition (KCL) shows a scale that exceeds 10µm thickness and is thus significantly thicker than the scale formed on the reference alloy. It can be seen that the chromia layer is much thicker while the spinel layer is of comparable thickness as in the case of the other alloys. Below the chromia layer an approximately 2µm thick bright Nb-rich oxide layer can be seen. Beneath the Nb-rich oxide an internal oxidation zone of Ti can be found. The Nb depleted zone (NbDZ) that was observed at 800°C can also be found at 900°C, however, at 900°C it is approximately 100µm deep so that no Laves phase precipitates can be seen in Fig. 6.6d.

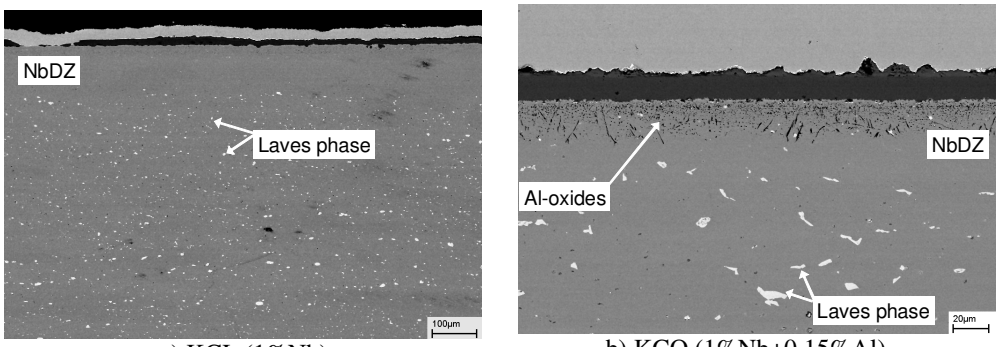

a) KCL (1%Nb) b) KCO (1%Nb+0.15%Al)

Fig. 6.7 The Nb depleted zone (NbDZ) on the alloys KCL (1% Nb addition) and KCO (1%Nb+0.15% Al addition) after 1000h at 900°C in air. Note the different magnifications.

Fig. 6.7a shows a low magnification image of KCL (1%Nb) exposed for 1000h at 900°C in air. An approximately 100µm deep layer below the oxide scale can be seen in which no Laves phase precipitates can be found. The combination of Nb and Si results in a different behaviour:

(i) the oxide scale thickness is similar (KCS) to the reference alloy or slightly thicker (KTA)
(ii) the Laves phase precipitates can be found directly below the oxide scale
(iii) no Nb-rich oxide layer can be observed

The metal/oxide interface of KCS (1%Nb+0.25%Si) is almost perfectly flat, which is believed to be related to the high creep strength close to the sample surface by the relatively high density of Ti-oxide precipitates. At the metal/oxide interface metal nodules can be found within the oxide scale, this is also the case for the alloys KTA (1%Nb+0.4%Si) and KUA

(2%W+0.5%Nb+0.25%Si). KTA exhibits a more porous scale and it can be seen that a thin silica layer is present at the metal oxide interface (see Fig. 6.8). There are relatively few titania particles in the IOZ which is due to the fact that the Ti level in the alloy is lower than in the other alloys. On the alloy with Nb and Al additions (KCO) a more than 15µm thick oxide scale can be found. Below the scale substantial internal oxidation of Ti- and Al-oxide can be seen. Although a few laves phase precipitates are present close to the metal/oxide interface, they are depleted compared to the bulk alloy as can be seen in Fig. 6.7b. Compared to KCL (1%Nb) alloy KCO (1%Nb+0.15%Al) exhibits certain similarities: the presence of a NbDZ and a thick chromia layer, however, the NbDZ is less distinct; it is only approximately 40µm deep and still contains some small Laves phase precipitates.

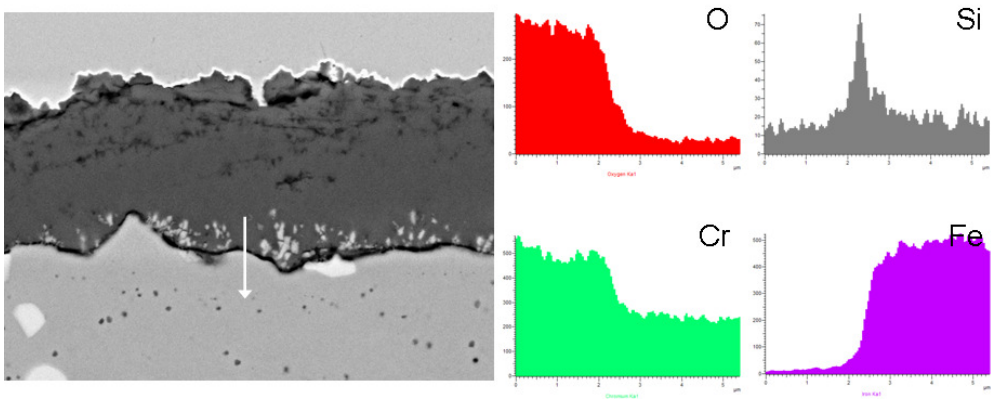

Fig. 6.8: EDX linescan at the metal oxide interface of alloy KTA (1%Nb+0.4%Si) after 1000h exposure at 900°C in air. The EDX data clearly shows the silica layer at the metal/oxide interface.

The alloy with combined additions of W, Nb and Si (KUA) exhibits an approximately10µm thick oxide scale which is relatively wavy (see Fig. 6.6h). This is believed to be related to the fact that only few Ti-oxide precipitates are present beneath the scale of KUA which is due to the fact that KUA contains less Ti than most of the other alloys. This results in a relatively low creep strength of the alloy near the metal oxide interface which allows buckling of the scale. The Laves phase precipitates remain stable near the sample surface and can be found in the direct vicinity of the metal oxide interface.

For a more detailed investigation TEM specimens of the oxide scales of the alloys KCL (1%Nb), KCS (1%Nb+0.25%Si) and KCR (Reference) where prepared by FIB in situ lift out technique with a focused ion beam instrument. Fig. 6.9 shows the corresponding TEM

images. Fig. 6.9 shows for the reference alloy that the scale is in good contact with the alloy and no pores or precipitates can be observed at the interface. In the centre part of the image a fine grained inner chromia scale can be seen with an average grain size of approximately 0.5µm. On top of the chromia layer the $(Cr,Mn)_3O_4$ outer scale with large grains of 1-2µm diameter can be seen. The spinel grains exhibit an orientation with the long axis along the growth direction of the scale. The chromia grains seem to be more equiaxed but also seem to have an orientation along the growth direction. The image of the alloy with Nb additions (KCL) shows the fine grained chromia scale in the upper part since the TEM lamella was too small to depict the whole oxide scale including the spinel layer. The morphology of the chromia scale is similar to that observed on the reference alloy although it is twice as thick as was indicated in Fig. 6.6. Between the chromia layer and the metal an Nb-rich oxide can be found. This layer is approximately 2µm thick with an average grain size of approximately 1µm. EDX analysis of the respective layer gives a composition of 45.6% O, 41.2% Nb, 9.5% Cr, 3.0% Ti, 0.5% Mn, 0.2% Fe (all at.%). The Nb/O ratio matches to NbO but the oxygen quantification with EDX is very unreliable. However, according to thermodynamic data [60] NbO is the stable oxide at oxygen partial pressures near the dissociation pressure of Cr_2O_3 as can be seen in Fig. 6.10.

Fig. 6.9c shows a bright field image of the oxide scale of the alloy KCS (1%Nb+0.25%Si). In the upper part of the figure the $(Cr,Mn)_3O_4$ layer can be seen. The morphology is similar to that found for the reference alloy. Below the spinel layer the Cr_2O_3 scale can be seen which also exhibits a similar morphology as seen for to the reference alloy although the grains seem to be slightly larger. The bright area at the metal/oxide interface corresponds to a gap in the sample; this is probably because of a number of pores that were enlarged by the ion beam during the sample preparation.

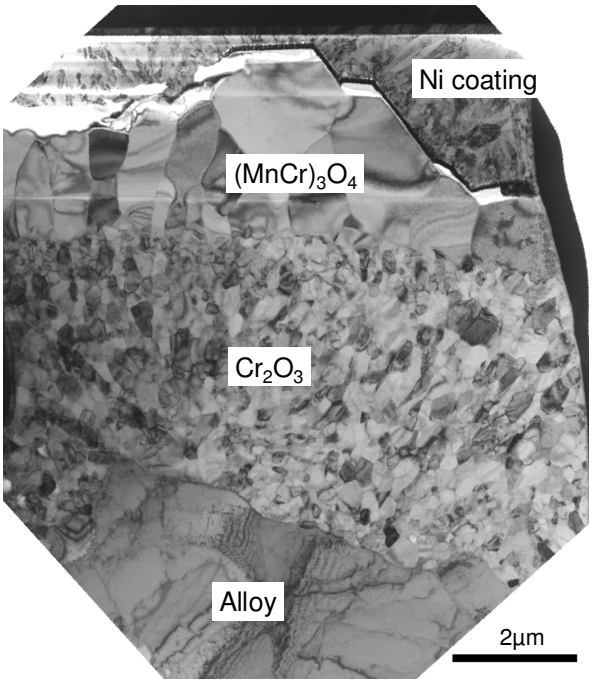

a) KCR (reference alloy)

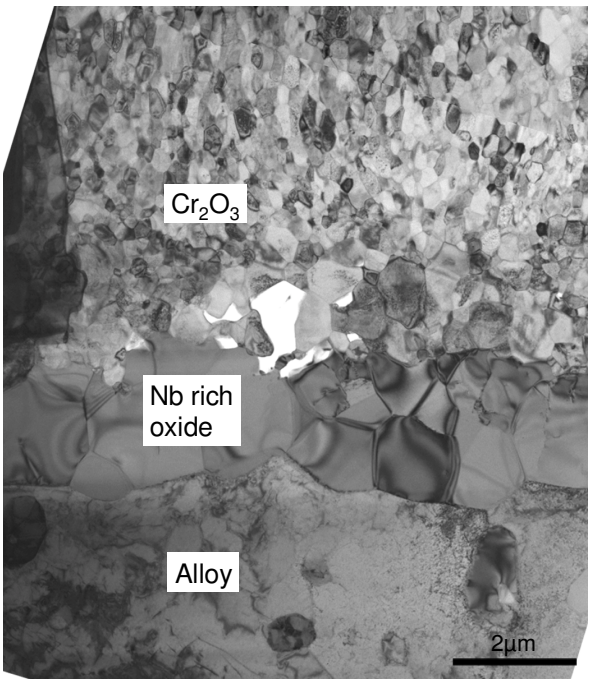

b) KCL (1%Nb)

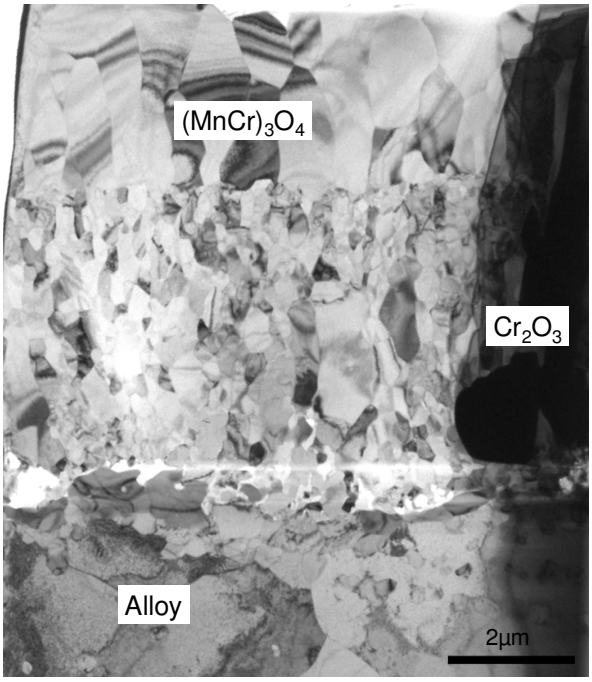

c) KCS (1%Nb+0.25Si)

Fig. 6.9: TEM bright field images of oxide scales on the alloys KCR, KCL, KCS after exposure in air at 900° for 1000h. The bright line close to the metal-oxide interface in Fig. 6.9c is due to inhomogeneous thinning during the FIB preparation.

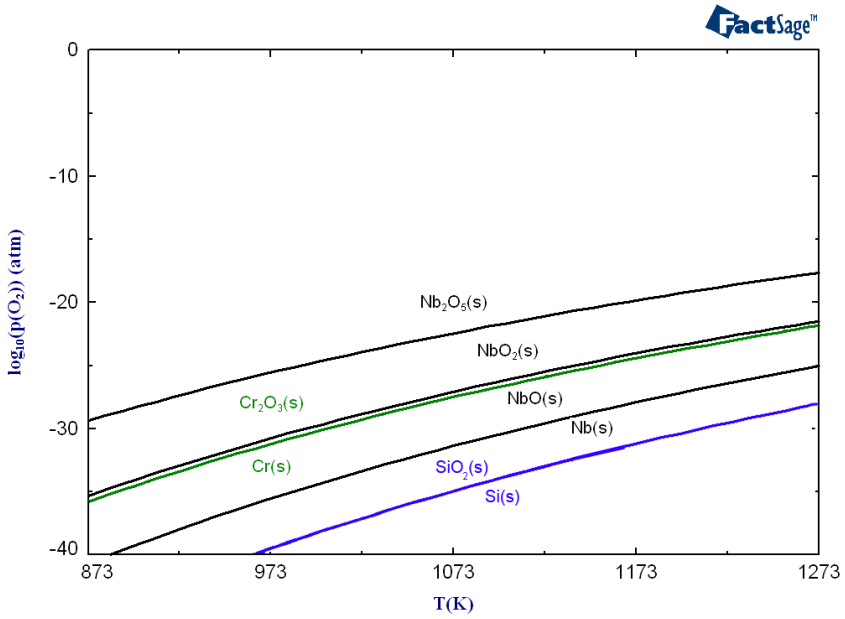

Fig. 6.10: Dissociation pressure of chromia , silica and different Nb oxides calculated using the FactSage database [60].

6.1.3 Long term oxidation behaviour in air at 800°C

In order to evaluate the different alloy modifications with respect to the application as SOFC interconnect, long term exposures similar to the projected life time of an SOFC stack are necessary. For SOFCs in mobile application the commonly projected service lifetime is in the range of 5000-10000h [53].

The weight gain curves of selected materials during 10000h exposure at 800°C in air are shown in Fig. 6.11. The weight gains observed after 10000h at 800°C are similar to those observed after 1000h at 900°C. This indicates that the accelerated testing at 900°C can at least so some extent be used to estimate long term behaviour at lower temperatures. If one compares the behaviour of the various alloys, similar trends as before can be observed. The alloy with Nb addition (KCL) shows the highest oxidation rate while all others show a similar behaviour. As observed at 900°C the alloy with Nb and 0.4% Si (KTA) exhibits slightly higher oxidation rates than the other alloys. The curve of the alloy with 2.7%W (KDN) is almost identical to that of the reference alloy (KCR). The weight gains of the alloys KCS (1%Nb+0.25%Si) and KUA (2%W+0.5%Nb+0.25%Si) are somewhat lower than the reference alloy which apparently exhibits a slightly higher oxidation rate after approximately 5000h compared to the first half of the experiment. Fig. 6.12 shows the parabolic rate constant k_P as a function of exposure time. It can be seen that the oxidation behaviour can be described by a parabolic rate law with reasonable agreement.

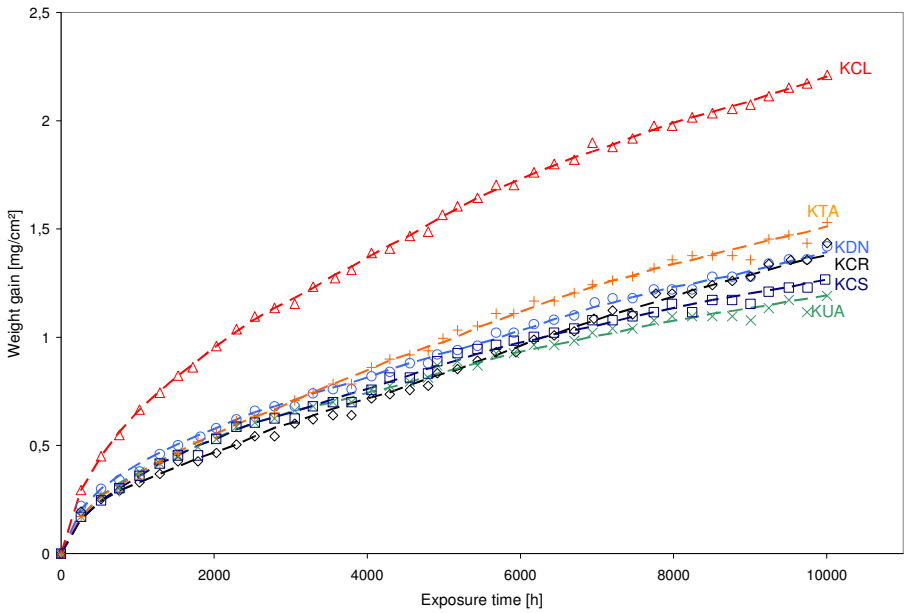

Fig. 6.11: Long term exposure of selected alloys at 800°C in air. Except for KCL the data points after 1000h are in good agreement with the data presented in Fig. 6.1 and Fig. 6.2.

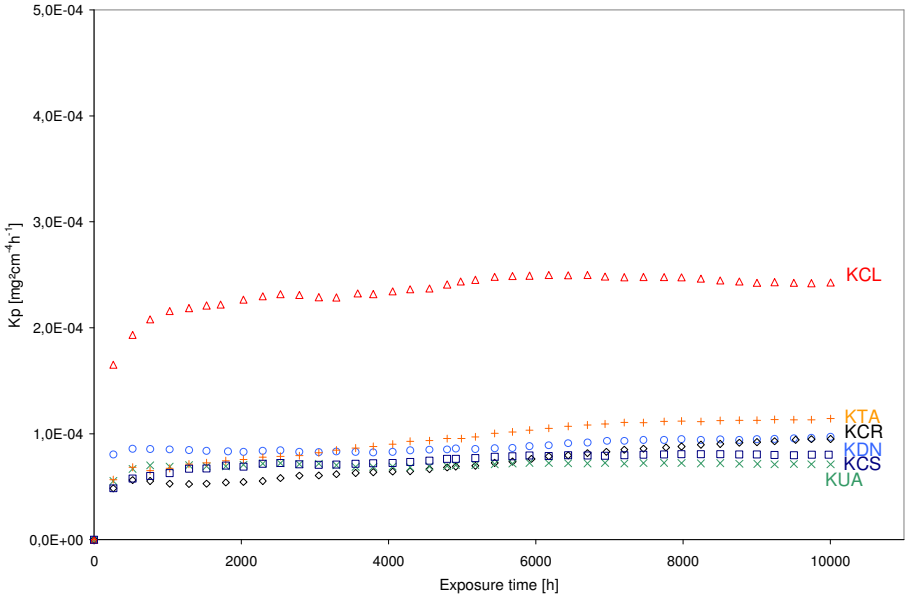

Fig. 6.12: Parabolic rate constant (k_p) as a function of exposure time calculated from the weight gain data shown in Fig. 6.11.

Fig. 6.13 shows SEM images of cross-sections of the respective samples after oxidation treatment. The oxide scale thickness of all alloys except KCL (1%Nb addition) is approximately 7µm. This is in good agreement with the weight gain data because an oxygen uptake of 1mg/cm² corresponds to approximately 6µm oxide scale in the case of Cr_2O_3 and 7µm for $(Mn,Cr)_3O_4$. The reference alloy exhibits a similar morphology as observed after 1000h exposure at 900°C. Somewhat more pronounced are oxide nodules protruding into the alloy. It is interesting to note that the nodules consist of $(Cr,Mn)_3O_4$ although the inner part of the scale consist of chromia. It is believed that during long term exposure (e.g. during the cooling for weight gain measurements) microcracks in the oxide scale are formed. This enables molecular oxygen to access the metal/scale interface and to oxidise Mn which cannot diffuse to the oxide surface.

The alloy with W additions does not show any major differences compared to the reference alloy. In contrast, the addition of Nb causes significantly faster scale growth resulting in a scale thickness of approximately 12µm which is in agreement with gravimetric data. The Nb depleted zone can be also observed, its depth varying with an average of approximately 30µm. The alloys with combined additions of (W), Nb and Si all show a similar behaviour. The Laves phase precipitates can be found directly at the metal oxide interface. The latter two alloys show less Ti-oxide particles in the internal oxidation zone than the other alloys which is due to the slightly lower Ti content in the alloy.

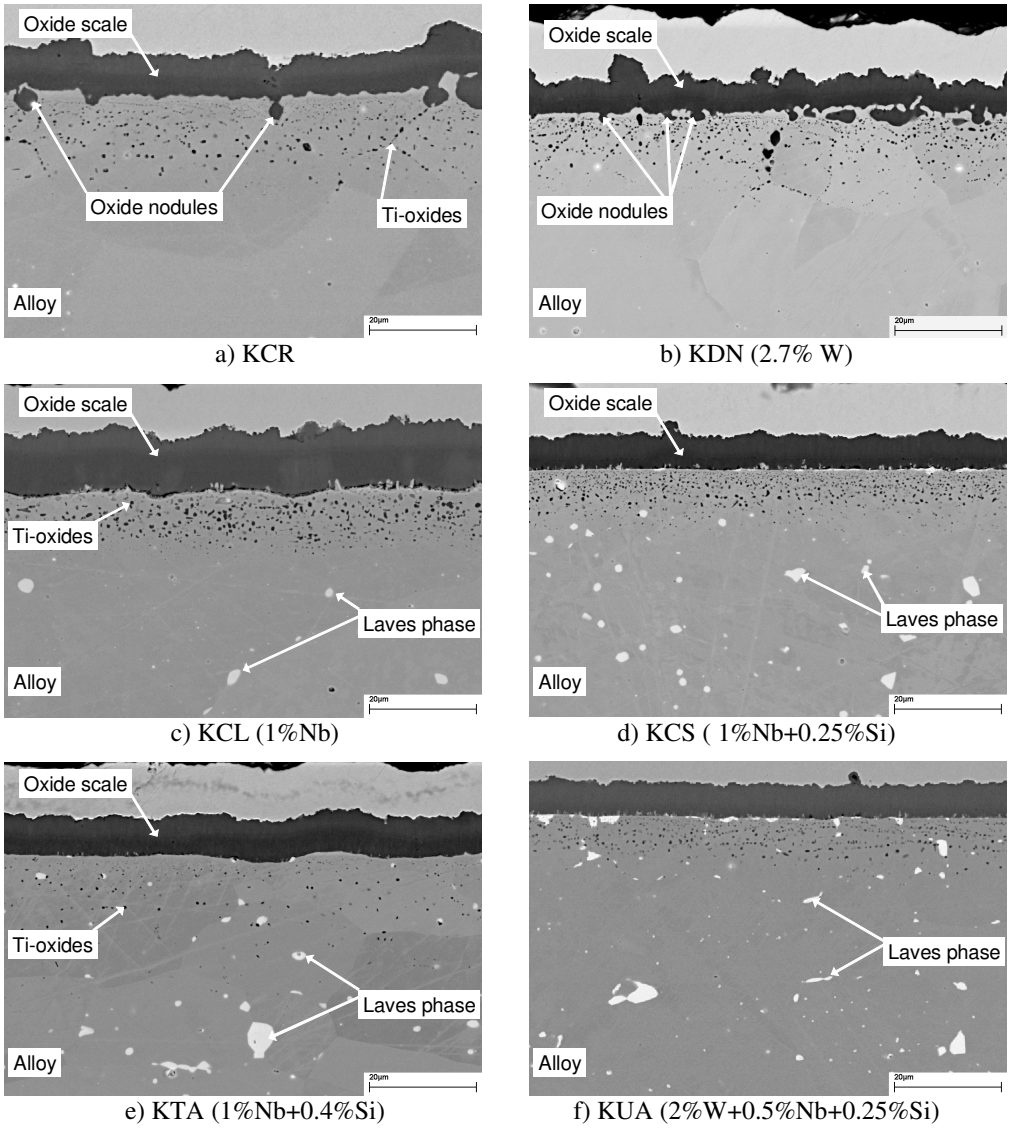

a) KCR b) KDN (2.7% W)

c) KCL (1%Nb) d) KCS (1%Nb+0.25%Si)

e) KTA (1%Nb+0.4%Si) f) KUA (2%W+0.5%Nb+0.25%Si)

Fig. 6.13: SEM images of cross-sections of the samples shown in Fig. 6.11 after air exposure at 800°C for 10000h.

6.1.4 Temperature dependence of oxidation behaviour

In order to investigate the temperature dependence of the air oxidation behaviour in a wide range and to get more insight in the actually prevailing rate laws during isothermal exposure, thermo gravimetric analysis at different temperatures were carried out. Fig. 6.14 shows the weight gain of the reference alloy (KCR) during isothermal oxidation at different temperatures. While at 700°C the weight gain is very low at 1000°C already after 70h a weight gain of almost 1mg/cm² is reached. From the respective weight gain data the parabolic rate constant k_P can be derived (see section 3.5.2). As an example k_P is shown as a function of exposure time in Fig. 6.15. The data for 800°C are in good agreement with the k_P value determined at the same temperature in the 10000h long term exposures (see Fig. 6.12). Although some scatter is observed, especially at 700°C, the data clearly show that the oxidation can be described with reasonable accuracy by a parabolic rate law.

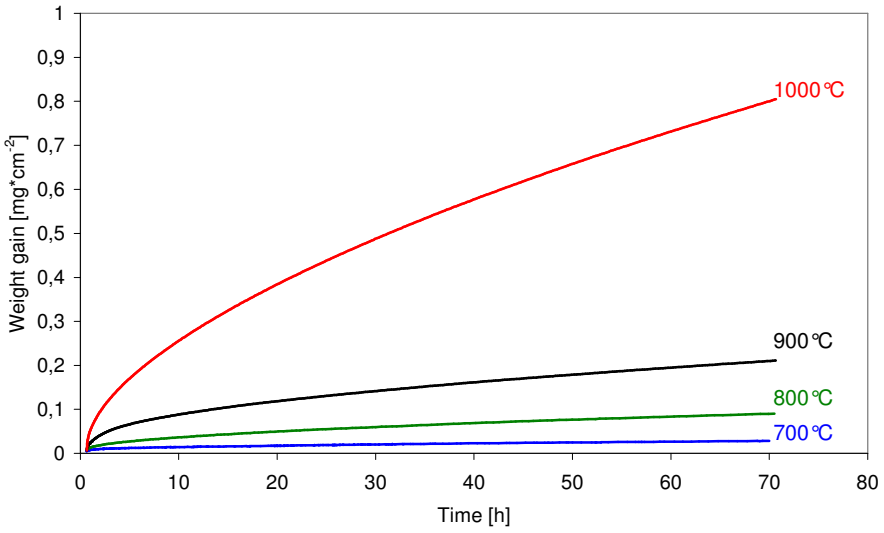

Fig. 6.14: Weight gain of the reference alloy (KCR) during isothermal oxidation in air at different temperatures.

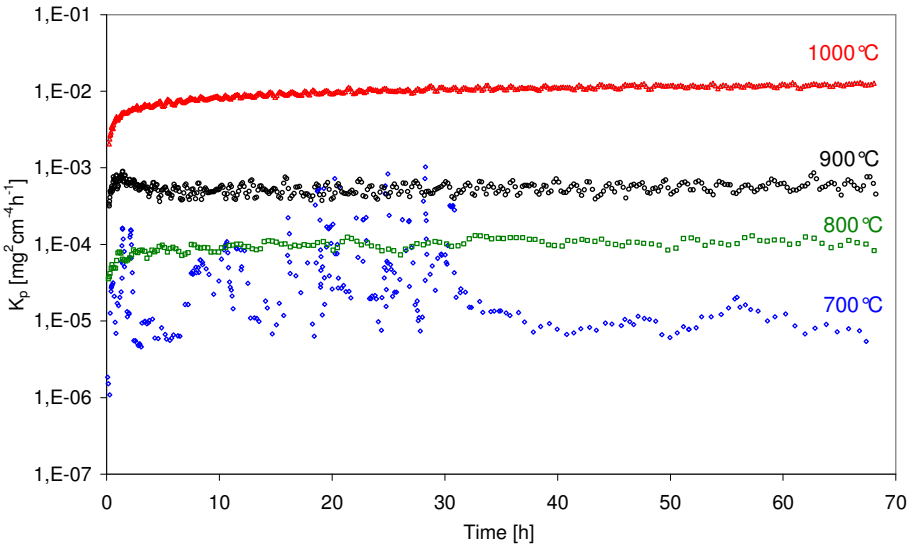

Fig. 6.15: Parabolic rate constant k_P as a function of exposure time at different temperatures for the oxidation of alloy KCR (reference) in air.

Fig. 6.16 and Fig. 6.17 show the k_P values as a function of temperature for various alloys. It can be seen that the k_p values for all alloys are very similar except for alloys KCL (1%Nb) and KCO (1%Nb+0.15%Al). In the case of KCL the high oxidation rates are related to the formation of a Nb-rich oxide below the chromia scale as well as the doping effect of Nb in the chromia scale (see chapter 6.1.2). KCL also shows a somewhat more pronounced temperature dependence than the other alloys. This might be caused by different rates of Nb incorporation into the oxide scale at different temperatures. It is suggested that Nb incorporation does not play a major role at lower temperatures (~700°C) while it increases the oxidation rate at higher temperatures thereby causing the more marked temperature dependence of KCL than for the other alloys. KCO (1%Nb+0.15%Al) exhibits a similar temperature dependence but generally higher k_P values than the other alloys. This is believed to be related to the widespread internal oxidation of Al in the alloy as described earlier (see section 6.1.2). This not only directly affects the weight gain but it is also known, that the volume increase due to internal oxidation can cause the formation of microcracks in the oxide scale which results in a higher scale growth rates [61].

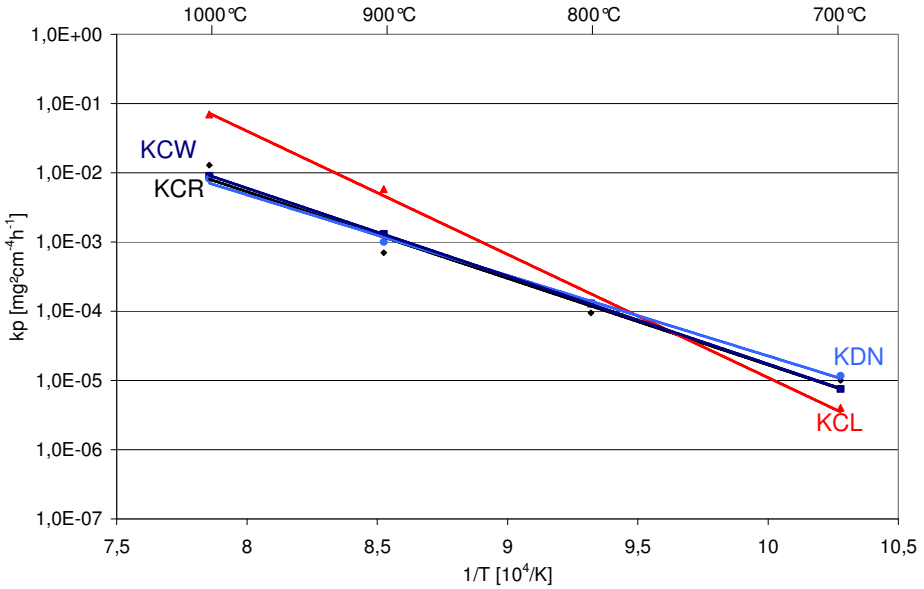

Fig. 6.16: Parabolic rate constant k_p as a function of temperature during oxidation of alloys KCW, KDN (1 and 2.7%W respectively) and KCL (1%Nb) in synthetic air.

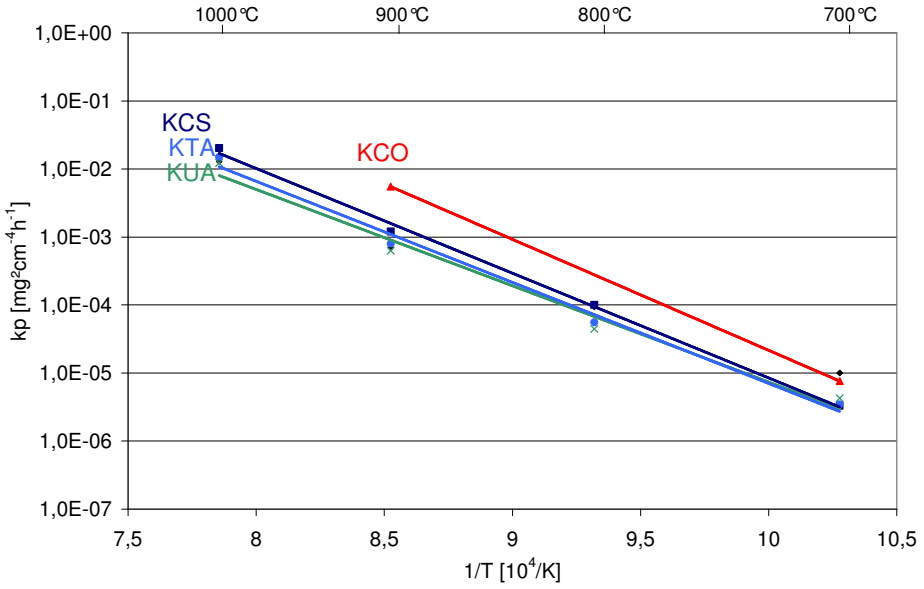

Fig. 6.17: Parabolic rate constant k_p as a function of temperature during oxidation of alloys KCS, KTA (both 1%Nb+Si) KCO (1%Nb+0.15%Al) and KUA (2%W+0.5%Nb+0.25%Si) in synthetic air.

6.1.5 Summary of air oxidation

The discontinuous oxidation behaviour at 800 and 900°C for 1000h and the experiments carried out at 800°C for 10000h allow similar conclusions. All alloys exhibit an oxide scale with an outer layer of $(Cr,Mn)_3O_4$ and an inner layer of Cr_2O_3 as main components. Below the oxide scale an internal oxidation zone of oxides of minor elements with high oxygen affinity can be found. Compared to the reference alloy (KCR) the addition of up to 2.7% W does not have a significant effect on the oxidation behaviour. In contrast, the addition of 1% Nb roughly doubles the weight gain of the samples. The increase in scale thickness is due to a thicker chromia layer, the amount of spinel remains virtually unaltered. It is believed that the more rapid growth of chromia is due to Nb doping of the chromia scale in a similar way as described for Ti doping of chromia [32, 62]. Additionally a Nb-rich oxide layer has formed below the chromia scale. In the alloy matrix, the Nb addition results in the formation of $(Fe,Cr)_2Nb$ precipitates, but, these precipitates dissolve close to the sample surface, due to Nb incorporation into the scale leading to a depletion zone (NbDZ). The width of the zone depends on the exposure time and duration; after 1000h at 800°C the zone is approximately 10µm wide and only larger precipitates are still present. After 10000h the width of the NbDZ has increased to approximately 30µm while after 1000h at 900°C a 100µm wide depletion zone has developed.

The combined addition of Nb and Si results in a completely different behaviour. It was shown by Huczkowski et al. [6] that the addition of Si has a negative effect on the oxidation behaviour compared to JS-3. However, the present results show that the combined addition of Nb and Si results in an oxide growth rate which is similar to that of JS-3. The scale morphologies of JS-3 and e.g. KCS (1%Nb+0.25%Si) are also very similar except some differences at the scale/metal interface. The combined addition of Nb and Si also has an effect on the Laves phase precipitates. If Si is added to the Nb containing alloy, neither a Nb-depleted zone nor a Nb-rich oxide can be found. Whether 0.25% or 0.4% Si is added to an alloy containing 1% Nb does not have a major effect on the morphology though the higher amount of Si results in the formation of a subscale silica layer and to somewhat higher oxidation rates.

Details of the Laves phase precipitates will be discussed in chapter 6.4, but, some results are important to explain the differences in oxidation behaviour. The Laves phase precipitates have

a high solubility for Si, thus Si is depleted in the matrix if Nb is present. The resulting decrease in Si activity explains why Si has no negative effect on the oxidation rate and no subscale silica formation is observed on KCS (1%Nb+0.25%Si). On the other hand in the alloy with 1%Nb and 0.4%Si (KTA) the Si level seems to be too high to tie up a sufficient amount of Si in the Laves phase precipitates. This results in the formation of a subscale SiO_2 film which can be observed on some samples (see Fig. 6.8). This also explains the slightly higher weight gain of KTA compared to KCS (1%Nb+0.25%Si). The addition of Si also affects the Laves phase precipitates: if no Si is present the Laves phase precipitates in the alloy become dissolved close to the sample surface. This is not the case if Si is added to the alloy.

The various ternary Fe-Nb-Si phase diagrams confirm that the Laves phase has a substantial solubility of Si, whereby the solubility strongly decreases with decreasing temperature. The ternary phase diagram at 1000°C (see appendix) indicates that Si stabilises the Laves phase with the result that it can form at lower Nb levels than in the binary Nb-Si system. From this one might conclude that Si addition decreases the solubility of Nb in α-iron. Assuming the activity coefficient of Nb not to be affected by the Si addition this could mean that in a two phase alloy ferrite +Laves phase the Nb activity is decreased by Si additions and thus the dissociation pressure of the oxide would be increased.

Fig. 6.10 showed that at 800°C, for Si, Nb and Cr activities of unity, the dissociation pressures of the most stable oxides are 10^{-35}bar, 10^{-32}bar and 10^{-28}bar respectively. However, in reality the activities of the respective elements in the alloy are substantially smaller than unity which affects the dissociation pressure of the respective oxides. If one rewrites the equation given in section 3.5.1, this results in

$$\frac{\exp\left(\frac{\Delta G^\circ}{RT}\right)}{a(M)^x} = pO_2$$

where pO_2 corresponds to the dissociation pressure of the respective oxide. Thus it can be seen that, considering the lower mole fractions of Nb and Si compared to Cr, the dissociation pressures of NbO and SiO_2 might rise to an extent that they are not stable below Cr_2O_3. Assuming the activities of Nb and Cr to equal their mole fractions in the alloy matrix (ideal solution) it can be calculated that the amount of Nb necessary to form NbO beneath Cr_2O_3 is

approximately 0.2at.% (~0.3wt.%). In the case of SiO_2 the critical Si concentration in the alloy equals $1*10^{-5}$at.%. Thus, assuming an ideal solution, it can be stated, that since the dissociation pressures of NbO and Cr_2O_3 are not too different, it is possible that minor differences in Nb concentration in the alloy matrix can determine whether NbO is stable beneath chromia or not, while in the case of Si the difference is too large that one would expect Si oxidation to occur beneath chromia under nearly all conditions.

However, in real alloys the activity coefficients γ can deviate substantially from unity thus the above calculations can not be considered quantitatively. A calculation of the respective activities using Thermocalc turned out to be not possible because the available thermodynamic data do not take into account that Si is present in the Laves phase which was observed experimentally (see chapter 6.4). However, under the premise that the activity coefficients γ of Si and Nb are not affected by this inaccuracy one can use the values of γ in combination with experimentally determined concentrations of Nb and Si to calculate the respective activities.

However, the result of such an approach was that the calculated activity coefficients were extremely low and the corresponding activities changed to an extent that, even if several percent of Nb and Si were present in the alloy, the respective oxides were supposed to be unstable beneath Cr_2O_3 which is apparently not in agreement with the experimental data. Nonetheless, the used approach is able to illustrate that differences in Nb and Si activity due to their strong interaction in the Laves phase might affect the stability of NbO and SiO_2 beneath Cr_2O_3 as was actually found in the present study.

In contrast alloys with combined additions of Nb and Al posses the highest oxidation rates of the studied alloys. The oxide scale thickness doubles compared to the reference alloy in the case of the 1000h exposure at 900°C. Since the thicker scale consists mainly of chromia, it is believed that the high growth rate is mainly due to Nb doping of chromia. However, the widespread internal oxidation of Al below the scale might also affect the scale growth rate as it was described by Huczkowski et al. [6] for Crofer 22 APU 1st. The Laves phase precipitates can be found close to the metal/scale interface, but there are less precipitates close to the surface compared to the bulk material. Thus it is believed that the addition of Al slows down the dissolution of Laves phase but cannot completely suppress it. The alloy with combined

additions of W, Nb and Si shows a behaviour very similar to that of the alloy with Nb and 0.25%Si. The oxide scale is of similar thickness compared to the reference alloy and the Laves phase precipitates remain stable even at the metal oxide interface.

6.2 Oxidation behaviour in simulated anode gas

The investigation of ferritic steels for SOFCs often focuses on exposures in air, although in the SOFC the interconnect material is not only in contact with air but also with gas on the anode side. Unfortunately the term anode gas does not reveal a defined composition as the composition depends on the parameters used to operate the fuel cell. Depending on the fuel, the main constituents are hydrogen or hydrocarbons and the reaction products usually water or, if hydrocarbons are used as fuel CO and CO_2 [63]. The concentration of reaction products also depends on the specific position in the stack, as it increases along the flow direction. In the current project an Ar-4%H_2 mixture instead of H_2 was chosen for safety reasons. At 900°C the exposures were carried out with a rather high concentration of water vapour of 20%. This concentration was chosen to make sure that the oxygen partial pressure of the gas will be well above the dissociation pressure of FeO. According to thermodynamic calculations [60] one would obtain a level very close to the dissociation pressure of FeO with a lower concentration of 2% of water vapour. In the second part of the current chapter the oxidation process in Ar-H_2-H_2O of Crofer 22 APU type materials will be investigated more closely.

6.2.1 Oxidation in Ar-H_2-H_2O

Fig. 6.18 shows the average weight gain after 1000h exposure in Ar-4%H_2-20%H_2O at 900°C in comparison to the weight gain in air. It can be seen that the weight gain after 1000h in Ar-H_2-H_2O is generally approximately half as high as in air but if one compares the alloys with each other the same ranking applies as in air. Except for the alloys with the highest weight gains KCL and KCO the relative errors of the of the weight gain data in Ar-H_2-H_2O are slightly higher than in air.

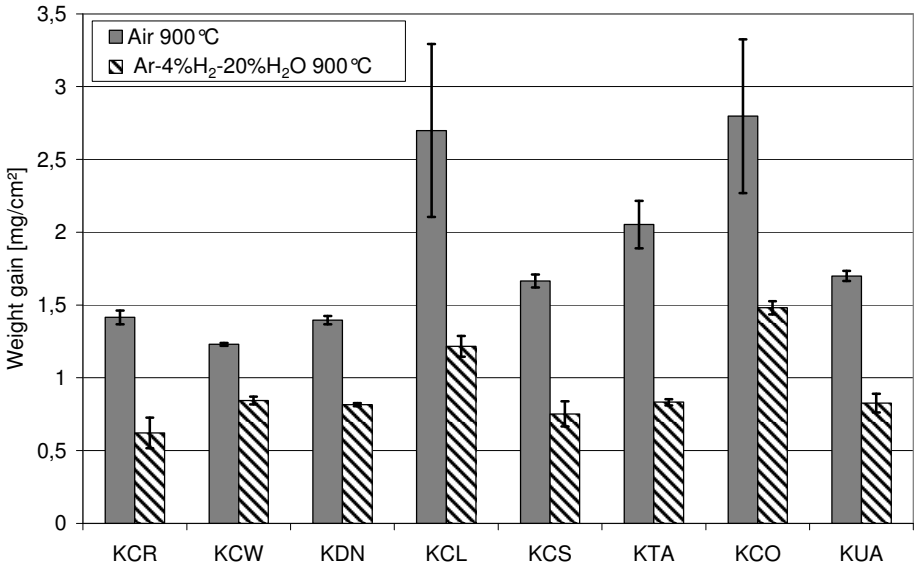

Fig. 6.18: Average weight gain of different alloys after 1000h exposure at 900°C in air and simulated anode gas.

Fig. 6.19 shows the weight gain for the alloys with W (KDN, KCW) and Nb (KCL) addition in comparison to the reference alloy (KCR). In the case of the reference alloy (KCR) the weight gain after 1000h is approximately 0.7mg/cm². For the other alloys the depicted weight gain curves correspond to samples that were in the furnace at the same time. If one compares the ranking of the different alloys, the same effects seem to apply as observed in air. The addition of Nb almost doubles the growth rate compared to the reference alloy while the addition of W does not seem to have a significant effect.

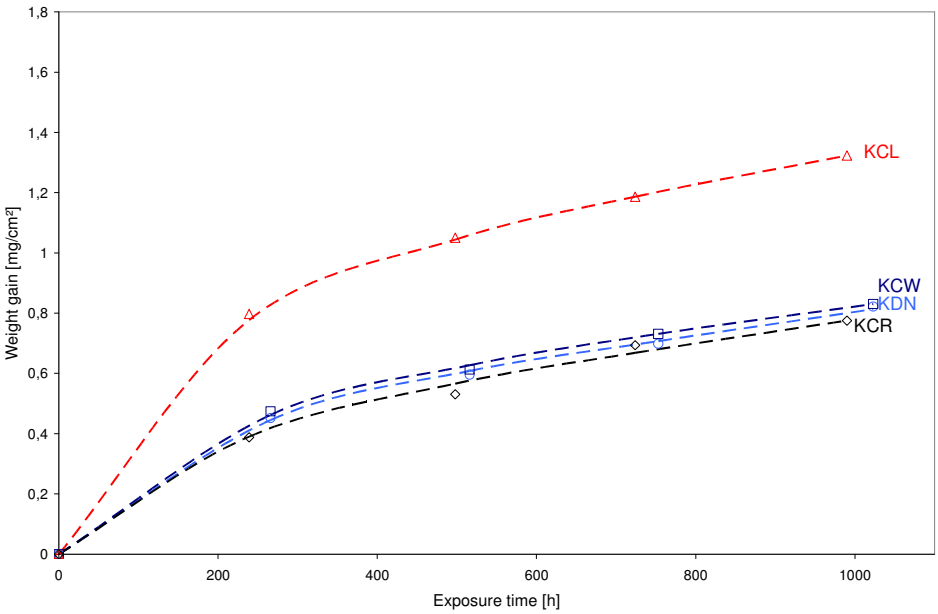

Fig. 6.19: Weight gain of various alloys during 1000h discontinuous exposure at 900°C in Ar-4%H_2-20%H_2O. KCR corresponds to the reference alloy KCW and KDN are alloys with W addition and batch KCL refers to an alloy with 1%Nb addition.

Fig. 6.20 shows the weight gain curves for alloys with combined additions of Nb and/or W and Si or Al. From KTA (1%Nb+0.4%Si) two samples where tested, and from all other materials three samples. The samples of KTA and KCO (1%Nb+0.15%Al) showed excellent reproducibility, the samples of KCS (1%Nb+0.25%Si) and KUA (W, Nb, Si) showed larger data scatter. In the case of KCS the other two samples had a weight gain after 1000h which was approximately 0.2mg/cm² lower than the sample depicted here, while the other samples of KUA (2%W+0.5%Nb+0.25%Si) had a weight gain which was approximately 0.1mg/cm² higher. In conclusion it seems that, although more scatter between data obtained for different samples occurs, the effects of the various alloy additions on oxidation rates were similar to those observed in air. The addition of Nb and Al results in a high oxidation rate while the combined addition of Nb and Si results in a similar weight gain as observed for the reference alloy. In Fig. 6.21 two samples of the reference alloy (KCR) are shown which were both exposed for 1000h at 900°C. While Fig. 6.21a shows the oxide scale after exposure in Ar-4%H_2-20%H_2O, Fig. 6.21b corresponds to the exposure in air. The results show that the scale formed in air is more than three times thicker than the scale formed in Ar-4%H_2-20%H_2O.

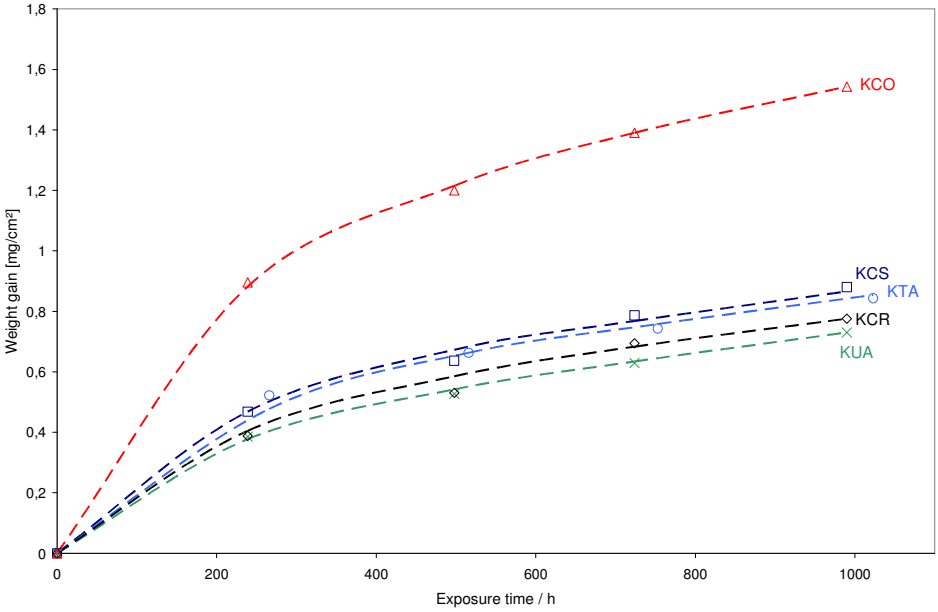

Fig. 6.20: Weight gain of various alloys during 1000h discontinuous exposure at 900°C in Ar-4%H_2-20%H_2O. KCR corresponds to the reference alloy KCO, KCS and KTA contain 1%Nb and 0.15%Al, 0.2%Si and 0.4%Si respectively. KUA corresponds to an alloy with 2%W+0.5%Nb+0.25%Si addition.

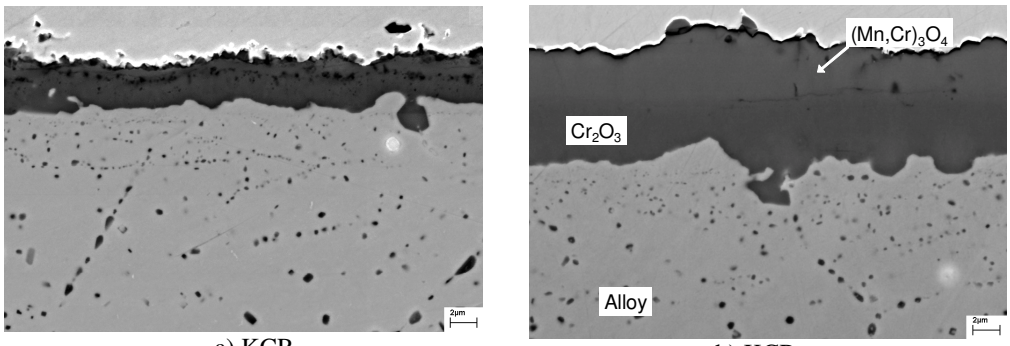

a) KCR b) KCR

Fig. 6.21: Comparison of the oxide morphology on alloy KCR (Reference) after 1000h oxidation at 900°C in Ar-4%H_2-20%H_2O (a) and air (b).

This is in agreement with the gravimetric data because the weight gains in air are generally substantially higher than in Ar-H_2-H_2O. Another apparent difference between the air and anode gas exposure is the porosity of the scale formed in Ar-4%H_2-20%H_2O. Especially at the interface between the $(Cr,Mn)_3O_4$ layer and the Cr_2O_3 layer a line of pores can be observed. In contrast, the scale formed in air is almost completely dense and the interface between inner

chromia and outer spinel layer can only be seen due to a slight difference in brightness in the backscattered electron image. Another difference between the air and anode gas exposure is the oxide surface. While the oxide scales formed in air show a smooth appearance (see also Fig. 6.6) the cross-sections of the samples oxidised in Ar-H_2-H_2O atmosphere show a plate like morphology. This is due to whisker formation on the sample surface which is typical for Cr-Mn spinel in low pO_2 atmospheres [64, 65].
Fig. 6.22 shows cross-sections of samples of the alloys discussed earlier. Generally the same differences between the exposure in air and in H_2-H_2O apply as discussed for the reference alloy, i.e. the porous oxide scales, especially at the spinel/chromia interface, and a whisker/plate type oxide surface are formed in simulated anode gas. As observed in air, no major differences between the alloys with W addition and the reference alloy can be found.

Interesting to note is a thin layer beneath the scale in Fig. 6.22b which does not show any sign of internal oxidation. This is believed to be due to a known mechanism [6]; compressive stresses as a result of internal oxidation cause the metal to creep resulting in outward metal flow. The fact that no internal oxidation can be observed in this area indicates that it occurs after the internal oxidation process and thus the alloy matrix is depleted in strong oxide forming elements. The same behaviour, though not equally pronounced, can also be observed in Fig. 6.22a, Fig. 6.21 or Fig. 6.6.

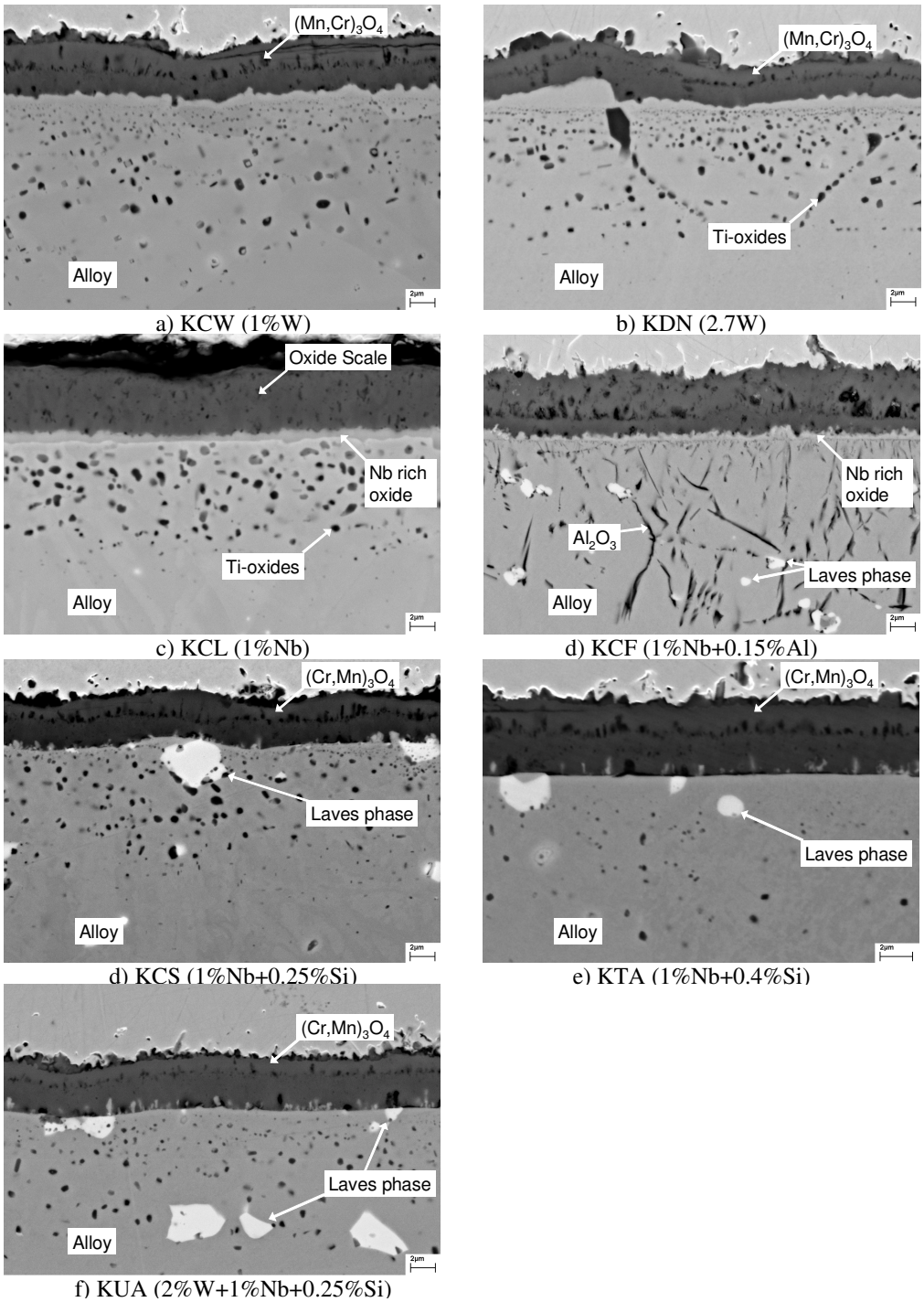

Fig. 6.22: SEM images of oxide scales formed on various alloys after 1000h exposure in Ar-4%H_2-20%H_2O at 900°. Note the slightly different magnification of Fig. 6.22e. KCF has very similar composition as KCO (1%Nb+0.15%Al) the exact composition of KCF can be found in the appendix.

On the image of the alloy with Nb addition (KCL) (Fig. 6.22c) the two-layered scale that was observed on all other alloys cannot be seen. Instead a homogenous scale with high porosity is observed. Other images of KCL exposed under the same conditions indicate that the $(Cr,Mn)_3O_4$ layer may have spalled off locally and thus Fig. 6.22c just shows the inner part of the scale. The Nb-rich oxide below the chromia scale can be clearly seen. Directly beneath, a number of precipitates can be seen that appear brighter than the Ti-oxide particles in the rest of the internal oxidation zone. This could be an indication for the formation of mixed (Ti, Nb)-oxides. In Fig. 6.22c no Laves phase precipitates can be seen. As described for the exposures in air this is due to the fact that a Nb depletion zone is formed because Nb is consumed due to its incorporation into the oxide scale. Fig. 6.23 shows low magnification images of KCL (1%Nb) and KCS (1%Nb+0.25%Si) to illustrate this effect. The NbDZ formed in the Ar-H_2-H_2O atmosphere at 900°C is substantially smaller than that formed in air.

Fig. 6.22d shows a cross-section of KCF (Nb+Al) where the composition is very similar to KCO except that KCF has a substantially lower La content. As already observed in air substantial internal oxidation of Al can be seen below the scale. The near surface depletion of Nb is not very pronounced, however, a Nb rich oxide below the scale can be seen as it was observed on KCL (1%Nb). The alloys with addition of (W), Nb and Si (KCS, KTA, KUA) do not show any significant difference, the Laves phase precipitates are stable directly below the scale which exhibits, as found for the other alloys, a high porosity compared to the exposures in air.

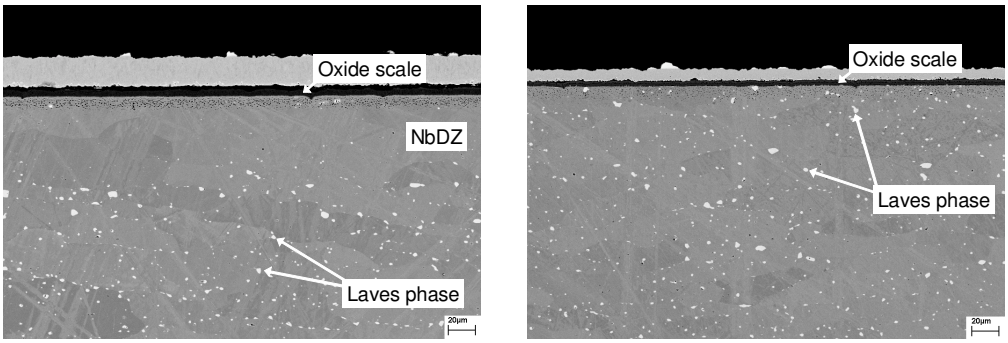

a) KCL (1%Nb) b) KCS (1%Nb+0.25%Si)

Fig. 6.23: Comparison between the oxide scales and depletion zones of the alloys KCL and KCS after 1000h exposure at 900°C in Ar-4%H_2-20%H_2O. The alloy with Nb addition (KCL) exhibits a 50µm wide Nb depleted zone (NbDZ) close to the sample's surface. In contrast Laves phase precipitates can be found directly below the oxide scale in the alloy with combined additions of Nb and Si.

6.2.2 Mechanism of scale formation

The most apparent difference between the oxide scale morphology in air and simulated anode gas is the band of pores at the interface between the chromia and the spinel layer. This is believed to be related to a difference in the spinel layer. It was shown by Naoumidis et al. [66] that $MnCr_2O_4$ has an exact stochiometry in low pO_2 atmospheres such as Ar-H_2-H_2O while in air it is stable over a wide range of compositions. The spinel is formed due to cation diffusion through the Cr_2O_3 layer. Thus during oxidation in simulated anode-gas the supply of Cr and Mn has to match to a ratio 2:1 to form a stochiometric spinel. Apparently this is not the case which causes pore formation at the interface $Cr_2O_3/MnCr_2O_4$ due to vacancy condensation. During air oxidation the spinel can be formed in a wide compositional range thus if the supply of Cr and Mn does not match to the stochiometry no pore formation occurs.

In order to get a better understanding of the oxidation process of Crofer 22 APU type materials in Ar-H_2-H_2O atmospheres the oxide scale of KCB (Crofer 22 APU 2^{nd}) after 15h exposure at 800°C in Ar-4%H_2-2%H_2O was investigated by a number of methods. Fig. 6.24 shows a TEM brightfield image and EELS (Electron Energy Loss Spectroscopy) maps of the corresponding area. The difference between the Mn rich outer spinel layer and the inner Cr_2O_3 layer can be clearly seen. Also clearly visible is the whisker type morphology of the sample surface. Below the scale at a steel grain boundary a Mn rich oxide nodule can be found which will be discussed shortly.

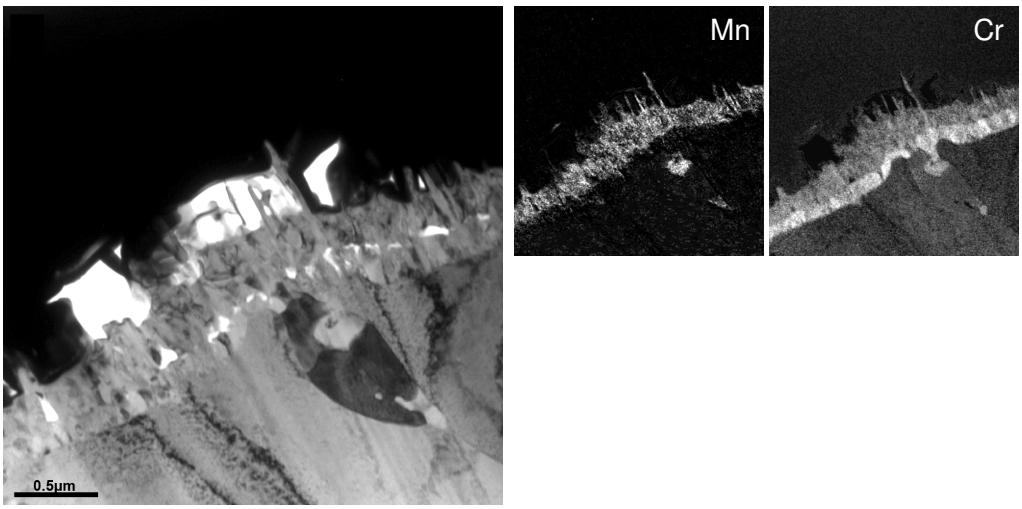

Fig. 6.24: TEM brightfield image and EELS maps for Mn and Cr of the oxide scale formed after 15h at 800°C in Ar-4%H_2-2%H_2O.

Fig. 6.25 shows Raman spectra which were measured on the oxide scales of Crofer 22 APU samples oxidised for various times in Ar-4%H_2-2%H_2O. There are two distinct peaks corresponding to Cr_2O_3 and $MnCr_2O_4$. If one compares the different exposure times it can be clearly seen that in Ar-H_2-H_2O first a chromia layer is formed and subsequently the spinel layer is formed on top of the chromia scale. It can be seen the opposite is true for the exposure in air: after 10 min the spinel peak much more distinct than the chromia peak while after 15h the peaks have about the same size.

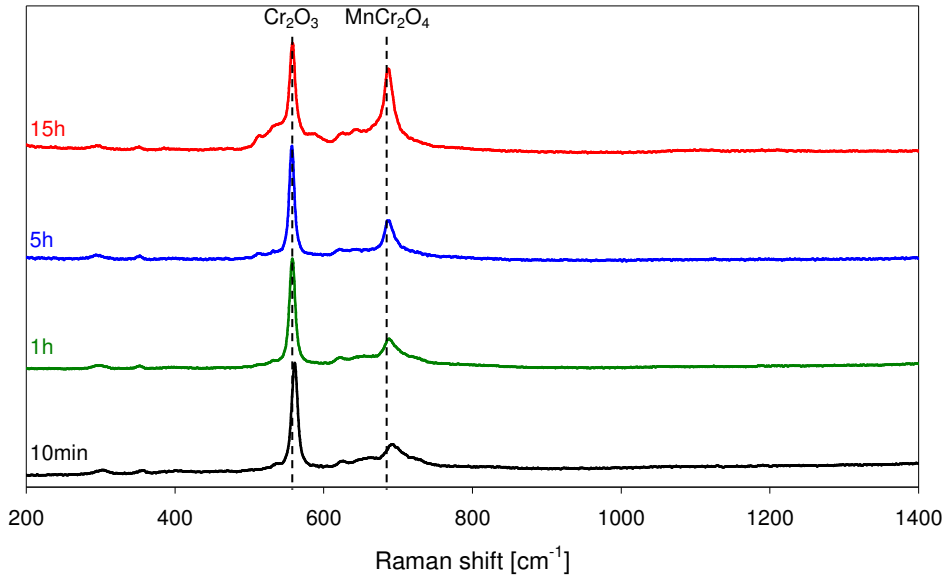

Fig. 6.25: Raman spectra measured on the oxide scale of Crofer 22 APU 2nd after various exposure times in Ar-4H_2-2H_2O at 800°C.

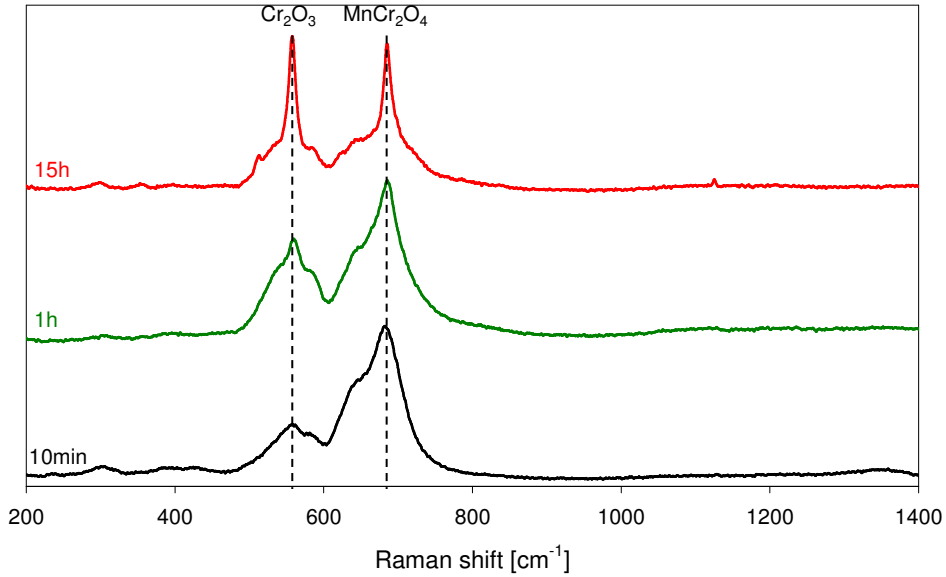

Fig. 6.26: Raman spectra measured on the oxide scale of Crofer 22 APU 2nd after various exposure times in air at 800°C.

Fig. 6.27 shows to Raman spectra obtained from different areas of a sample exposed for 15h at 800°C in Ar-4%H_2-2%H_2O. One spectrum corresponds to the alloy grain boundary area while the other one was taken within the grain area. Comparing the spectra reveals that in the

spectrum from the grain boundary the spinel peak (681cm^{-1}) has a higher intensity than the peak that corresponds to Cr_2O_3 while the oxide scale formed on the grain centre shows the opposite.

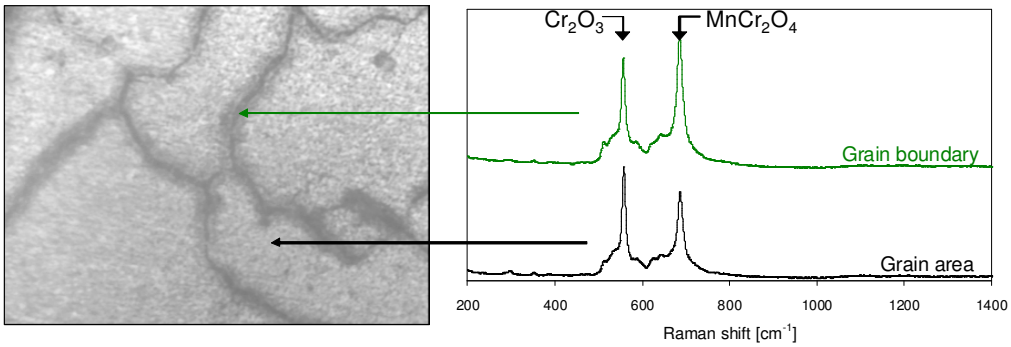

Fig. 6.27: Raman spectra obtained from the oxide scale of Crofer 22 APU (2nd) after 15h exposure at 800°C in Ar-4%H_2-2%H_2O in different areas.

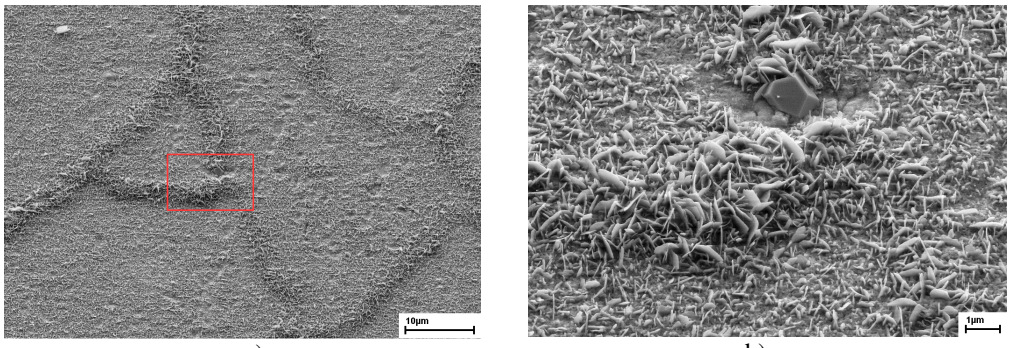

a) b)

Fig. 6.28: Surface morphology of Crofer 22 APU 2nd (KCB) after 15h exposure at 800°C in Ar-4%H_2-2%H_2O.

This can be explained if one considers Fig. 6.28 and Fig. 6.29. The plan view images show that the oxide scale formed over the alloy grain boundaries is thicker than that on the grain areas. The higher magnification in Fig. 6.28b also reveals a morphology of blades and whiskers that is typical for the oxidation of this material in Ar-H_2-H_2O [67]. The cross-section in Fig. 6.29 shows that at the grain boundary oxide nodules can be found similar to those observed in the TEM image in Fig. 6.24. The EELS analysis revealed that these nodules are rich in Cr and Mn. It is believed that the formed oxide is also of spinel type. This explains the strong Raman signal from the spinel at the grain boundaries. According to Huczkowski et al. [6] the subscale spinel formation can be explained by micro cracks in the oxide that allow

molecular oxygen to penetrate the scale and oxidise the steel apparently this mechanism is favoured along grain boundaries.

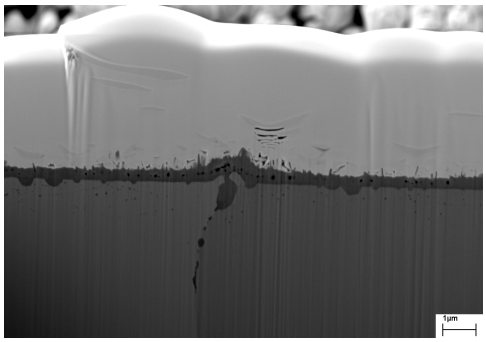

Fig. 6.29: Cross-section of the oxide scale of Crofer 22 APU formed at a grain boundary after 15h at 800°C in Ar-4%H_2-2%H_2O. Secondary electron imagine obtained with a LEO 1540 cross beam instrument.

6.2.3 SNMS analysis of scale formed in Ar-H_2-H_2O

To further investigate the oxidation behaviour of Crofer 22 APU type materials in Ar-4%H_2-2%H_2O short term exposures were carried out and the oxide scales were investigated by SNMS. The samples were kept in the furnace which was set to 800°C for 10min, 60min and 24h respectively. After 2.5min the temperature exceeded 700°C during heating and when the samples were removed from the furnace their temperature reached 300°C within less than 3min.

Fig. 6.30 shows the SNMS profile of the sample exposed for 10min. While the y-axis gives concentrations of the different elements the x-Axis refers to sputtering time in seconds which corresponds to the depth within the sample. During the so called transient oxidation when the fresh sample surface is exposed all metals that can form oxides in the respective atmosphere will oxidise simultaneously. In the current case after 10min the surface scale composition already has differentiated to some extent. However, the Mn concentration of less than 10% indicates that no continuous spinel layer has formed instead a substantial amount of Fe can be found on the surface. At the metal/oxide interface a peak of Mn and Ti can be found.

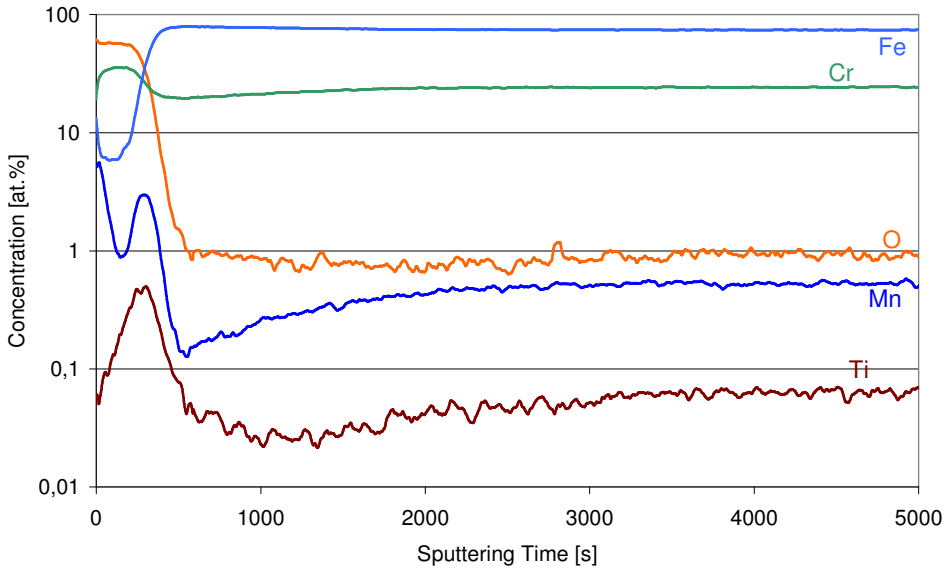

Fig. 6.30: SNMS profile of KCR (Reference) after 10min oxidation in Ar-4%H_2-2%H_2O.

After 1h of oxidation in Ar-4%H_2-2%H_2O (see Fig. 6.31) the outer spinel layer seems to be continuous. At the metal/scale interface a second Mn peak can be observed which is believed to be related to the inner spinel (Cr, Mn, Ti)$_3O_4$. The Ti concentration increases parallel with the Mn peak but the Ti concentration decreases towards the sample surface. This is believed to be due to the fact that some Ti is dissolved in the chromia layer which is well known to occur at low pO_2 [32]. The O peak at 4000s is due to plasma instabilities. In general the quantification of low oxygen concentrations is not reliable [59].

The analysis after 24h exposure, which is shown in Fig. 6.32, indicates very similar results. The Fe concentration in the scale is clearly lower than after 10 minutes of exposure. Mn shows a double peak; the major peak at the oxide surface corresponding to the $MnCr_2O_4$ and an inner peak near the metal oxide interface. Ti can be found in the chromia layer and close to the metal oxide interface. It is likely that the Ti peak corresponds to the Ti dissolution in the Cr_2O_3 scale, the Ti in the inner (Cr,Mn, Ti)$_3O_4$ spinel as well as Ti which becomes internally oxidised in the alloy.

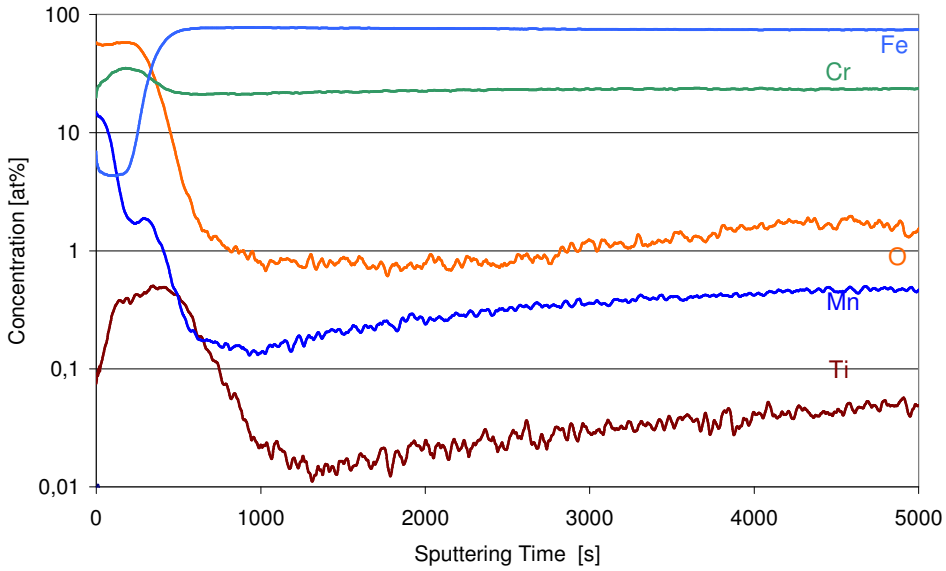

Fig. 6.31: SNMS profile of KCR (Reference) after 60min oxidation in Ar-4%H_2-2%H_2O. The increase of the oxygen at approximately 5000s is due to plasma instabilities.

For comparison SNMS profiles of different alloy modifications after 24h at 800°C in Ar-4%H_2-2%H_2O are shown below. The results of alloy KDN (2.7%W) (see Fig. 6.33) clearly show that W is not incorporated into the oxide scale. Ti exhibits a peak of several percent at a sputtering time of approximately 1500s which is believed to be to the fact that the Ti concentration in the alloy is relatively high (i.e. 0.11% compared to 0.06% for the reference alloy). Otherwise no major differences compared to the data obtained for the reference alloy can be observed.

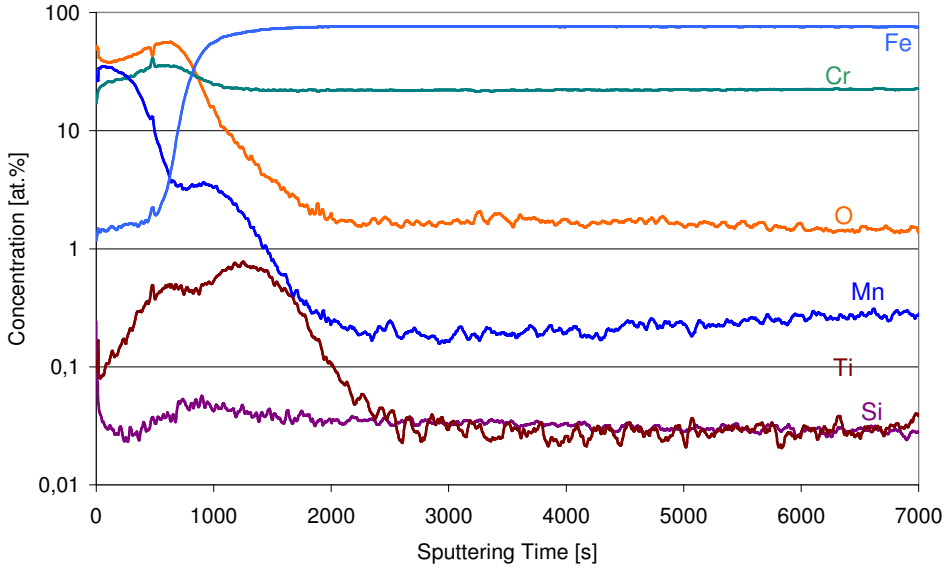

Fig. 6.32: SNMS profile of KCR (Reference) after 24h oxidation in Ar-4%H_2-2%H_2O.

Fig. 6.34 shows the SNMS analysis of the scale formed on KCL (1%Nb) after 24h at 800°C in Ar-4%H_2-2%H_2O. It can be clearly seen that significant amounts of Ti and Nb are present near the metal/scale interface. The Ti peak is located slightly deeper in the material probably due to internal oxidation of Ti. The Nb peak corresponds to the Nb-rich oxide formed at the metal/scale interface (see Fig. 6.22). While substantial amounts of Ti can be found in the Cr_2O_3 the amount of dissolved Nb is significantly lower. Nb shows a pronounced depletion in the alloy near the scale alloy interface.

The SNMS results for the alloy with combined additions of Nb and Si (KCS) are shown in Fig. 6.35. The curves show a similar behaviour as the reference alloy except for a slight enrichment of Nb together with Si at the metal/scale interface. Such a Nb enrichment was not observed in the SEM cross-sections and no explanation can presently be given. The Nb depletion in the alloy is less pronounced than in the Si free alloy due to the far less pronounced enrichment of Nb in the inner part of the oxide scale.

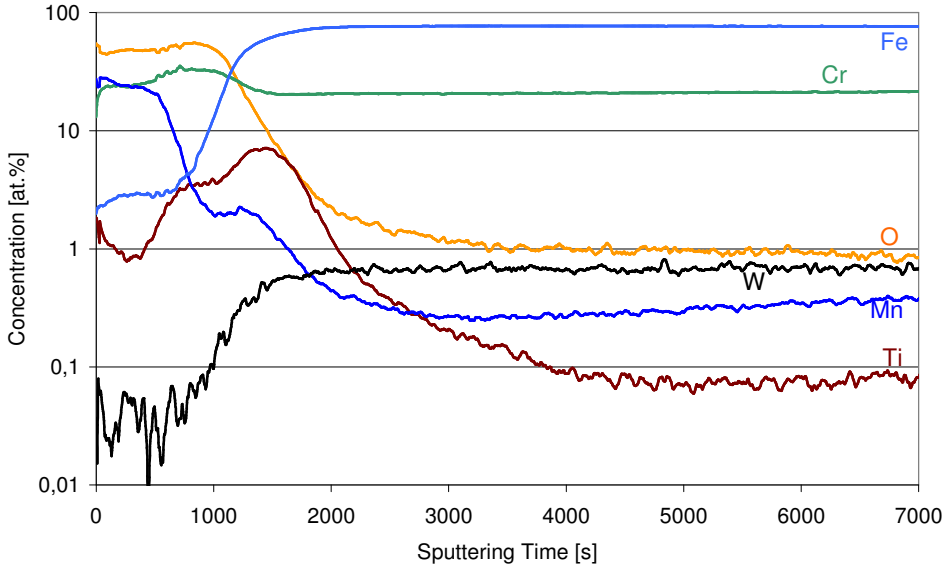

Fig. 6.33: SNMS profile of KDN (2.7%W addition) after 24h oxidation in Ar-4%H_2-2%H_2O.

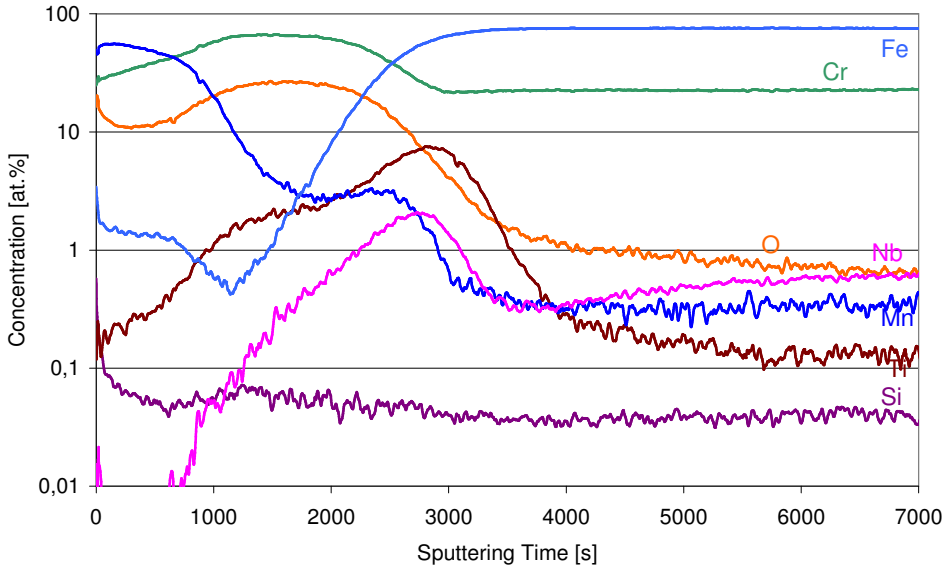

Fig. 6.34: SNMS profile of KCL (1%Nb) after 24h oxidation in Ar-4%H_2-2%H_2O.

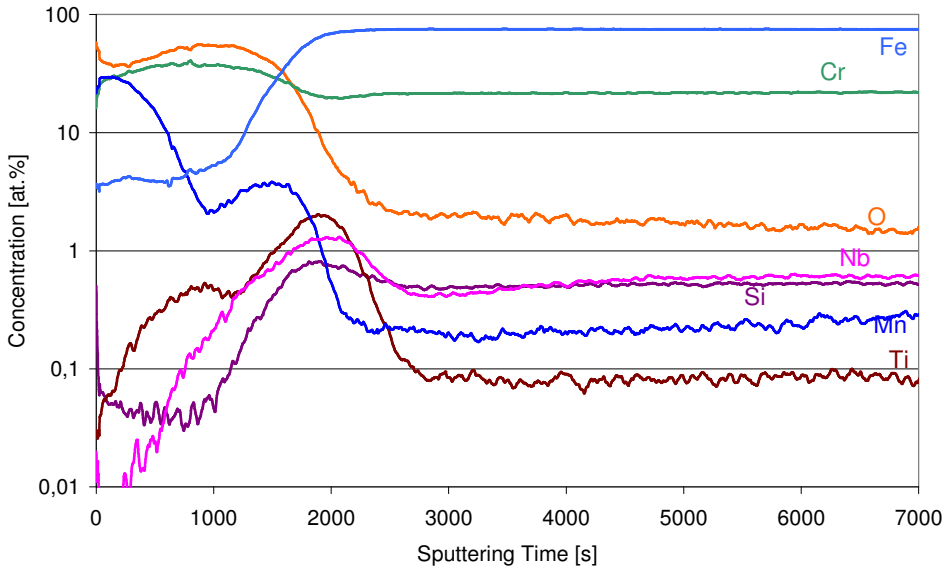

Fig. 6.35: SNMS profile of KCS (1%Nb+0.25%Si) after 24h oxidation in Ar-4%H_2-2%H_2O.

6.3 Specimen thickness dependence of oxidation rate

Selected alloys were tested under cyclic conditions because in the SOFC application the interconnect material will be subject to thermal cycling especially in mobile applications. The experiments were carried out with an accumulated time of 1000h at 900°C in laboratory air. Every 2h the samples were cooled for 15min to room temperature by pressurised air. Weight change measurements were carried out every 36h.

Huczkowski et al. [6] found out that under these conditions ferritic alloys may exhibit a thickness dependence of the oxidation behaviour whereby thin specimens show higher oxide growth rates than thick samples. Fig. 6.36 shows the weight gain of four specimens of different thickness of alloy KCB (Crofer 22 APU 2nd) during cyclic oxidation at 900°C. It is apparent that the thinner specimens oxidise faster than the thicker ones.

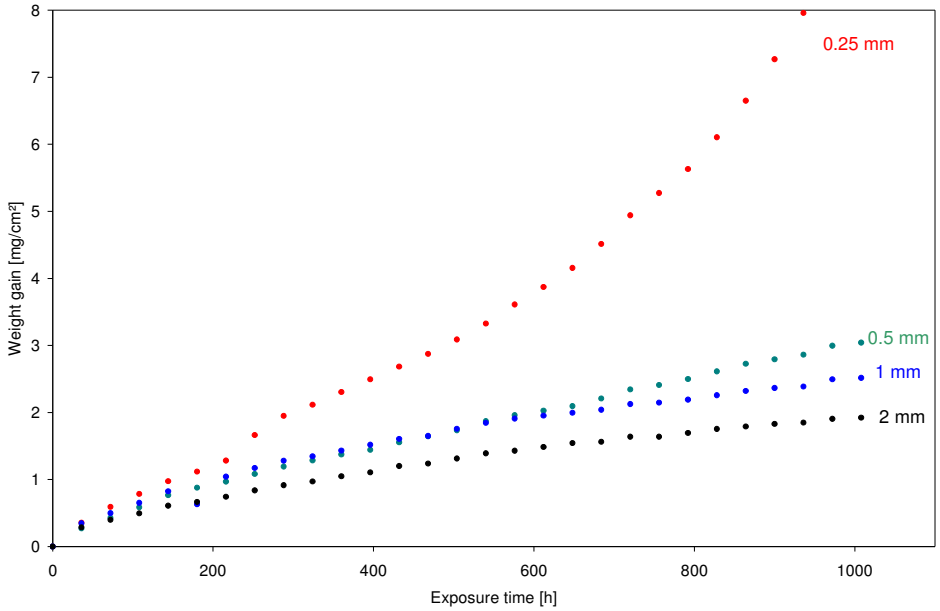

Fig. 6.36: Weight gain of specimens of KCB (Crofer 22 APU 2nd) of different thickness during cyclic oxidation in air at 900°C.

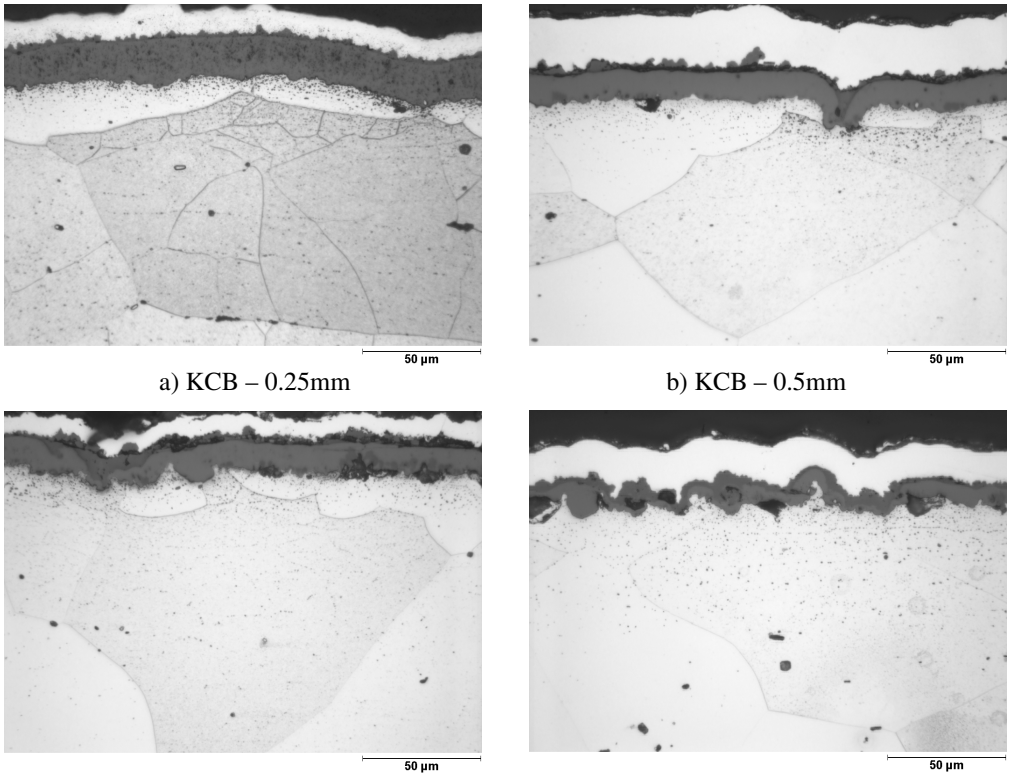

a) KCB – 0.25mm b) KCB – 0.5mm

c) KCB – 1mm d) KCB – 2 mm

Fig. 6.37: Optical micrographs of specimens of different thicknesses of Crofer 22 APU 2nd (KCB) after 1000h cyclic oxidation at 900°C.

The specimen of 2mm thickness gained 2mg/cm² after 1000h of exposure while the 0.5mm thick specimen gained 3mg/cm². In the first 200h the thinnest specimen (0.25mm) already showed a higher weight gain than the other samples, and after 200h the oxidation rate increased considerably as local breakaway occurred.

Fig. 6.37 shows cross-sections of the respective samples shown in Fig. 6.36. It can clearly be seen that the scale formed on the 0.25mm thick sample is much thicker than the scale observed on the 2mm sample, while the samples with thicknesses of 0.5mm and 1mm show an intermediate thickness. This is in agreement with the differences in weight gain shown in Fig. 6.36. However, the drastic increase in weight of the thinnest sample is due to local Fe oxide formation, as can be seen in Fig. 6.38a. Compared to the other samples the scale of the 0.25mm sample exhibits very substantial porosity. Fig. 6.37 clearly shows a correlation between initial specimen thickness and morphology of the scale alloy interface. The thinner

samples show a smoother interface while the scales on the thick samples show significant buckling. This effect is believed to be stress related; it is well-known that oxide scale formation may result in considerable growth stresses within the oxide during isothermal exposure [68]. Due to the newly formed oxide in a constrained volume the scale will be subject to compressive stresses, which results in tensile stresses in the metallic substrate. At high temperatures these tensile stresses can cause creep of the metallic substrate [69].

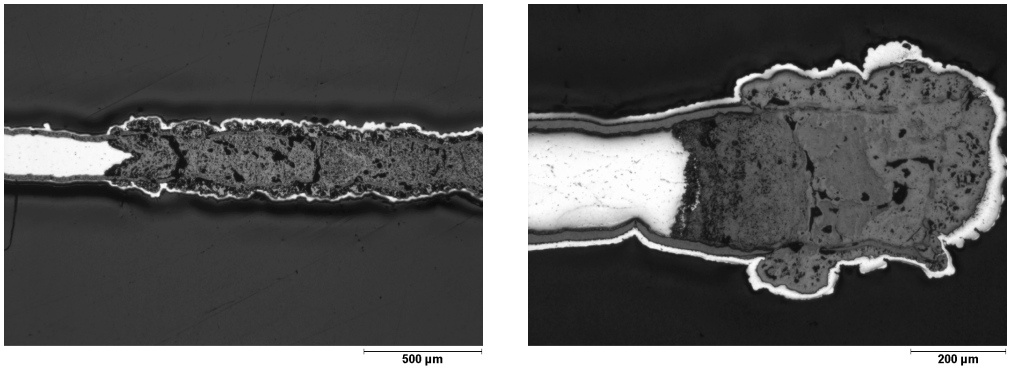

a) KCB b) KCL

Fig. 6.38: Breakaway oxidation observed on the 0.25mm thick samples of KCB (Crofer 22 APU 2nd) and KCL (1%Nb addition) (see Fig. 6.42) after cyclic oxidation in air at 900°C.

It is suggested that a thin specimen will be subject to creep due to the oxidation induced tensile stresses in the substrate. However, due to its larger cross-section a thick specimen will not creep to the same extent. Consequently the 0.25mm specimen in Fig. 6.37 shows a smooth interface because growth stresses in the oxide were reduced by substrate creep. The 0.5mm thick specimen also shows a smooth interface apart from some areas with an indented oxide scale. These seem to be regions where the scale cracked to relieve growth stresses. The 1mm sample shows a more uneven interface and a number of large pores at the metal/oxide interface. The 2mm sample marks the other extreme case: in the thick specimen the stress is too low to cause significant creep of the bulk material, thus stresses in the scale can only be relieved by near surface creep or by buckling of the scale which is observed to a large extend in Fig. 6.37. According to the proposed theory of substrate creep due to oxidation induced stresses, the sample dimensions should increase during oxidation [69]. Table 7 gives the sample dimensions before and after the exposure. It has to be noted that the accuracy of the

measurement is poor, and an accurate measurement is especially difficult if the sample has bent due to an uneven stress distribution. However, it can be clearly seen that the 0.25mm specimen of KCB (Crofer 22 APU 2nd) has increased in length by approximately 10% due to the compressive growth stresses in the oxide scale. The 0.5mm thick specimen also increased in length by 1mm, whereas the 1 and 2mm thick samples do not exhibit significant elongation. Thus, strictly speaking, the sample surface on the thin samples is not constant but a function of time. This can contribute to some extent to the higher weight gains of thin samples. However, Huczkowski [6] showed that the effect is not significant. The micrographs also clearly show thicker oxide scales on the thin samples, which proves that the oxidation process is actually faster.

The growth stresses in the oxide are mainly generated due to differences in volume between the metal and the respective oxide. This is commonly described by the Pilling-Bedworth Ration (PBR) which corresponds to the ratio between the molar volumes of the oxide and the respective metal.

$$PBR = \frac{V_{Ox}}{V_M}$$

Most oxides have PBR values >1 which would lead in an unconstrained oxide to a strain. If one assumes pure inward growth the isotropic strain equals [70]

$$\varepsilon = \sqrt[3]{PBR} - 1$$

However, since the oxide can not freely expand the strain will lead to the formation of a compressive stress in the oxide (for PBR values >1). Applying Hooke's law these stresses can be calculated, but the values differ greatly from experimentally determined values [70].

The compressive stresses in the oxide will induce tensile stresses in the substrate. In a first mathematical approximation a number of simplifications are required. These include e.g. constant growth stress further the time dependence of the growth stress is ignored. However, considering Fig. 6.39 it is apparent that

$$\sigma_{Substrate} \cdot d = -2\sigma_{Ox} \cdot x$$

which can be rewritten as

$$\sigma_{Substrate} = -2\sigma_{Ox} \cdot \frac{x}{d}$$

thus if the stresses in the oxide are constant at a given oxide thickness, the tensile stresses increase with decreasing specimen thickness.

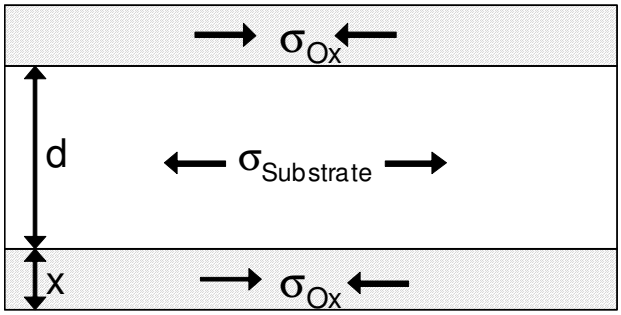

Fig. 6.39: Schematic drawing of growth induced stresses in the oxide scale.

If one applies Nortons creep equation

$$\dot{\varepsilon} \propto (\sigma_{Substrate})^n$$

combining this with the equation above it immediately follows that

$$\dot{\varepsilon} \propto \left(\frac{1}{d}\right)^n$$

If one considers that at 900°C n is > 1 it can be seen that once a critical sample thickness is reached small variations in sample thickness have a significant impact on the creep rate as can be also seen in Table 7.

	Addition compared to reference alloy	Sample thickness	Initial length [mm]	Length after exposure [mm]	Elongation [%]
KCB	-	0.25mm	20.16	22.2	10
KCB	-	0.5mm	20.2	21.2	5
KCB	-	1mm	20.16	20.3	0.7
KCB	-	2mm	20.03	20.1	0.4
KCL	1 Nb	0.25mm	19.65	22.5	15
KCL	1 Nb	0.5mm	19.84	21	6
KCL	1 Nb	1mm	19.84	20	0.8
KCL	1 Nb	2mm	19.84	19.9	0.3
KDN	2.7 W	0.27mm	19.88	21.3	7
KDN	2.7 W	0.5mm	19.72	20.5	4

KDN	2.7 W	1mm	19.7	20	1.5
KDN	2.7 W	2mm	19.83	19.8	-0.15
KCS	1Nb, 0.25Si	0.25mm	19.81	22	11
KCS	1Nb, 0.25Si	0.59mm	19.79	20.1	1.6
KCS	1Nb, 0.25Si	1mm	18.61	18.7	0.5
KCS	1Nb, 0.25Si	2mm	19.83	20	0.9
KUA	2W 0.5Nb 0.25Si	0.3mm	18.8	22?	17?
KUA	2W 0.5Nb 0.25Si	0.5mm	18.65	18.7	0.3
KUA	2W 0.5Nb 0.25Si	1mm	19.4	19.5	0.4

Table 7: Elongation of samples of various alloys during cyclic oxidation at 900°C in air. Cross-section of the respective samples are shown in Fig. 6.37and Fig. 6.47-Fig. 6.51.

In the previous paragraph only stresses due to oxide growth were considered. However, the thermal expansion mismatch between the oxide scale and the substrate can also generate strains which result in substantial stresses during thermal cycling. Since the thermal expansion coefficient of the substrate is larger than the CTE of the oxide, the alloy will exhibit tensile stresses during cooling while the oxide is subject to compressive stresses. In the high temperature part of the cooling step the metallic substrate might creep due to the tensile stress which is generated. In the subsequent heating step the substrate elongates more than the oxide and the stresses would be nullified, but because of the substrate creep during the previous cooling step, the oxide now might encounter tensile stresses which will result in tensile cracking. A schematic drawing of the mechanism is shown in Fig. 6.40.

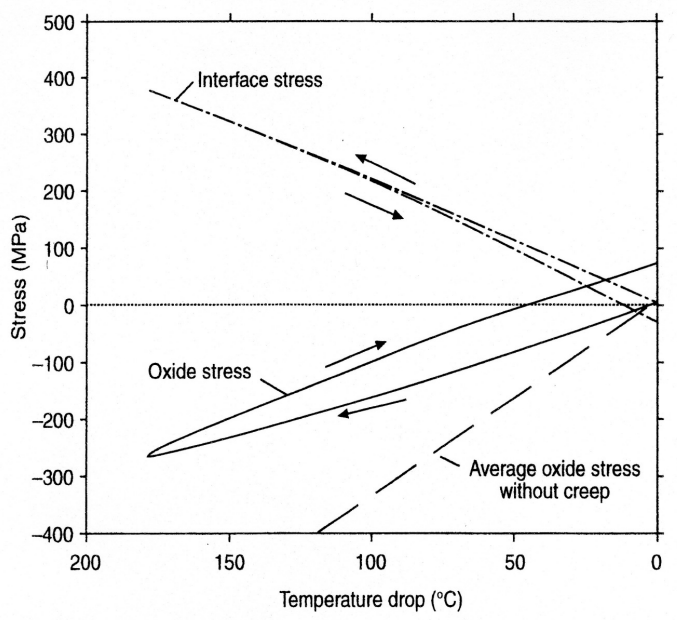

Fig. 6.40: Schematic diagram of the stress formation in the oxide scale during thermal cycling of the specimen leading to tensile cracking [71].

It is difficult to determine which effects are caused by growth induced stresses and which are related to stresses due to thermal cycling. The cross-sections in Fig. 6.37 indicate that the scale was mainly subject to compressive stresses. For example the crack in Fig. 6.37b seems to result from compression of the scale, the same is true for the buckling in Fig. 6.37d. At the same time the elongated grains below the scale in Fig. 6.37a indicate creep of the metal due to tensile stresses in the substrate.

The results obtained during cyclic oxidation are compared with data obtained during discontinuous oxidation in Fig. 6.41. The open symbols correspond to cyclic oxidation data while the filled symbols correspond to samples oxidised discontinuously. Samples of different thickness are also shown which is indicated by the different colours and symbols. The clearest difference in the results obtained with the different methods is that the samples of 0.5mm exhibit significantly higher weight gains than the 0.5mm thick sample that was oxidised discontinuously. If one compares the 1mm samples the weight gain after 1000h of the sample which was oxidised under cyclic conditions is approximately 0.5mg/cm² higher than the

sample which was oxidised discontinuously. The 2mm sample also shows a higher weight gain for the cyclic oxidation although the difference is quite small.

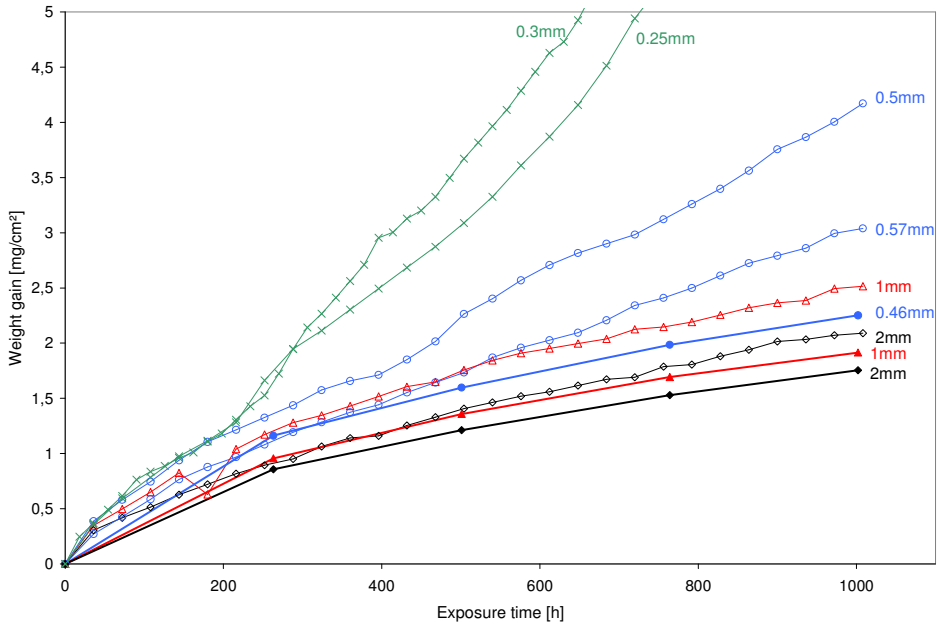

Fig. 6.41: Oxidation of KCB (Crofer 22 APU 2nd) in air at 900°C. The black curves correspond to samples of 2mm thickness while the red, blue and green curves correspond to 1, 0.5 and ~0.3mmm thick samples, respectively. The open symbols mark cyclic (2h/15min) oxidation results, the filled symbols indicate discontinuous oxidation data.

Fig. 6.42 shows the weight gain data of KCL (Nb addition) during cyclic oxidation at 900°C. Compared to the data obtained from KCB (Crofer 22 APU 2nd) the oxidation rate is faster which is in agreement with the earlier observed data (see e.g. Fig. 6.4). The comparison of the weight gain recorded for the 2mm specimen and the data obtained on a 2mm specimen during discontinuous oxidation in air at 900°C (see chapter 6.1.2) shows that the cyclic oxidation leads to an approximately 25% increased oxidation rate. The thickness dependence of the oxidation rate of KCL (1% Nb) is similar to that obtained for KCB (Crofer 22 APU 2nd). The 0.25mm thick specimen of KCL shows breakaway after less than 400h while the thicker specimens do not exhibit any significant increase of the oxidation rate. The 0.5mm thick specimen experiences an increased oxidation rate compared to the 1 and 2mm thick specimens which show almost identical weight gains.

The weight gains measured on samples of different thicknesses of KDN (2.7%W addition) (see Fig. 6.43) show a similar thickness dependence of the oxidation rate as observed on the other alloys: thinner samples exhibit higher oxidation rates than thicker samples. However, the differences between the various samples of this alloy are less pronounced than those of KCB (Crofer 22 APU 2nd): the 2mm and the 0.5mm thick sample differ after 1000h in weight gain by less than 0.5mg/cm². The 0.25mm sample is the only sample which shows a significantly higher weight gain than the other samples, but does not exhibit any indication of breakaway oxidation.

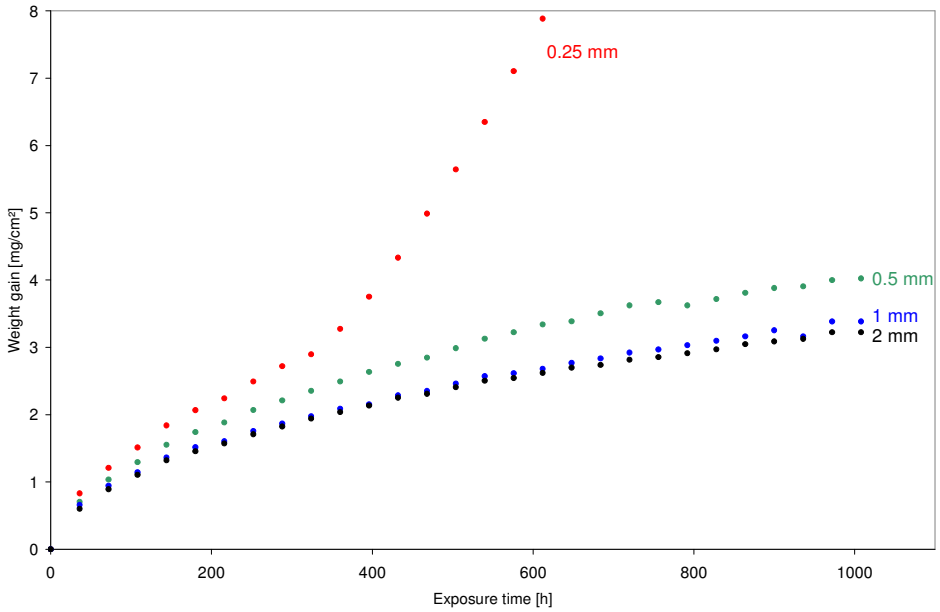

Fig. 6.42: Weight gain for specimens of KCL (1% Nb addition) of different thickness during cyclic oxidation in air at 900°C.

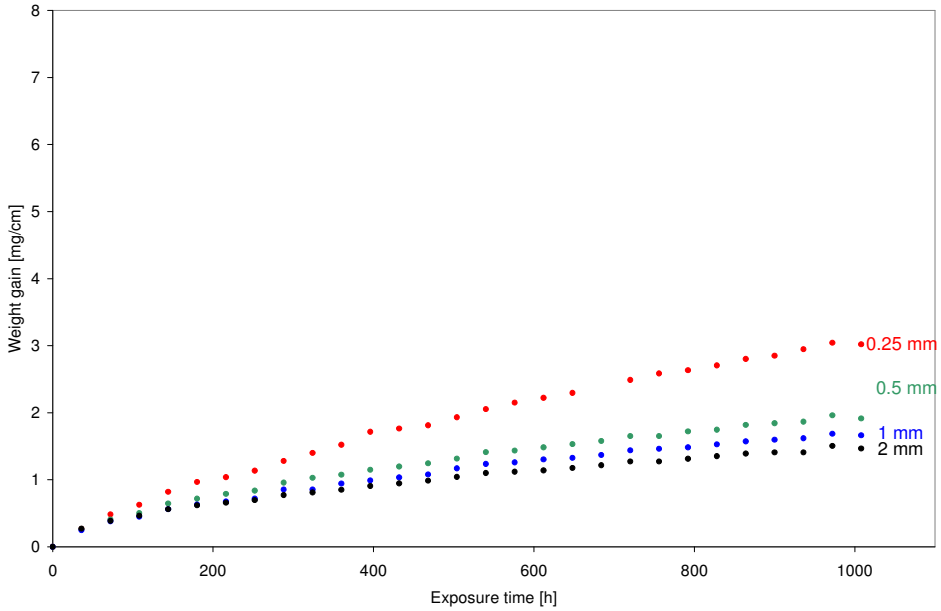

Fig. 6.43: Weight gain for specimens of KDN (2.7% W addition) of different thickness during cyclic oxidation in air at 900°C.

The weight gains recorded for KCS (1%Nb+0.25%Si) are shown in Fig. 6.44. As expected from the earlier observed results (see chapter 6.1.2) the oxidation rate of KCS is lower than that of KCL (Nb addition). Compared to the discontinuous oxidation under the same conditions the weight gain is slightly higher. However, most interesting is a less pronounced thickness dependence of the oxidation rate than for the alloys discussed above. Although the same trend is visible: the thin specimens oxidise faster than thicker ones, the difference between the 0.25mm and the 2mm thick specimen is less than 1mg/cm². Fig. 6.45 and Fig. 6.46 show the thickness dependence for KTA (1%Nb+0.4%Si) and KUA (2%W+0.5%Nb+0.25%Si). These alloys show a very similar behaviour as KCS (1%Nb+0.25%Si): the thinner specimens exhibit a higher oxidation rate than the thick ones but the difference is less pronounced than in the case of Crofer 22 APU 2nd. Thus, if one considers 2mm samples, these alloys show a similar oxidation rate as KCB (Crofer 22 APU 2nd) but with decreasing specimen thickness the oxidation rate of Crofer 22 APU will increase drastically whereas the alloys with combined additions of (W), Nb and Si will experience only a slight increase

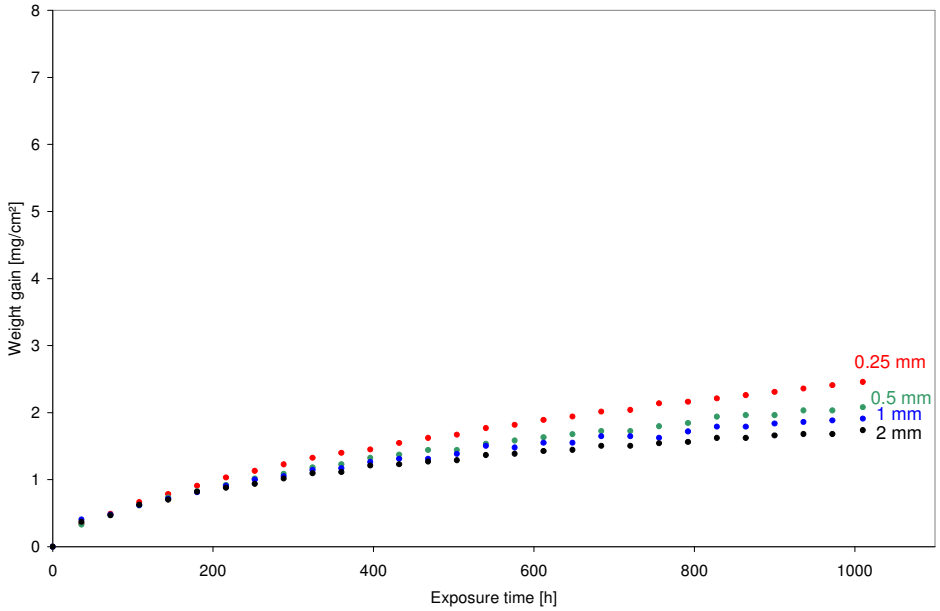

Fig. 6.44: Weight gain of specimens of KCS (1%Nb+0.25%Si) of different thickness during cyclic oxidation in air at 900°C.

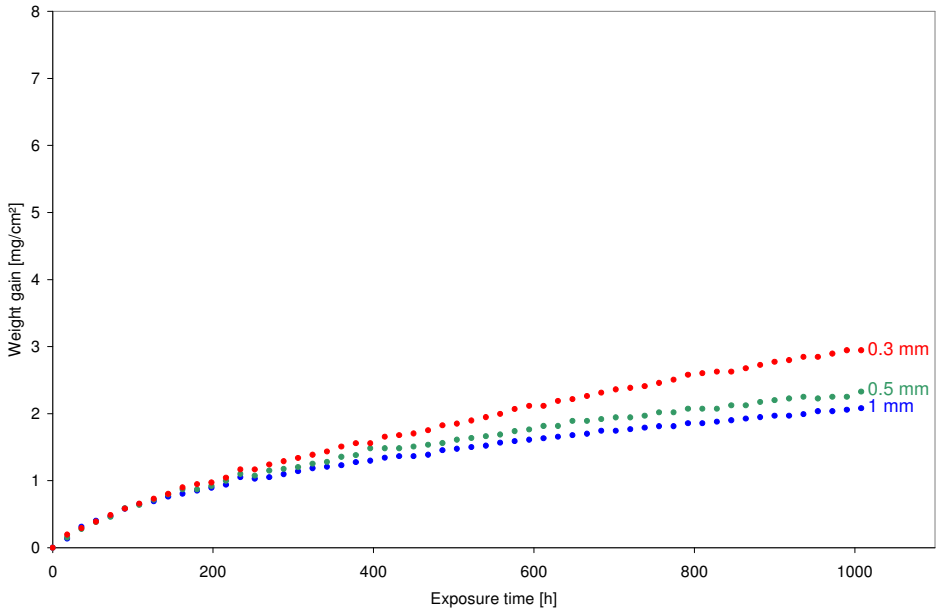

Fig. 6.45: Weight gain of specimens of KTA (1%Nb+0.4%Si) of different thickness during cyclic oxidation in air at 900°C.

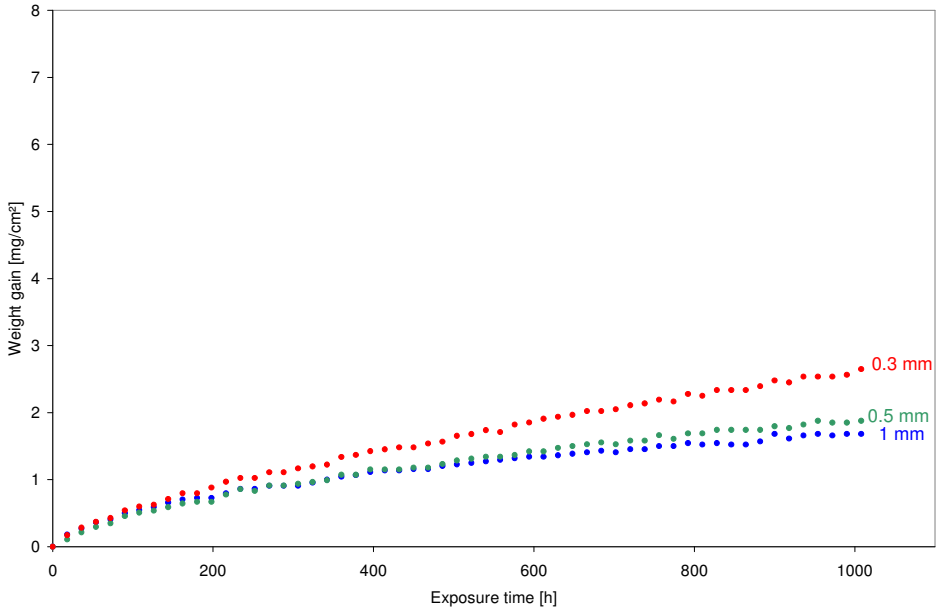

Fig. 6.46: Weight gain of specimens of KUA (2%W+0.5%Nb+0.25%Si) of different thickness during cyclic oxidation in air at 900°C

Cross-sections of different specimens of KCL (1% Nb addition) (see Fig. 6.47) show similar trends in respect to specimen thickness dependence as observed for KCB (Crofer 22 APU 2nd). The scales of the 0.25mm and 0.5mm thick samples show some waviness but no cracks are visible which is believed to be due to stress relief by creep of the substrate. In contrast, the 1mm and even more pronounced the 2mm specimens have an oxide scale which exhibits severe buckling since the substrate is too thick to deform plastically. According to Table 7 the 0.25mm and 0.5mm thick samples also exhibit notable sample elongation due to creep. Fig. 6.38b shows that breakaway oxidation occurred on the 0.25mm thick specimen of KCL (1% Nb) which explains the increase in weight gain rate of this specimen after approximately 300h.

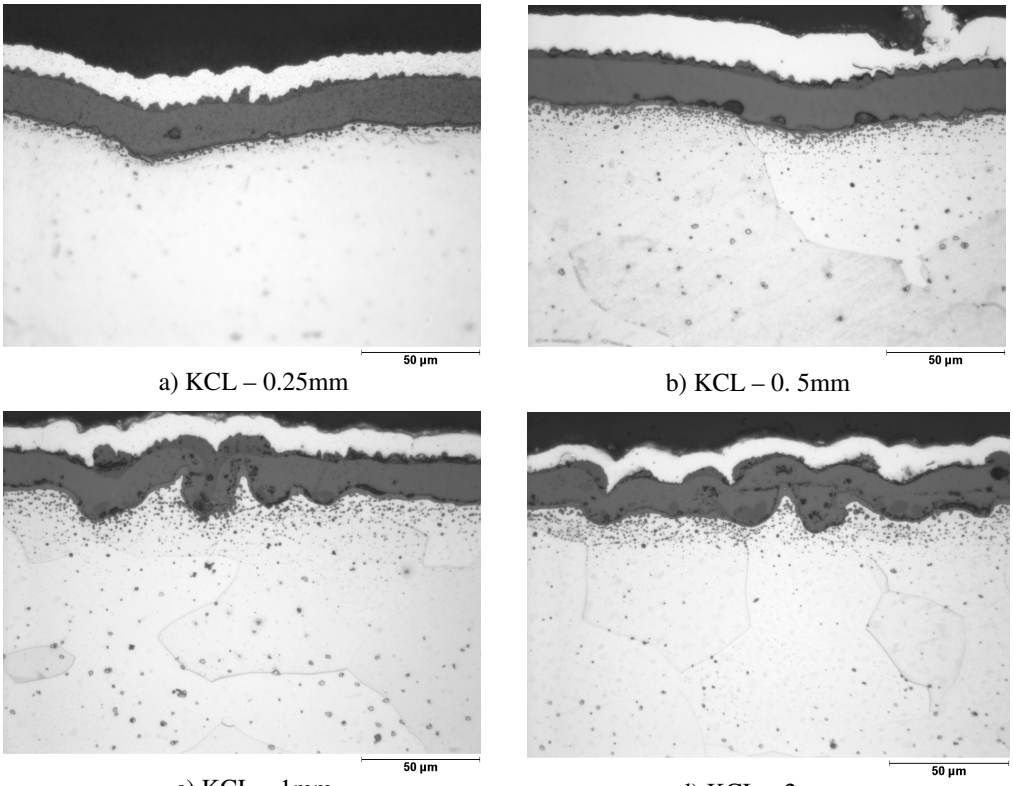

a) KCL – 0.25mm b) KCL – 0. 5mm

c) KCL – 1mm d) KCL – 2mm

Fig. 6.47: Specimens of different thickness of KCL (1%Nb addition) after cyclic oxidation at 900°C in air.

KDN (2.7% W addition) shows a similar behaviour to KCB (Crofer 22 APU 2nd) and KCL (1%Nb addition) as can be seen in Fig. 6.48. The two thin samples have a wavy scale which does not show any buckling. In contrast, the oxide scales on the 1 and 2mm samples show extensive buckling. The comparison of the scale thicknesses confirms the weight gain data: the scale of the 0.25mm sample is thicker than that of the other samples. The sample elongation after the exposure is slightly lower than that observed for KCB and KCL but indicates qualitatively the same trend with respect to dependence of specimen thickness.

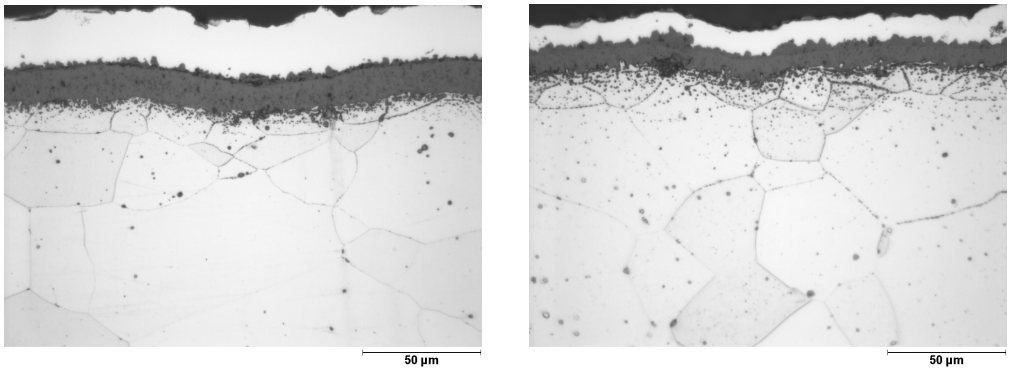

a) KDN – 0.25mm b) KDN – 0.5mm

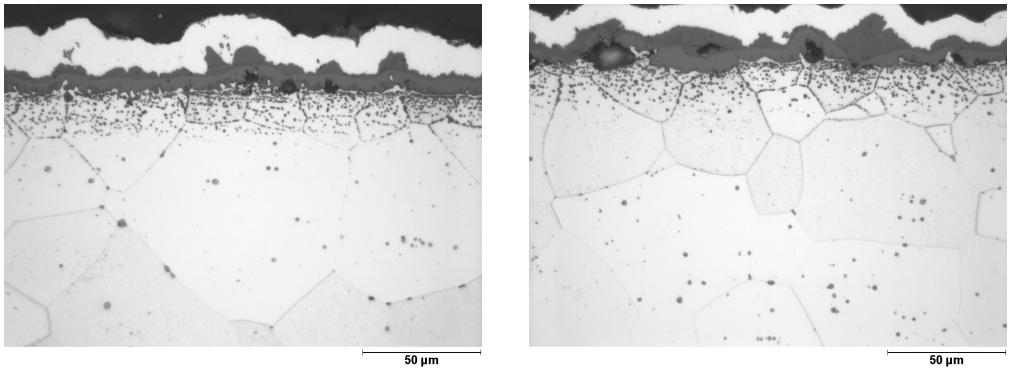

c) KDN –1mm d) KDN – 2mm

Fig. 6.48: Specimens of different thickness of KDN (2.7% W) after cyclic oxidation at 900°C in air.

Fig. 6.49 shows cross-sections of the respective samples of KCS (1%Nb+0.25%Si) of which the weight gain data were shown in Fig. 6.44 (note the different magnification in the images). The 0.25mm thick sample shows a porous scale and a wavy interface as it was observed for the other samples discussed above. With 10% the sample elongation is also in the same range as for the alloys discussed above (see Table 7). In contrast to the other samples the 0.5mm thick sample already shows extensive buckling similar to the 1 and 2mm thick samples, whereas the elongation of the sample is with 0.3mm hardly detectable (see Table 7).

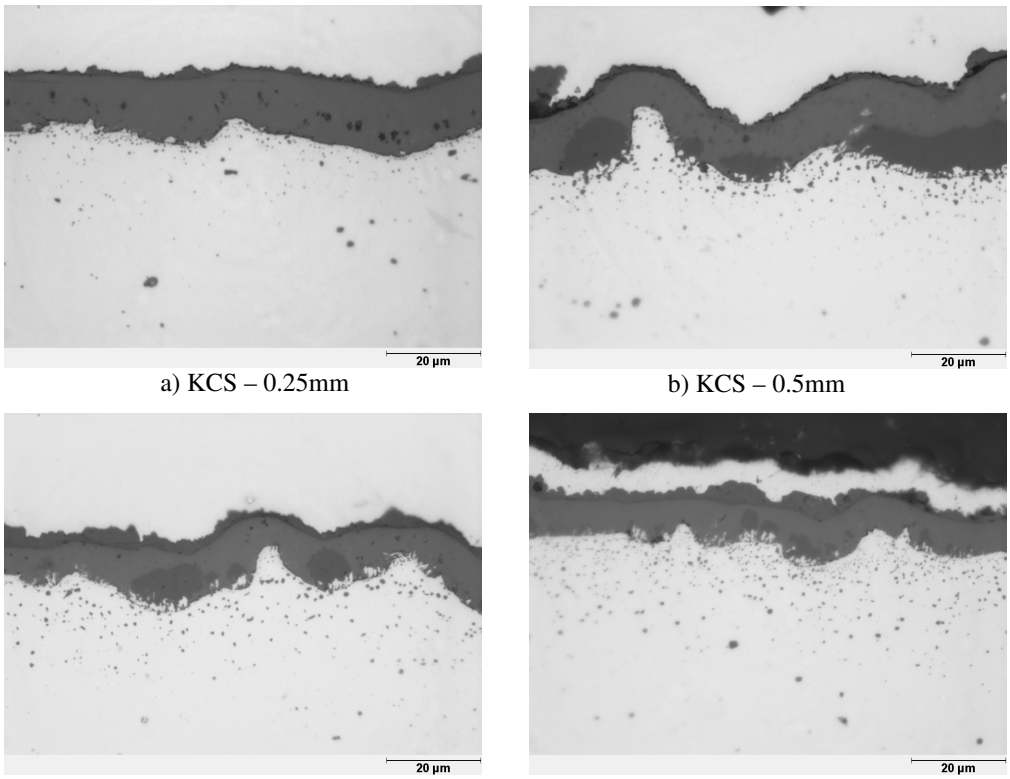

a) KCS – 0.25mm b) KCS – 0.5mm

c) KCS –1mm d) KCS – 2mm

Fig. 6.49: Specimens of different thickness of KCS (1%Nb+0.25%Si) after cyclic oxidation at 900°C in air.

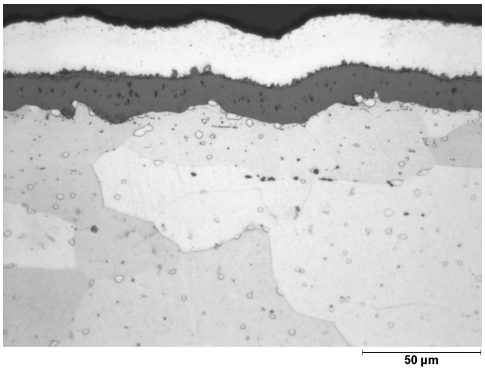

a) KTA – 0.25mm

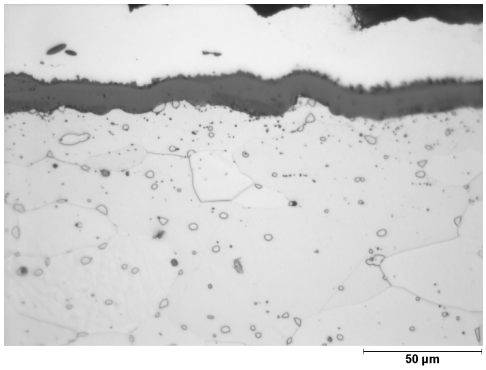

b) KTA – 0.5mm

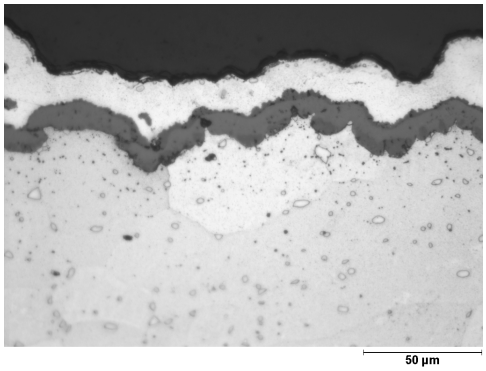

c) KTA – 1mm

Fig. 6.50: Specimens of different thickness of KTA (1%Nb+0.4%Si) after cyclic oxidation at 900°C in air.

The cross-sections in Fig. 6.50 (KTA) and Fig. 6.51 (KUA) show a similar behaviour with respect to specimen thickness dependence as that observed for KCS (1%Nb+0.25%Si). The 0.3mm samples show a relatively smooth interface but the 0.5mm sample, as well as the 1mm sample, exhibit some buckling. The fact that the buckling is less pronounced than observed on KCS might be related to the fact that KTA (1%Nb+0.4%Si) and KUA (2%W+0.5%Nb+0.25%Si) contain less Ti. Thus fewer Ti-oxide precipitates, which are believed to locally increase the creep strength, are formed below the scale.

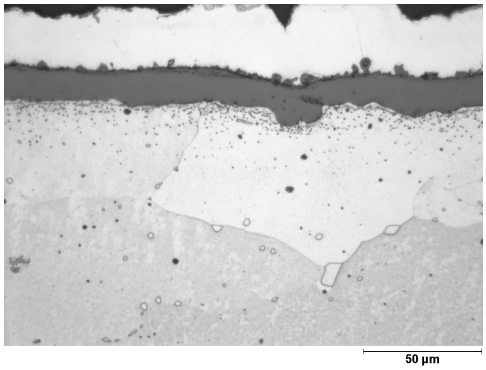

a) KUA – 0.3mm

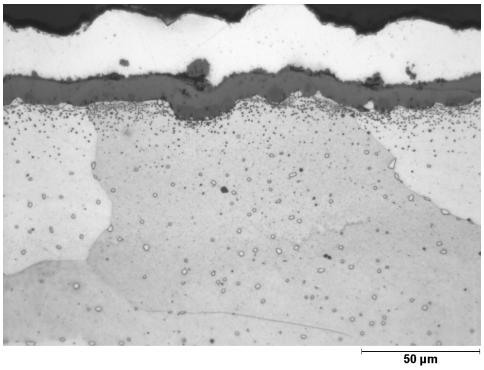

b) KUA – 0.5mm

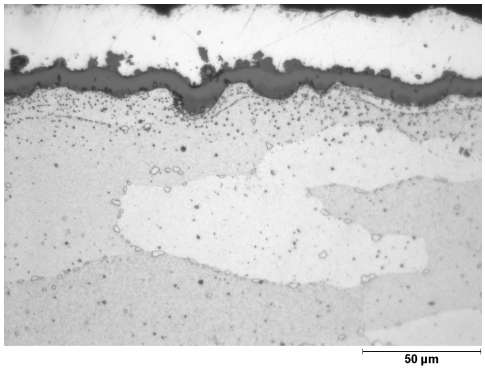

c) KUA – 1mm

Fig. 6.51: Cross-section of samples of KUA (2%W+0.5%Nb+0.25%Si) with different thicknesses.

The comparison of cyclic with discontinuous oxidation of KCB (Crofer 22 APU 2nd) (see Fig. 6.41) shows that cyclic oxidation of 0.5mm specimens at 900°C results in a substantially increased oxidation rates compared to specimens oxidised discontinuously. Generally all the specimens oxidised cyclically seemed to show slightly higher weight gains. The data discussed above indicate some differences in the thickness dependence of the oxidation behaviour between e.g. KCB (Crofer 22 APU 2nd) and KUA (2%W+0.5%Nb+0.25%Si). Thus comparison of cyclic with discontinuous oxidation was also carried out for KUA, the corresponding curves are shown in Fig. 6.52. It can be clearly seen that thermal cycling does not affect the oxidation rate of KUA notably.

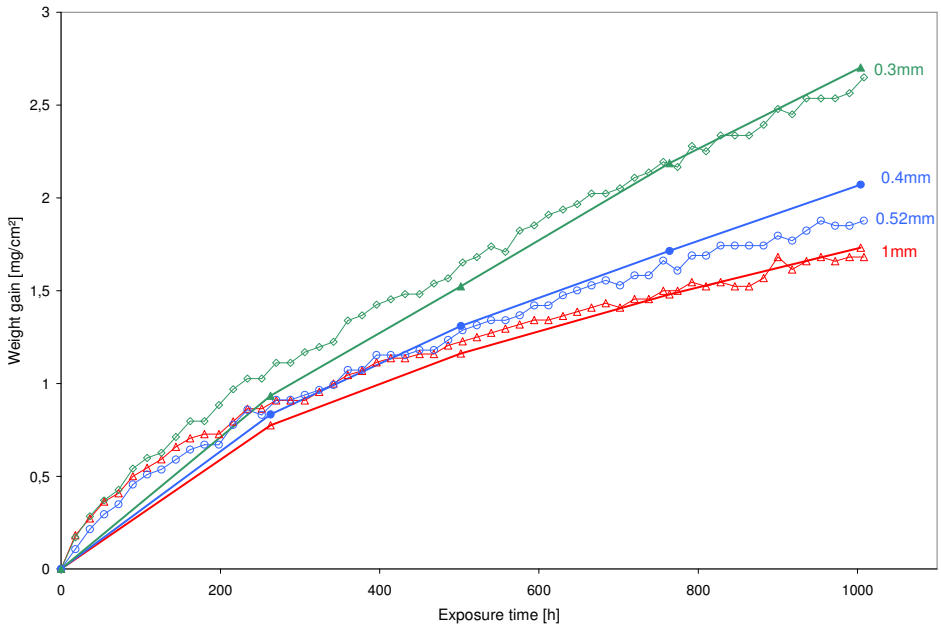

Fig. 6.52 Weight gain of KUA (2%W+0.5%Nb+0.25%Si) during oxidation in air at 900°C. The red curves correspond to samples of 1mm thickness while the blue and green curves correspond to 0.5 and ~0.3mmm thick samples, respectively. The open symbols mark samples oxidised cyclically (2h/15min) and the full symbols indicate discontinuous oxidation data

6.3.1 Discussion of the thickness dependence on the oxidation behaviour

The effect of thickness dependence on the oxidation rate of Fe-Cr alloys at 800 and 900°C was found by Huczkowski et al. [6]. In his study a number of mechanisms were discussed which might explain the observed effects. Huczkowski et al. [6] illustrated that the oxidation rate at a given time is not related to the prevailing Cr content in the bulk alloy at that time. Instead, it was proposed that the thickness dependence of the oxidation rate is mainly due to depletion of minor elements, Mn in particular. Because this element is rapidly incorporated into the scale and due to its low concentration in the alloy it will quickly deplete to very low concentrations. It is apparent that in thin specimens the Mn reservoir is exhausted earlier than in thick specimens which obviously affects the oxidation behaviour. However, Zurek et al. [7] recently found a thickness dependence of the oxidation rate for NiCr base alloy at 1050°C the effect was observed independent of the fact whether Mn, Y or Mn+Y were added to the alloy. Another proposed mechanism is a doping effect. During thermal cycling microcracks will

form and re-heal in the oxide scale consuming Cr and Mn. If specimens of different thickness are considered, the thicker specimens with a larger Cr and Mn reservoir will maintain a higher Cr and Mn concentration at the metal scale interface. Consequently, during oxide growth the scale of thin specimens will incorporate more Fe than as in the case of a thick sample. Since the Fe-doped oxide will exhibit higher growth rates, the scale on thin specimens tends to grow faster than on thick samples. Both of these effects rely on depletion of scale forming elements in the alloy; however most of the weight gain curves show a thickness dependence of the oxidation rate from the very beginning of the experiment. This makes it unlikely that the thickness dependence is related to a depletion phenomenon. In reference [61] Huczkowski et al. proposed, that the thickness dependence of the of the oxidation rate is related to differences in oxide growth stresses due to different ways of stress relaxation in thick and thin substrates.

It is widely known that growth stresses of the oxide scale may lead to plastic deformation of the substrate [69]. It was discussed above that growth stresses in chromia scales are generally assumed to be compressive. Consequently the metallic substrate experiences tensile stresses. If the stresses are sufficiently high this will cause plastic deformation of the substrate by creep. The data in Table 7 indicates substantial sample elongation of the thin samples due to creep of the substrate. This mechanism also explains the observed differences of morphologies of the metal/scale interface in different alloys and specimens of different thickness. The thin samples show rather smooth, wavy oxide scales whereas the thick samples frequently show buckling scales. In the case of thin samples the compressive growth stresses in the oxide scale are relaxed by creep of the substrate. The thick samples do not creep to that extent. Thus the stresses can be relieved only by cracking and/or buckling of the scale.

However, if one compares the alloy variations some differences can be observed. The differences are especially pronounced in case of the 0.5mm thick specimens, thinner specimens will creep in any case while thicker specimens will just exhibit very limited creep. The 0.5mm specimens of the alloys KCB (Crofer 22 APU 2nd), KCL (Nb addition) and KDN (W addition) show quite smooth metal/oxide interfaces while the oxide scales of KCS, KTA (both Nb and Si addition) and KUA (W, Nb and Si addition) exhibit more extensive buckling. This correlates with the observed thickness dependence of the oxidation rate: KCB, KCL and to a limited extent KDN show a more substantial thickness dependence than the alloys KCS, KTA and KUA. As described in section 4 one of the aims of the alloy development was to increase the creep strength of Crofer 22 APU by single or combined additions of W, Nb and

Si. The effect of these additions on the creep strength will be discussed in detail in section 6.6 but some general information is given here: The creep strength of KCB (Crofer 22 APU 2nd) is very poor; the W addition in KDN results in a notable increase in creep strength, while the alloys with Nb addition KCL, KCS, KTA and KUA possess a creep strength that is several orders of magnitude higher than Crofer 22 APU 2nd. However, as KCL (1%Nb addition) exhibits a Nb depleted zone close to the surface in which no Laves phase precipitates can be found, the creep strength in the near surface region will probably not exceed that of KCB (Crofer 22 APU 2nd) significantly.

It is believed that the variations in creep strength cause the observed differences in thickness dependence of the oxidation behaviour. As it was pointed out above, buckling of the scale occurs if the compressive stresses within the oxide cannot be relieved by creep of the substrate. This can either occur when the specimen is too thick or when the inherent creep strength of the material is too high. In the case of the 0.25mm thick samples all alloys will exhibit significant creep. However, the cross-sections of the 0.5mm or 1mm samples show that the oxide scales of the alloys with high creep strength tend to exhibit more buckling than those of weak materials like KCB (Crofer 22 APU 2nd).

It was also observed that the thickness dependence of the oxidation rate is more pronounced for weak alloys than for alloys with a high creep resistance (see Fig. 6.41-Fig. 6.46). It was shown that the thick samples of e.g. KCB (Crofer 22 APU 2nd), and KUA (2%W+0.5%Nb+0.25%Si) exhibit similar oxidation rates, whereas the 0.5mm samples of KCB show considerably higher oxidation rates than the corresponding samples of KUA. It is believed that the oxidation rate is affected by the state of stress in the oxide. It is proposed that an unconstraint oxide grows faster than an oxide under compressive stress [72]. The low creep strength of KCB allows stress relief by substrate creep and thus leaves the oxide scale of KCB in a lower state of compressive stress as than in the case of KUA, where the high creep strength limits the stress relief by metal creep.

The stress in an oxide may influence the transport properties of point defects in two ways: it has an effect on the diffusivity and second it can influence the concentration of defects.
Generally the diffusivity (D) can be described as

$$D = A\exp\left(\frac{-\Delta G^*}{RT}\right)$$

where G* corresponds to the Gibbs free energy required for a diffusion jump. Since Gibbs free energy is defined as [7]

$$\Delta G^* = H^* - T\Delta S^* + \left(\frac{\partial \Delta G^*}{\partial P}\right)_T P$$

the variation of Gibbs free energy with pressure (P), which is commonly neglected, is also referred to as activation volume (ΔV*). In different studies the activation volume was determined experimentally for various materials [73], however, data are scarce and to the authors knowledge no data exist for chromia. In the case of zirconia growth on Zr, Dollins and Jursich [72] explained the subparabolic growth by a decreasing diffusion coefficient of oxygen vacancies.

The state of pressure can also affect the concentration of defects and thereby the material transport through the oxide scale [74]. The vacancy concentration will increase in regions where tensile stresses are present and decrease in regions with compressive stresses according to the following equation:

$$c_V = c_V^0 \exp\left(\frac{P\Delta V^F}{RT}\right)$$

where c_V represents the vacancy concentration and ΔV^F the change in activation volume due to the formation of a vacancy.

It is widely accepted that, as oxidation proceeds, the compressive stresses in the oxide scale increase. It is also known that this affects the oxidation behaviour. Evans [75] proposed that the reduced oxide growth rates due to compressive stresses could be related to a lower vacancy concentration at the metal/oxide interface. In a recent work Żurek et al. [7] estimated a possible effect of stress on the growth rate of chromia scales on a NiCr based alloy. It was concluded that the effect on the lattice diffusivity of defects cannot explain the observed differences in oxidation behaviour. Thus it was suggested that the reduced growth rates in oxides under compressive stress are probably due to lower concentration of vacancies. However, Dollins and Jursich [72] suggested that compressive stresses might have a more pronounced effect on the diffusivity along grain boundaries because of the more open structure of such defects. Since grain boundary diffusion is known to contribute substantially to the material transport in the oxide scale this might play an important role.

6.4 Alloy Microstructure

6.4.1 Effect of alloying elements

In the preceding chapters the effects of the addition of Nb and W on the phase equilibria and alloy microstructure have already been mentioned briefly. This chapter will give a more detailed discussion of the observed effects.

The main alloying elements of the reference alloy (KCR) are Fe and 22%Cr. This results in a ferritic matrix. Due to the low levels of impurities hardly any precipitates, except for oxidised La, which was added as reactive element, can be found. The alloys KCW and KDN contained 1 and 2.7% W respectively. According to the phase diagram depicted in Fig. 6.53 the solubility limit for W in an Fe-22 Cr alloy is approximately 4wt.% at 600°C. Cr addition seems to slightly increase the solubility of W in the ferrite matrix. This is in agreement with the current investigations which did not show any evidence of secondary phases after exposures between 700 and 1000°C for up to 10000h.

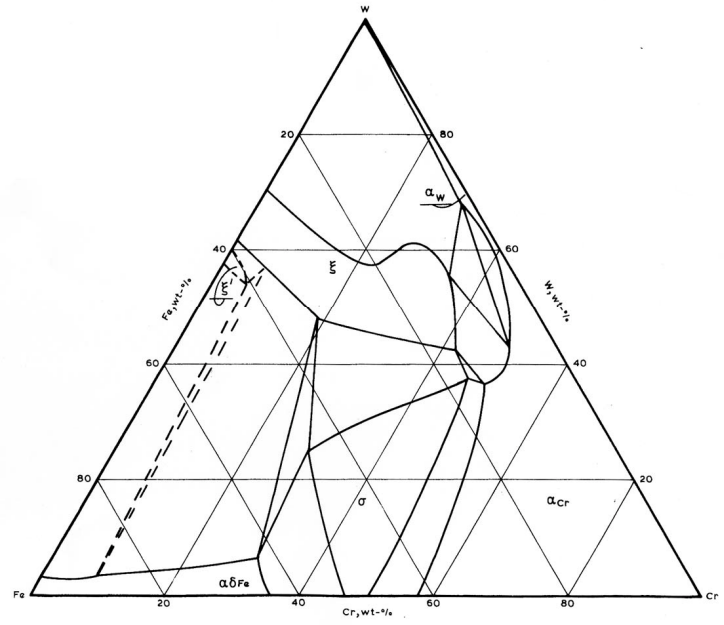

Fig. 6.53: Ternary phase diagram Fe-Cr-W at 600°C [76].

The addition of 1% Nb (KCL) resulted in precipitation of the Laves phase (see Fig. 6.7) on the basis of Fe_2Nb. An amount of 2 vol.% Laves phase was determined by digital image analysis after 10000h exposure at 800°C. EDX analysis of the precipitates after 1000h at 800°C indicated a composition of 62 at.% Fe, 11% Cr and 26% Nb. The comparison with the Fe-Nb phase diagram suggests that the precipitates are of the type $(Fe,Cr)_2Nb$.

The combined addition of Nb and Si shows a very similar microstructure as observed for KCL (1%Nb); again the percentage of precipitates after 10000h at 800°C was determined to be 2%. However, compositional analysis by EDX revealed that Si has a high solubility in the precipitates. The analysis of the precipitates in KCS (1%Nb+0.25%Si) after 1000h at 900°C showed a composition of 57% Fe, 11% Cr, 27% Nb and 5% Si (all at.%). This explains why Si has no negative effect on the oxidation behaviour if it is added in combination with Nb: the high affinity for Si of the Laves phase reduces the amount of Si in the matrix. For KTA (1%Nb+0.4%Si) similar observations were found except that the amount of Si in the precipitates was even slightly higher than for KCS.

Thermodynamic modelling using Thermocalc [77] confirmed the experimental results. Fig. 6.54 shows the mole fraction of different phases as a function of temperature. It can be seen that the Laves phase is stable to approximately 980°C while a substantial amount of σ-phase can be found up to a temperature of approximately 680°C. However, if one investigates the compositions of the respective phases shown in Table 8 it becomes apparent that this is not in agreement with experimental data. It can be seen that the used database does not take into account that Si is incorporated into the Laves phase. However, if considers the ternary Fe-Nb-Si phase diagrams shown in the appendix it can be seen that substantial amounts of Si are incorporated into the Laves phase and that Si is stabilising the Laves phase.

wt%	Fe	Cr	Nb	Si
Matrix	77.1	22.2	0.36	0.25
Laves phase	51.2	3.6	45.1	0

Table 8: Calculated composition of the matrix and the Laves phase at 900°C.

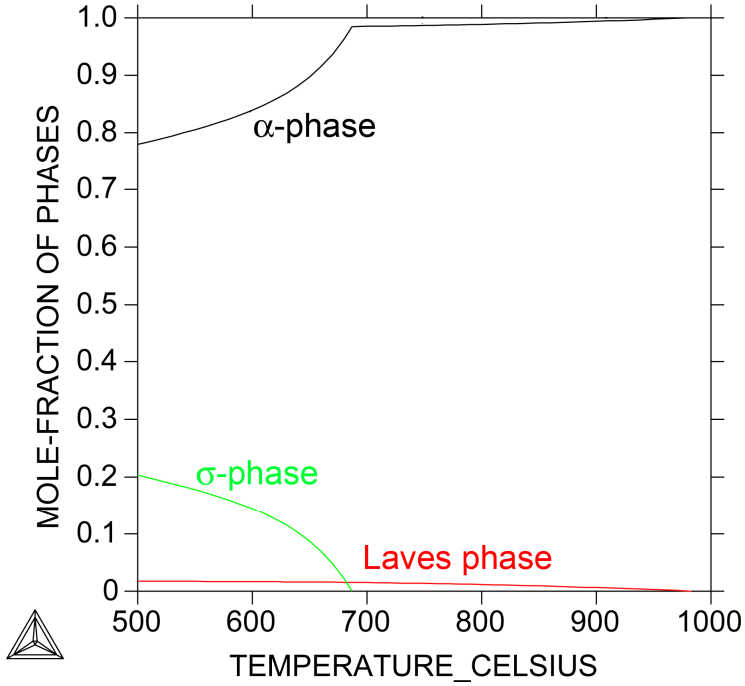

Fig. 6.54: Calculated mole fraction of the different phases as a function of temperature for an alloy Fe-22%Cr-1%Nb-0.25%Si (all wt%).

As discussed earlier, the alloy containing Nb differs from the alloys with combined additions of Nb and Si in three significant ways: (i) the high growth rate of the scale which is believed to be due to Nb-doping (ii) the formation of a Nb-rich oxide beneath the scale (iii) the formation of a Nb-depleted zone below the scale in which no Laves phase precipitates can be found. It is believed that the high Si content in the Laves phase precipitates is the explanation for these differences.

It is proposed that in the case of the alloy with combined additions of Nb and Si the Si in the Laves phase stabilises the Laves phase precipitates. Thus the precipitates remain stable and the Nb activity in the alloy is reduced to such a level, that Nb can no longer be oxidised beneath the chromia scale. Consequently none of the discussed effects are observed. In contrast the alloy with Nb and Al additions (KCO) exhibited a different behaviour. EDX analysis did not show any evidence of Al in the Laves phase precipitates, with the result that the alloy showed high scale growth rates and extensive internal oxidation of Al.

The combined addition of W, Nb and Si (KUA) causes a much finer microstructure than observed for the W free alloy containing only Nb/Si; the difference can be seen in Fig. 6.55. Image analysis indicates that the amount of Laves phase in KUA is slightly higher than in the alloys with a single addition of 1% Nb.

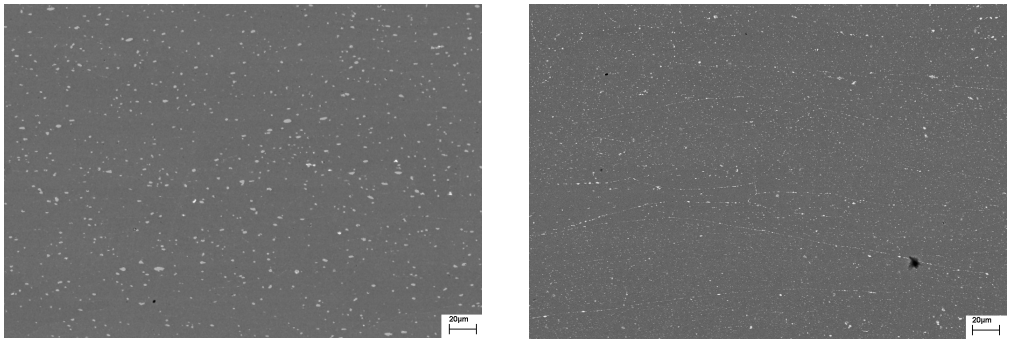

a) KTA (1%Nb+0.4%Si) b) KUA (2%W+0.5%Nb+0.25%Si)

Fig. 6.55: Differences in microstructure between KTA (1%Nb+0.4%Si) and KUA (2%W+0.5%Nb +0.25%Si) after 1000h exposure at 800°C.

6.4.2 Effect of time and temperature on the Laves phase formation

Fig. 6.56 shows cross-sections of KUA (2%W+0.5%Nb+0.25%Si) after different exposure times in air at 800°C. After 72h the smallest precipitates that can be seen are approximately 0.3µm in diameter while the largest precipitates are 0.8µm in diameter. After 1000h 0.3µm sized particles can be still found but precipitates with diameters exceeding 1µm are also visible. The density of precipitates also seems to be slightly lower. It has to be taken into account that an oxide scale has formed on the samples which can affect the distribution of precipitates. In fact in Fig. 6.56b it seems that a zone of 5-10µm exists in which fewer small precipitates can be found. Fig. 6.56c shows the microstructure after 5000h at 800°C. The image was taken approximately 30µm form the sample surface. Within the image a clear size distribution of precipitates can be seen. In the upper part only few small precipitates (<1µm) can be found while in the lower part these precipitates are evenly distributed. The reason for this is a near surface depletion region of small precipitates which can be seen more clearly in Fig. 6.56d. It can be also seen that the size of the largest precipitates has increased substantially; after 5000h some precipitates exceed 5µm in diameter. Fig. 6.57 shows the microstructure after 10000h at 800°C. While in the centre of the sample fine precipitates can be found, only few large precipitates can be found in a near surface area which is about 40µm deep. The mechanism for this depletion is unknown, though it seems that actually no depletion but accelerated precipitate coarsening occurs. The coarsening of precipitates due to

the growth of larger precipitates at the expense of smaller ones is widely known as Ostwald ripening. In Fig. 6.57 it seems that the distribution of large precipitates is not homogenous but that there are slightly more large precipitates in the near surface region. The acceleration of Ostwald ripening near the surface could be related to a higher vacancy concentration in the alloy due to the scale growth which causes a higher diffusivity in the matrix. However, the Cr depletion in the alloy matrix below the scale could also cause a lower Cr content in the Laves phase precipitates resulting in larger precipitates.

This process resembles the depletion of Laves phase precipitates in the alloy with Nb addition (KCL) but one major difference has to be mentioned: neither could for KUA (W, Nb, Si addition) a effect negative effect on the oxidation behaviour be observed nor did the formed oxide scale show any indication of the influence of Nb e.g. no Nb-rich oxide below the scale. It is, however, possible that the same mechanism applies but due to the presence of Si it is dramatically reduced. Thus the, effect can only be seen on the finest precipitates. E.g. the effect can not be observed in the case of the alloy KCS (1%Nb+0.25%Si) because this alloy in general does not show such fine precipitates.

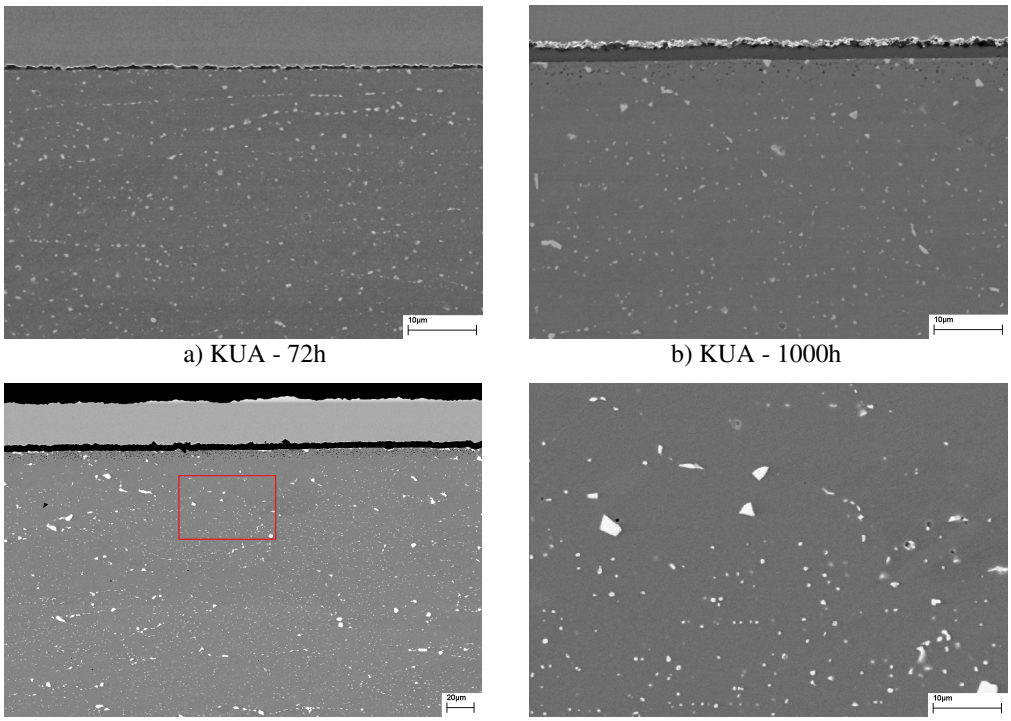

a) KUA - 72h b) KUA - 1000h

c) KUA - 5000h d) KUA - 5000h

Fig. 6.56: Cross-sections of KUA (2%W+0.5%Nb+0.25%Si) after different exposure times at 800°C in air. Fig. 6.56d is a higher magnification of the area marked in Fig. 6.56c.

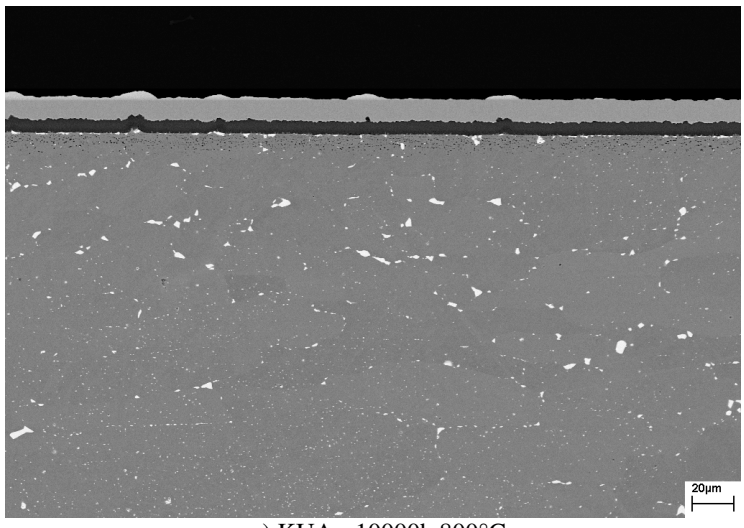

a) KUA - 10000h 800°C

Fig. 6.57: Cross-section of KUA (2%W+0.5%Nb+0.25%Si) after 10000h exposure at 800°C in air.

Fig. 6.58 shows the effect of temperature on the microstructure of KUA (2%W+0.5%Nb +0.25%Si). The samples were exposed for 72h in air at different temperatures. While Fig. 6.58a shows mainly small precipitates with a diameter significantly below 1µm, Fig. 6.58b shows also some larger precipitates. The microstructure after 72h at 900°C looks similar to that after 1000h at 800°C (Fig. 6.56b). After 72h at 1000°C the average precipitate size has increased to approximately 2µm. Fig. 6.58d shows a lower magnification image of the sample exposed to 1000°C. It can be seen that some near surface depletion occurs at 1000°C, to a lesser extent this can be also seen at 900°C. However, the effect of temperature on this effect seems to be less significant than the effect of long exposure times. This is contrary to the dissolution of Laves phase precipitates in KCL (1%Nb addition) where higher temperatures accelerated the dissolution of precipitates much more substantial than longer exposure times (compare Fig. 6.3 with Fig. 6.7 and Fig. 6.13.)

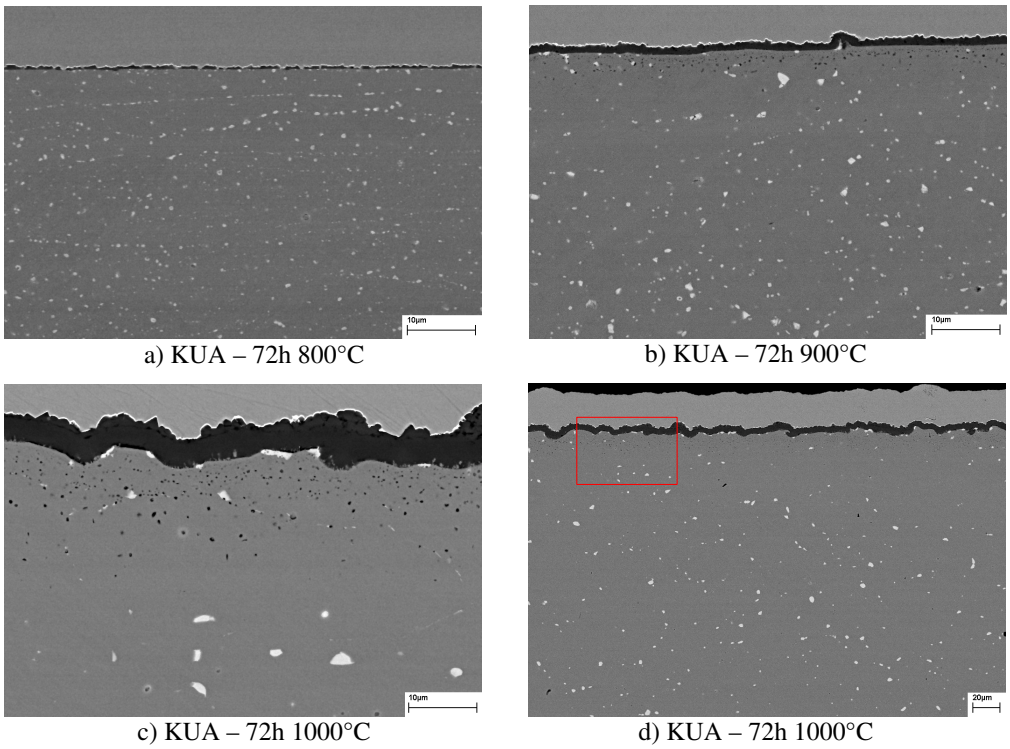

a) KUA – 72h 800°C

b) KUA – 72h 900°C

c) KUA – 72h 1000°C

d) KUA – 72h 1000°C

Fig. 6.58: Cross-sections of KUA (2%W+0.5%Nb+0.25%Si) after different exposure times at 800°C, 900°C and 1000°C in air. Fig. 6.56c is a higher magnification of the area marked in Fig. 6.56d.

In order to investigate the stability and the composition of the Laves phase as a function of temperature, the model alloy LWU (1.5%W+1%Nb+0.6%Si) was manufactured. To increase

the accuracy of the measurements the contents of Nb and Si were increased with respect to KUA. The samples were kept in the furnace at different temperatures for 1000h in an evacuated quartz capsule and were subsequently quenched to room temperature. The results of the WDX analysis are depicted in Fig. 6.59. It can be seen that with increasing temperature the amount of Nb in the Laves phase increases while the amount of Si and W decrease. The concentration of Cr is constant while the amount of Fe is increasing. Thus, although the composition of the Laves phase shows minor differences at the different temperatures this is not expected to have a notable effect on the SOFC relevant properties.

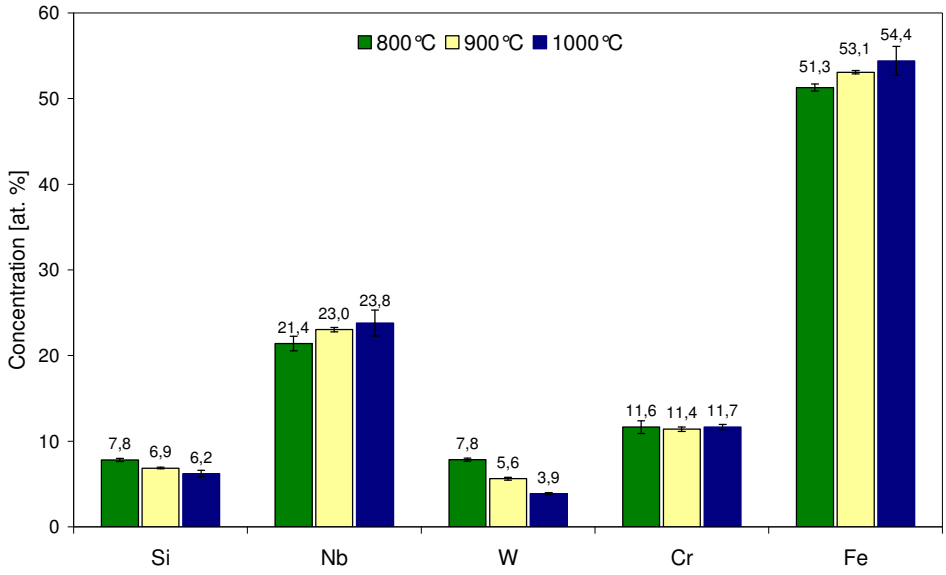

Fig. 6.59: Composition of the Laves phase precipitates as a function of temperature. Measured on LWU (1.5%W+1%Nb+0.6%Si) with WDX.

Fig. 6.60 shows the microstructure of KSY, which has a similar composition as KUA (2%W+0.5%Nb+0.25%Si), after 7500h at 600°C. It can be seen that some larger precipitates with a diameter of 0.5µm and a high number of fine precipitates with a diameter of less than 100nm can be found. The precipitates are situated mainly at grain boundaries and dislocations as can be seen in Fig. 6.60b and c. These defects are sites where nucleation of precipitates is favoured and thus show a higher density of precipitates.

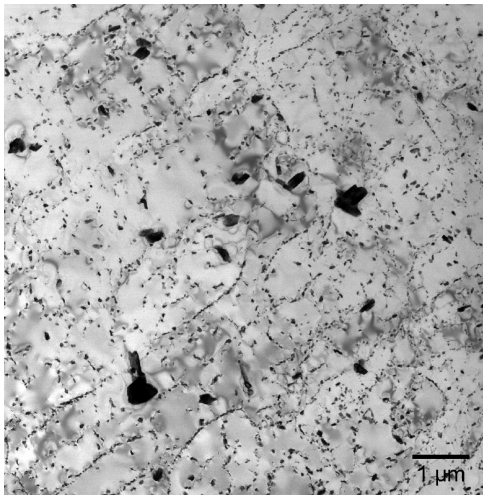

a)

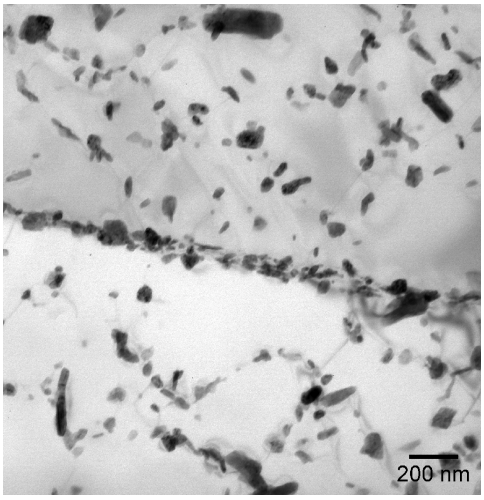

b)

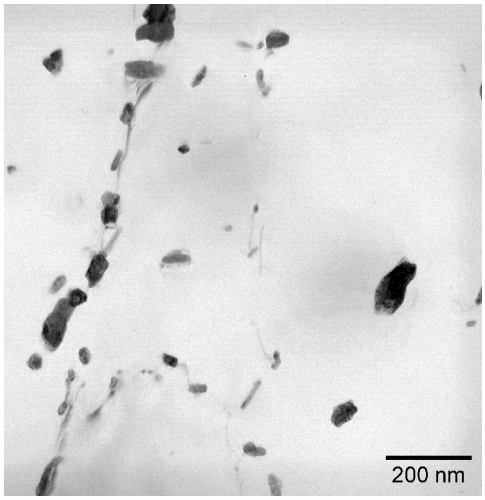

c)

Fig. 6.60: TEM micrographs of KSX (1.7%W, 0.6%Nb, 0.25%Si) after 7500h at 600°C. The specimens were prepared from a sample that was subject to a creep test. However, the respective specimen was taken at the head of the sample which did not exhibit substantial strain at the applied load. Fig. 6.61b shows a high concentration of precipitates at an alloy grain boundary. Fig. 6.62c shows a string of precipitates formed along a dislocation.

6.5 Electrical conductivity of oxide scales

A high electrical conductivity of the scale is of major importance for the interconnect application in order to keep the ohmic resistance in the fuel cell as low as possible. High electrical conductivity usually corresponds to a high concentration of point defects in the oxide. On the other hand, a high concentration of point defects usually results in rapid oxide growth. It turned out that chromia offers a good compromise between conductivity and protectiveness of the oxide scale in SOFC applications [46].

In the literature there are two common ways to present results of conductivity measurements: first the more physical approach by giving the conductivity σ of the material and second reporting area specific resistance (ASR), also termed contact resistance. This is especially common with respect to fuel cell research. Both variables are related to each other by the scale thickness *L*.

$$ASR = R * A = \frac{L}{\sigma}$$

The temperature dependence of the conductivity can be described with the following Arrhenius type equation [26]

$$\sigma = \frac{A}{T} * \exp\left(\frac{-Q}{RT}\right)$$

The work by Pirón et al. [3] showed that the then available commercial ferritic steels could not meet the requirements with respect to low electrical resistance of the oxide scales. The subsequently developed alloy JS-3 exhibited an area specific resistance that was 1-2 orders of magnitude lower than that of most traditional alloys (see Fig. 6.63). The commercial version of JS-3, Crofer 22 APU, exhibited even in the first heat, which contained considerable amounts of impurities, a similar area specific resistance as JS-3.

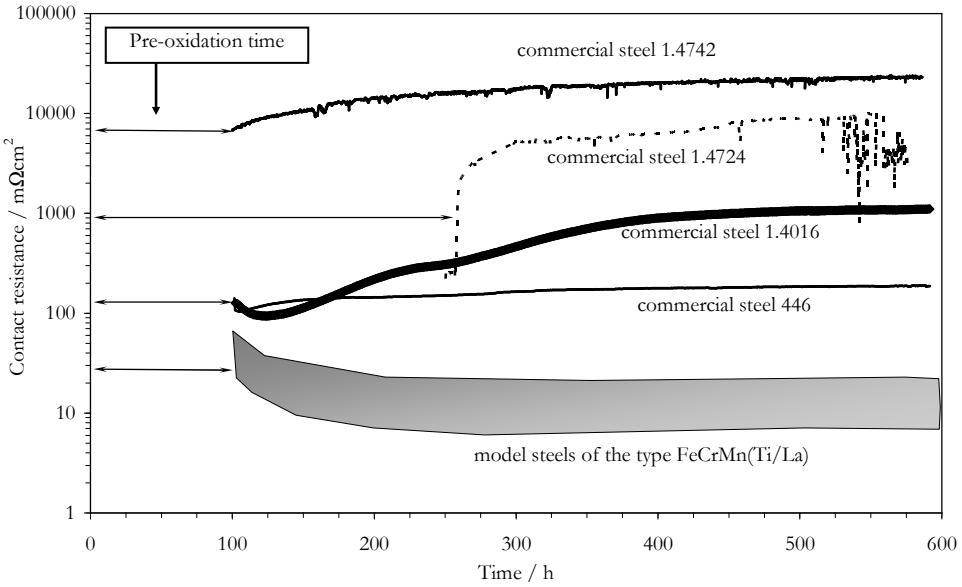

Fig. 6.63: Comparison of contact resistances (800°C, air) of conventional steels and FeCrMn(Ti/La) steels such as JS-3 or Crofer 22 APU [4]

The aim of the present investigation of the electrical properties of the oxide scales was to evaluate whether the modifications of the alloy composition would have a negative effect on the scale conductivity. Fig. 6.64 shows the area specific resistance of different samples of Crofer 22 APU (2^{nd}) which has a very similar composition as the reference alloy (KCR). The first 100h correspond to the preoxidation time before the samples were covered with Pt paste. Subsequently the resistance is measured during the next 300h at 800°C. Afterwards the samples are cooled in 50°C steps each lasting for 10h. This temperature drop results in an increase in resistance as can be observed in the graph. It can be seen that most of the samples exhibit at 800°C ASR values the range of 10-20mΩ·cm² which is an agreement with the data presented by Quadakkers et al.[4].

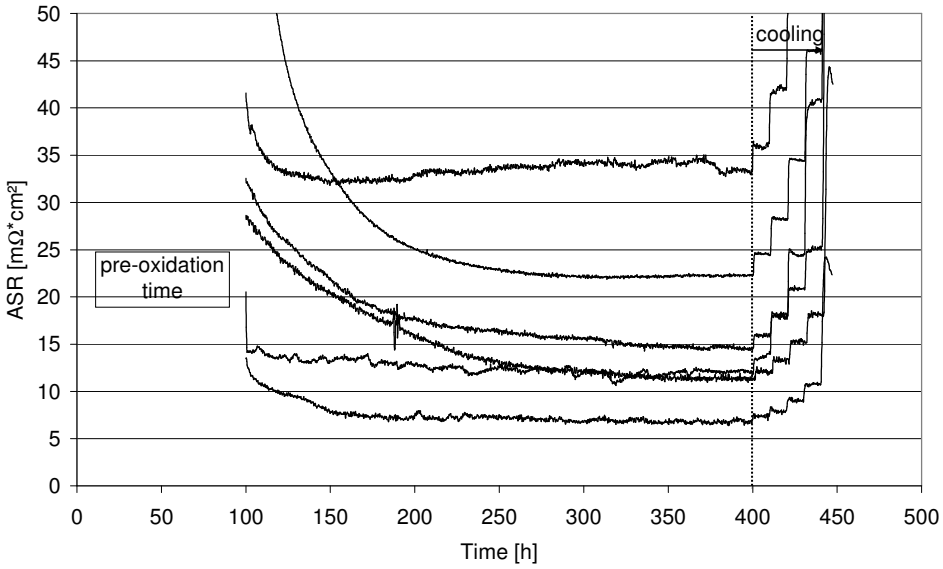

Fig. 6.64: Area specific resistance of different samples of Crofer 22 APU 2nd at 800°C in air. Cooling occurred in steps of 50°C holding time at each temperature was 10h.

Fig. 6.65 shows area specific resistance data for alloys with W and Nb addition (KDN and KCL respectively). It can be seen that the recorded data for both alloys are in the same margin as it was observed for Crofer 22 APU.

Subsequently, the behaviour of alloys with combined additions of Nb and Si were studied. The results are presented in Fig. 6.66. In the case of KCS (1%Nb+0.25%Si) similar ASR values as obtained on Crofer 22 APU can be observed. The data of the alloy with slightly more Si (KTA) are at the upper end of scatter band obtained for Crofer 22 APU. This might be due to subscale silica formation as observed in chapter 6.1 metallographic investigation did not show any evidence for subscale silica formation.

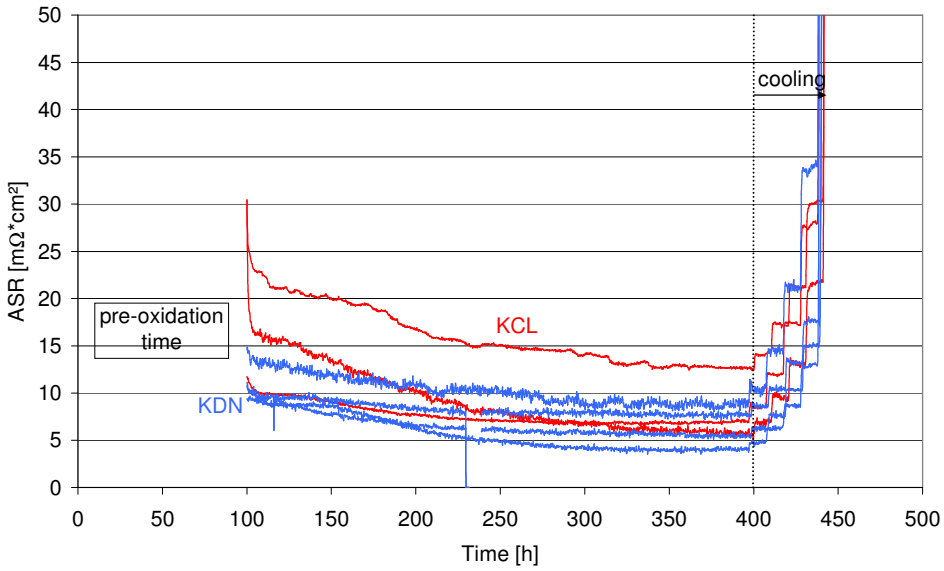

Fig. 6.65: Area specific resistance of different samples of KDN (2.7% W addition) and KCL (1%Nb addition) at 800°C in air. Cooling occurred in steps of 50°C holding time at each temperature was 10h.

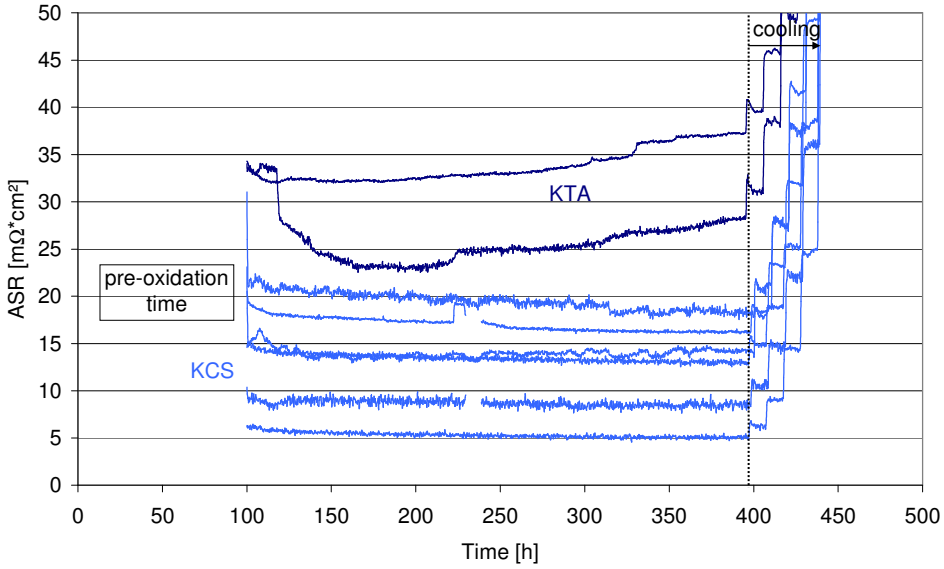

Fig. 6.66: Area specific resistance of different samples of KCS (1%Nb+0.25%Si) and KTA (1%Nb+0.4%Si) at 800°C in air. Cooling occurred in steps of 50°C holding time at each temperature was 10h.

Fig. 6.67 shows resistance data recorded for KUA (2%W+0.5%Nb+0.25%Si). The data vary between 10-20mΩ*cm² which is within the scatter band of Crofer 22 APU (see Fig. 6.64). Thus it can be concluded that none of the discussed alloy modifications had a major effect on the electrical scale resistance of the scale. Only (KTA 1%Nb+0.4%Si) exhibited slightly higher ASR values which might be due to subscale silica formation (see Fig. 6.8). However, SEM investigation of the samples did not show any evidence for subscale silica formation. In any case the slightly higher ASR values of KTA could also be attributed to a statistical variation.

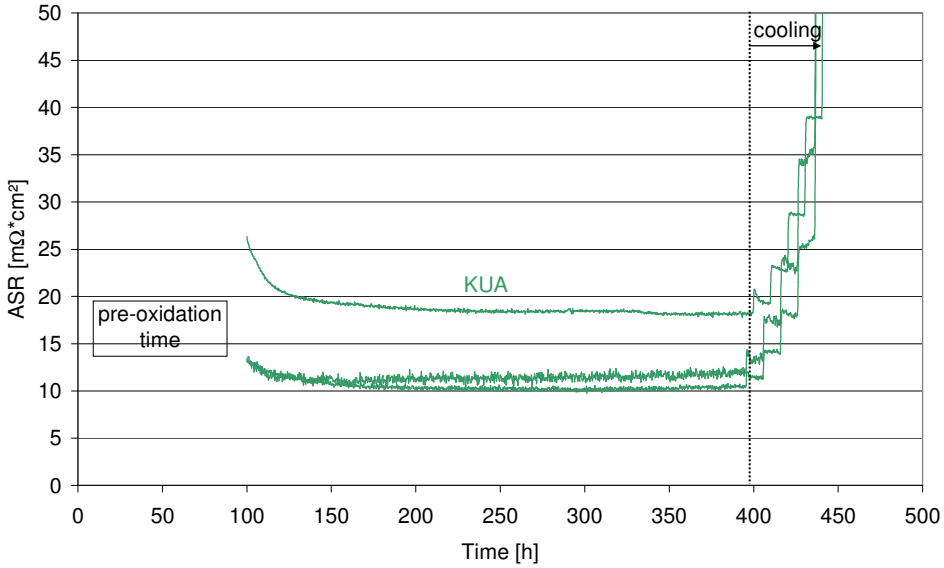

Fig. 6.67: Area specific resistance of KUA (2%W+0.5%Nb+0.25%Si) at 800°C in air. Cooling occurred in steps of 50°C holding time at each temperature was 10h.

The resistance data obtained during the stepwise cooling at the end of the experiments were used to investigate the temperature dependence of the electronic conductivity. Fig. 6.68 shows log(σT) as a function of inverse temperature for selected alloys. One has to keep in mind that the conductivity value is calculated from a measured resistance which is mainly the sum of the contribution of the spinel and the chromia layer, thus here the term "apparent conductivity" is used.

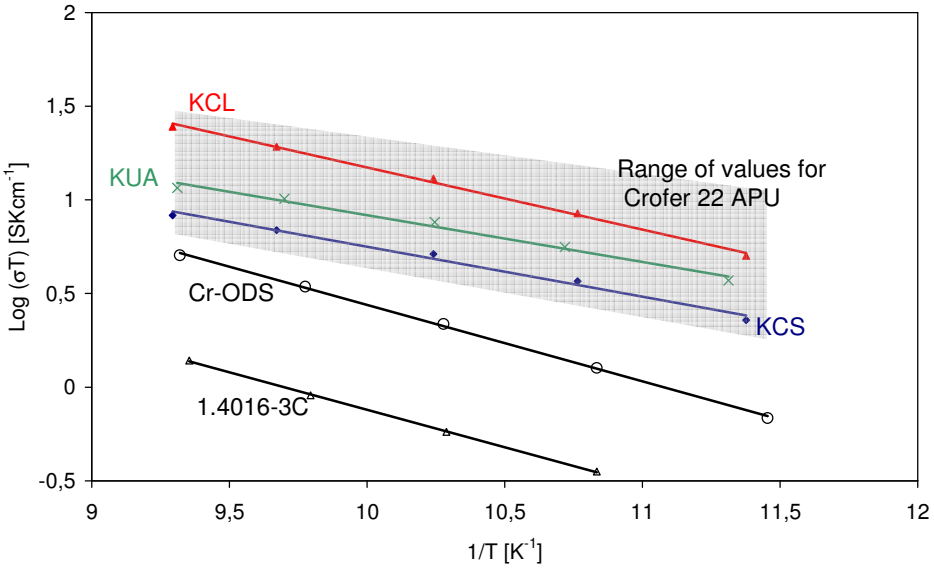

Fig. 6.68: Apparent conductivity of selected steel modifications. Data for a Cr base ODS alloy as well as a commercial 16% Cr steel were taken from [5, 46].

It can be seen that the conductivity of the selected alloys is within the margin of values that was measured on Crofer 22 APU (2nd). The scale conductivity of KCL (1%Nb addition) is at the upper end of that range. If one considers the fact that the scales formed on KCL are notably thicker than those formed on the other alloys (e.g. KCS or KUA) and the fact that the measured resistances were at the lower end of the scatter band this seems to indicate that the electrical conductivity of the chromia layer formed on KCL is higher than that on the other alloys. This might be caused by the proposed of Nb-doping of the chromia scale (see chapter 6.1.5).

For the interconnect application electrical conductivity of the scale formed in low pO_2 gases which are present at the anode side is also of importance. Such measurements were tried but no reasonable data could be produced. Fig. 6.69 shows typical ASR curves measured in air and simulated anode gas. After 100h of measurement the samples were cooled in 50°C steps each lasting for 10h. For the measurement in air the cooling corresponds to a stepwise increase of resistance. Such behaviour is expected for any semi-conductor material e.g. chromia or Cr/Mn spinel. However, the measurements in Ar-H_2-H_2O showed that the recorded data were independent of temperature. Such temperature dependence is typical for metals and indicates a short circuiting of the scale.

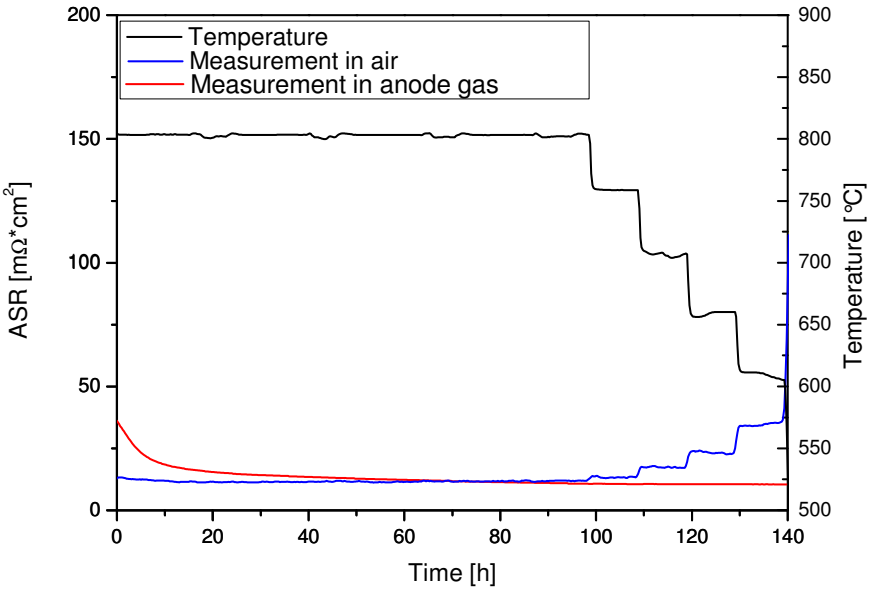

Fig. 6.69: Typical ASR curves obtained for a 100h measurement and subsequent stepwise cooling.

The work of Huczkowski et al. [6] indicates that Pt, which is used as a contact material for the samples, is not an inert material at 800°C in air. The author observed differences in oxide morphology and suggested that the oxide scales under Pt become thinner during long term exposures. It is believed that the same effect applies here but is even much stronger in low pO_2 atmospheres than in air. This is in agreement with observations by Lu et al. [78] who observed the dissolution of different oxides in contact with Pt. Although the experiments were carried out at significantly higher temperatures than in the present study it could be shown that the reaction is more pronounced in low pO_2 gases. Thus it is believed that local thinning of the scale results in short circuiting of the scale and results in the observed metallic behaviour during cooling. In SEM investigations of cross-sections no such spot could be observed. Therefore, it is believed that this occurs only locally and thus no evidence can be given. In chapter 7.2 the effect of metallic coatings on oxide scales will be discussed in more detail.

6.6 Creep Tests

As explained in section 3.7 the creep strength can be increased by two mechanisms: first solid solution strengthening with elements having a different atomic size than the host metal and some solubility in the matrix; second by precipitation strengthening due to the formation of secondary phases. In recent years the development of metallic materials for interconnects focused on the optimisation of the oxidation resistance and a low scale resistivity. This was mainly achieved by decreasing the amount of impurities in the alloy. However, due to the low amount of impurity elements the creep strength of the material is rather low.

In the current alloy modifications both strengthening mechanism were considered. Nb was added to obtain a precipitation strengthening effect and W was added as solid solution strengthening element. The combined effect of both elements was investigated as well.

The creep samples were machined form 16mm steel sheets and thus different designations compared to the 2mm plates in the previous chapters are used. Table 9 gives the designations of the 16mm plates compared with the designations of the 2mm steel sheets used in the previous sections.

2mm batch	**16mm batch**	**Remarks**
KCR	KCP	Reference alloy
KCW	KCU	1% W addition
KDN	KDM	2.7% W addition
KCL	KCM	1%Nb addition
KCO	KCN	1%Nb, 0.15%Al addition
KCS	KCK	1%Nb, 0.25%Si addition
KTA	KSZ	1%Nb, 0.4%Si addition
KUA	KUB	2%W, 0.5%Nb, 0.25%Si addition
KSY	KSX	1.75%W, 0.6%Nb, 0.25%Si addition, no La

Table 9 Overview of alloys used for creep testing, the detailed compositions are given in the appendix

Fig. 6.70 shows creep curves of different alloy modifications at 700°C and an applied stress of 10MPa. The black curve corresponds to the reference alloy, which exhibited rupture after

less than 500h. The addition of 1% W results in a substantial increase in lifetime of the sample. The addition of 2.7%W results in a further improvement of the creep strength due to solid solution strengthening. After approximately 9000h the creep rate of this alloy increases as tertiary creep is taking place. Failure after approximately 10000h. The addition of Nb to the reference material results in the formation of Laves phase precipitates which has a dramatic effect on the creep strength of the material. After 10000h all of the alloys exhibit only approximately 0.1% elongation which is close to the accuracy of the measurement during the used multi-specimen creep test. It can be seen that under the given conditions the alloys with the combined additions of Nb and Si (KCK) or Nb +Al (KCN) show a similar behaviour as the material with just Nb addition (KCM). It was shown before (see section 6.1.2) that the Laves phase precipitates tend to become unstable close to the sample surface if no Si is added to the alloy. This effect does not play an important role here as the diameter of the samples is 6.4mm and second the temperature is probably too low to cause notable dissolution of Laves phase precipitates.

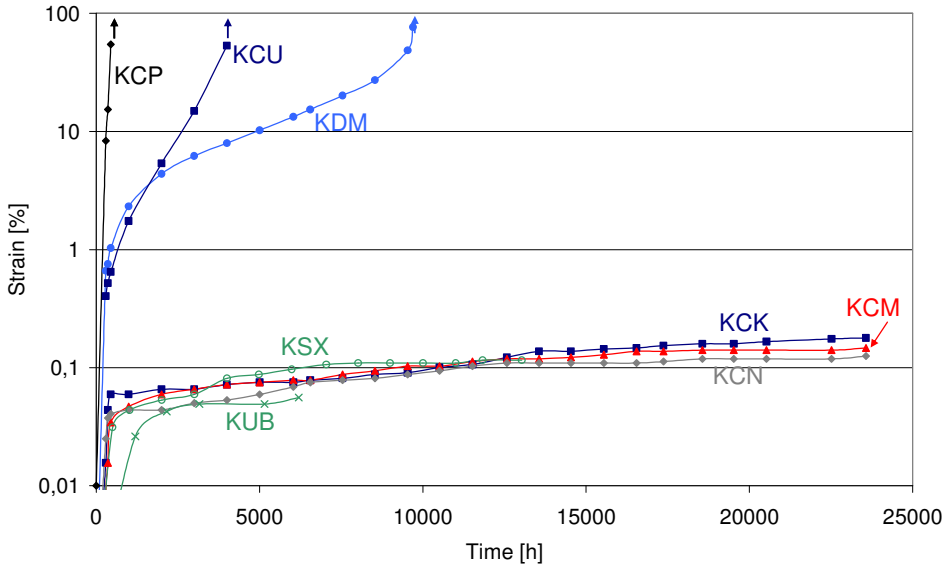

Fig. 6.70: Creep data of different alloy variations at 700°C and an applied stress of 10MPa. The arrows at the end of the curves indicate rupture of the sample.

The data for KUB (2%W+0.5% Nb+0.25%) is limited to 6000h because this alloy was received later. For KSX, which has a very similar composition as KUB except the lack of La,

data have been recorded for 13000h showing that at 700°C no difference compared with the alloys having only additions of Nb as strengthening element can be observed.

Fig. 6.71: Images of the specimens of KCP before and after testing at 700°C and 10Mpa.

Fig. 6.72 shows creep data measured at 800°C with an applied stress of 10MPa. Under these conditions the alloys containing no W (KCK, KSZ) exhibit failure after less than 1000h. The alloy with 2%W 0.5%Nb and 0.25%Si (KUB) shows less than 0.2% strain within the first 5000h. The last data points show an increase to 0.5%. However, the composition of KSX is very similar to that of KUB except the lack of La and a slightly higher content of Nb. Since KSX exhibited failure after about 15000h, it is expected that the KUB specimen will fail at a similar time.

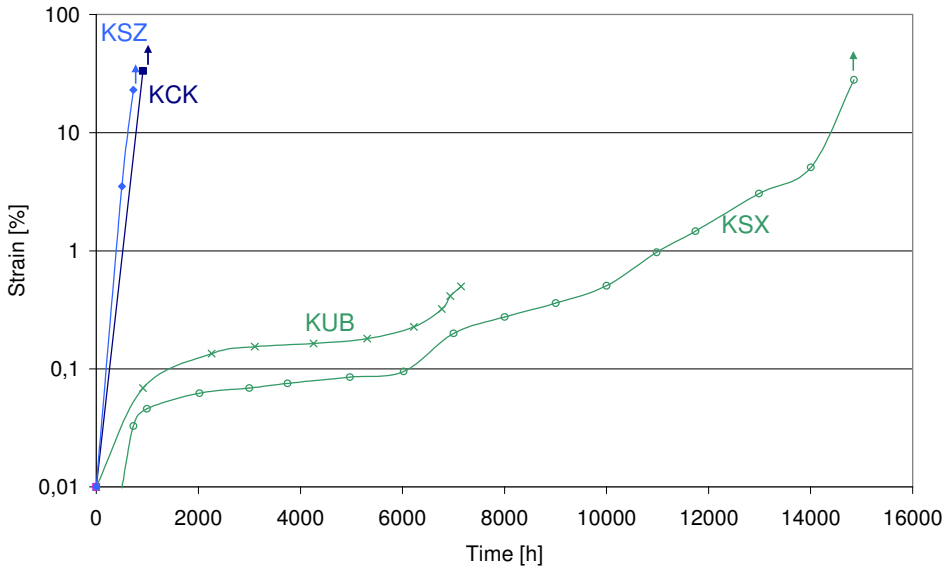

Fig. 6.72: Creep data of different alloy variations at 800°C and an applied stress of 10MPa. The arrows at the end of the curves indicate rupture of the sample.

Fig. 6.73 shows the time to rupture at 700°C for various stresses for different materials. It can be seen that Crofer 22 APU exhibits early rupture e.g. after 2000h with an applied stress of 10MPa. The data for KSX do not mark rupture but correspond to the last acquired data points with respective strain values of 0.1 and 0.2%. For comparison the austenitic steels 304H and 316L and the ferritic steel P92 were added.

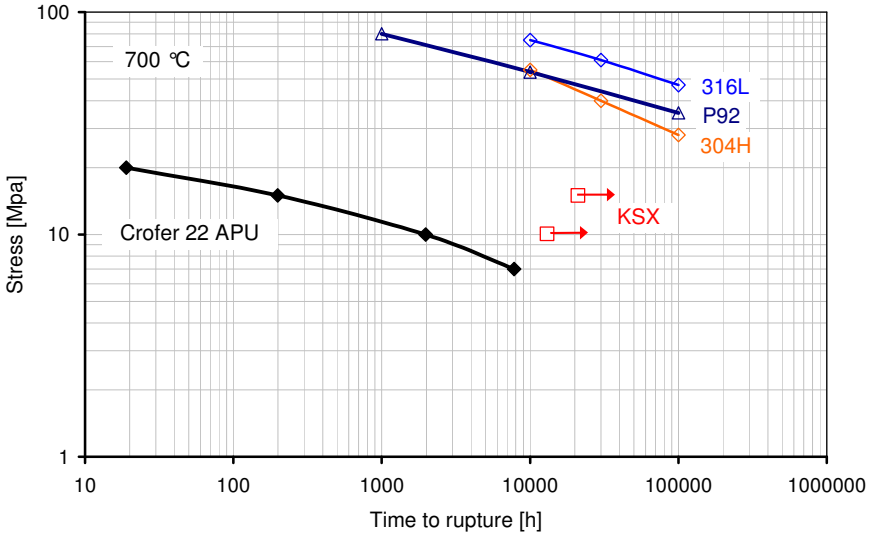

Fig. 6.73: Time to rupture during creep tests at 700°C. KSX (1.7%W+0.6%Nb+0.25%Si) has not ruptured after 20000h. Data points for KSX do not show rupture but the last acquired data points. Data from 316L, P92 and 304H were taken from ECCC data sheets [79].

Fig. 6.74 shows the time to rupture as a function of temperature at a stress of 145MPa it can be seen that KSX (1.7%W+0.6%Nb+0.25%Si) exhibits a similar creep strength as the ferritic steel P92. For comparison a number of other commonly used high temperature alloys are added.

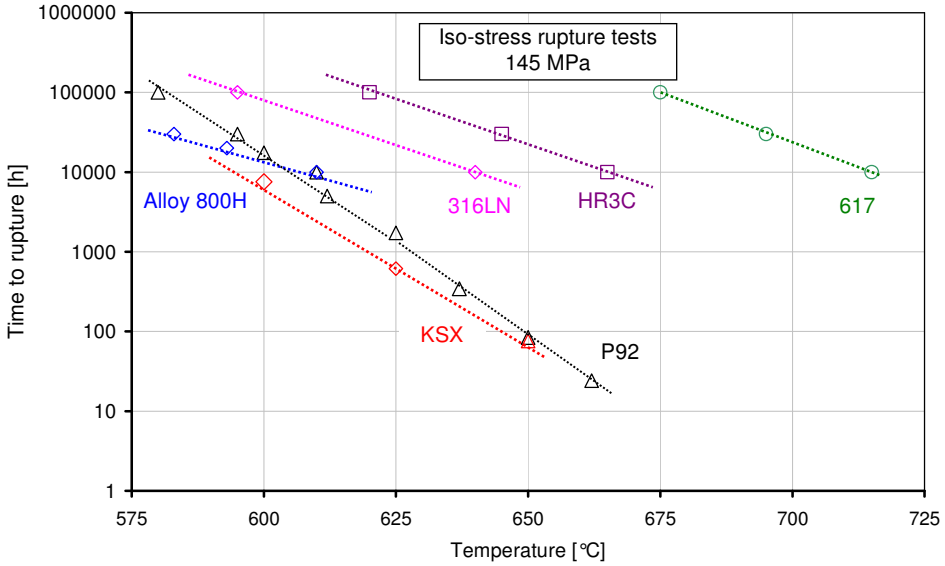

Fig. 6.74: Time to rupture as a function of stress and temperature for KSX (1.7%W+0.6%Nb+0.25%Si) and various other high temperature materials [79].

6.7 Ductility

In Fig. 6.75 the tensile strength R_m and the elongation at rupture are plotted as a function of temperature for Crofer 22 APU and for KUA (2%W+0.5%Nb+0.25%Si). It can be seen that the temperature dependence of the tensile strength for both materials is very similar. At room temperature both materials exhibit a tensile strength of 450 MPa which decreases significantly above a temperature of approximately 400°C. The similar tensile strengths of the two materials are believed to be related to the fact that in the as received, solution annealed, state the volume fraction of precipitations in KUA is low (see section 5.1). The elongation at rupture for Crofer 22 APU at room temperature is approximately 40% and increases substantially above 600°C. The modified steel with W, Nb and Si additions exhibits at room temperature an elongation at rupture of 24% which is lower than that of Crofer 22 APU but nevertheless sufficient to allow deformation and stamping at room temperature.

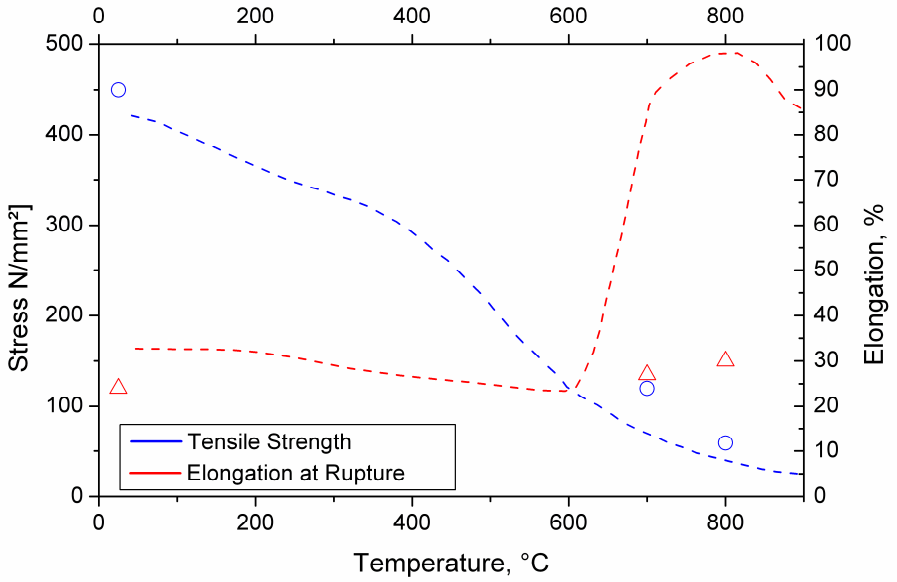

Fig. 6.75: Tensile strength and elongation at rupture for Crofer 22 APU (lines) and KUA (2%W+0.5%Nb +0.25%Si) (data points). Data for Crofer 22 APU were taken from [80].

6.8 Thermal expansion characteristics

A further important property for any material used in a SOFC is a thermal expansion coefficient which matches to the other cell components. Otherwise, thermally induced stresses might destroy the cell during temperature changes. The highest temperature which the assembled cell faces, depends on the design and materials used but generally occurs during the assembly, e.g. during the brazing process.

Fig. 6.76 shows the linear thermal expansion of different materials. It can be seen that the thermal expansion of the ferritic alloys is very similar to that of NiO/YSZ, a typical anode material. For comparison YSZ and the austenitic steel 304 are inserted in the graph. The slope of the latter corresponds to a coefficient of thermal expansion (CTE) of 17-18*$10^{-6}K^{-1}$.

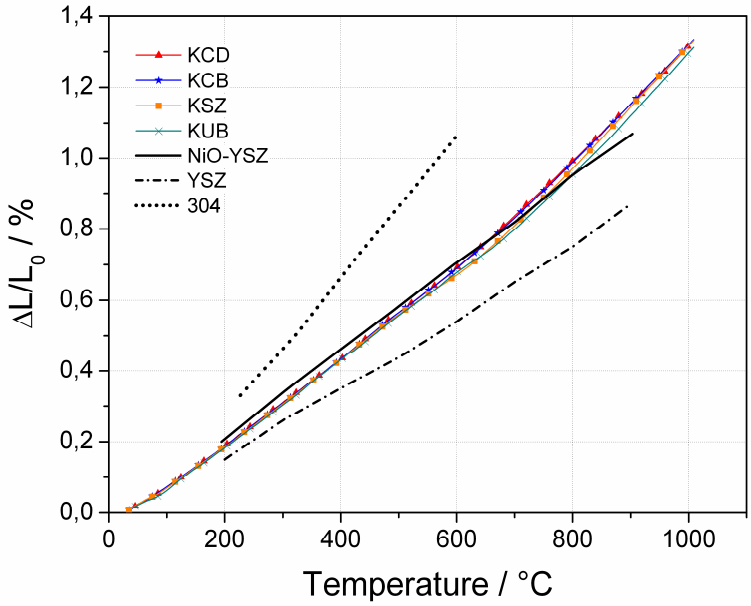

Fig. 6.76: Linear thermal expansion for different materials. The coloured curves correspond to the different modifications of Crofer 22 APU investigated in the present study. The black line represents a NiO/YSZ anode cermet [81] while the dash-dot line corresponds to pure YSZ [81]. For comparison, the thermal expansion of a 304 austenitic steel is shown [82].

For a more detailed comparison of the different alloys the coefficient of thermal expansion as a function of temperature is shown in Fig. 6.77. For comparison the CTE of NiO/YSZ is added as well. It can be seen that the values of the steels are very similar to that of the cermet. However, the anode material has an almost constant CTE while those of the ferritic alloys are increasing. Consequently the CTEs of the ferritic steels are lower than that of NiO/YSZ below 600°C whereas at temperatures above approximately 700°C the CTE of the ferritic alloys exceeds that of the anode material. This will have a significant advantage: after the joining process the ferritic alloy will contract slightly more than the NiO/YSZ. This will cause compressive stresses in the anode which is advantageous because ceramics are more sensitive to tensile than to compressive stresses.

It can be seen in Fig. 6.77 that the discussed alloy modifications do not have a significant effect on the CTE. The blue curve corresponds to Crofer 22 APU 2nd, while KCD and KDM designate alloys with 1%Nb and 2.7%W addition respectively.

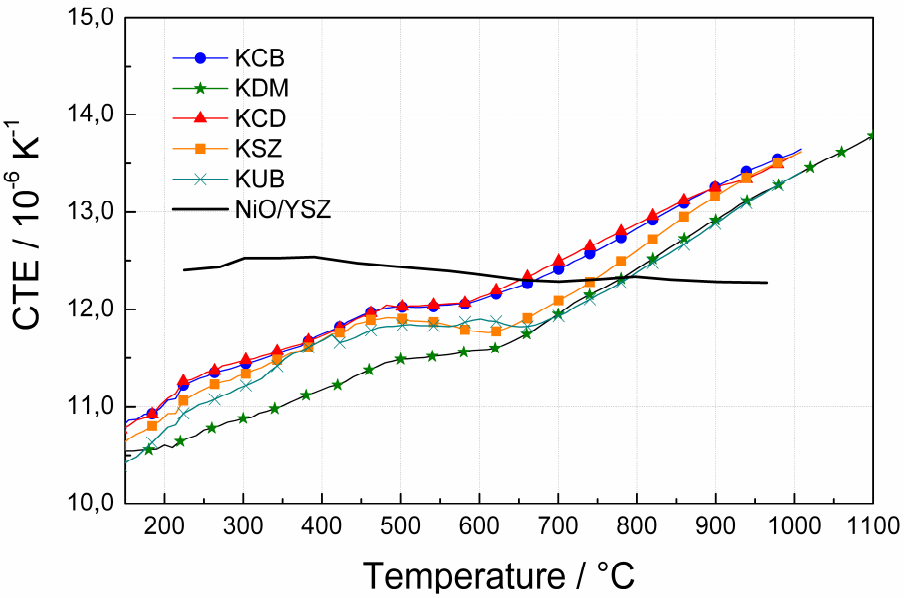

Fig. 6.77 Coefficients of thermal expansion (CTE) as a function of temperature for different alloy modifications. The data for NiO/YSZ cermet were taken from [81].

KSZ corresponds to the alloy with 1%Nb and 0.4%Si while KUB refers to the alloy with combined additions of 2%W, 0.5%Nb and 0.25%Si. Although the differences are quite small

it can be seen that the alloys with W addition (KDM and KUB) exhibit slightly lower CTE values than the W-free alloy which is in agreement with observations from Ueda et al. [82].

6.9 Other alloy modifications

In this chapter a number of other alloy modifications are discussed which for the sake of legibility have been excluded form the discussion so far. In the first section the interaction of W and Si is investigated. The aim of the study was to estimate whether the desired incorporation of Si into the Laves-phase could be obtained in Nb-free alloys. In the subsequent chapter an alloy with a composition similar to that of KUA (2%W+0.5%Nb+0.25%Si) but a lower Cr content is investigated. A lower Cr content might be required and sufficient for SOFCs operating e.g. at 600° because σ-phase formation might cause embrittlement of the high Cr material at these temperatures. Finally the effects of the addition of Mo and V on the oxidation behaviour are discussed. These elements are potentially suitable alloying additions to increase alloy creep strength.

6.9.1 Effect of W and Si

As can be seen in the Fe-Cr-W phase diagram considerable amounts of W are required to form secondary phases, which might tie up Si. Thus two alloys were chosen: LJF (4.9%W+0.3%Si) and LJH (7%W+0.25%Si). The weight gain curves of the corresponding alloys during discontinuous oxidation in air at 900°C are shown in Fig. 6.78. It can be seen that that both alloys show very similar weight gains of approximately 2mg/cm² after 1000h which is slightly higher than KUA and similar to the weight gain observed for KTA (1%Nb+0.4%Si).

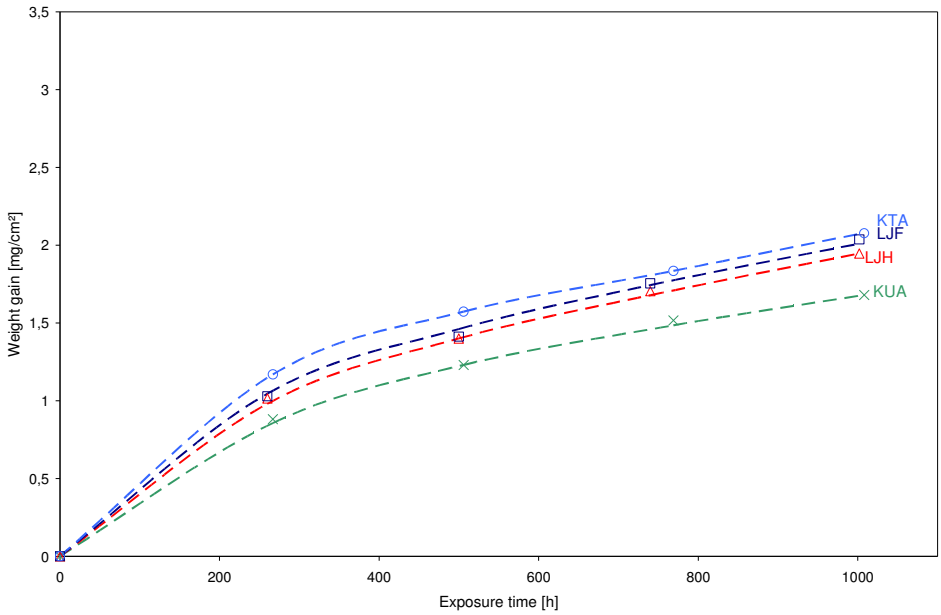

Fig. 6.78: Weight gain of LJF (4.9%W+0.3%Si), LJH (7%W+0.25%Si) KTA (1%Nb+0.4%Si) and KUA (2%W+0.5%Nb+ 0.25%Si) after 1000h at 900°C in air.

Fig. 6.79 shows the corresponding cross-sections of the alloys LJF (4.9%W+0.3%Si), and LJH (7%W+0.25%Si) after exposure. The oxide scale on both alloys is approximately 10µm thick which is in agreement with the results from section 6.1.2. The most striking feature is a SiO_2 layer close to the metal/scale interface. Such a morphology is typical for ferritic steels containing minor additions of Si (see Fig. 3.9). It is believed that the volume increase due to internal oxidation triggers metal creep resulting in outward transport of metal. This causes the formation of metal inclusions in the scale. These inclusions are devoid of any internal oxidation due to the fact that they are formed after a critical extent of internal oxides has formed. This mechanism has been described by previously and was already discussed in section 3.10 and explains the differences between the first commercial heat of Crofer 22 APU and later versions with lower Al and Si content.

The extensive formation of SiO_2 shows that the W-rich precipitates do not tie up Si to such an extent as was observed for Nb/Si containing alloys. This is in agreement with EDX analysis which does not give any indication for Si in the precipitates. Both materials in fact show two types of precipitates, whereby the amount of precipitates is considerably higher in LJH (7%W+0.25%Si). There are small precipitates with a diameter of 1-3µm which appear

brightest in the backscattered electron image indicating a high W content. EDX analyses revealed the composition of these precipitates to match to that of the Laves phase $(Fe,Cr)_2W$. The larger precipitates with an approximate diameter of 10-20µm contain about 10 at.% W. These precipitates are believed to be of the type $Fe_7(Cr,W)_6$. This composition not only agrees with the results of the EDX analysis but also thermodynamic modelling using Thermocalc [77] indicated this to be the most stable precipitated phase. However, the σ phase is also known to dissolve substantial amounts of W so no final conclusion can be achieved what phase the large precipitates are.

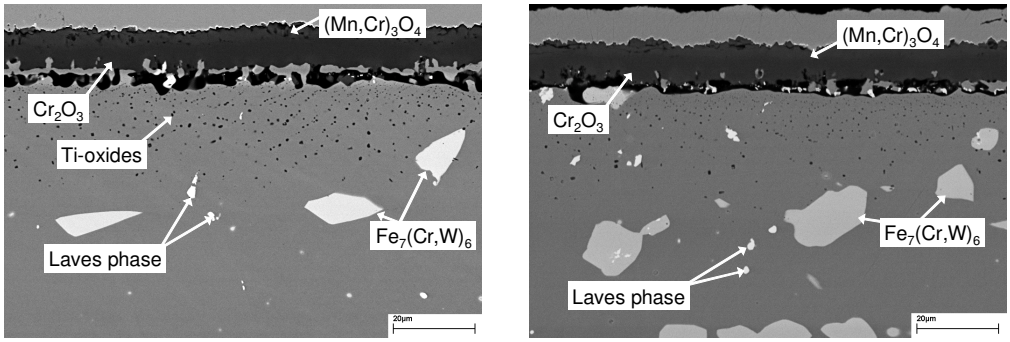

a) LJF b) LJH

Fig. 6.79: SEM-BSE images of cross-sections of LJF (4.9%W+0.3%Si) and LJH (7%W+0.25%Si) after 1000h of exposure at 900°C in air.

6.9.2 Variation of Cr content

LJN corresponds to an alloy with a very similar composition as KUA (2%W+0.5%Nb+0.25%Si) but a lower Cr content of only 18%. Such an alloy would not only result in lower manufacturing costs but would also be less prone to embrittlement due to potential σ phase formation than the 22% Cr version (see section 3.8). Fig. 6.80 shows that the weight gain curves of KUA and LJN are virtually identical during exposure at 900°C in air and in Ar-4%H_2-20%H_2O.

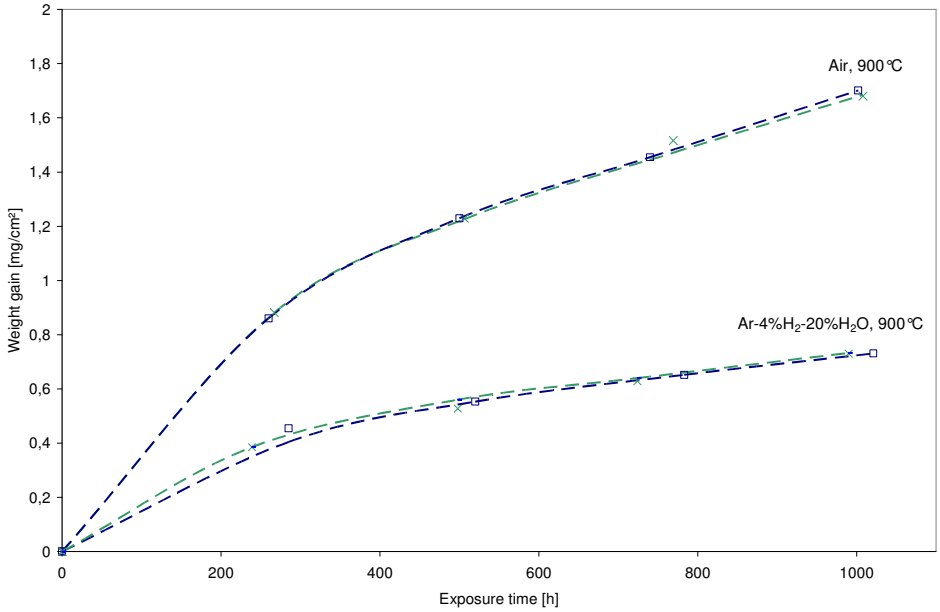

Fig. 6.80: Cross-sections of KUA (22%Cr, 2%W, 0.5%Nb, 0.25%Si) and LJN (18%Cr, 2%W, 0.5%Nb, 0.25%Si) after 1000h at 900°C in air.

The area specific resistance of scales formed on LJN was found to be similar to that of the alloys discussed in chapter 6.5. Due to the lower Cr content the coefficient of thermal expansion (CTE) of this alloy is expected to be higher. However, according to literature data the lower Cr content 18% seems to have only a minor impact on the CTE [83]. Thus, the lower Cr content does not seem to have a significant impact on any of the investigated properties but might turn out to be beneficial at intermediate temperatures (below 600°C) due to reduction of σ phase formation compared to the 22% Cr alloy. However, a major drawback of the lower Cr content is the smaller Cr reservoir in the component. In the case of thin interconnects this might lead to occurrence of breakaway oxidation [61].

6.9.3 Effect of Mo and V

In order to investigate the effect of other transition elements, the alloys KYW (0.5% V addition) and KYU (2% Mo addition) were manufactured. Both elements show considerable solubility in Fe thus the elements are potentially suitable as solid solution strengthening elements i.e. they might replace W in the alloy. The weight gain data during oxidation at 800°C in air in Fig. 6.81 indicate that the addition of Mo has no major effect on the oxidation

rate. However, the addition of V results in a remarkable increase in oxidation rate, which is even higher than what was observed for the alloy with single Nb addition (KCL).

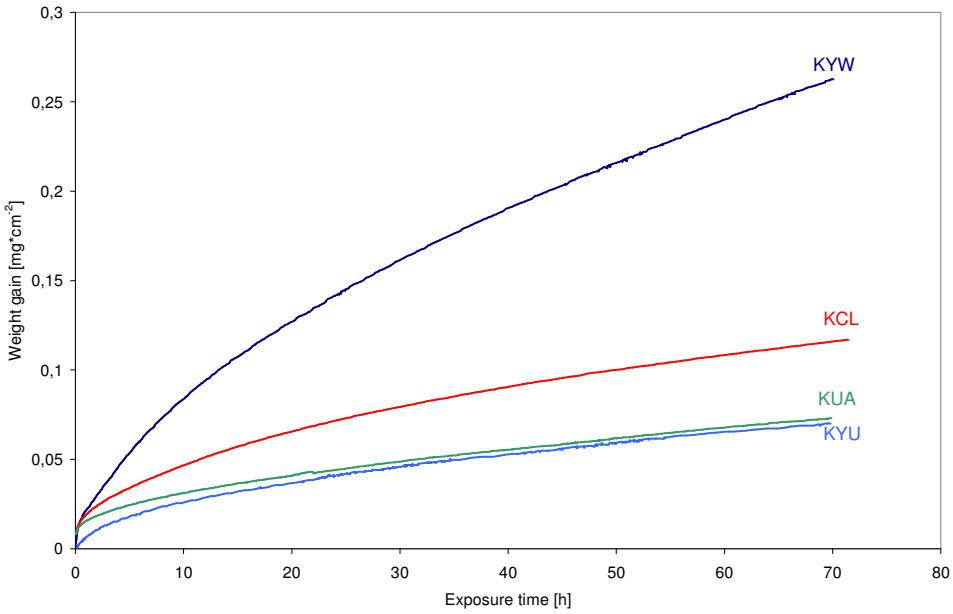

Fig. 6.81: Weight gain during isothermal oxidation in air at 800°C. KYU corresponds to an alloy with 2% Mo addition while KYW posses 0.5%V addition. KUA (2%W+0.5%Nb+0.25%Si) and KCL (1%Nb) were added for comparison.

Fig. 6.82 shows cross-sections of KYU (Mo addition) and KYW (V addition) after exposure for 100h in air at 800°C. The results show that the scale on KYU (2%Mo) is about 1µm thick and smooth. For comparison Fig. 6.82d shows the oxide scale formed on KUA (2%W+0.5%Nb+0.25%Si) after 72h oxidation in air at 800°C which looks very similar. As already indicated by the high weight gain, on alloy KYW (0.5%V) a much thicker scale has formed. The cross-section shows a whisker surface morphology, although the spikes probably correspond to blades. The blades are almost 10µm long and cover the whole surface, although between different blades the scale remains thin.

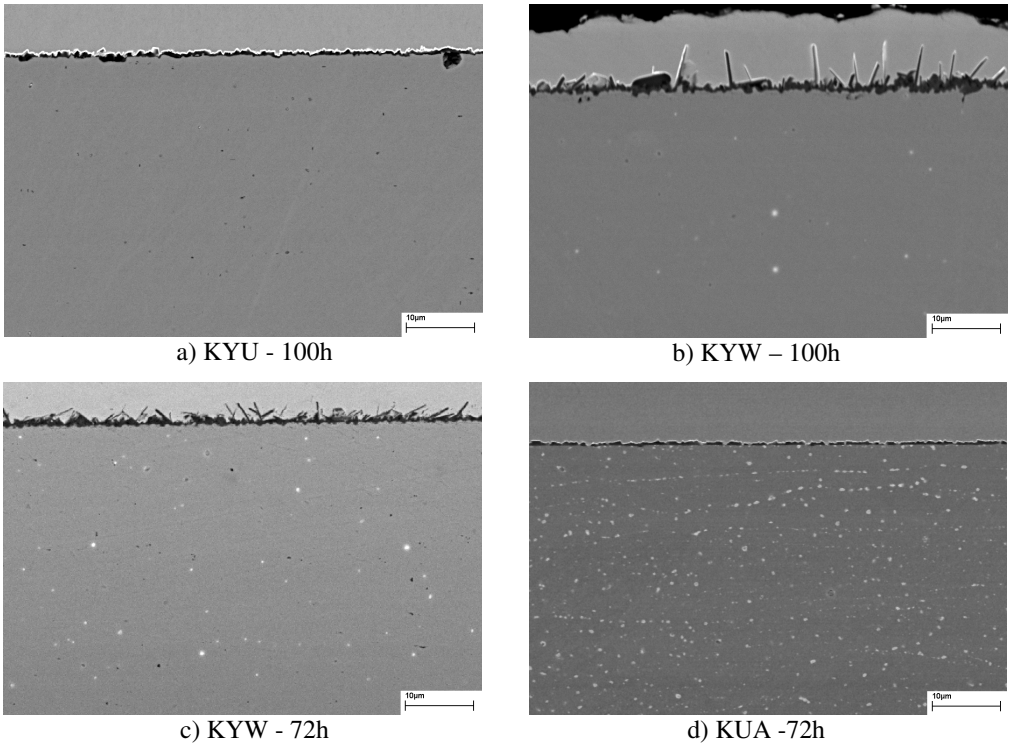

a) KYU - 100h b) KYW – 100h

c) KYW - 72h d) KUA -72h

Fig. 6.82: Cross-sections of alloy KYU (2% Mo), KYW (0.5%V) and KUA (2%W+0.5%Nb+0.25%Si). Fig. 6.82 a and b show the scale formed after 100h oxidation in laboratory air at 800°C. Fig. 6.82 c and d shows cross-section of scales formed in KYW and KUA after isothermal oxidation for 72h in dry synthetic air at 800°C.

The formation of blades in air is surprising as this is a morphology that is usually observed in low pO_2 atmospheres like Ar-H_2-H_2O [64, 84]. To the authors knowledge the mechanism of blade formation is not clearly understood. Under the premise that the mechanism of blade formation is somewhat similar to whisker formation some conclusions can be drawn. Whisker formation is known to occur if the gas phase diffusion is the rate determining step in the oxide growth process [24]. Possibly V doping increases the cation transport in the scale to an extent that diffusion processes in the scale are no longer the rate determining step of scale growth. However, whisker formation is only known to occur in low pO_2 atmospheres but not in air. Further the formation of whiskers is attributed to the catalysis of H_2O dissociation on the whisker tip [84], but blades can be clearly seen in Fig. 6.82c although the exposure was carried out in dry synthetic air.

Although the mechanism of the effect of V additions on the scale growth mechanism are not completely clear, the results show that V is an undesired addition in ferritic interconnect steels because it has a detrimental effect on the oxide growth rate. Mo on the other hand seems to have no negative effect on the oxidation behaviour, however, it has to be mentioned that Mo is known to stabilise the σ-phase which can cause embrittlement of the steel [38].

7. Anode side protective coatings

7.1 Definition of the problem

It was discussed in chapter 3.11 that the direct contact of Ni with the ferritic steel may deteriorate the cell performance due to interdiffusion of Ni the steel and of Fe and Cr into the Ni-rich component. If a porous substrate, usually a ferritic steel, is used the problem is especially severe because e.g. Cr can diffuse directly into the anode where the formation of Cr_2O_3 might block electrochemically active sites. Interdiffusion related problems have been reported in various publications [54, 55]. However, also for a self supported cell design where Ni-wires are commonly used to contact the cell to the interconnect, interdiffusion problems are likely to arise. Fig. 7.1 shows an image which was obtained during a stack "autopsy" at Forschungszentrum Jülich. It shows the interface between a Ni-wire from the Ni-mesh and the ferritic interconnect steel. It can be seen that after 3000h at 800°C diffusion of interconnect elements into the Ni-mesh caused oxide formation at the grain boundaries. At the same time Ni diffusion into the ferritic interconnect plate resulted in the formation of austenite in the interface region. As described earlier, the formation of austenite can cause problems during stack operation because the coefficient of thermal expansion (CTE) of austenite is significantly higher than that of ferrite or any other SOFC component. Additionally the diffusivity of Cr is higher in ferrite than in austenite thus the critical Cr content to form a protective oxide is substantially higher on an austenitic steel [3].

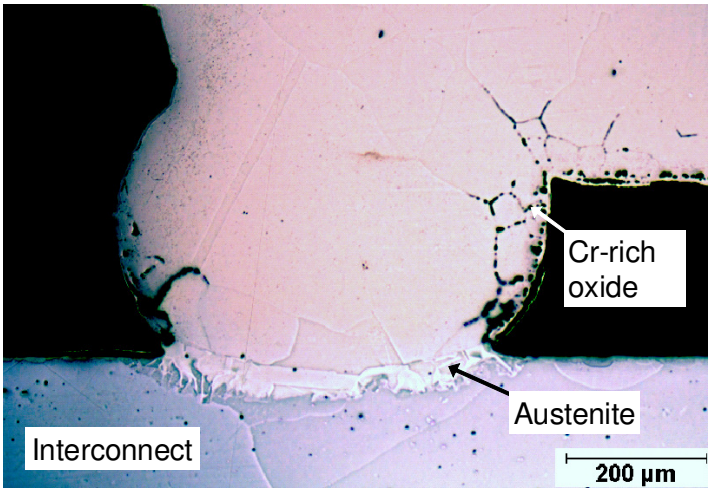

Fig. 7.1: Optical microscopy image of a Ni wire in direct contact with the interconnect plate obtained from FZJ stack F1002-61 after 3000h of operation at 800°C [85].

These results illustrate the requirement of a barrier layer at the anode side to inhibit interdiffusion of Ni into the interconnect as well as diffusion of interconnect elements into the Ni base material. Such a barrier layer requires the following properties:

- High electronic conductivity
- Similar thermal expansion coefficient as the interconnect
- Stability in SOFC anode atmosphere
- Compatibility with ferritic steel and Ni

As model system, in the current investigation a Ni sputter coating was used to simulate the Ni mesh or Ni base anode. This has to be distinguished from the Ni coating that was applied on the sample galvanically after exposure during sample preparation.

7.2 Metallic Coatings

7.2.1 Reference system

As reference for the study the interaction of various coating types an approximately 10µm thick Ni-sputter-coating with bare Crofer 22 APU substrate was investigated. The samples were exposed for 1000h at 800°C in Ar-4%H_2-2%H_2O. As can be seen in Fig. 7.2a and b Ni has diffused into the steel causing the formation of an approximately 30-40µm deep layer of austenite. At the same time Fe, Cr and Mn diffuse into the Ni layer resulting in a Ni concentration of less than 30%. During the exposure Cr and Mn become oxidised at the Nickel surface.

Fig. 7.2c and d show a Ni coating on a pre-oxidised Crofer 22 APU substrate after 1000h of exposure under the same conditions. A pre-oxidation scale could be considered as simplest solution to inhibit interdiffusion. However, it can be seen that the oxide scale becomes dissolved under the Ni layer: instead of a continuous chromia base scale only isolated oxide nodules can be seen at the interfaced between steel and Ni-layer. Due to the direct metallic contact no notable effect on the interdiffusion can be seen; the amount of austenitisation is similar to the case without preoxidation scale and again extensive diffusion of Fe, Cr and Mn into the Ni coating can be observed. This result shows that the pre-oxidation of the interconnect is not a suitable option as the oxide scale becomes dissolved under a Ni coating.

In order to investigate this effect in more detail a number of samples with metallic coatings on bare and pre-oxidised Crofer 22 APU substrates were prepared and will be discussed subsequently. The selection of the metals was based on the following considerations: Cu and Ag where chosen since these metals have a high solubility for oxygen and it was thus expected that the oxide scale below the coating would remain stable. Additionally both metals have a low solubility for Fe and Cr and were thus considered as potentially suitable as diffusion barrier [40]. Although Co mixes with ferrite it has a higher oxygen solubility than Ni and was included as well. W was investigated as well, although the very low thermal expansion coefficient of W makes it doubtful whether it is suitable to be applied in the SOFC. However, the high melting point suggests slow diffusion of other elements through W.

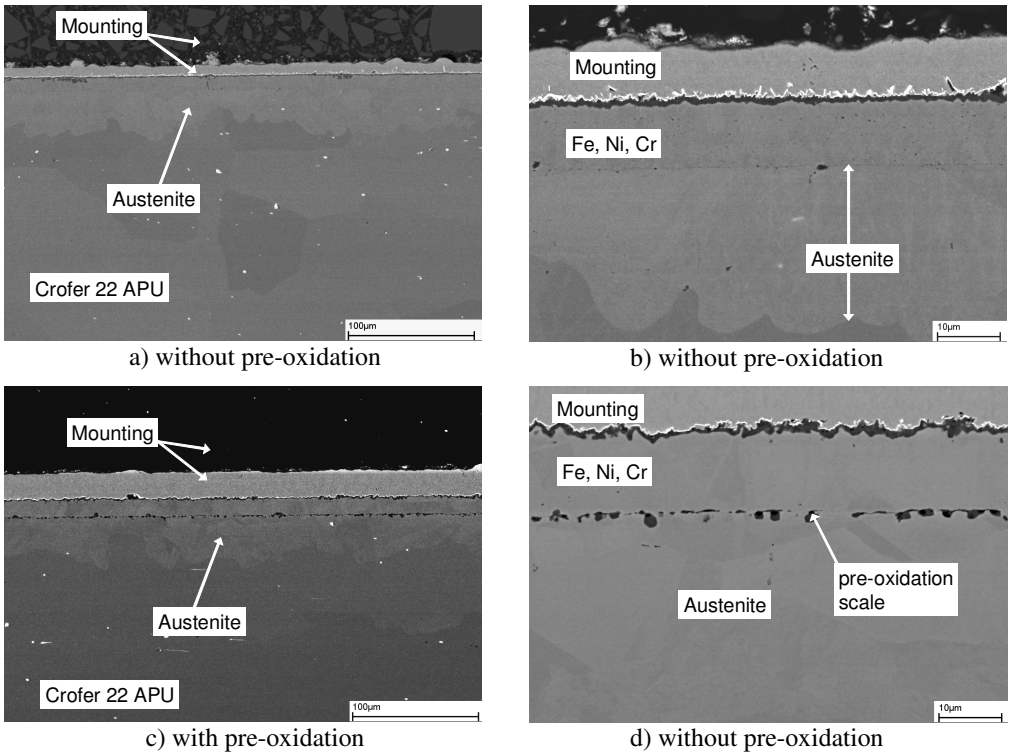

Fig. 7.2: Ni sputter coating on bare and pre-oxidised Crofer 22 APU 2nd (KCB) after 1000h exposure at 800°C in Ar-4H_2-2H_2O. The pre-oxidation was carried out for 20h under the same conditions.

7.2.2 Cu layer

Fig. 7.3 shows cross-sections of samples with a Cu layer applied instead of a Ni layer, but exposed under the same conditions. It can be seen that in the case of a Cu coating on bare Crofer 22 APU (Fig. 7.3a) the Cu layer does not block diffusion of Cr and Mn. Consequently an oxide scale is formed on top of and within the Cu layer. The scale is very thick (about 10µm) compared to less than 3µm on uncoated Crofer 22 APU. It exhibits a very disordered structure and contains numerous Cu inclusions. In most areas a thin layer of Cu can be found on top of the scale thus, strictly speaking, the oxide scale is not formed on top of the Cu layer but within the upper part of the Cu layer. EDX analysis showed that the scale comprises of a (Cr,Mn)-oxide probably of spinel type. In contrast to the Ni coating which contained large amounts of Cr and Fe, the Cu coating is almost pure. This is in agreement with the corresponding binary phase diagrams which show a low solubility of Fe (less than 2%) and

hardly any for Cr in Cu [40]. This also explains why no Cu diffuses into the steel substrate could be detected.

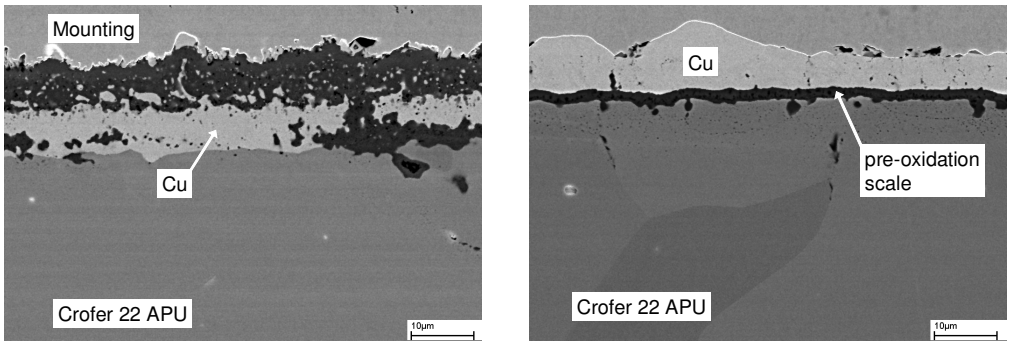

a) without pre-oxidation b) with pre-oxidation

Fig. 7.3: Cu-sputter coating on bare and pre-oxidised Crofer 22 APU 2nd (KCB) after 1000h at 800°C in Ar-4H_2-2H_2O. The pre-oxidation was carried out for 20h under the same conditions. The Ni coating at the upper part of the image was applied after the exposures during the metallographic preparation.

In the case of the Cu coating on preoxidised Crofer 22 APU (Fig. 7.3b) a completely different behaviour can be observed. The preoxidation scale remains stable under the Cu coating. Due to this fact no diffusion of substrate alloying elements into the Cu layer occurs. Consequently, no oxide scale is formed on top or within the Cu layer. The morphology of the oxide scale is different from that on an uncoated sample: at the metal oxide interface oxide nodules can be seen which extend into the substrate. This feature was already known for metal coatings on Crofer 22 APU. It was shown by Huczkowski et al. that these nodules consist mainly of a (Cr,Mn)-oxide [6]. It is believed that these nodules comprise of the inner $(Cr,Mn,Ti)_3O_4$ spinel discussed in chapter 6.2.1.

7.2.3 Cu as a barrier layer

The fact that during the Ar-H_2-H_2O exposure the oxide scale beneath a Cu layer remained stable, gave rise to the question whether such an intermediate Cu layer could have a beneficial effect to impede the interdiffusion between ferritic steel and Ni rich component. Although Cu and Ni exhibit complete miscibility [40] and thus not suitable as barrier layer, the pre-oxidation scale itself is believed to be an efficient barrier provided it remains stable below the metallic coating. To answer this question, a sample of Crofer 22 APU which was pre-oxidised and subsequently coated with Cu and Ni was manufactured. The latter coating was applied to simulate the presence of a Ni-mesh or the anode. The corresponding cross-section after 1000h

exposure at 800°C can be seen in Fig. 7.4. As expected, Ni and Cu have completely mixed, but the pre-oxidation scale remains stable and shows virtually the same morphology as that formed beneath a pure Cu coating. According to EDX analysis the coating contains more than 50% Ni which after 1000h did not have a noticeable effect on the pre-oxidation scale. Thus a Cu coating on the steel seems to be a solution to the problem [86]. Although Cu does not act as diffusion barrier itself it stabilises the pre-oxidation scale which efficiently inhibits diffusion. However, if one considers a real stack with a larger Ni reservoir in the anode the rapid mixing of Cu and Ni causes the formation of a (Ni, Cu) alloy with very high Ni concentration to be in contact with the ferritic steel. It is believed that eventually with increasing Ni content the (Ni, Cu) alloy will show a behaviour like pure Ni instead of pure Cu and the pre-oxidation scale will dissociate.

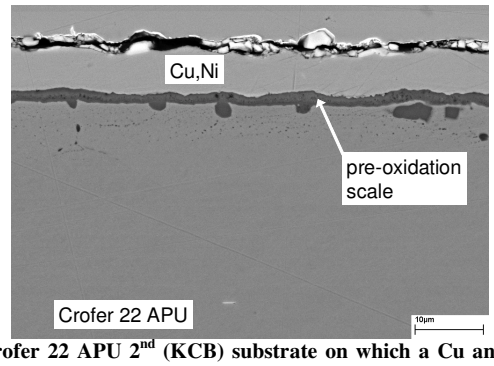

Fig. 7.4: Pre-oxidised Crofer 22 APU 2nd (KCB) substrate on which a Cu and a subsequent Ni coating was applied after 1000h at 800°C in Ar-4H_2-2H_2O. The bright particles at the sample surface correspond to a W rich compound formed due to volatile W that evaporated from adjacent samples.

7.2.4 Co layer

A similar behaviour as observed for Cu can be observed for Co coatings on Crofer 22 APU substrates. In the case of a Co coating on bare Crofer 22 APU (Fig. 7.5a) Cr and Mn diffuse through the Co layer and form an outer scale although some oxide nodules also can be found within the Co coating. Fig. 7.5b shows a Co coating on preoxidised Crofer 22 APU. The morphology is very similar as that observed for the Cu coating on pre-oxidised Crofer 22 APU: the pre-oxidation scale of 2µm thickness remains stable beneath the coating. This results in the inhibition of diffusion of alloying elements into the coating.

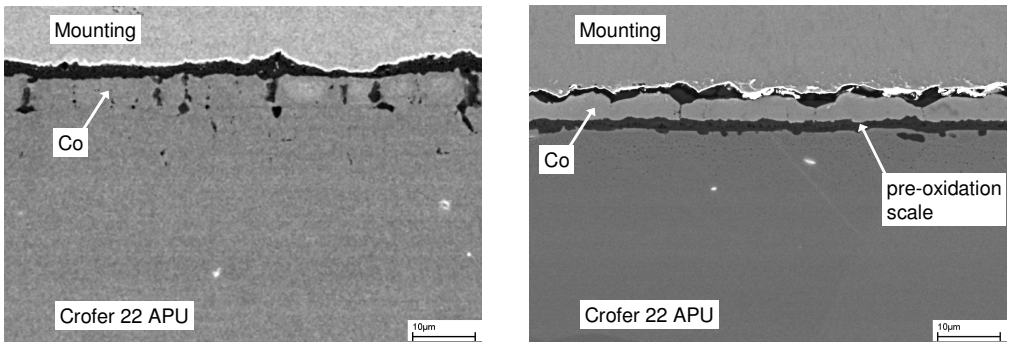

a) without pre-oxidation b) with pre-oxidation

Fig. 7.5: Co-sputter coating on bare and pre-oxidised Crofer 22 APU 2nd (KCB) after 1000h at 800°C in Ar-4H_2-2H_2O. The pre-oxidation was carried out for 20h under the same conditions. The Ni coating at the upper part of the image was applied after the exposures during the metallographic preparation.

7.2.5 Ag layer

Fig. 7.6 shows the effect of a Ag coating on Crofer 22 APU. If Ag is sputtered on bare Crofer 22 APU, Cr and Mn diffuse through the Ag layer which results in the formation of an outer oxide scale of 3-8µm thickness. The Ag layer itself was found to be pure which is in agreement with the respective binary phase diagrams that show no solubility for Fe and Cr in Ag [40]. At the coating/substrate interface Ag nodules can be found in the steel. If Ag is sputtered on pre-oxidised Crofer 22 APU (Fig. 7.6b) the behaviour does not change significantly. Although the pre-oxidation scale seems to remain continuous, it does not inhibit interdiffusion of the respective elements. An outer oxide scale approximately 5µm in thickness containing of Cr and Mn can be found. This scale exhibits extensive whisker formation at the surface and shows oxide nodules penetrating into the Ag coating. Below the pre-oxidation scale similar Ag inclusions can be found as were observed in the case of a Ag coating on bare Crofer 22 APU.

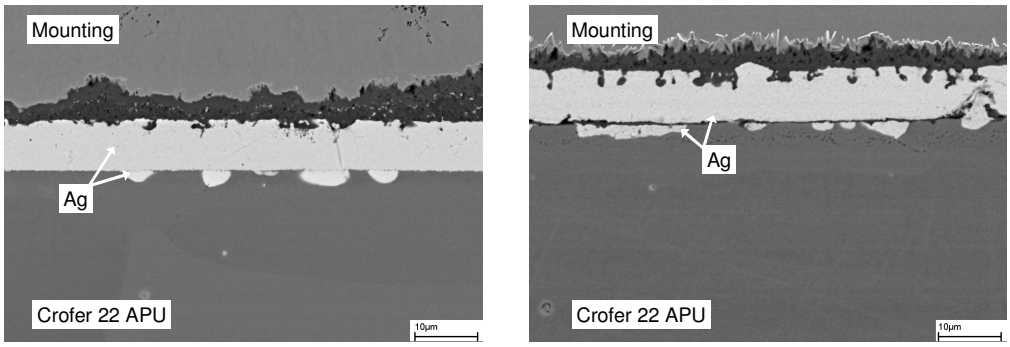

a) without pre-oxidation b) with pre-oxidation

Fig. 7.6: Ag-sputter coating on bare and pre-oxidised Crofer 22 APU 2nd (KCB) after 1000h at 800°C in Ar-4H_2-2H_2O. The pre-oxidation was carried out for 20h under the same conditions. The Ni coating at the upper part of the image was applied after the exposures during the metallographic preparation.

The results indicate that for all investigated coatings a pre-oxidation is required to inhibit outer scale formation. It is believed that the scale morphology in these experiments depends on the diffusion rates of oxygen as well as Cr and Mn in the metallic. In the case of Cu and Co the pre-oxidation scale slows the outward diffusion of Cr and Mn. This enables O to penetrate the coating and oxidise any Cr and Mn at the coating substrate interface. If no pre-oxidation scale is present Cr and Mn diffuse faster than O and hence the new oxide is formed at the outer part or within the coating.

The pre-oxidation of the substrate does not have a major effect in the case of the Ni- and Ag coatings. For the Ni coating it can be clearly seen that the preoxidation scale below the coating becomes dissolved during long term exposure. A similar mechanism is believed to take place in the case of the Ag coating. Although the scale seems to be continuous, the diffusion of Ag into the substrate indicates that this is, at least locally, not the case. According to thermodynamics the pre-oxidation scale will dissolve if the oxygen activity drops below the dissociation pressure of the respective oxide. It is proposed that the activity is governed by the amount of oxygen and hydrogen that diffuse through the coating. Thus the diffusivities and solubilities of O and H in the respective metals have to be considered. The diffusivity of H is generally assumed to be higher than that of O. However, if in some metals the difference in H and O diffusivities is very high, this should cause a low oxygen activity below the coating and might cause dissolution of the oxide scale. The diffusivity of H in the four discussed metals at 800°C is approximately $1*10^{-8}$ m²/s. The diffusivity of O in Ag and Cu is about one order of magnitude lower while in Co and Ni it is approximately $1*10^{-14}$ m²/s [87-

89]. Hence, although there are major differences in diffusivities of H and O in the different metals, there is no clear correlation with the differences in morphology observed here. However, one also has to consider the solubility of O and H in the respective metals. Reliable solubility data for the relevant conditions are scarce. According to Fromm et al. [87] the solubility of H is highest in Ni. The H solubility in Co is slightly lower while the solubilities in Cu and Ag are one and two orders of magnitude lower. The data for the solubility of oxygen in the respective metals at pO_2 values of ~10^{-18}bar are inconsistent, however, if one assumes that the same ranking applies as at ambient oxygen pressure it follows that Ag and Cu have the highest oxygen solubilities [40, 87]. The solubility of O in Co is significantly lower but higher than that in Ni which is known from oxidation experiments [26]. Thus the differences in solubility of O and H in the various metals might explain the observed differences oxidation behaviour of the metal coating on the steel substrate. From the investigated metals Ni has the highest solubility for H and the lowest solubility for O which might cause the dissolution of the oxide scale. Cu possesses a high O solubility but a low one for H which is in agreement with the experimental results. The same is true for Ag, however, it does not match with the experimental results as the oxide below the Ag layer is at least partly dissolved.

7.2.6 W as a barrier layer

A W coating on a bare Crofer 22 APU (2^{nd}) substrate was also investigated. After 100h of oxidation no Cr or Mn can be found at the sample surface. Instead, the oxide scale is formed at the steel/coating interface. However, as can be seen in Fig. 7.7b, W exhibits extensive reaction with Ni so that the use of W as a possible diffusion barrier appears doubtful. In this case a W coating was sputtered on a pure Ni substrate. It can be seen that already after 100h at 800°C considerable diffusion has taken place. Although no Ni can be detected in the W coating, W has diffused into the Ni resulting in the formation of a more than 10µm thick layer of Ni_4W. As this component has a defined stochiometry the Ni and W concentrations are constant in this region. Beneath this layer the W concentration drops from approximately 11 at.% to a value below the detection limit of the EDX at a depth of 20µm. This is in agreement with the Ni-W phase diagram [40] which shows a solubility of slightly more than 10 at.% W in Ni.

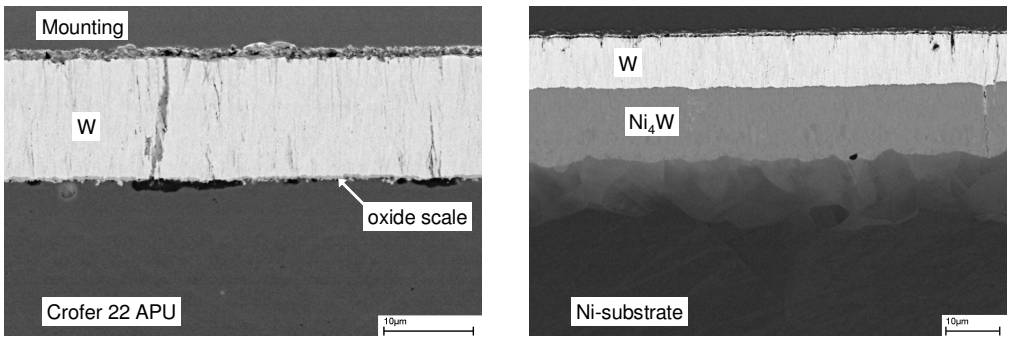

a) Crofer 22 APU-W b) Ni-W

Fig. 7.7: W coatings on Crofer 22 APU (no preoxidation) and Ni-substrates after 100h exposure at 800°C in Ar-4H_2-2H_2O.

Fig. 7.8 shows the cross-section and an EDX linescan of a sample with a Crofer 22 APU substrate which was sputter-coated with W and Ni, where the latter coating was applied to simulate the anode/Ni-mesh. It can be seen that W is not an efficient diffusion barrier because after 1000h at 800°C in Ar-4H_2-2H_2O substantial diffusion of Cr and Mn has occurred and these elements formed a mixed outer oxide with W. Below this outer scale a Ni rich layer can be found. Although the linescan shows a low level of Cr in the W layer, point analysis revealed a Cr content of approximately 5 at.% which clearly shows that W seems to be unsuitable as diffusion barrier, not only because of the strong interaction with Ni, which would eventually cause the complete dissolution of the W layer, but also because it does not inhibit outward diffusion of Cr and Mn.

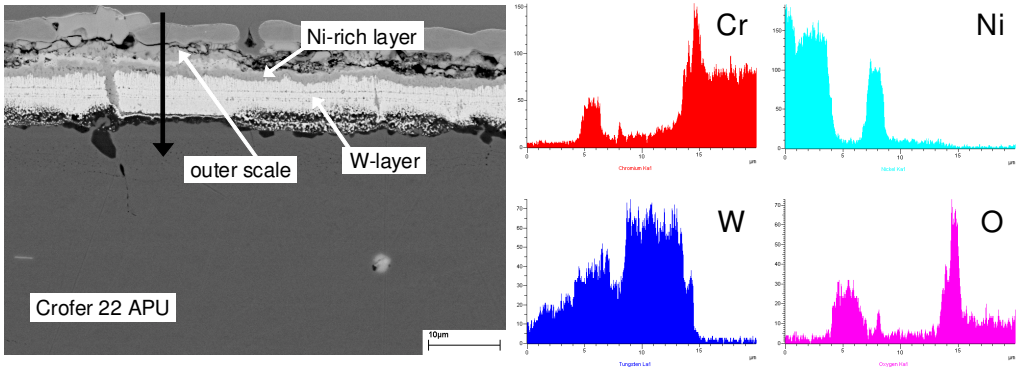

Fig. 7.8: Crofer 22 APU (KCB) coated with W and Ni after 1000h at 800°C in Ar-4H_2-2H_2O. The black arrow marks the position of the EDX linescan which is shown in the right part of the figure.

7.2.7 Summary of the results with metallic coatings

It is concluded that all the investigated metallic coatings seem to be unsuitable as diffusion barrier coatings. It turned out that even if the binary phase diagrams show very little or no solubility of metal A in B, it appears that B cannot block the diffusion of A if on the other side of B an element with high solubility or affinity to A is present. Further, the high solubility of many metals in Ni suggests that these are unsuitable as barrier materials as they will be consumed after longer times if the Ni reservoir is sufficiently large.

7.3 Ceramic coatings

7.3.1 Selection of materials

Due to the lack of materials compatibility metallic coatings seemed unsuitable as barrier coatings and further studies focused on ceramics materials, oxides in particular. While the electronic conductivity of metals is usually quite high that of ceramic materials varies widely. Another factor which limits the number of potentially suitable oxide materials is the fact that many oxides are not thermodynamically stable in typical anode gas.

For a first screening of materials based on literature review the focus was turned to materials which were proposed in literature as SOFC anode materials since a for diffusion barrier a similar set of properties is required as for the anode. Out of the large variety of proposed materials conductivity data for selected oxides which were measured at 800°C are plotted in Fig. 7.9 as a function of pO_2. The data show that the pO_2 can have a significant effect on the conductivity of the various materials.

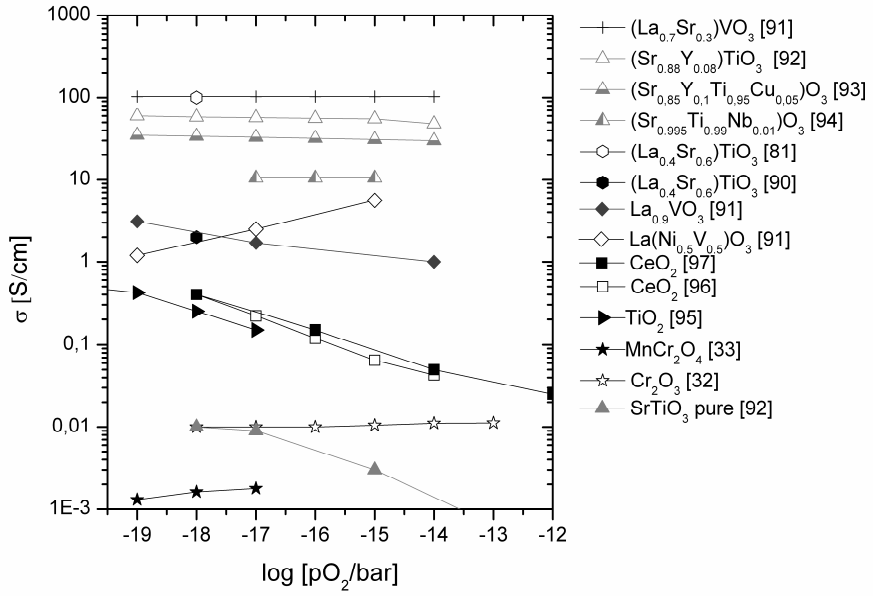

Fig. 7.9: Electrical conductivity of different oxides at 800°C. It can be seen that minor amounts of impurities can have a extensive effect on the conductivity [31, 33, 81, 90-97].

In spite of the fact that it is difficult to compare values obtained by different authors due to differences in specimen preparation or experimental setup the values can be used as rough estimates concerning the potential suitability of a given material. It can be seen that some materials exhibit an excellent conductivity, however these materials seem to be very sensitive to the exact concentration of dopants. For instance the doped $SrTiO_3$ type materials exhibit conductivities of 10-60 S/cm compared to less than 0.01S/cm for pure $SrTiO_3$.

Another important factor which has to be considered is that some materials exhibit conductivities which are very sensitive to the manufacturing process. For instance the values reported by Marina et al. [81] and Fu et al. [90] for $La_{0.4}Sr_{0.6}TiO_3$ differ by almost two orders of magnitude although the same material is used. However, the values reported by Fu et al. refer to material sintered in air while Marina et al. used material which was sintered in H_2. In the latter study much lower conductivity values for samples sintered in air are reported as well. These results indicated that the high conductivity values reported for bulk samples can probably not be reproduced for thin sputter coatings.

In the thick anode a high electronic conductivity is of major importance to keep the ohmic resistance as low as possible, however, in the case of a diffusion barrier coating only a thin layer is required so that materials with significantly lower conductivity may still be useful. For example, the conductivity of pure ceria is approximately 0.3S/cm at 800°C and a pO_2 of 10^{-18} bar; this is fairly low compared to the earlier discussed materials, but if one considers a layer of only 3µm thickness, this corresponds to an additional ASR of only 1mΩcm² imparted be the CeO_2 layer. Since this contribution is negligible compared to the overall cell resistance it was decided to focus on ceria coatings.

7.3.2 Ceria as diffusion barrier

Pure CeO_2 has a fluorite structure which is known to tolerate considerable reduction before a phase change occurs. The main defects in CeO_{2-x} are oxygen vacancies and Ce^{3+} ions. While the concentration of oxygen vacancies determines the oxygen ion conductivity, the Ce^{3+} ions govern the electronic conductivity. The concentration of both types of defects, and therefore also the conductivity, increases with decreasing pO_2. The defect chemistry can be also altered by doping. In the case of acceptor doping, e.g. with Gd, the ionic conductivity is increased at

the expense of the electronic conductivity while doping with higher valency dopants e.g. Nb increases the electronic conductivity [96-98]. However, in the current work the studies focused for simplicity on pure ceria because exact dopant levels are difficult to adjust in sputter coatings.

Fig. 7.10 shows a cross-section of a ceria coating on a Crofer 22 APU (KCB) substrate after 115h exposure at 800°C in Ar-4H_2-2H_2O. The CeO_2 coating is about 5µm thick and exhibits minor porosity, concentrated in the outer part. At the coating/substrate interface a number of pores can be seen as well. EDX analysis showed that the oxide formed on the steel beneath the coating comprises of Cr and Mn with Mn located in the outer part. However, neither any outward diffusion of the alloying elements of the steel substrate into the CeO_2 coating nor any reaction of the ceria coating with the steel substrate could be observed.

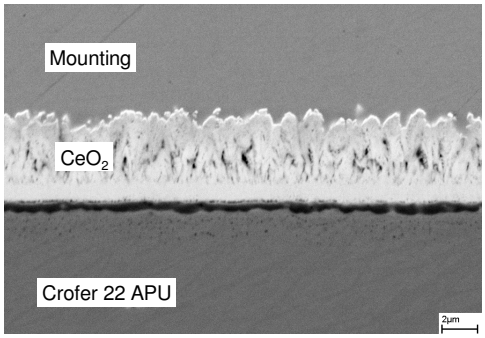

Fig. 7.10: Crofer 22 APU substrate with ceria coating after 100h at 800°C: Neither any reaction with the substrate nor diffusion through the coating can be observed.

Due to these promising results a Crofer 22 APU (KCB) substrate was sputter-coated with a CeO_2 coating and a Ni coating, the latter simulating the anode, and subsequently exposed for 1000h in simulated anode gas. The corresponding cross-section and EDX data after exposure are shown in Fig. 7.11. The 4µm CeO_2 layer which appears bright in the backscattered image can be divided into two parts; an inner layer of about 1µm thickness that appears to be dense and an outer porous part showing a columnar structure. At the interface between ceria coating and the oxide formed on the steel a number of pores can be observed. The oxide scale comprises of in inner Cr rich and an outer Mn-rich part. The EDX linescans show that there is no indication of interdiffusion through the ceria coating: no Ni can be detected in the steel and no Fe, Cr or Mn in the Ni-layer.

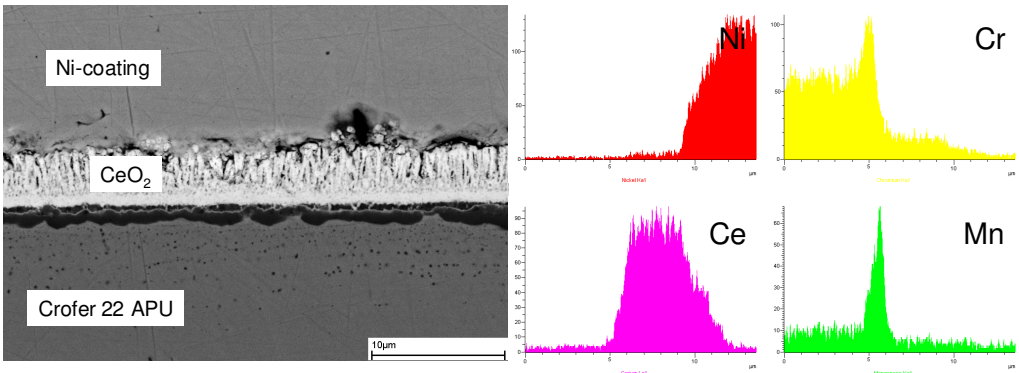

Fig. 7.11: Crofer 22 APU substrate with ceria coating and Ni coating that was applied before exposure to simulate the anode/Ni-mesh. After 1000h at 800°c no interdiffusion can be detected with EDX.

The void formation at the interface between the ceria layer and the oxide growing on the steel surface seems to be a major drawback for this coating system because the void formation is expected to increase the contact resistance and may give rise to spallation.

In order to improve the contact between steel substrate and ceria coating a Cu layer was introduced. Cu was chosen since it was shown above that a Cu coating does not adversely affect the pre-oxidation scale during anode gas exposure. Cu is believed to be beneficial for two reasons: first it ensures good electrical contact over the whole substrate/coating interface and second it is expected that the ductile Cu can compensate any stresses which might be generated due to, for example, oxide growth.

The Cu coating was sputtered on a pre-oxidised Crofer 22 APU substrate which was subsequently coated with CeO_2 and finally a Ni layer was applied. A cross-section of the sample which was exposed for 1000h at 800°C in Ar-4%H_2-2%H_2O can be seen in Fig. 7.12. The EDX data show that CeO_2 is a very efficient diffusion barrier. Although Ni and Cu exhibit a substantial mutual solubility the 2.5µm CeO_2 inhibits any interdiffusion. At none of the interfaces any substantial porosity visible. Only in the oxide scale formed on the steel substrate a string of pores can be seen which was also found for uncoated steel substrates in Ar-H_2-H_2O atmospheres (see section 6.2).

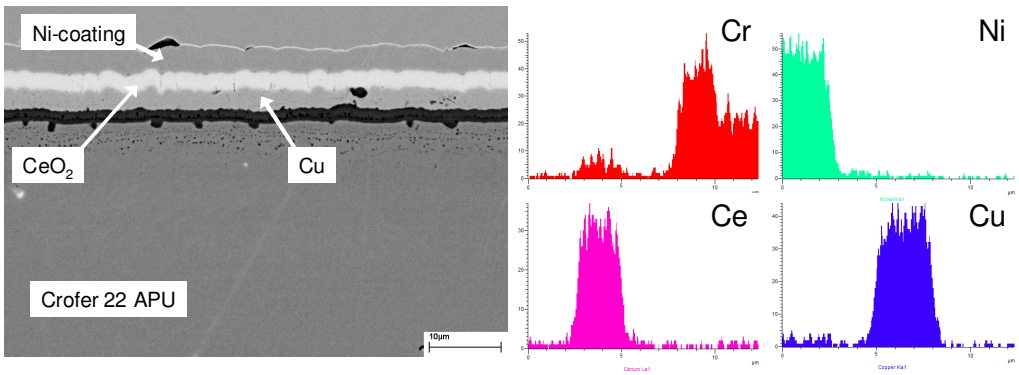

Fig. 7.12: Pre-oxidised Crofer 22 APU substrate which was coated subsequently with Cu, CeO_2 and Ni before 1000h of exposure at 800°C in Ar-4%H_2-2%H_2O. No interdiffusion between steel and Ni-coating can be detected with EDX.

7.3.3 Conductivity of ceria

Since ceria is stable under anode conditions and further seems to be very efficient as diffusion barrier, the electric conductivity of a number of CeO_2 coated materials was investigated in more detail. Fig. 7.13 shows the temperature dependence of the electrical conductivity of pure ceria. It compares experimental values (filled symbols) with data from literature (open symbols). The experiments in the current work investigation were carried out in Ar-4%H_2-2%H_2O. At 800°C the equilibrium oxygen partial pressure in this atmosphere equals 10^{-19}bar. Since this equilibrium oxygen partial pressure is temperature dependent all values are plotted as a function of temperature and the corresponding oxygen partial pressure in Ar-4%H_2-2%H_2O at the respective temperature, which is shown on the upper axis. The literature data were reported by different authors and are in reasonable agreement if one considers the differences in the experimental setup used in the different studies. For example, the values reported by Tuller et al. [97] were measured on single crystals while the values by Zhou et al. [99] refer to a polycrystalline material with 5µm grains. Samples A and B correspond to ceria samples cut from the same material as the sputter targets. The obtained data show excellent reproducibility and are in good agreement with the literature data. The red symbols correspond to conductivity data of a 2.6µm thick ceria sputter coating an Al_2O_3 substrate. It can be seen that these conductivity values are only slightly lower than the values obtained form the bulk ceria material. This shows that ceria not only fulfils a number of important requirements for a diffusion barrier layer but also can be easily applied by sputtering without a significant change of its electronic conductivity.

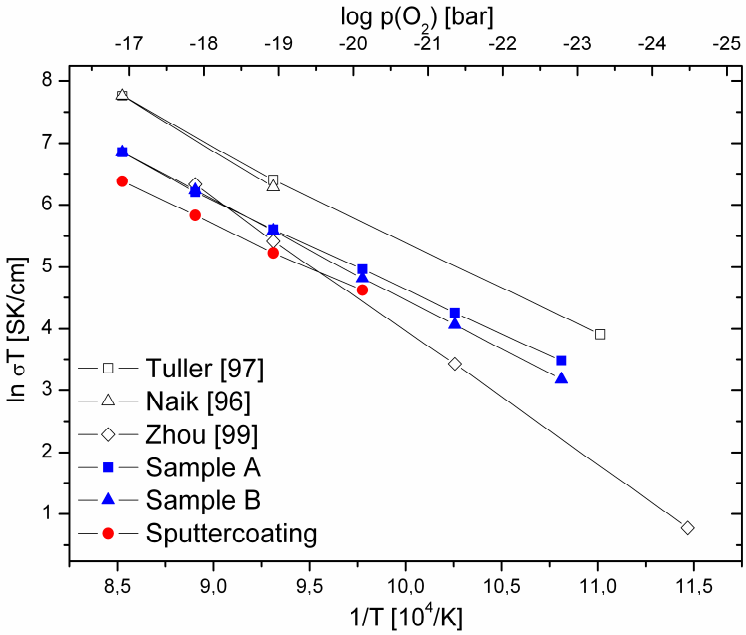

Fig. 7.13: Electronic conductivity of ceria as a function of temperature and pO_2 (referring to equilibrium oxygen partial pressure in Ar-4H_2-2H_2O). Closed symbols correspond to experimental data (blue: bulk, red: sputter coating on Al_2O_3 substrate) open symbols correspond to literature data from [96, 97, 99].

After these studies on bulk ceria and ceria sputtered on inert Al_2O_3 substrates CeO_2 sputter coatings on Crofer 22 APU substrates were investigated with respect to their electric conductivity. The plot in Fig. 7.14 shows the apparent conductivity data for different ceria-based coating systems as a function of temperature. The term "apparent conductivity" is used because, strictly speaking, the measured electrical resistance, from which the conductivity is calculated, corresponds to the sum of the resistances of the CeO_2 coating, the resistance of the oxide scale formed on Crofer 22 APU as well as possible interfacial resistances. Additionally, the resistance of the thermally grown oxide scale on the Crofer 22 APU substrate is the sum of the contribution by the chromia as well as the spinel layer.

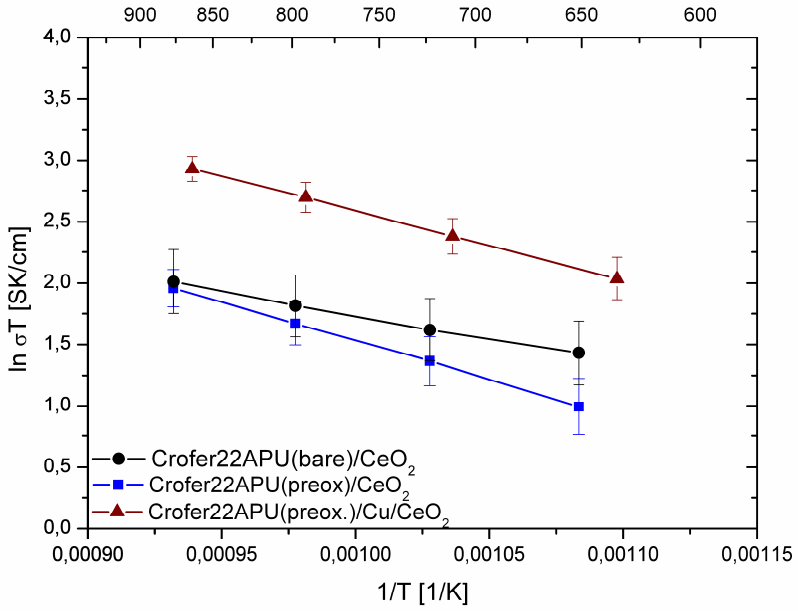

Fig. 7.14: Apparent conductivity of different ceria based coating systems on Crofer 22 APU substrate. CeO_2 on a bare Crofer 22 APU substrate (black), CeO_2 on a pre-oxidised Crofer 22 APU substrate (blue), CeO_2 on a pre-oxidised Crofer 22 APU substrate with an intermediate Cu contact layer below the CeO_2 coating (red). All coatings had a thickness of approximately 3µm.

The curves are the median values of 4 samples from each material combination and it can be seen that the values show some scatter. The difference between CeO_2 coatings on bare and pre-oxidised Crofer are close to the error margin of the experiment. However, it seems that, especially at lower temperatures, the conductivity of the samples with pre-oxidised substrates is lower, which might be attributed to the fact the oxide scale beneath the CeO_2 coating is thicker. On the other hand the intermediate Cu coating between pre-oxidised Crofer 22 APU and the CeO_2 coating clearly had a beneficial effect on the conductivity values as well as the data scatter. With such a coating system ASR values of less than 20mΩ·cm² at 800°C can be achieved.

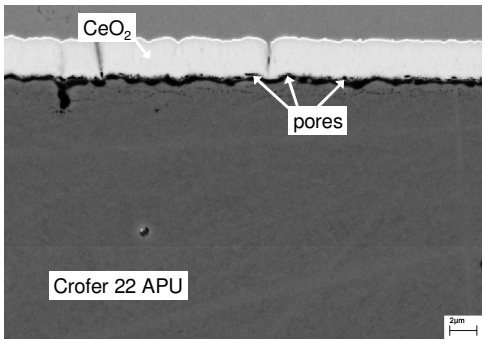

a) KMT(bare)/CeO_2

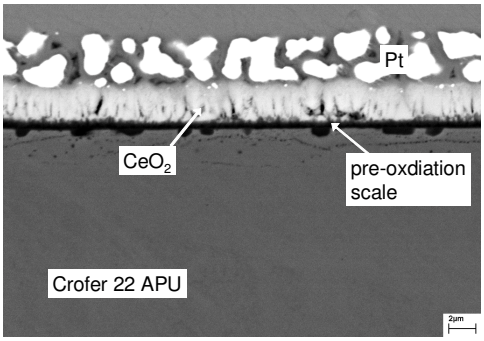

b) KMT(pre-oxidised)/CeO_2

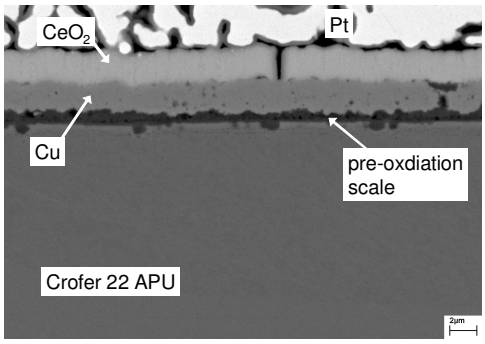

c) KCB(pre-oxidised)/Cu/CeO_2

Fig. 7.15: Cross-sections of selected samples after conductivity measurement. The Pt-paste in Fig. 7.15a spalled off when the sample was taken out of the furnace.

Fig. 7.15a shows a cross-section of one of the samples with a CeO_2 coating on a bare Crofer 22 APU substrate. The coating is dense and shows good contact to the substrate, although a number of pores can be seen at the oxide/coating interface. Fig. 7.15b shows the coating on a pre-oxidised Crofer 22 APU substrate. No pores can be found at the oxide/coating interface, but the ceria coating shows a substantial porosity. This might be related to the fact that, due to whisker formation the surface of the pre-oxidised substrate is less flat than that of a non-oxidised steel substrate. In the case of the intermediate Cu layer (Fig. 7.15c) the CeO_2 layer again has a high density and does not show any porosity. Below the CeO_2 coating the Cu layer can be found which also possesses a high density. Within the Cu layer some oxide nodules can be found but it is believed that these do not have a substantial adverse effect on the electronic conductivity of the sample.

7.4 Anode side protective coatings: Summary

The diffusion of Ni into the interconnect and of Fe, Cr and Mn into the Ni-mesh or Ni base anode may cause problems during SOFC stack operation. A pre-oxidation scale on the interconnect is not capable of blocking interdiffusion because the scale becomes disintegrated in contact with Ni. A similar effect was observed for Ag layers on pre-oxidised steel substrates but not for Cu and Co layers.

A pre-oxidation scale in combination with a Cu coating proved to work as a diffusion barrier, however, due to fast mixing of Cu and Ni it seems doubtful whether in a stack a Cu coating will be effective as interdiffusion barrier due to the large Ni reservoir in the anode. W based coatings show strong interaction with Ni and therefore seem to be unsuitable as a barrier layer.

In contrast ceria based coatings turned out be very effective interdiffusion barrier layers. Ceria possesses good thermodynamic stability in combination with a sufficiently high electrical conductivity. In the current study literature data could be confirmed which stated the electrical conductivity of ceria at 800°C at a pO_2 of 10^{-19}bar to be approximately 0.3S/cm. Similar values could be achieved for thin sputter coatings of ceria.

Interdiffusion studies using a ceria coating between a Crofer 22 APU substrate and a Ni coating indicated no sign of interdiffusion through the ceria coating after 1000h at 800°C. However, the apparent conductivity of ceria coated Crofer 22 APU substrates is much lower than the conductivity of ceria itself. This is due to the fact that the oxide scale will also have a significant contribution to the overall contact resistance. Unfortunately, it was not possible to directly measure the conductivity of oxide scales in Ar-H_2-H_2O atmospheres (see chapter 6.5) but the literature data plotted in Fig. 7.9 indicate that the conductivities of Cr_2O_3 and especially $MnCr_2O_4$ are several orders of magnitude lower than that of ceria. Thus, even though the oxide scale is much thinner than the ceria coating it will have a considerable contribution to the overall resistance. The contact across the substrate/coating interfaces, which turned out be to be poor in some cases, is also going to have some effect. It was shown that a Cu coating below the ceria coating significantly improves the contact which causes the higher conductivity of the samples with CeO_2 interdiffusion barrier and intermediate Cu layer.

8. Conclusions

High Cr ferritic steels are promising candidate construction materials for SOFC interconnects. Numerous stack tests indicated that with steels such as Crofer 22 APU which were specifically designed for the use in SOFCs long term stack operation can be obtained. However, in a number of applications SOFC market requirements demand a reduction of fuel cell size and/or weight and thus of interconnect thickness. However, if thin components are going to be used in the stack, high creep strength interconnect materials will be required.

In the current project it could be shown that the addition of Nb to a ferritic 22%Cr steel causes the formation of Laves phase precipitates which results in an increase of creep strength over several orders of magnitude. The addition of W also has an additional beneficial effect on the creep strength but to a much lesser extent. However, the combined addition of W and Nb results in the formation of much finer Laves phase precipitates than in the case of single Nb additions and consequently the increase in creep strength is even more pronounced.

It is known that manufacturing related impurities even in low concentrations can have a major impact on the oxidation behaviour of the steel. To achieve optimum oxidation properties very low levels of Si and Al are required, which results in high manufacturing costs because the elements are commonly used as de-oxidants in conventional alloy manufacturing. Thus, in the current study the interplay between the Laves phase precipitates and manufacturing related impurities was also investigated. It could be shown out that Si has a high solubility in the Laves phase of the type $Fe_2(Nb,W)$ which results in a low Si activity in the alloy matrix.

If a modified steel is going to be used as SOFC interconnect material it is important to show that the alloy modifications which aimed at increasing the creep strength had no significant adverse effect on any of the SOFC relevant properties. In earlier studies oxidation resistance turned out to be one of the critical aspects. From the present results it could be derived that the addition of W does not have a detrimental effect on the growth rate of the surface oxide while Nb causes substantially increased oxidation rates due to Nb doping of the Cr_2O_3 scale. However, the combined addition of Si and Nb stabilises the Laves phase precipitates which results in an oxidation rate that is similar to that of the reference alloy. Thus, if the amounts of

Nb and Si are carefully adjusted, similar oxidation rates can be obtained as for Crofer 22 APU. However, in combination with a much higher creep strength.

Since the interconnect is exposed not only to air but also to a fuel atmosphere, the developed materials were also tested in Ar-H_2-H_2O. Compared to air the scales formed in this gas exhibit some considerable differences. The scales are more porous and the growth rates are generally lower than those in air. However, it could be shown that the effect of the various alloying elements on the oxidation rates is very similar as in air.

In the course of this study also other SOFC relevant properties such as CTE of the steels and electrical conductivity of the oxide scales were investigated. The experimental results showed that the alloy modifications had no relevant adverse effect on these properties.

If thin components are going to be applied in the SOFC not only creep has to be considered but special emphasis has to be put on the oxidation resistance. It was shown earlier that thin walled components of materials such as Crofer APU exhibit considerably higher oxidation rates than thick walled components. The oxidation results of the new steels indicate that the thickness dependence of the oxidation rate is related to differences in stress relaxation in the scale by metal creep. It was found that materials with high creep strength show no or only very limited thickness dependence of the oxidation rates. It was concluded that the constrained oxide on a high creep strength material exhibits slower growth rates than the scales formed on a weaker material such as Crofer 22 APU, on which the oxide growth stresses are more easily relaxes due to creep of the steel substrate.

Materials compatibility issues are a major problem in the SOFC. The volatility of Cr species on the cathode side is a widely known problem. However, interdiffusion between steel and Ni rich anode or wire mesh is to be of major concern. The investigation of a fuel cell stack showed that interdiffusion of interconnect elements into a Ni-mesh could be observed as well as Ni diffusion into the interconnect where it causes the formation of austenite. The relatively high thermal expansion coefficient of austenite compared to ferrite is expected to deteriorate stack performance during service. Therefore a number of barrier coatings to inhibit interdiffusion processes were evaluated.

The pre-oxidation of the ferritic steel turned out to be not a suitable option to suppress interdiffusion because the oxide scale appeared to become dissolved beneath a Ni coating when exposed in an Ar-H_2-H_2O atmosphere. A similar effect could be observed if a Ag coating is applied on the pre-oxidised steel. This effect was not observed if a Cu or Co layer is used. However, metallic coatings seem to be unsuitable as a barrier coating due to fast dissolution in Ni which is likely to cancel the effect of a barrier coating if the Ni reservoir in the anode or wire mesh is sufficiently large.

On the contrary, CeO_2 proved to be an effective diffusion barrier with sufficiently high electrical conductivity for SOFC purposes. It turned out that interfacial resistances as well as the thermally grown oxide on Crofer 22 APU have a significant effect on the electrical conductivity of the total system. A Cu contact coating between CeO_2 and the substrate had a beneficial effect because it reduced the interfacial resistances due to suppression of void formation at the interface between CeO_2 layer and growing oxide scale.

In summary, the modification of Crofer 22 APU by a suitable combination of the alloying additions Nb, W and Si allows the design of lightweight stacks by using thinner interconnect plates than was possible with the standard material. Further, a diffusion barrier coating was developed for the anode side of the cell which is able to limit interdiffusion between steel and Ni rich anodes or wire mesh which is expected to be of great importance for the overall stack performance.

9. References

1. N.N., *World Energy Outlook 2007 - Executive Summary*. 2007, IEA.
2. B. Eliasson and U. Bossel. *The Future of the Hydrogen Economy: Bright or Bleak?*, *THE FUEL CELL WORLD*, 2002, Lucerne, Switzerland.
3. F.J. Pirón Abellán and W.J. Quadakkers, *Development of Ferritic Steels for Application as Interconnect Materials for Intermediate Temperature Solid Oxide Fuel Cells (SOFCs)*, Berichte des Forschungszentrums Jülich, JUEL-4170,Jülich, Germany, ISSN 0944-2952, 2005.
4. W.J. Quadakkers, J. Pirón Abellán, V. Shemet, and L. Singheiser, *Metallic interconnectors for solid oxide fuel cells - a review,* Materials at High Temperatures, 2003, **20**(2), p. 115-127.
5. P. Huczkowski, N. Christiansen, V. Shemet, L. Niewolak, J. Pirón Abellán, L. Singheiser, and W.J. Quadakkers, *Growth mechanisms and electrical conductivity of oxide scales on ferritic steels proposed as interconnect materials for SOFC's,* Fuel Cells, 2006, **6**(2), p. 93-99.
6. P. Huczkowski and W.J. Quadakkers, *Effect of geometry and composition of Cr steels on oxide sale properties relevant for interconnector applications in Solid Oxide Fuel Cells (SOFCs)*, Schriften des Forschungszentrums Jülich, Reihe Energietechnik/Energy Technology 65, Jülich Germany, ISSN 1433-5522, 2007.
7. J. Zurek, G.H. Meier, E. Essuman, M. Hansel, L. Singheiser, and W.J. Quadakkers, *Effect of specimen thickness on the growth rate of chromia scales on Ni-base alloys in high- and low-pO2 gases,* Journal of Alloys and Compounds, (In Press, Corrected Proof), p. doi:10.1016/j.jallcom.2007.12.015.
8. A.B. Stambouli and E. Traversa, *Solid oxide fuel cells (SOFCs): a review of an environmentally clean and efficient source of energy,* Renewable and Sustainable Energy Reviews, 2002, **6**(5), p. 433-455.
9. A.J. Appleby and F.R. Foulkes, *Fuel Cell Handbook* Krieger Publishing, 1993, Malabar, US.
10. G. Hoogers, *Fuel Cells* CRC Press, 2003, Boca Raton, FL.
11. J. Larminie and A. Dicks, *Fuel Cell Sytems Explained* John Wiley & Sons, 2003, Chichester, UK.
12. N.Q. Minh, *Solid oxide fuel cell technology-features and applications,* Solid State Ionics, 2004, **174**(1-4), p. 271-277.
13. S.P.S. Badwal and K. Foger, *Solid oxide electrolyte fuel cell review,* Ceramics International, 1996, **22**(3), p. 257-265.
14. A.B. Stambouli and E. Traversa, *Fuel cells, an alternative to standard sources of energy,* Renewable and Sustainable Energy Reviews, 2002, **6**(3), p. 295-304.
15. L. Antoni, *Materials for Solid Oxide Fuel Cells : the challenge of their stability,* Materials Science Forum, 2004, **461-464**, p. 1073-1089.
16. S.C. Singhal and K. Kendall, eds. *High Temperature Solid Oxide Fuel Cells: Fundamentals, Design and Applications*, 2006, Elsevier, Oxford, UK.
17. K. Chen, Z. Lu, X. Chen, N. Ai, X. Huang, X. Du, and W. Su, *Development of LSM-based cathodes for solid oxide fuel cells based on YSZ films,* Journal of Power Sources, 2007, **172**(2), p. 742-748.
18. W.Z. Zhu and S.C. Deevi, *A review on the status of anode materials for solid oxide fuel cells,* Materials Science and Engineering A, 2003, **362**(1-2), p. 228-239.
19. J.W. Fergus, *Metallic interconnects for solid oxide fuel cells,* Materials Science and Engineering A, 2005, **397**(1-2), p. 271-283.

20. J.W. Fergus, *Lanthanum chromite-based materials for solid oxide fuel cell interconnects,* Solid State Ionics, 2004, **171**(1-2), p. 1-15.
21. S.M. Haile, *Fuel cell materials and components,* Acta Materialia, 2003, **51**(19), p. 5981-6000.
22. F. Tietz, H.P. Buchkremer, and D. Stöver, *10 Years of materials research for solid oxide fuel cells at Forschungszentrum Jülich,* Journal of Electroceramics, 2006, **17**(2-4), p. 701-707.
23. G. Schiller, R.H. Henne, M. Lang, R. Ruckdaschel, and S. Schaper, *Development of vacuum plasma sprayed thin-film SOFC for reduced operating temperature,* Fuel Cells Bulletin, 2000, **3**(21), p. 7-12.
24. N. Birks, G.H. Meier, and F.S. Pettit, *Introduction to the High Temperature Oxidation of Metals* Cambridge University Press, 2006, Cambridge.
25. C. Wagner, *Beitrag zur Theorie des Anlaufvorgangs,* Z. Phys. Chem., 1933, **21**, p. 25-41.
26. P. Kofstad, *High Temperature Corrosion* Elsevier, 1988, Barking, UK.
27. I.G. Wright, *Metals Handbook 9th Edition*, Vol. 13 Corrosion, 1987, Metals Park, OH.
28. P. Kofstad, *Protective Properties of Chromia and Alumina Scales,* Materials Science Forum, 1996, **154**, p. 99-108.
29. W.J. Quadakkers, H. Holzbrecher, K.G. Briefs, and H. Beske, *Differences in growth mechanisms of oxide scales formed on ODS and conventional wrought alloys,* Oxidation of Metals, 1989, **32**(1), p. 67-88.
30. K. Kofstad and K.P. Lillerud, *On High Temperature Oxidation of Chromium,* J. Electrochem. Soc. , 1980, **127**.
31. A. Holt and P. Kofstad, *Electrical conductivity and defect structure of Cr_2O_3. II. Reduced temperatures (<~1000°C),* Solid State Ionics, 1994, **69**(2), p. 137-143.
32. A. Holt and P. Kofstad, *Electrical conductivity of Cr_2O_3 doped with TiO_2,* Solid State Ionics, 1999, **117**(1-2), p. 21-25.
33. N. Sakai, T. Horita, Y.P. Xiong, K. Yamaji, H. Kishimoto, M.E. Brito, H. Yokokawa, and T. Maruyama, *Structure and transport property of manganese-chromium-iron oxide as a main compound in oxide scales of alloy interconnects for SOFCs,* Solid State Ionics, 2005, **176**(7-8), p. 681-686.
34. B. Chalmers, *Pysical Metallurgy* John Wiley & Sons, 1959, New York.
35. J.K. Tien and G.S. Ansell, eds. *Alloy and Microstructural Design*, 1976, Academic Press, London, UK.
36. H.-J. Bargel and G. Schulze, *Werkstoffkunde* Springer, 2000, Berlin.
37. R.W.K. Honeycombe, *Steels Microstructure and Properties* Edward Arnold, 1987, London, UK.
38. G.F. Vander Voort, *Embrittlement of Steels*, ASM Handbook, Vol. 1 Properties and Selection: Irons, Steels and High-Performance Alloys, 1990, Materials Park, OH 708-711.
39. H. Okamoto, ed. *Phase Diagrams of Binary Iron Alloys*, 1993, ASM Materials Park, US.
40. *Binary Alloy Phase Diagrams*, ASM International: Materials Park, OH.
41. J.P.P. Huijsmans, F.P.F. van Berkel, and G.M. Christie, *Intermediate temperature SOFC - a promise for the 21st century,* Journal of Power Sources, 1998, **71**(1-2), p. 107-110.
42. B.C.H. Steele, *Materials for IT-SOFC stacks: 35 years R&D: the inevitability of gradualness?,* Solid State Ionics, 2000, **134**(1-2), p. 3-20.
43. Z. Yang, P. Singh, J.W. Stevenson, and G.G. Xia, *Investigation of Modified Ni–Cr–Mn Base Alloys for SOFC Interconnect Applications* J. Electrochem. Soc., 2006, **153**.

44. S.C. Singhal, *Advances in solid oxide fuel cell technology,* Solid State Ionics, 2000, **135**(1-4), p. 305-313.
45. A.C. Muller, D. Herbstritt, and E. Ivers-Tiffee, *Development of a multilayer anode for solid oxide fuel cells,* Solid State Ionics, 2002, **152-153**, p. 537-542.
46. W.J. Quadakkers, J. Pirón Abellán, and V. Shemet, *Metallic materials in solid oxide fuel cells,* Mater. Res., 2004, **7**.
47. R. Hojda and W.J. Quadakkers, *Verbessertes Produkt Crofer 22 APU,* ThyssenKrupp techforum, 2005, p. 22.
48. N.N., *Crofer 22 APU Material Data Sheet 4046*. Dec 2006, TyssenKrupp VDM Werdohl, Germany.
49. V.A.C. Haanappel, V. Shemet, S.M. Gross, T. Koppitz, N.H. Menzler, M. Zahid, and W.J. Quadakkers, *Behaviour of various glass-ceramic sealants with ferritic steels under simulated SOFC stack conditions,* Journal of Power Sources, 2005, **150**, p. 86-100.
50. N.H. Menzler, D. Sebold, M. Zahid, S.M. Gross, and T. Koppitz, *Interaction of metallic SOFC interconnect materials with glass-ceramic sealant in various atmospheres,* Journal of Power Sources, 2005, **152**, p. 156-167.
51. P. Batfalsky, V.A.C. Haanappel, J. Malzbender, N.H. Menzler, V. Shemet, I.C. Vinke, and R.W. Steinbrech, *Chemical interaction between glass-ceramic sealants and interconnect steels in SOFC stacks,* Journal of Power Sources, 2006, **155**(2), p. 128-137.
52. J.W. Fergus, *Effect of cathode and electrolyte transport properties on chromium poisoning in solid oxide fuel cells,* International Journal of Hydrogen Energy, 2007, **32**(16), p. 3664-3671.
53. M. Stanislowski, J. Froitzheim, L. Niewolak, W.J. Quadakkers, K. Hilpert, T. Markus, and L. Singheiser, *Reduction of chromium vaporization from SOFC interconnectors by highly effective coatings,* Journal of Power Sources, 2007, **164**(2), p. 578-589.
54. T. Franco, R. Ruckdäschel, M. Lang, G. Schiller, and P. Szabo. *Diffusion and Protecting Barrier Layers in a Substrate Supported SOFC Concept*, *7th European Fuel Cell Forum*, 2006, Lucerne: E-Proceedings of the 7th European Fuel Cell Foum.
55. S.J. Visco, C.P. Jacobson, I. Villareal, A. Leming, Y. Matus, and L.C.D. Jonghe. *Inhibition of Diffusion between Metallic Substrates and Ni-YSZ-Anodes during Sintering*, *Solid Oxide Fuel Cells-VIII (SOFC-VIII)*, 2003: Electrochemical Society, Pennington, NJ.
56. P. Villars , A. Prince , and H. Okamoto *Handbook of ternary alloy phase diagrams*, Handbook of ternary alloy phase diagrams, Vol. 7 ASM International, 1995, Materials-Park, OH.
57. K. Yamamoto, *Design of Laves phase strengthened ferritic heat resisting steels in the Fe-Cr-Nb(-Ni) system,* Materials Science & Engineering. A, Structural materials, 2002, **329**, p. 249-254.
58. P. Metzger, K.A. Friedrich, H. Muller-Steinhagen, and G. Schiller, *SOFC characteristics along the flow path,* Solid State Ionics, 2006, **177**(19-25), p. 2045-2051.
59. W.J. Quadakkers and H. Viefhaus. *The Application of Surface Analysis Techniques in High Temperature Corrosion Research*, *EFC Workshop "Methods and Testing in High Temperature Corrosion"*, 1994, Frankfurt, Germany.
60. *FACTsage Software*, GTT Technologies: Aachen, Germany.
61. P. Huczkowski, S. Ertl, J. Pirón-Abellán, N. Christiansen, T. Höfler, V. Shemet, L. Singheiser, and W.J. Quadakkers, *Effect of Component Thickness on Lifetime and*

Oxidation Rate of Chromia Forming Ferritic Steels in Low and High pO2-Environments, Materials at high temperatures, 2006, **22**, p. 253-262.
62. P.J. Ennis and W.J. Quadakkers. *Corrosion and Creep of Nickel-Base Alloys in Steam Reforming Gas High Temperature Alloys - Their Exploitable Potential*, 1985, Petten, NL: Elsevier, London.
63. J. Hammer, S. Laney, R. Jackson, K. Coyne, F. Pettit, and G. Meier, *The Oxidation of Ferritic Stainless Steels in Simulated Solid-Oxide Fuel-Cell Atmospheres,* Oxidation of Metals, 2007, **67**(1), p. 1-38.
64. A.N. Hansson and M.A.J. Somers, *Influence of the oxidation environment on scale morphology and oxidation rate of Fe–22Cr,* Materials at High Temperatures, **22**(3/4), p. 223-229.
65. L. Mikkelsen and S. Linderoth, *High temperature oxidation of Fe-Cr alloy in O_2-H_2-H_2O atmospheres; microstructure and kinetics,* Materials Science and Engineering A, 2003, **361**(1-2), p. 198-212.
66. A. Naoumidis, H.A. Schulze, W. Jungen, and P. Lersch, *Phase studies in the chromium-manganese-titanium oxide system at different oxygen partial pressures,* Journal of the European Ceramic Society, 1991, **7**(1), p. 55-63.
67. S. Ertl, *Untersuchung zur oxidationsbedingten Lebensdauer von Chromstählen für die Anwendung in der Hochtemperaturbrennstoffzelle (SOFC),* PhD Thesis*,* 2006, RWTH Aachen, Germany
68. A. Galerie, *Stress and Adhesion of Chromia-Rich Scales on Ferritic Stainless Steels in Relation with Spallation,* Materials Research, 2004, **7**(1), p. 81-88.
69. H.E. Evans, *Stress effects in high temperature oxidation of metals,* International material reviews, 1995, **40**, p. 1-40.
70. B. Panicaud, J.L. Grosseau-Poussard, and J.F. Dinhut, *On the growth strain origin and stress evolution prediction during oxidation of metals,* Applied Surface Science, 2006, **252**(16), p. 5700-5713.
71. H.E. Evans. *Interfacial Crack Growth During Temperature Changes*, *Cyclic Oxidation of High Temperature Materials*, 1999, Frankfurt/Main.
72. C.C. Dollins and M. Jursich, *A model for the oxidation of zirconium-based alloys,* Journal of Nuclear Materials, 1983, **113**(1), p. 19-24.
73. H. Mehrer, *The Effect of Pressure on Diffusion,* Defect and Diffusion Forum, 1996, **129-130**, p. 57-76.
74. H.E. Evans, D.J. Norfolk, and T. Swan, *Perturbation of Parabolic Kinetics Resulting from the Accumulation of Stress in Protective Oxide Layers* J. Electrochem. Soc., 1978, **125**(7), p. 1180-1185.
75. H.E. Evans, D.J. Norfolk, and T. Swan, *Perturbation of Parabolic Kinetics Resulting from the Accumulation of Stress in Protective Oxide Layers,* J. Electrochem. Soc., 1978, **125**(7), p. 1180-1185.
76. G.V. Raynor and V.G. Rivlin, *Phase Equilibria in Iron Ternary Alloys* The Institute of Metals, 1988, London, UK.
77. *ThermoCalc*, Thermo-Calc Software AB: Stockholm, SE.
78. F.-H. Lu, M.L. Newhouse, R. Dieckmann, and J. Xue, *Platinum-a non-inert material reacting with oxides,* Solid State Ionics, 1995, **75**, p. 187-192.
79. D.G. Robertson and S.R. Holdsworth, eds. *ECCC Data Sheets 2005*, ETD Ltd, Surrey, UK.
80. N.N., *Crofer 22 APU Material Data Sheet 4046*. July 2005, TyssenKrupp VDM Werdohl, Germany.

81. O.A. Marina, N.L. Canfield, and J.W. Stevenson, *Thermal, electrical, and electrocatalytical properties of lanthanum-doped strontium titanate,* Solid State Ionics, 2002, **149**(1-2), p. 21-28.
82. M. Ueda and H. Taimatso. *Thermal Expansivity and High-Temperature Oxidation Resistance of Fe-Cr-W Alloys Developed for a Metallic Separator of SOFC*, *4th European Solid Oxide Fuel Cell Forum*, 2000, Lucerne, Switzerland.
83. M. Ueda and H. Taimatso, *Thermal Expansivity and High-Temperature Oxidation Resistance of Fe-Cr-W Alloys,* Materials Transactions JIM, 1999, **40**(12), p. 1390-1395.
84. M. Hänsel, W.J. Quadakkers, and D.J. Young, *Role of Water Vapor in Chromia-Scale Growth at Low Oxygen Partial Pressure,* Oxidation of Metals, 2003, **59**(3), p. 285-301.
85. V. Shemet, *unpublished results*, 2007, Forschungszentrum Jülich
86. L. Niewolak, W.J. Quadakkers, and L. Singheiser, *Interconnector for a Fuel Cell Stack, and Method for Production*, Deutsche Patentanmeldung, DE 10 2006 024 039 A1 (2006)
87. E. Fromm, *Gases and Carbon in Metals*, Pysics Data Fachinformationszentrum Energie-Physik-Mathematik GmbH, Karlsruhe, 1982.
88. A.D. Kidson, *The diffusion of H, D, and T in solid metals*, Landolt Börnstein, ed. H. Mehrer, Vol. 26 Springer, 1990, Berlin.
89. A. LeClaire, *The diffusion of H, D, and T in solid metals*, Landolt Börnstein, ed. H. Mehrer, Vol. 26 Springer, 1990, Berlin.
90. Q.X. Fu, F. Tietz, and D. Stöver, *$La_{0.4}Sr_{0.6}Ti_{1-x}Mn_xO_{3-\delta}$ Perovskites as Anode Materials for Solid Oxide Fuel Cells,* J. Electrochem. Soc., 2006, **153**(4), p. D74-D83.
91. S. Hui and A. Petric, *Conductivity and stability of $SrVO_3$ and mixed perovskites at low oxygen partial pressures,* Solid State Ionics, 2001, **143**(3-4), p. 275-283.
92. S. Hui and A. Petric, *Electrical Properties of Yttrium-Doped Strontium Titanate under Reducing Conditions,* J. Electrochem. Soc., 2002, **149,**(1), p. J1-J10.
93. S. Hui and A. Petric, *Electrical conductivity of yttrium-doped $SrTiO_3$: influence of transition metal additives,* Materials Research Bulletin, 2002, **37**(7), p. 1215-1231.
94. T. Kolodiazhnyi and A. Petric, *The Applicability of Sr-deficient n-type $SrTiO_3$ for SOFC Anodes,* Journal of Electroceramics, 2005, **15**(1), p. 5-11.
95. J.F. Marucco, J. Gautron, and P. Lemasson, *Thermogravimetric and electrical study of non-stoichiometric titanium dioxide TiO_{2-x}, between 800 and 1100°C,* Journal of Physics and Chemistry of Solids, 1981, **42**(5), p. 363-367.
96. I.K. Naik and T.Y. Tien, *Electrical Conduction in Nb_2O_5-Doped Cerium Dioxide,* J. Electrochem. Soc., 1979, **126**(4), p. 562-566.
97. H.L. Tuller and A.S. Nowick, *Defect Structure and Electrical Properties of Nonstoichiometric CeO_2 Single Crystals,* J. Electrochem. Soc., 1979, **126**(2), p. 209-217.
98. M. Mogensen, N.M. Sammes, and G.A. Tompsett, *Physical, chemical and electrochemical properties of pure and doped ceria,* Solid State Ionics, 2000, **129**(1-4), p. 63-94.
99. X.-D. Zhou, W. Huebner, and H.U. Anderson, *Size Effect on the Electronic Properties of Doped and Undoped Ceria,* Defect and Diffusion Forum, 2005, **242-244**, p. 277-289.
100. V. Raghavan, *Phase Diagrams of Ternary Iron Alloys* Indian Institute of Metals, 1987.
101. P. Villars , A. Prince , and H. Okamoto *Handbook of ternary alloy phase diagrams*, Handbook of ternary alloy phase diagrams, Vol. 8 ASM International, 1995, Materials-Park, OH.

10. Appendix

2 mm	Cr	Mn	La	Ti	Nb	W	Al	Si	other	16mm
JDA	22.5	0.42	0.09	0.05	-	-	0.12	0.1		-
KCB	22.2	0.45	0.10	0.07	-	-	0.01	0.02		-
KCF	22.46	0.49	0.03	0.07	1.19	-	0.15	0.02		KCA
KCL	22.23	0.52	0.16	0.15	1.11	-	0.001	0.02		KCM
KCO	22.7	0.52	0.15	0.12	1.07	-	0.15	0.07		KCN
KCR	23.2	0.53	0.16	0.06	-	-	0.006	0.03		KCP
KCS	22.2	0.5	0.12	0.1	1.05	-	0.012	0.25		KCK
KCW	22.3	0.51	0.12	0.1	-	0.9	0.01	-		KCU
KDN	20.7	0.53	0.13	0.11	-	2.7	0.01	0.06		KDM
KMT	22.7	0.39	0.05	0.08	-	-	<0.01	<0.01		-
KSY	22.6	0.45	0	0.04	0.57	1.75	0.003	0.25		KSX
KTA	22.5	0.44	0.09	0.07	1	-	0.006	0.42		KSZ
KUA	22.3	0.43	0.06	0.06	0.48	2.02	0.009	0.24		KUB
KYU	22.4	0.40	0.01	0.05	-	-	<0.01	0.03	2.0 Mo	
KYW	23.1	0.41	0.13	0.05	-	-	<0.01	0.02	0.5 V	-
LJF	22.6	0.46	0.09	0.07	-	4.91	0.01	0.28		LJG
LJH	22.7	0.47	0.15	0.06	-	7.2	0.01	0.25		LJK
LJN	18.5	0.44	0.12	0.06	0.51	1.88	0.01	0.27		LJO
LWU	22.4	<0.01	<0.01	<0.01	1.0	1.5	<0.01	0.63		-

Table 10: Composition of the investigated materials in wt% according to ICP-OES analysis measured in the central division of analytical chemistry (ZCH) at FZJ. The P concentration in all alloys was <0.01%. Data for JDA and KCB were taken from reference [6]. All data are given in wt%.

2 mm	C	S	N	O	16mm
JDA	0.008	<0.001	0.0113	0.0046	-
KCB	0.017	0.02	0.0023	0.011	-
KCL	0.007	0.002	0.0145	0.0062	KCM
KCF	0.011	0.002	0.0725	0.0036	KCA
KCO	0.0005	0.0008	0.0187	0.0045	KCN
KCR	0.01	0.001	0.0076	0.0046	KCP
KCS	0.01	0.002	0.0151	0.0065	KCK
KCW	0.013	0.002	0.0151	0.0067	KCU
KDN	0.009	0.002	0.0056	0.0049	KDM
KMT	0.001	0.001	0.0075	0.107	-
KSY	0.003	0.003	0.0112	0.0085	KSX
KTA	0.003	0.002	0.0153	0.0068	KSZ
KUA	0.005	0.001	0.0051	0.0077	KUB
KYU	0.002	0.003	0.0062	0.0025	-
KYW	0.002	0.001	0.0068	0.0023	-
LJF	0.0015	<0.0005	0.0036	0.0071	LJG
LJH	0.0010	0.0011	0.0050	0.0071	LJK
LJN	0.0011	0.0012	0.0055	0.0047	LJO
LWU	0.004	0.0042	0.0004	0.0454	-

Table 11: Impurities in the investigated materials in wt% according to IR spectroscopy measured in the central division of analytical chemistry (ZCH) at FZJ. Data for JDA and KCB were taken from [6].

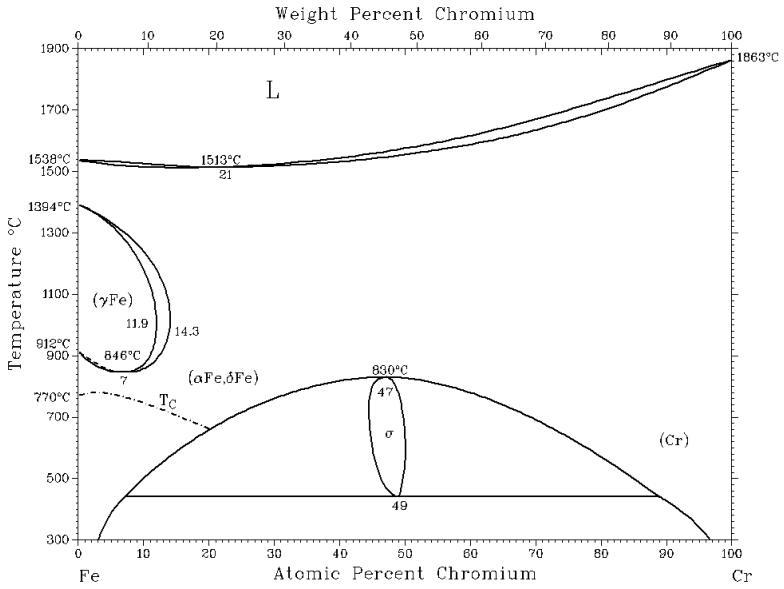

Fig. 10.1: Cr-Fe binary phase diagram [40]

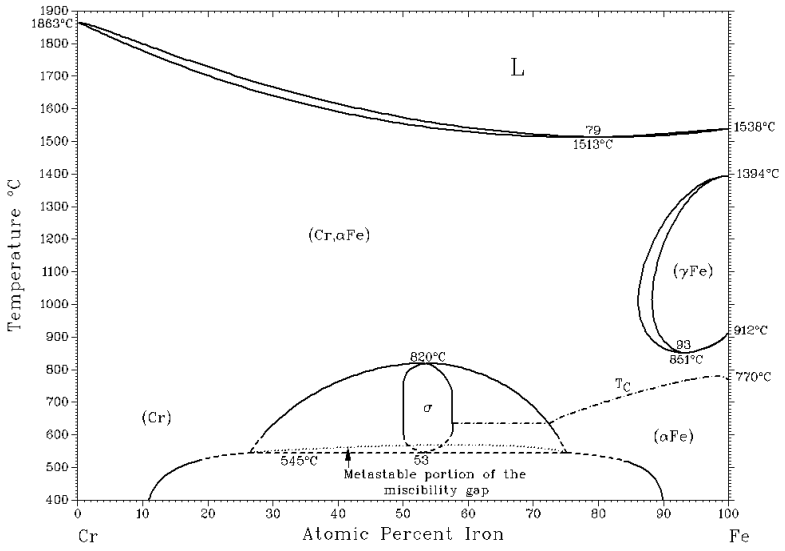

Fig. 10.2: Cr-Fe binary phase diagram published in 1993 [40]

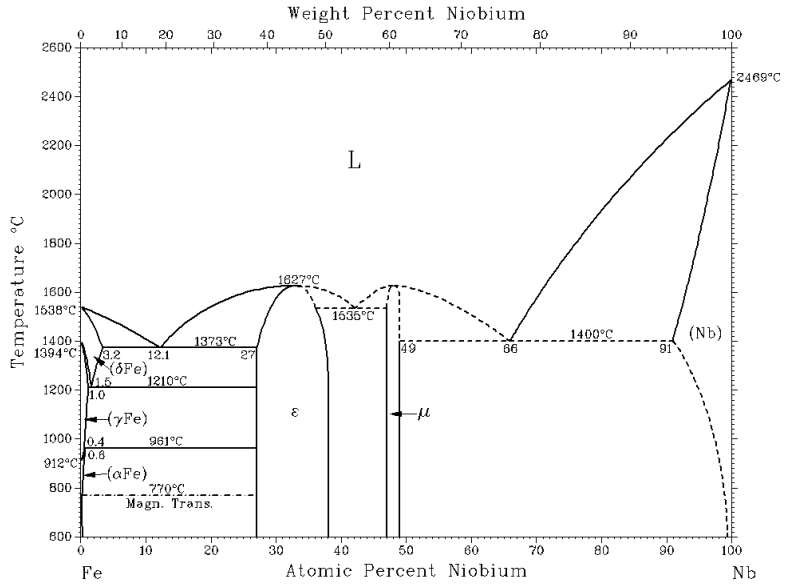

Fig. 10.3. Fe-Nb binary phase diagram [40]

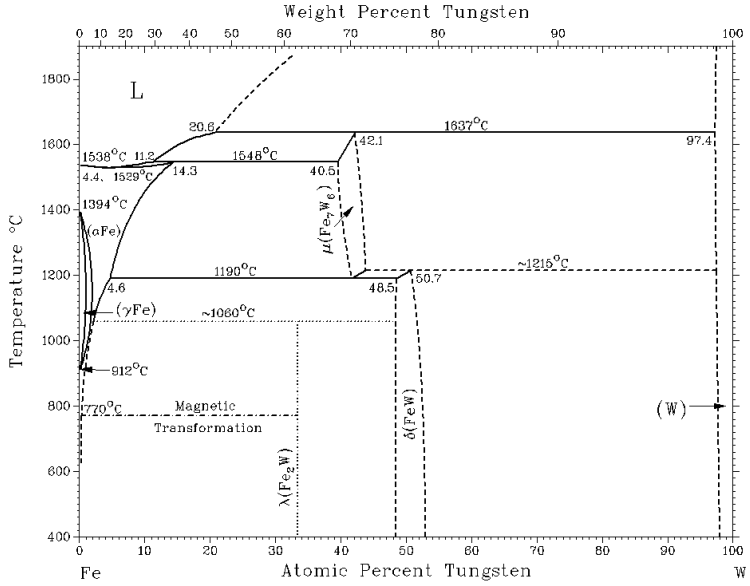

Fig. 10.4: Fe-W binary phase diagram [40]

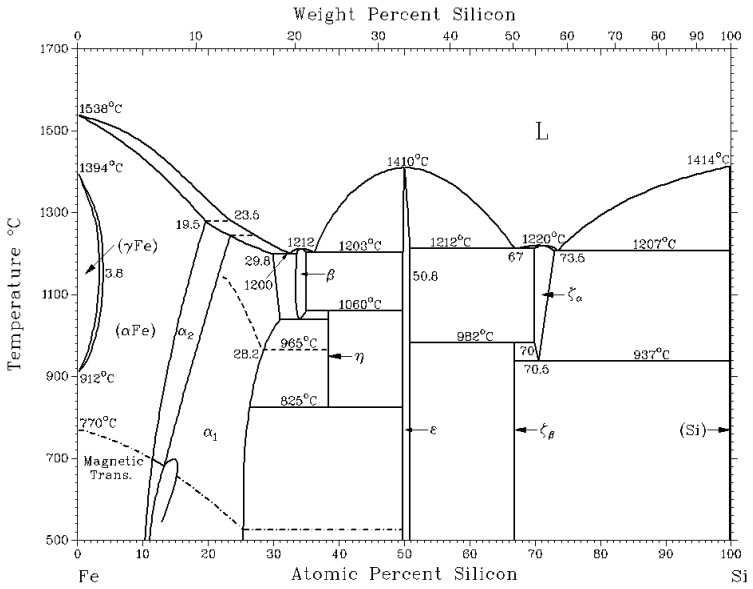

Fig. 10.5: Fe-Si binary phase diagram [40]

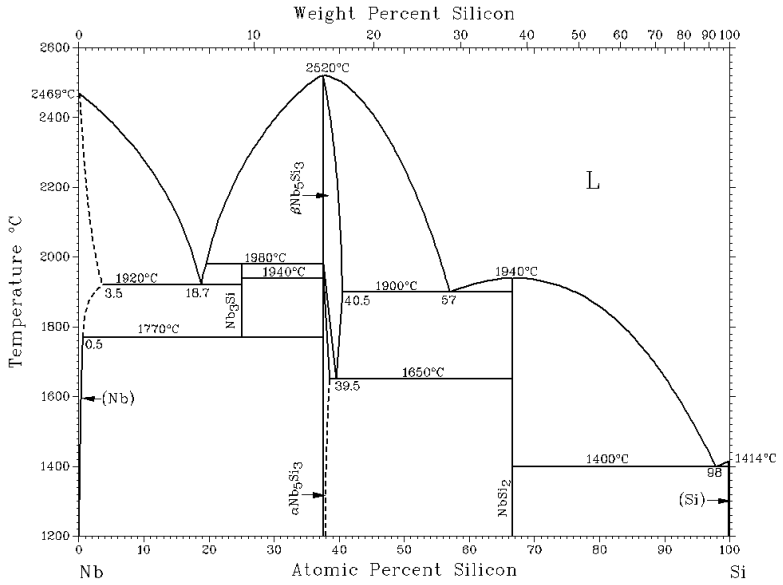

Fig. 10.6: Nb-Si binary phase diagram [40]

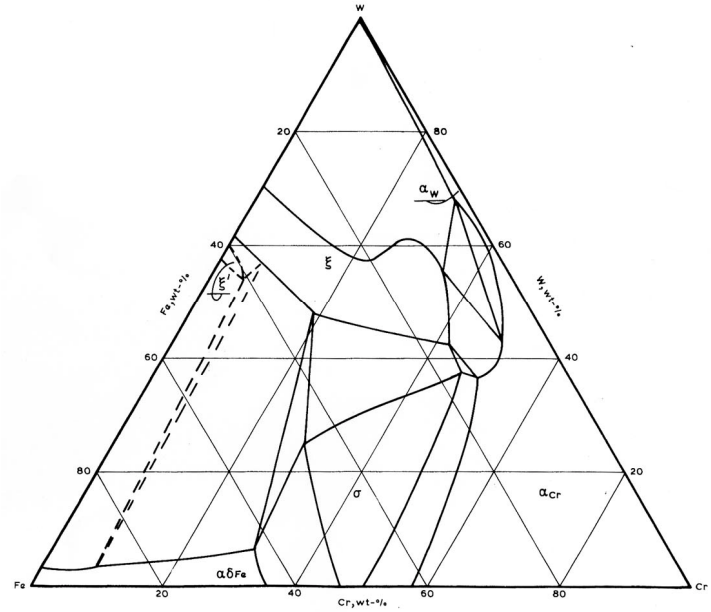

Fig. 10.7: Cr-Fe-W ternary phase diagram at 600°C [76]

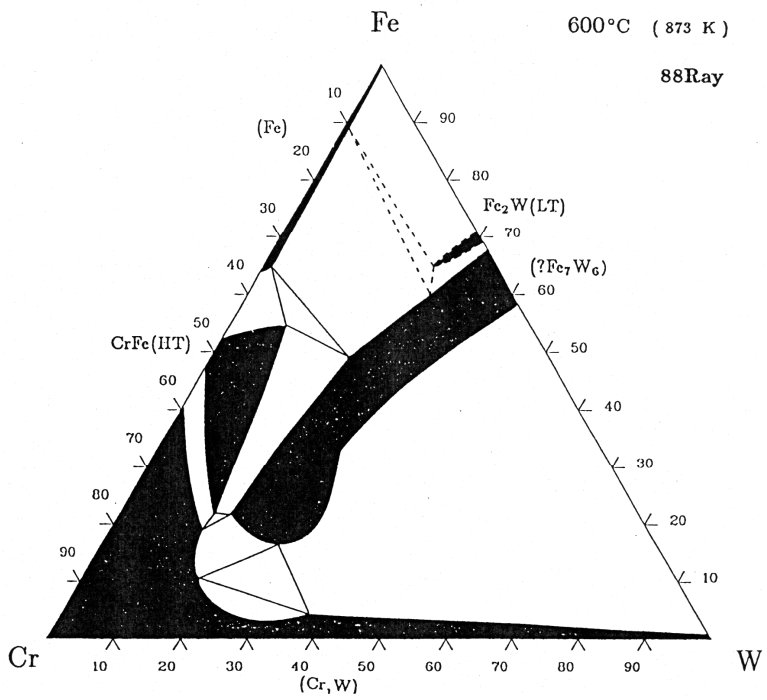

Fig. 10.8: Cr-Fe-W ternary phase diagram at 600°C [56]

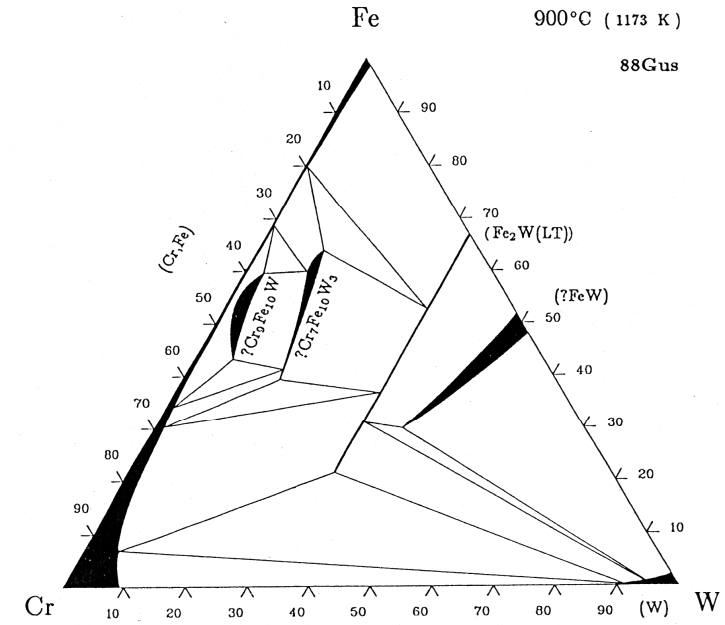

Fig. 10.9: Cr-Fe-W phase ternary diagram at 900°C [56]

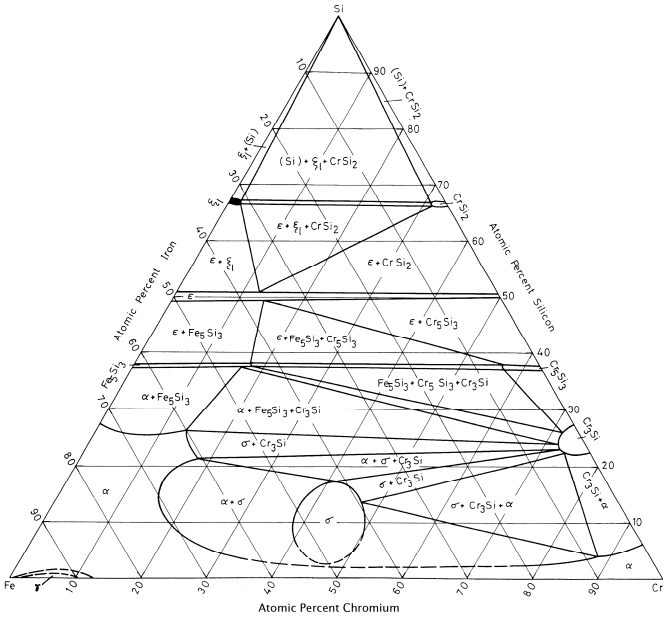

Fig. 10.10: Cr-Fe-Si ternary phase diagram at 900°C [100]

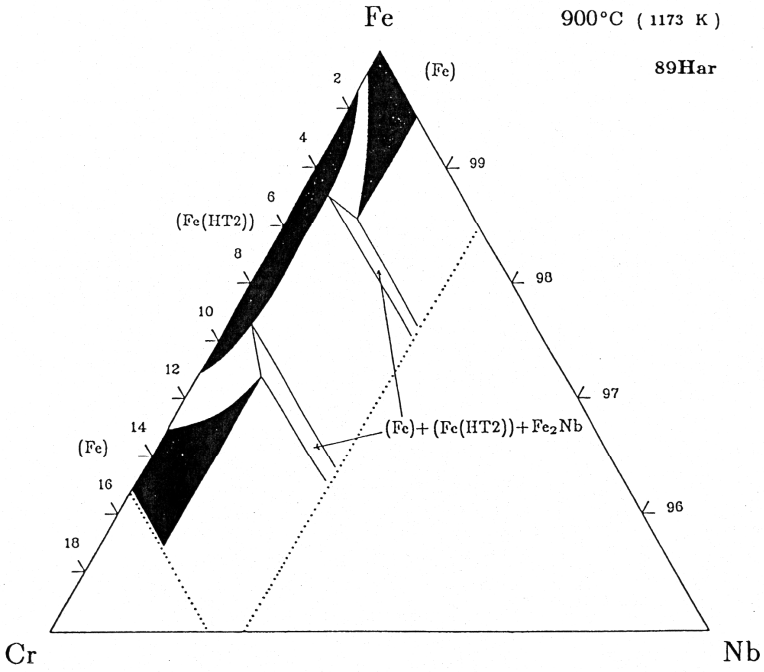

Fig. 10.11: Cr-Fe-Nb ternary phase diagram at 900°C [56]

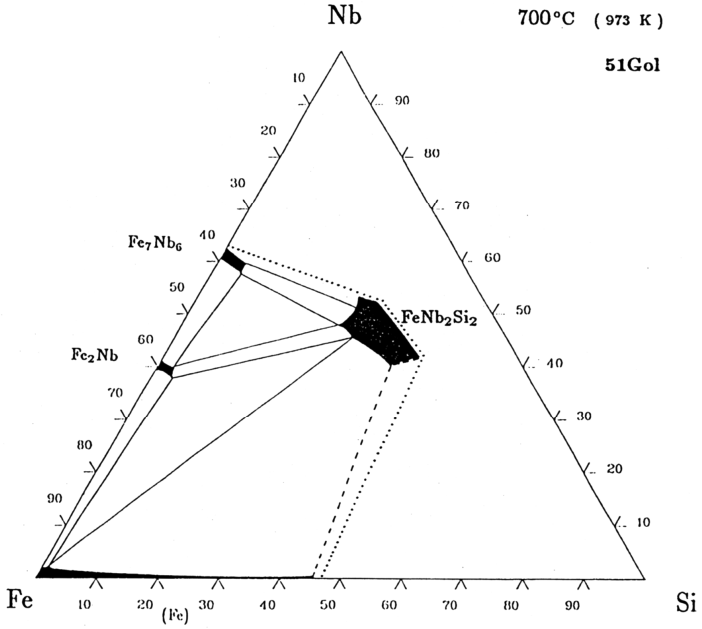

Fig. 10.12: Cr-Fe-Nb ternary phase diagram at 700°C [101]

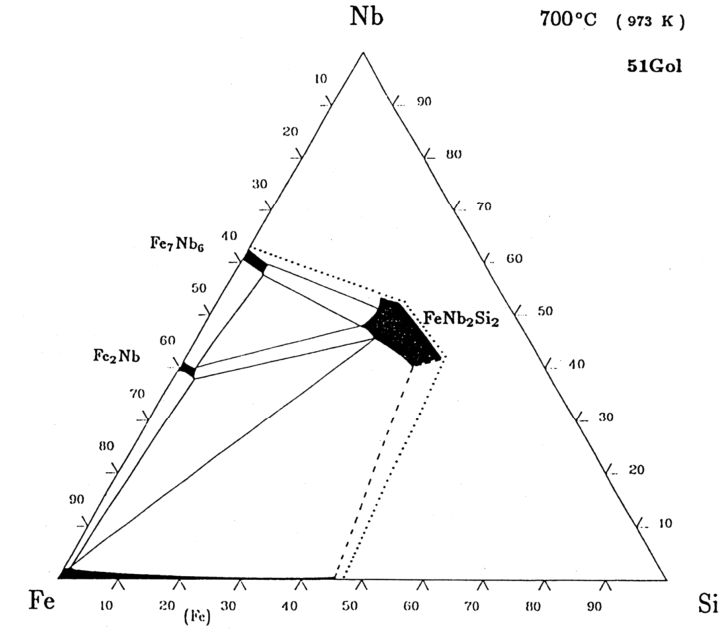

Fig. 10.13: Fe-Nb-Si ternary phase diagram at 700°C [101]

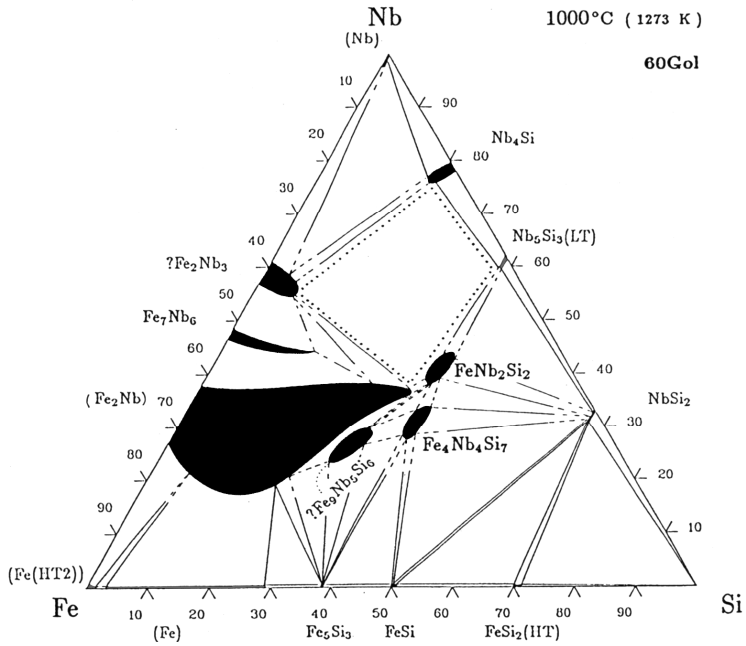

Fig. 10.14: Fe-Nb-Si ternary phase diagram at 1000°C [101]

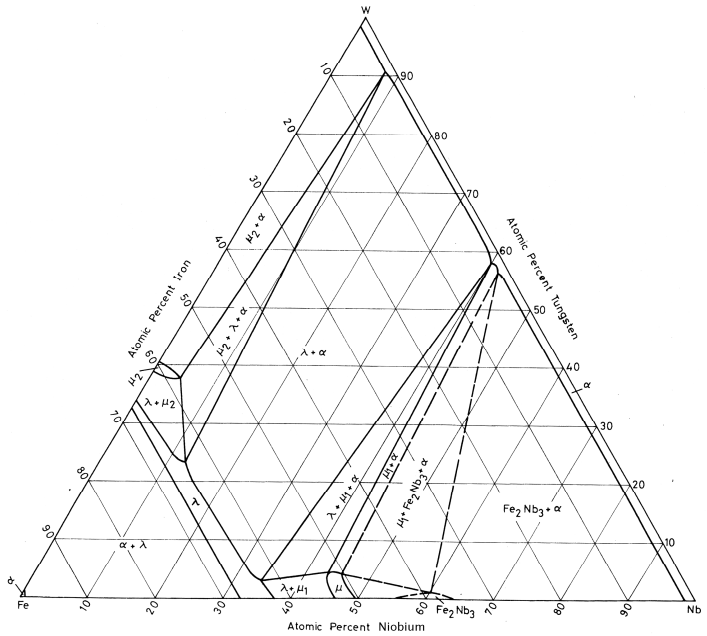

Fig. 10.15: Fe-Nb-W ternary phase diagram at 900°C [100]

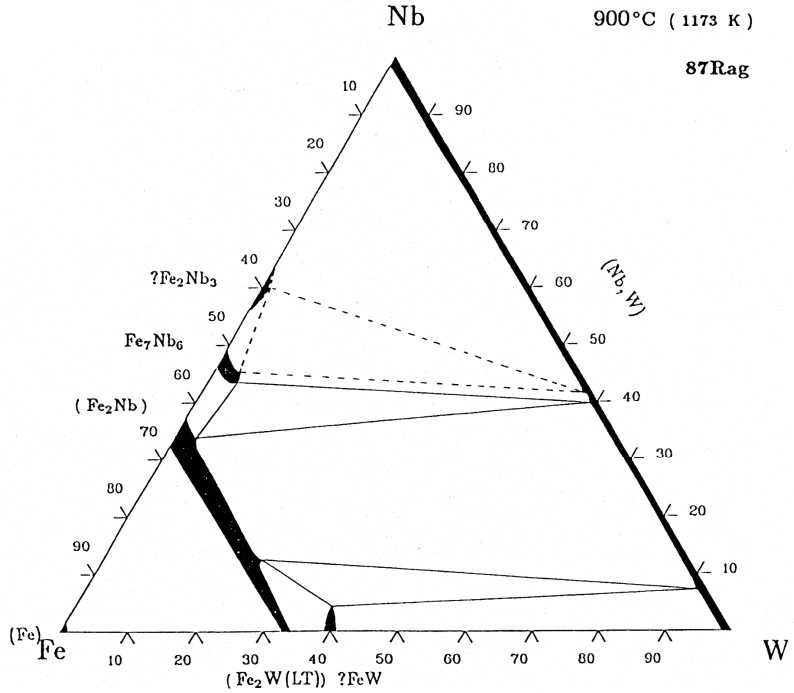

Fig. 10.16: Fe-Nb-W ternary phase diagram at 900°C [101]

Acknowledgements

I would like to thank Prof. L. Singheiser and W.J. Quadakkers not only for supervising my studies, fruitful discussions, helpful advice but also for an enjoyable style of leadership. Special thanks go to L. Niewolak for the excellent teamwork and good collaboration.

I am grateful to H. Hattendorf for the good cooperation and F. Tietz for the CTE measurements as well as N. Merki, H. Lippert and M. Michulitz for the chemical analysis of the materials.

I want to express special thanks to P.J. Ennis not only for the mechanical testing of the materials but also for proofreading my work.

Further I owe gratitude to, E. Wessel for help with the SEM, A. Kick and H. Cosler for conducting the high temperature exposures, J. Bartsch and V. Gutzeit for the optical microscopy and assistance with metallographic problems, H.J. Penkalla and D. Eßer for the TEM investigations, P. Huczkowski, T. Hüttel, J. Pirón Abellán, M. Subanović, J. Toscano, J. Żurek, D. Porbatzki, A. Schlüter, C. Weber, S. Ertl and M. Möllenhoff for many scientific and non-scientific discussions as well as many other colleagues from IEF-2 as well as FZJ for their help on various issues and the nice environment to work in.

In addition, I want to thank K. Natesan and his group at Argonne National Lab to host me as well as the Chalmeristerna for showing me that “rusting” can be an interesting area of research.

Finally I want to address thanks to Meike for visiting me in Jülich against earlier promise and my family, including my sister, for their support in countless issues.

1. **Einsatz von multispektralen Satellitenbilddaten in der Wasserhaushalts- und Stoffstrommodellierung – dargestellt am Beispiel des Rureinzugsgebietes**
   von C. Montzka (2008), XX, 238 Seiten
   ISBN: 978-3-89336-508-1

2. **Ozone Production in the Atmosphere Simulation Chamber SAPHIR**
   by C. A. Richter (2008), XIV, 147 pages
   ISBN: 978-3-89336-513-5

3. **Entwicklung neuer Schutz- und Kontaktierungsschichten für Hochtemperatur-Brennstoffzellen**
   von T. Kiefer (2008), 138 Seiten
   ISBN: 978-3-89336-514-2

4. **Optimierung der Reflektivität keramischer Wärmedämmschichten aus Yttrium-teilstabilisiertem Zirkoniumdioxid für den Einsatz auf metallischen Komponenten in Gasturbinen**
   von A. Stuke (2008), X, 201 Seiten
   ISBN: 978-3-89336-515-9

5. **Lichtstreuende Oberflächen, Schichten und Schichtsysteme zur Verbesserung der Lichteinkopplung in Silizium-Dünnschichtsolarzellen**
   von M. Berginski (2008), XV, 171 Seiten
   ISBN: 978-3-89336-516-6

6. **Politikszenarien für den Klimaschutz IV – Szenarien bis 2030**
   hrsg.von P. Markewitz, F. Chr. Matthes (2008), 376 Seiten
   ISBN 978-3-89336-518-0

7. **Untersuchungen zum Verschmutzungsverhalten rheinischer Braunkohlen in Kohledampferzeugern**
   von A. Schlüter (2008), 164 Seiten
   ISBN 978-3-89336-524-1

8. **Inorganic Microporous Membranes for Gas Separation in Fossil Fuel Power Plants**
   by G. van der Donk (2008), VI, 120 pages
   ISBN: 978-3-89336-525-8

9. **Sinterung von Zirkoniumdioxid-Elektrolyten im Mehrlagenverbund der oxidkeramischen Brennstoffzelle (SOFC)**
   von R. Mücke (2008), VI, 165 Seiten
   ISBN: 978-3-89336-529-6

10. **Safety Considerations on Liquid Hydrogen**
    by K. Verfondern (2008), VIII, 167 pages
    ISBN: 978-3-89336-530-2

11. **Kerosinreformierung für Luftfahrtanwendungen**
    von R. C. Samsun (2008), VII, 218 Seiten
    ISBN: 978-3-89336-531-9

12. **Der 4. Deutsche Wasserstoff Congress 2008 – Tagungsband**
    hrsg. von D. Stolten, B. Emonts, Th. Grube (2008), 269 Seiten
    ISBN: 978-3-89336-533-3

13. **Organic matter in Late Devonian sediments as an indicator for environmental changes**
    by M. Kloppisch (2008), XII, 188 pages
    ISBN: 978-3-89336-534-0

14. **Entschwefelung von Mitteldestillaten für die Anwendung in mobilen Brennstoffzellen-Systemen**
    von J. Latz (2008), XII, 215 Seiten
    ISBN: 978-3-89336-535-7

15. **RED-IMPACT**
    Impact of Partitioning, Transmutation and Waste Reduction Technologies on the Final Nuclear Waste Disposal
    SYNTHESIS REPORT
    ed. by W. von Lensa, R. Nabbi, M. Rossbach (2008), 178 pages
    ISBN 978-3-89336-538-8

16. **Ferritic Steel Interconnectors and their Interactions with Ni Base Anodes in Solid Oxide Fuel Cells (SOFC)**
    by J. Froitzheim (2008), 169 pages
    ISBN: 978-3-89336-540-1

Abstract:
This work describes the development of new ferritic interconnect steels with increased creep strength. Different modifications were tested with respect to corrosion resistance in air as well as in simulated anode gas. In addition to the investigations of corrosion resistance and creep strength it could be shown that other SOFC relevant properties remained unchanged. Finally potential interdiffusion reactions between interconnect steel and a Ni rich component and their inhibition by a diffusion barrier were discussed.

Author
Jan Froitzheim studied Materials Science first at the Technical University Darmstadt and later at Chalmers University of Technology, Göteborg, Sweden. 2005 – 2008 he worked as a PhD student in the high temperature corrosion group of Dr. Quadakkers at the Institute for Energy Research (IEF-2) in the Forschungszentrum Jülich. The content of this book was submitted as a PhD thesis to the Technical University Aachen (RWTH).

Institute of Energy Research
IEF-2 Materials Microstructure and Characterization
The research topics of IEF-2 are focussed on the development and characterization of materials for efficient gas and steam power plants, for high temperature fuel cells and for future fusion reactor components subjected to high thermal loads. The scientific expertises of the institute cover microstructural investigations, surface analysis techniques and the physical, chemical, mechanical and corrosion behaviour of metallic high temperature materials and of ceramic materials used either as structural components or as elements of coating systems.

Band | Volume 16
ISBN 978-3-89336-540-1

JÜLICH
FORSCHUNGSZENTRUM